Carlos Miguel Almeida Leitão

INFLUENCE OF BASE MATERIAL PLASTIC PROPERTIES AND PROCESS PARAMETERS ON FRICTION STIR WELDABILITY

Dissertation for the degree of Doctor of Philosophy in Mechanical Engineering, specialization in Production Technologies, supervised by Professor Dulce Maria Esteves Rodrigues, presented at Mechanical Engineering Department of the Faculty of Sciences and Technology of the University of Coimbra.

2013

· U C ·

Universidade de Coimbra

Acknowledgements

It would not have been possible to write this doctoral thesis without the help and support of the kind people around me, to only some of whom it is possible to give particular mention here.

This thesis would not have been possible without the help, support and patience of my supervisor, Professor Dulce Rodrigues, not to mention her advice and unsurpassed knowledge.

I would like to thank the support given within the host institution, CEMUC (Centro de Engenharia Mecânica da Universidade de Coimbra), chaired by Professor Valdemar Fernandes and, in ECAT (Experimental and Computer Aided Technology) research group, chaired by Professor Altino Loureiro. The good advice, support and friendship of all professors and colleagues of ECAT research group, CEMUC and DEMUC (Departamento de Engenharia Mecânica da Universidade de Coimbra) has been invaluable on both an academic and a personal level, for which I am extremely grateful.

I also want to emphasize the crucial role of ISQ (Instituto da Soldadura e Qualidade) which provided the material analysed in the present work.

I would like to acknowledge the funding provided by the FCT (Fundação para a Ciência e Tecnologia), through the SRFH/BD/46252/2008 fellowship.

Last but not least, I also would like to thank my wife Solange for her personal support and great patience at all times. My parents and friends have given me their unequivocal support throughout, as always, for which my mere expression of thanks likewise does not suffice.

Abstract

In the present work the weldability in friction stir welding (FSW) of two aluminium alloys currently used in welded construction, the Al-Mg-Si (AA6082-T6) and the Al-Mg (AA5083-H111) alloys, is analysed and related with base materials plastic properties at high temperatures and strain rates. The weldability of both alloys was evaluated by performing a deep morphological, microestrutural and mechanical characterization of a large number of welds produced under a wide range of welding conditions. Simultaneously, the plastic behaviour of both base materials was characterized by accomplishing an extensive mechanical characterization program, which included performing uniaxial tests, under different temperatures and loading conditions, as well as a deep literature review on microestrutural and phenomenological modelling of aluminium alloys plasticity. The hardening behaviour of the aluminium alloys, at high temperatures and strain rates, was then related to base material weldability. It was found that the AA6082 alloy, which displays intense flow softening during tensile loading at high temperatures, and is sensitive to dynamic precipitation and overageing under intense non-uniform deformation, displays good weldability in FSW. Under the same welding conditions, the AA5083 alloy, which in quasi-static conditions displays steady flow behaviour at high temperatures, and is sensitive to moderate hardening at high strain rates, displays poor weldability.

The relations between FSW parameters, classified as independent variables, and base material properties and weld inspection results, classified as dependent variables, were also explored based on torque sensitivity analysis. It was possible to depict a strong influence of base material properties and plate's

thickness on the torque recorded during welding. Torque sensitivity analysis also showed the suitability of this output process parameter for capturing the different sensitivity of both base materials to varying tool rotation and traverse speeds. In spite of this, the evolution of torque with tool traverse and rotation speed was found to be satisfactorily described by a unique power law equation, for both base materials, indicating that the torque registered during welding is a suitable output parameter to be used in FSW process control.

Finally, an extensive mechanical characterization of the welds produced for both alloys was accomplished using testing procedures, and strain data analysis techniques, developed under the scope of current work. From this work it was possible to conclude that the global strength of the welds was relatively independent of welding conditions, for both alloys tested in current work. In this way, the most suitable welding parameters for each alloy should be the ones that conduct to the best performance in terms of welding productivity.

Resumo

No presente trabalho é analisada a soldabilidade por *Friction Stir Welding (FSW)* de duas ligas de alumínio, correntemente utilizadas em construção soldada, a liga Al-Mg-Si (AA6082-T6) e a liga Al-Mg (AA5083-H111), e relacionada com o comportamento plástico a altas temperaturas e velocidades de deformação dessas mesmas ligas. A análise de soldabilidade baseou-se na caracterização morfológica, microestrutural e mecânica de um grande número de soldaduras, produzidas com base num leque muito variado de condições operatórias, para ambas as ligas. Simultaneamente à análise de soldabilidade, o comportamento plástico dos materiais base de ambas as ligas foi caracterizado através da realização de um amplo programa de caracterização mecânica, o qual incluiu a execução de testes uniaxiais, a diferentes temperaturas e condições de solicitação, bem como uma revisão bibliográfica profunda, sobre modelação microestrutural e fenomenológica do comportamento plástico de ligas de alumínio. Deste modo, foi possível relacionar o comportamento mecânico dos materiais base, a elevadas temperaturas e velocidades de deformação, com a sua soldabilidade em FSW. Desta análise concluiu-se que a liga AA6082, a qual evidenciou forte amaciamento quando solicitada à tracção a altas temperaturas, devido à sua sensibilidade aos fenómenos de precipitação dinâmica e envelhecimento sob de condições de deformação intensa e não uniforme, demonstra uma boa soldabilidade em *FSW*. Contrariamente ao registado para a liga AA6082, a liga AA5083, que apresenta um comportamento mecânico quase perfeitamente plástico, quando sujeita a condições de solicitação quási-estáticas a alta temperatura, bem como

encruamento moderado, em condições de elevada velocidade de deformação, apresenta fraca soldabilidade sob as mesmas condições de soldadura.

A relação entre os parâmetros de *FSW*, classificados como variáveis independentes, e as propriedades do material de base e a qualidade das soldaduras, classificadas como variáveis dependentes, foi também explorada com base na análise da evolução do binário registado pelo equipamento de soldadura durante o processo de ligação. Com base neste estudo foi possível confirmar a forte influência das propriedades do material base e da espessura da chapa no valor do binário registado durante o processo. O estudo da evolução do binário permitiu também demonstrar a aptidão deste parâmetro de saída do equipamento na captação das diferenças de sensibilidade de ambos os materiais de base à variação da velocidade de rotação e da velocidade de avanço da ferramenta. A modelação da evolução do binário, com a velocidade de avanço e a velocidade de rotação da ferramenta, permitiu confirmar que esta é satisfatoriamente descrita através de uma lei de potência, para ambos os materiais de base, indicando que este parâmetro (binário) será adequado para ser utilizado como parâmetro de controlo do processo FSW.

Finalmente, procedeu-se a uma extensa caracterização mecânica das soldaduras produzidas para ambas as ligas de alumínio, a qual foi realizada com base em procedimentos de teste e técnicas de tratamento de dados, desenvolvidas no âmbito deste trabalho. Através deste estudo foi possível concluir que, na ausência de defeitos, a resistência global da ligação é relativamente independente das condições de soldadura, para ambas as ligas de alumínio analisadas neste trabalho. Deste modo, para cada uma das ligas, a selecção dos parâmetros mais adequados para a realização das soldaduras dependerá apenas de factores ligados à economia do processo, ou seja, à garantia das condições de produtividade mais vantajosas, normalmente ligas à utilização de velocidades de soldadura mais elevadas.

Index of Contents

Index of Figures

Tables Index

1
Introduction and reading guide

This first chapter intends to contextualize the reader into the subject of the thesis and to provide a brief summary of text organization and chapter content.

This Page Intentionally Left Blank

Motivation

In our days the Friction Stir Welding (FSW) process is being considered one of the most interesting techniques for the joining of metallic alloys. However, the extended application of this welding process in industry still requires an accurate knowledge of the joining mechanisms, the metallurgical and mechanical transformations induced by it on the base materials, and based on this knowledge, the establishment of suitable welding parameters for the similar and dissimilar joining of a large range of materials in varied weld configurations, such as, different plate thicknesses or joint geometries. Analysing the literature on this subject, it was easy to conclude that most of the works published were focused on the analysis of the influence of process parameters, and heat generation during FSW, on the final properties of the welds. However, in spite of being a solid state welding process in which plastic deformation is considered the major mechanism promoting the joining of the plates, works relating base materials plastic properties, at high temperatures and strain rates, with base materials weldability in FSW are still very scarce. Actually, it is also very difficult to find in literature references comparing the weldability in FSW of different base materials, under a large range of welding conditions. In this context, the analysis of the influence of base materials plastic behaviour on weldability in FSW of two aluminium alloys was established as the main subject in the present work.

Reading guide

Two base materials, a heat-treatable (AA6082-T6) and a non-heat treatable (AA5083-H111) aluminium alloy, characterized by markedly different strengthening mechanisms and microstructural evolution at high temperatures, were used to perform the analysis of the influence of base materials plastic behaviour on weldability by FSW. In order to establish a relation between material flow during FSW, the plastic properties of the base materials, at high temperatures and strain rates, and weld characteristics, an extensive microstructural and mechanical characterization work, of the base materials and similar friction stir welds, produced using a large set of welding conditions, was performed.

The friction stir welds were done, by the Instituto de Soldadura e Qualidade (ISQ), from both base materials using different tool and welding parameters. Due to the strong influence of plate thickness, on heat generation and dissipation during welding, two different plate thicknesses were used for each base material. A detailed description of the welding conditions tested is provided in *Chapter 3 - Experimental Procedure*. In this chapter are also described all the metallographic and mechanical characterization techniques used in this work. Since some of the mechanical characterization procedures were developed under the scope of current work, namely, the mechanical characterization of welds based on Digital Image Correlation (DIC) and shear testing procedures, a detailed description of each of these procedures, as well as of all the tests accomplished to validate it, are also provided in this chapter. This information is also published in three papers placed in Annexes *A* to *C*.

In *Chapter 4 - Visual inspection and morphological analysis*, the results of the visual inspection and metallographic analyses of the welds, performed according to the procedures described in Chapter 3, are detailed. These results enabled to compare the weldability in FSW of both alloys and to establish some relations between process parameters and defect formation during FSW. Again, the results of this analysis are already published in two papers which are provided in Annexes *D* and *E*.

The next step in the investigation consisted in analysing the mechanical behaviour of the base materials, at varied temperatures and strain rates, in shear and tension, as is also described in Chapter 3. The mechanical behaviour of the base materials, is discussed and compared in *Chapter 5 - Analysis of base materials plastic behaviour*, based on the stress-strain response recorded during the experimental programme, as well as on an extensive literature review on microstructural and phenomenological modelling of aluminium alloys plasticity. The relation between base materials weldability and plastic properties is finally established in *Chapter 6 - Analysis of the influence of base materials plastic properties on weldability*. A study of the influence of base material plastic properties, on welding conditions and process control, is also performed in *Chapter 7 - Torque sensitivity analysis*. The main results and conclusions from these chapters were published in the papers provided in Annexes *F* to *H*.

Finally, in *Chapter 8 - Mechanical characterization of the welds*, the results of the mechanical characterization of the full set of non-defective welds produced under the scope of current work is provided, being thoroughly discussed the relation between weld plastic properties, microstructure and process parameters. Most of the results presented in this chapter are already published in the papers in Annexes *A* to *H*. The main conclusions of the research performed, and described along the thesis, are summarized in *Chapter 9*, named, *Outputs and future research*.

List of papers that are the base of this thesis

Annex *A* - C. Leitão, I. Galvão, R.M. Leal, D.M. Rodrigues. *"Determination of local constitutive properties of aluminium friction stir welds using digital image correlation"*, Materials & Design 33(1), pp. 69-74, 2012.

Annex *B* - C. Leitão, M.I. Costa, K. Khanijomdi, D. M. Rodrigues. "*Assessing strength and local plastic behaviour of welds by shear testing"*, Materials & Design, 51 pp. 968 – 974, 2013.

Annex *C* - C. Leitão, A. Loureiro, D.M. Rodrigues. *"Assessment of mechanical shear response using digital image correlation",* 15th International Conference on Experimental Mechanics (ICEM'12). 22-27 July. Porto, Portugal.

Annex *D* - D.M. Rodrigues, C. Leitão, R. Louro, H. Gouveia, A. Loureiro. *"High speed friction stir welding of aluminium alloys".* Science and Technology of Welding and Joining, 15(8), pp. 676-681, 2010.

Annex *E* - C. Leitão, A. Loureiro, D.M. Rodrigues. "*Influence of base material properties on defect formation during FSW*", International Congress on Advances in Welding Science and Technology for Construction, Energy and Transportation Systems. 24-25 October 2011. Antalya, Turkey.

Annex *F* - C. Leitão, R. Louro, D.M. Rodrigues. *"Analysis of high temperature plastic behaviour and its relation with weldability in friction stir welding for aluminium alloys AA5083-H111 and AA6082-T6"*, Materials & Design, 37, pp. 402-409, 2012.

Annex *G* - D.M Rodrigues, C. Leitão, R. Louro, A. Loureiro. "*Viscoplastic materials behaviour and its influence on friction stir weldability"*. 8th International Symposium on Friction Stir Welding. 18 - 20 May 2010. Germany.

Annex *H* - C. Leitão, R. Louro, D.M. Rodrigues. *"Using torque sensitivity analysis in accessing Friction Stir Welding/Processing conditions"*, Journal of Materials Processing Technology, 212(10), pp. 2051-2057, 2012.

2
Scientific Background

In this chapter is presented the state of the art concerning to aluminium alloys and the Friction Stir Welding (FSW) process. More precisely, in the first part of the chapter will be shown the generalities about aluminium alloys, and, in particular, about the AA6082-T6 heat treatable and, the AA5083-H111 non-heat treatable aluminium alloys, which are used in this work.

In the second part of the chapter, a full description of the FSW process will be presented, as well as a review on the known influences of process parameters on FSW results.

This Page Intentionally Left Blank

About aluminium alloys

As known, aluminium is considered a light weight material (2.76 g/cm^3). The FCC crystallographic structure of this material ensures its structural stability up to the melting point (657 ºC), simultaneously insuring a high number of slip planes that promotes its excellent plastic properties.

Aluminium strength is currently improved by using alloying elements, such as Copper (Cu), Magnesium (Mg), Silicon (Si), Zinc (Zn) and Lithium (Li), which display suitable solubility in aluminium. Other elements, such as Cromium (Cr), Manganese (Mn) and Zirconium (Zn) are also used as alloying elements, however, due to its lower solubility, these elements give rise to compounds that mainly help in controlling the grain structure. Actually, the aluminium alloys (Al alloys) are categorized into different families according to the alloying element used to obtain the required properties. Beyond the alloying elements, the Al alloys mechanical properties may be also enhanced by using different strengthening procedures. In this way, each aluminium alloy presents unique properties, which are distinguished by a unique Aluminium alloy designation.

Aluminium alloy families

The wrought aluminium alloys, such as that used in current work, are usually identified using a nomenclature, which, according to the ANSI H35.1(M)-1997 standard, as shown in Figure 2.1, is composed by the "AA" followed by 4 digits (AA*abcd*), where the first digit (*a*), which is a value comprised between 1 and 9, identifies the major alloying class. Accounting to the alloying content and type, each aluminium alloy class presents different mechanical and metallurgical properties, as it is shown in Figure 2.2, where the ultimate tensile

stress ranges, obtained from the literature (ASM-International, 1995), for each class of aluminium alloys of Figure 2.1 are displayed. From the figure it is possible to depict the higher strength of the 7xxx family when compared, for example, with the 1xxx family alloys. In this way, the differences between alloy classes define the application field of each aluminium alloy, fact that can also be assessed observing Figure 2.1, where are also described the main applications for each aluminium class.

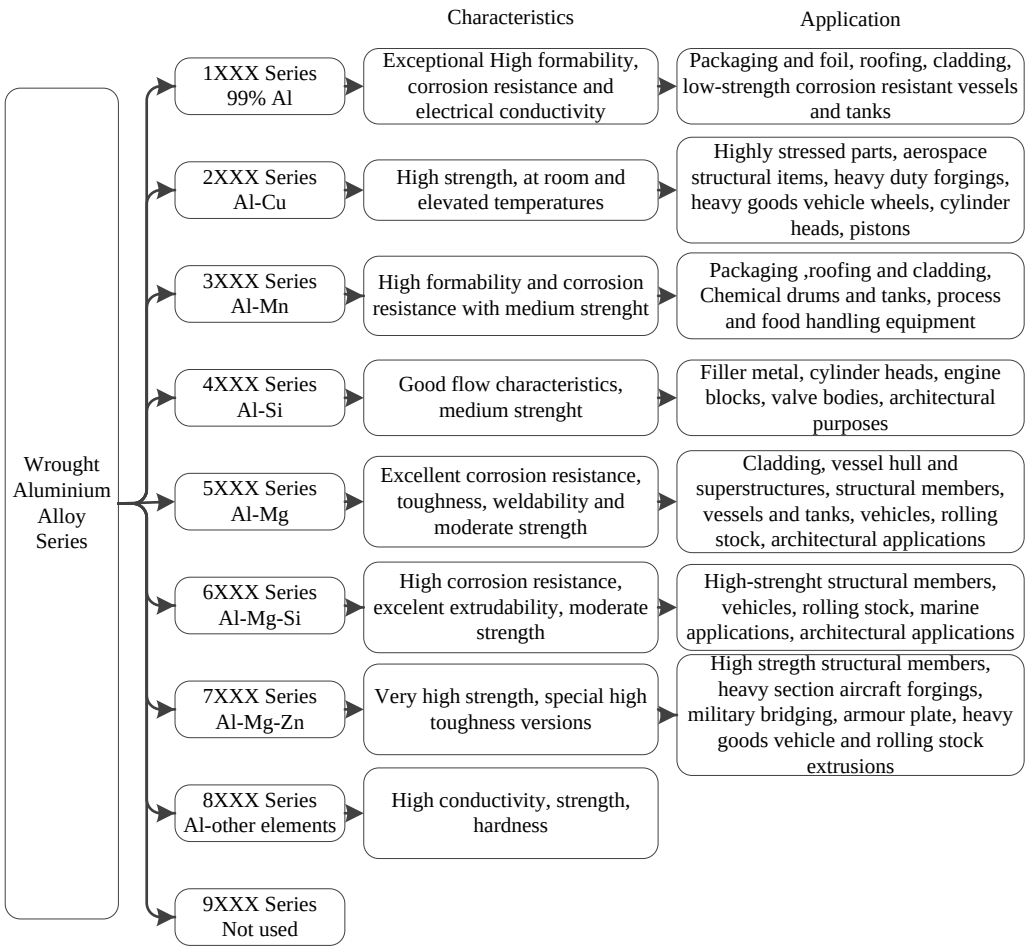

Figure 2.1 – Aluminium alloying elements and series name correspondence, and individual applicability. (ASM International, 1995)

The tensile strength ranges in Figure 2.2 can be attributed to different alloy compositions, alloy contents and/or strengthening processes. In this way, the second digit of the standardized alloy designation (*b*) signalizes variations from the original alloy composition, being 0 (zero) if it refers to the original composition. On the other hand, third and fourth digits (*c* and *d*) designate specific alloys within each series.

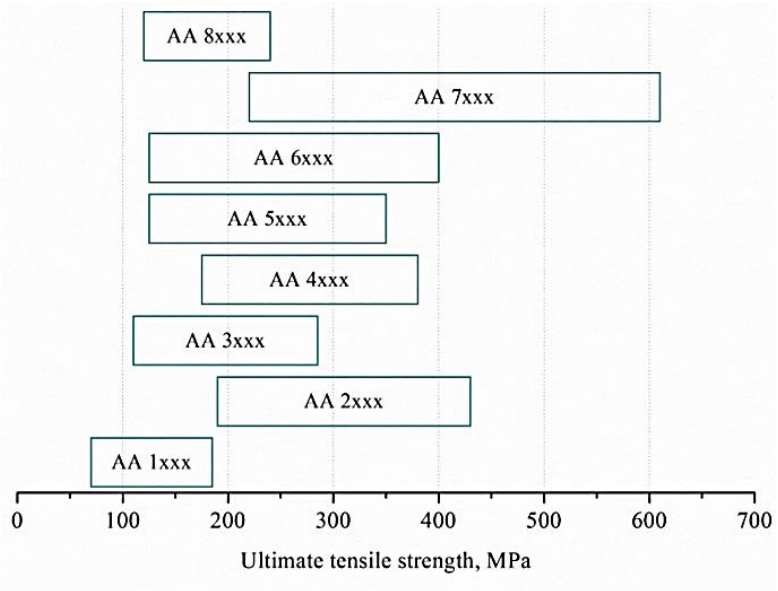

Figure 2.2 – Ultimate tensile strength ranges comparison between aluminium alloy different series. (ASM International, 1995)

The wrought aluminium alloys can be also classified as heat and non-heat treatable alloys. Meanwhile the non-heat treatable aluminium alloys are mainly hardened by cold working, the heat treatable aluminium alloys are hardened by heat treatment. From the previously referred series, the 2xxx, 6xxx, 7xxx and 8xxx series are heat-treatable alloys and, the 1xxx, 3xxx, 4xxx and 5xxx series are non-heat treatable alloys.

Aluminium alloy strengthening mechanisms

The strength of wrought aluminium alloys, for either heat or non-heat treatable alloys can be improved by different processing methods. In Table 2.1 are shown the five basic wrought aluminium temper designations, of which, the most commonly used are the *T* (thermally treated) and *H* (strain hardened) tempers. In fact, according to Benedyk (2010), these two temper classes are valued for their ability to provide high strength-to-weight ratio alloys: the H temper, by work hardening, and the T temper, by precipitation hardening.

Table 2.1 – Basic temper designations

F	As fabricated
O	Annealed
W	Solution heat-treated
T	Thermally treated
H	Strain-hardened

According to ANSI H35.1(M)-1997 standard, the strain hardened alloys are usually identified using the "H*xx*" acronym, as described in Table 2.2, after the alloying designation. In this acronym the first suffix refers to the secondary treatment used to influence the properties and the second suffix indicates the degree of strain hardening, varying from 0 to 9. A third suffix can also be added when the degree of control of temper or the mechanical properties are different from the 0 condition, but close to the two-digit H temper designation.

Table 2.2 – H Temper denominations

H1	Cold worked only
H2	Cold worked Partially annealed
H3	Cold worked Stabilized

The precipitation hardening temper designations, governed by the ANSI H35.1(M)-1997 standard, are identified by a "T*xx*" acronym, after the alloying designation. As is possible to depict from Table 2.3, the temper conditions can be numbered from 1 to 10, according to the strengthening sequence. Different heat treatments conduct to different precipitate size and density, which, consequently, promotes different mechanical behaviours and strength, even using the same volume of alloying compounds.

Table 2.3 – T Temper denominations

T1	Cooled from an elevated temperature shaping process and naturally aged
T2	Cooled from an elevated temperature shaping process, cold worked and naturally aged
T3	Solution heat-treated, cold worked and naturally aged
T4	Solution heat-treated and naturally aged
T5	Cooled from an elevated temperature shaping process, and then artificially aged
T6	Solution heat-treated and then artificially aged
T7	Solution heat-treated and overaged
T8	Solution heat-treated, cold worked, and then artificially aged.
T9	Solution heat-treated, artificially aged, and then cold worked.
T10	Cooled from an elevated temperature shaping process, cold worked, and then artificially aged

Precipitation hardening

The precipitation hardening of an aluminium alloy is only possible if the alloy contains an element, such as Copper (Cu), Zinc (Zn), Silicon (Si) and/or Magnesium (Mg), which has a decreasing solubility in aluminium at decreasing temperatures.

The precipitation strengthening process is performed in three different steps: solution heat-treating, quenching to a lower temperature and, finally, ageing. The final alloy mechanical properties are defined during the ageing stage by controlling the time and ageing temperature, as can be depicted by observing Figure 2.3, where it is schematized the strength evolution versus ageing time for an Al-Cu alloy. As observed in the figure, during ageing, the dispersoids present in the supersaturated solid solution (SSSS) will precipitate, in a first step, forming small solute clusters of precipitates, called *Guinier-Preston* (GP) zones which are solute rich domains that are fully coherent with the matrix. The GP zones are extremely fine with sizes in the range of tens of angstroms. After that, the continued precipitation of particles, leads to the formation of larger particles, which promotes weaker resistance to dislocations movement and, consequently, non-optimized mechanical properties. The different steps of ageing are respectively signalized, in Figure 2.3, as under, peak and over aged.

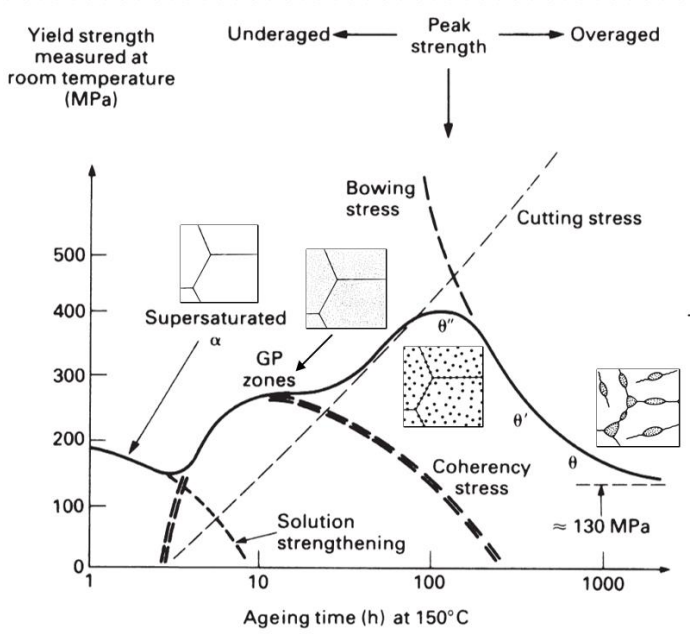

Figure 2.3 – The yield strength of quenched Al–4 wt% Cu changes during ageing at 150°C. (Adapted from Ashby and Jones, 1998)

Strain hardening

The work hardening is used extensively to produce strain-hardened tempers of non-heat treatable alloys.

After cold work, the entanglement of internal dislocations and the increase of its density lead to a strength increase and, a decrease on ductility. The dislocation structure resulting from cold working of aluminium is less stable than the strain-free, annealed state.

During the annealing procedure, which includes the recovery, the recrystallization and the grain growth stages, the internal stresses are reduced, and grain size increased, which slightly affects the general strength and increases substantially the material ductility and elongation, as can be depicted from the mechanical and microstructural properties evolution diagram shown in Figure 2.4. It also important to emphasize that, during recovery, due the temperature and/or time applied, the dislocations are greatly reduced in number and often rearranged into a cellular sub-grain structure internal stresses induced by cold work, will be reduced. With increasing time and heating temperature, recovery proceeds and sub-grain size gradually increases. In ASM-International (1995), is also referred that, in this stage, many of the sub-grains have boundaries that are completely free of dislocations.

Finally, heating for longer times, at higher temperatures, the grain growth, which improves the alloy ductility, is promoted. During this stage, it is also important to emphasize that, dispersoids of Mn, Cr and Zn can be used in order to supress the grain growth and control the alloy final mechanical properties.

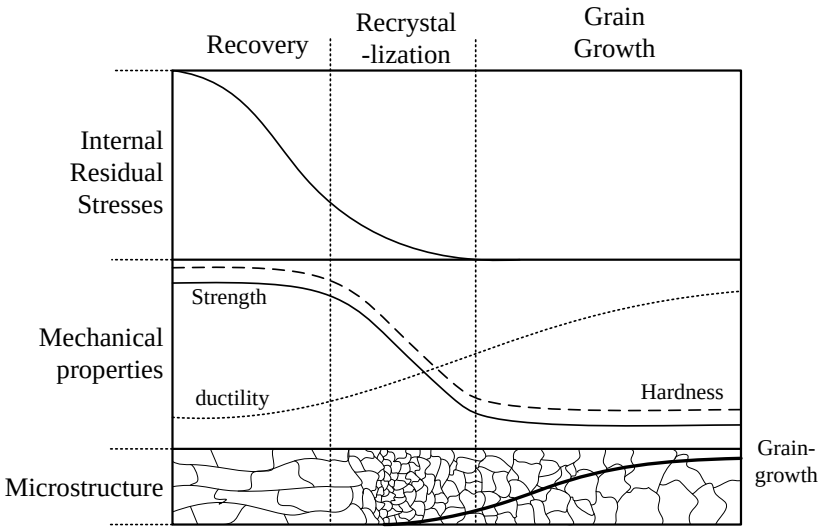

Figure 2.4 – Scheme of the evolution of internal residual stresses, mechanical properties and microstructure, verified during annealing.(adapted from NDT-ed, 2013)

Studied Alloys

In current work friction stir weldability is analysed for two aluminium alloys, very popular in welding construction: the AA6082-T6 heat treatable and the AA5083-H111 non heat-treatable aluminium alloys. The main alloying elements of these alloys are the Magnesium (Mg) and Silicium (Si), and the Magnesium (Mg), respectively.

The AA6082-T6 alloy

The well-known AA6082-T6 aluminium alloy, which composition and mechanical proprieties are described in Table 2.4, is proposed as a material for high duty applications, such as structural frames, pylons, towers and bridges.

Being a heat-treatable alloy, the strength of the artificially aged AA6082-T6 alloy is based on the precipitate distribution within the material. According

to the reference literature (Read-Hill, 1972; ASM International, 1995; Smallan and Bishop, 1999; Totten and Mckanzie, 2003), for the Al-Mg-Si alloys, the hardening precipitates are those of β family. After natural or artificial ageing, as described in precipitation sequence,

$$SSSS \rightarrow \text{GP zones} \rightarrow \beta'' \rightarrow \beta' \rightarrow \beta\ (Mg_2Si)$$

where, β'' and β' are intermediate precipitation phases, the β precipitates evolve in order to form stable binary precipitates Mg_2Si.

Table 2.4 – Chemical composition (%wt) and mechanical properties at room temperature, of AA6082-T6 alloy

Chemical Composition [%wt]								
Cr	Cu	Fe	Mg	Mn	Si	Ti	Zn	Other
<0.25	<0.1	<0.5	0.6-1.2	0.4-1.0	<0.15	0.7-1.3	<0.1	<0.2
Mechanical Properties								
Hardness [HV]		YS [MPa]		UTS [MPa]		Elongation [%]		$T_{solidus}$ [ºC]
95-105		240-290		280-340		5-11		575-650

The AA5083-H111 alloy

This Al-Mg (AA5xxx family) alloy is also pointed as structural aluminium, used for transportation and military related applications. The main advantages of this alloy are its moderate-strength and weldability (considering conventional fusion welding processes), presenting also a good corrosion resistance. In Table 2.5 are described the composition and the mechanical proprieties of the AA5083-H111 alloys.

Table 2.5 – Chemical composition (%wt) and mechanical properties at room temperature, of AA5083-H111 alloy

Chemical Composition [%wt]								
Cr	Cu	Fe	Mg	Mn	Si	Ti	Zn	Other
0.05-0.25	<0.1	<0.4	4.0-4.9	0.4-1.0	<0.4	<0.15	<0.25	<0.05

Mechanical Properties				
Hardness [HV]	YS [MPa]	UTS [MPa]	Elongation [%]	$T_{solidus}$ [ºC]
71.3-78.8	131-165	221-276	12-13.9	574-638

The H111 temper promotes a strength value close to O condition, due the work hardening imparted by shaping processes, less than required for H11 temper.

The Friction Stir Welding (FSW) process

In the year of 1991, the Welding Institute (TWI) (Thomas and Nicolas, 1997) introduced the friction stir welding process to the community, as a remarkably simple joining process. As schematized in Figure 2.5, this welding technology uses a non-consumable rotating tool, with a specially designed pin and shoulder, which is inserted into the abutting edges of the sheets or plates to be joined, and subsequently, traversed along the joint line. In this technology, the temperature promoted by the friction of the tool with the plates surface is high enough to plasticize the material without reaching its melting point, which complementary with the dragging of the material, also promoted by the tool, leads to the weld formation.

According to Figure 2.5, where the FSW tool was represented rotating in the clockwise direction and traveling into the page, it is possible to distinguish two different metal flow sides, which are the advancing side (*AS*) and the retreating side (*RS*). Meanwhile in the advancing side (*AS*), represented at the left side of the figure, the tool rotation direction is the same as the tool travel direction, in the retreating side the tool rotation is opposite to the tool travel direction.

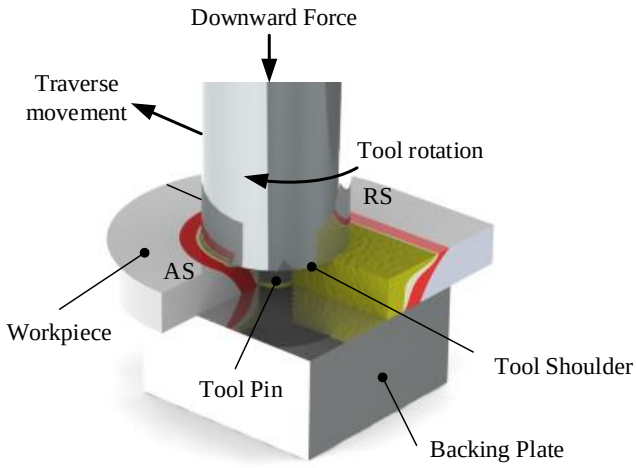

Figure 2.5 – Friction Stir Welding Scheme.

In Figure 2.6, the FSW joining sequence is schematically shown in four steps, among which the tool is permanently in rotation. In the first step (see Figure 2.6a), the tool approaches the plates to be joined until the pin tip reaches its surface. In the second step, the rotating too is inserted into the abutting surfaces until the contact between the tool shoulder and the blank surface is established, promoting heating by friction and, consequently, the softening of the material beneath (see Figure 2.6b). The contact between the tool shoulder and the work piece creates a reactive force perpendicular to the blank surface,

called downward force. In this stage, the tool is maintained in the same position during a certain time interval, which is named “dwell-time”. After the dwell period, in the third step (Figure 2.6c), the tool is animated with constant traverse movement, which complemented by the tool rotational movement and downward force, promotes the heating of the material and its flow beneath the shoulder and around the pin. In the last step, at the end of the weld (Figure 2.6d), the tool starts the ascending movement, being extracted from the plates, leaving a final print (see detail *i* in Figure 2.6d), which is characteristic of FSW welds. This feature is commonly pointed as a process handicap, considering that it acts as “the weakest link effect” to the mechanical properties (Huang *et al.*, 2011) and causes time loss when weld post-processing techniques are needed to remove it. In fact, some simple techniques were already developed in this field, such as the use of two complementary plates, located at the beginning and at the end of the plates to be welded.

In the detail (*ii*) of Figure 2.6d), it is also possible to observe a weld surface image and conclude that the weld crown morphology is similar to feed marks in machining, promoted by the tool action during the process (Edwards and Ramulu, 2009). These marks are characterized by regularly spaced bands, which, according to Mishra *et al.* (2007) are directly related with tool traverse and rotational speeds.

Since its development, the main research efforts in FSW envisaged the production of good quality welds, the mechanical and metallurgical characterization of the welds. Initially the studies were mainly focused on aluminium, but nowadays, the research fields on FSW include the production of similar and dissimilar welds using other alloys and/or materials, which is very difficult to perform using conventional fusion welding processes. The first aluminium alloys welded by FSW were those commonly applied in the aerospace and transportation industries, i.e., the almost pure AA1xxx aluminium alloy (Murr *et al.*, 1997; Flores *et al.*,1998) and the heat-treatable

alloys, such as the, Al-Mg-Si (Liu *et al.*, 1997; Thomas and Nicolas, 1997; Murr *et al.*, 1998), the Al-Mg-Zn (Rhodes *et al.*, 1997; Mahoney *et al.*, 1998) and the Al-Li-Cu (Li *et al.*, 1999a,b ; Benavides at al., 1999) aluminium alloys. FSW of the non-heat treatable aluminium alloys was introduced later, being mainly addressed to the Al-Mg alloys (Jata *et al.*, 2000; Jin *et al.*, 2000).

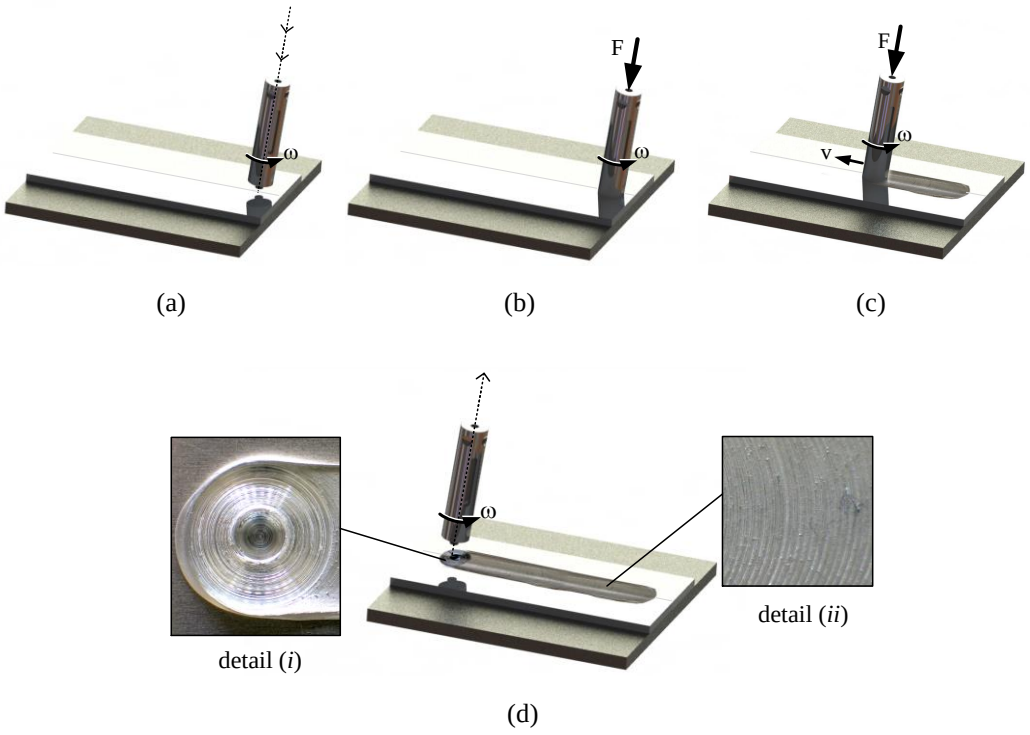

Figure 2.6 – Scheme of FSW relevant process steps: approximation (a), plunge (b), travel (c), and tool ascend (d).

Nowadays, the FSW of aluminium alloys and other materials is a widely studied subject and, consequently, several review works can be found, such as, Mishra and Ma (2005), Mishra and Mahoney (2007); Nandan *et al.*(2008), Threadgill *et al.*(2009), Murr (2010) and Çam (2011).

Another research field, also considered with a high level of interest, is the production of dissimilar welds, as represented in Figure 2.7, where are shown the most relevant works in this field, according to the ISI – Web of Science index. Eberl *et al.* (2010) argues that the FSW process and the high performance of its welds, constitutes a new opportunity in terms of aerospace design. Thick friction stir welded parts will contribute to optimise material usage, by manufacturing nearer net shape products, as well enable tailoring the mechanical response of the final structural part, by the construction of tailor welded blanks (TWBs), which is important in transportation industry. Optimising the alloy location, within the structure, according to their properties, can improve the efficiency of the fabricated parts.

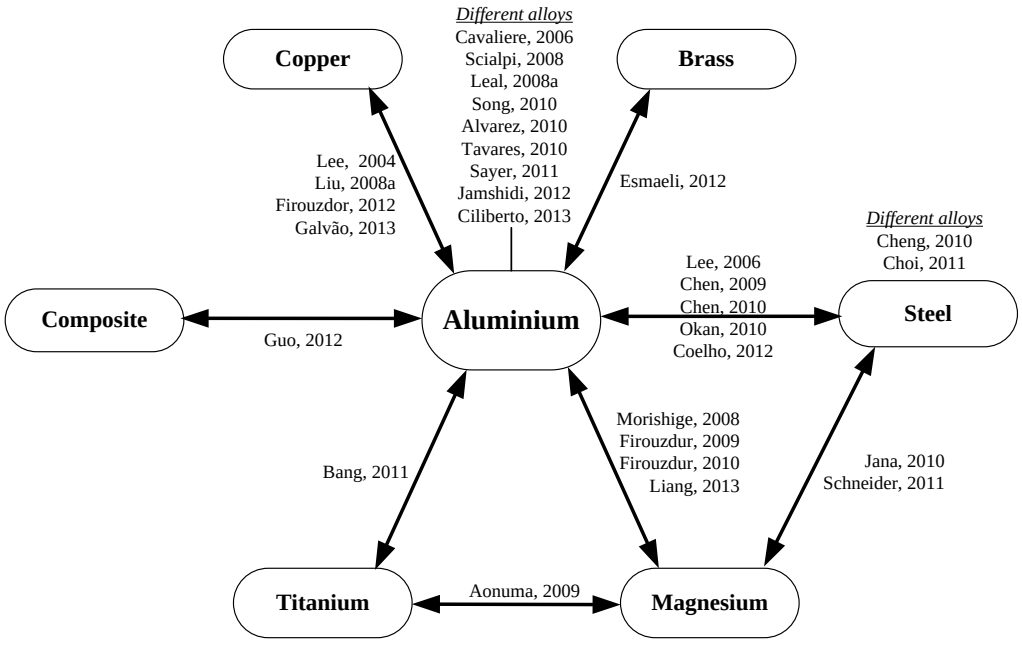

Figure 2.7 – Material pairs already addressed in the literature for dissimilar FSW.

The FSW technique also presents a high versatility and low level of restrictions concerning joint configuration. In Figure 2.8 are shown schemes of some allowed joint configurations using FSW (Mishra and Ma, 2005), and it is possible to depict the butt (Figure 2.8a), the lap (Figure 2.8b), the multi-lap (Figure 2.8c), the edge butt (Figure 2.8d), the T-butt (Figure 2.8e), the T-lap (Figure 2.8f) and the Fillet (Figure 2.8g) weld joints.

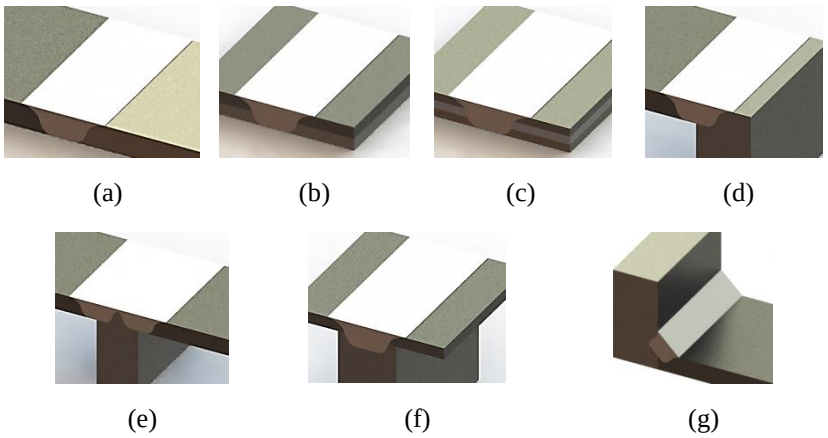

Figure 2.8 – FSW joint configurations (adapted from Mishra and Ma, 2005)

Another improvement promoted by the use of the FSW technology, relays in the decrease of the time loss in edge preparation before welding, since there is no need of a special surface preparation. Nevertheless, the use of this technology requires that the two plates or sheets must be placed on a backing plate and clamped firmly to prevent the abutting joint faces from departing. The development of free spaces between the abutting joint faces compromises the weld consolidation, and consequently, leads to bad welding results.

As in other well-known welding technologies, it is imperative to insure the production of good quality welds, free of defects, in order to make the FSW technology industrially reliable. The scientific community had already identified the most common defects associated with this technology, which are shown in Figure 2.9. Despite not being yet established any standardization concerning their classification (Kim *et al.*, 2006; Chen *et al.*, 2006; Iordachescu *et al.*, 2009) the main types of defects already detected were the formation of a large mass of flash (see Figure 2.9a), internal and/or superficial cavities (see Figure 2.9b) and grooves (see Figure 2.9c). The origin of these defects is currently attributed to inappropriate heat input and/or deficient stirring of the materials, both influenced by the utilization of inadequate process and/or tool parameters (Elangovan and Balasubramanian, 2008; Padmanaban and Balasubramanian, 2009). Arbegast (2008) stated that, the complex interactions between the tool and the material, the base material properties and the process parameters, strongly affects the formation of defects. This fact shows the importance of understanding the process mechanisms, by depicting the role played by each process parameter during the process and, consequently, on final weld results.

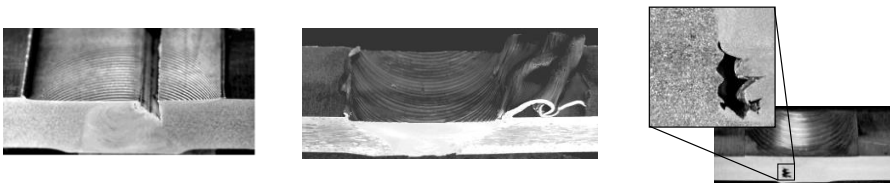

(a) (b) (c)

Figure 2.9 – Main types FSW defects.

FSW Process Parameters

In Figure 2.10 are schematically shown the main parameters affecting the FSW process, which can be categorized as static (Figure 2.10a) and dynamic parameters (Figure 2.10b). The static parameters are mainly related to the tool characteristics such as, the dimension and geometry of both shoulder and pin. In Figure 2.10a) are shown the key dimensions of a concave shoulder tool, which is the most widely used FSW tool. As shown in the figure, the tool dimensions to be considered are the shoulder diameter (D_s), the pin diameter (D_p), the concavity angle (α_s) and the pin length (L_p). On the other hand, the parameters associated to the tool positioning and the movement during the process, which are schematically shown in the Figure 2.10b), are considered as dynamic parameters, which, according to the figure, are the plunge depth (l_{dz}), the tilt angle (α), the rotational speed (ω), the traverse speed (v) and the downward force (F_z).

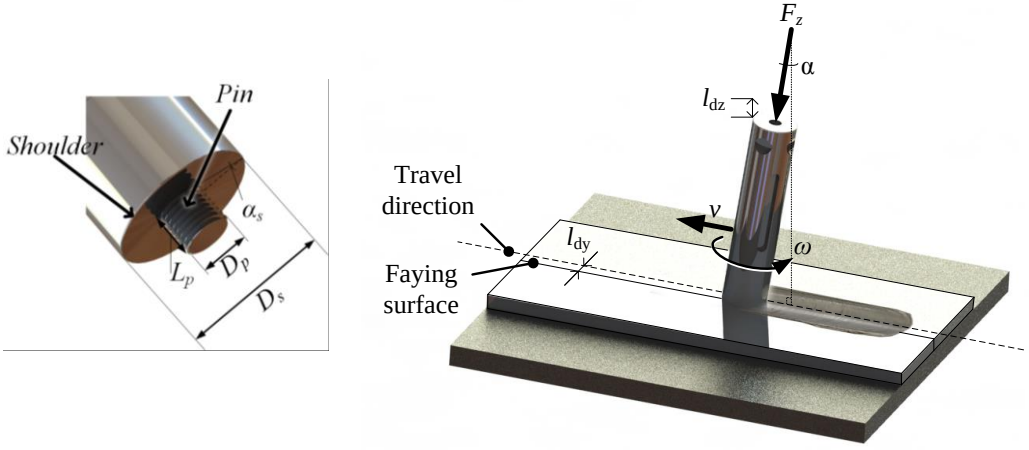

(a) (b)

Figure 2.10 – Scheme of the FSW static (a) and dynamic (b) parameters.

However, other process parameters, besides those already considered, may play a key role in final weld results. These process parameters, such as the tool positioning relatively to the faying surface of the plates (l_{dy}), the plates thickness (t) and, particularly, in dissimilar FSW, the base material positioning, at the retreating or at advancing side. This positioning is intrinsically related with base material plastic behaviour, which despite being consensually assumed with strong influence on weldability, has never been treated as a weld parameter. In the diagram of Figure 2.11 are shown all process parameters, including those which are not commonly considered as process parameters (grey blocks).

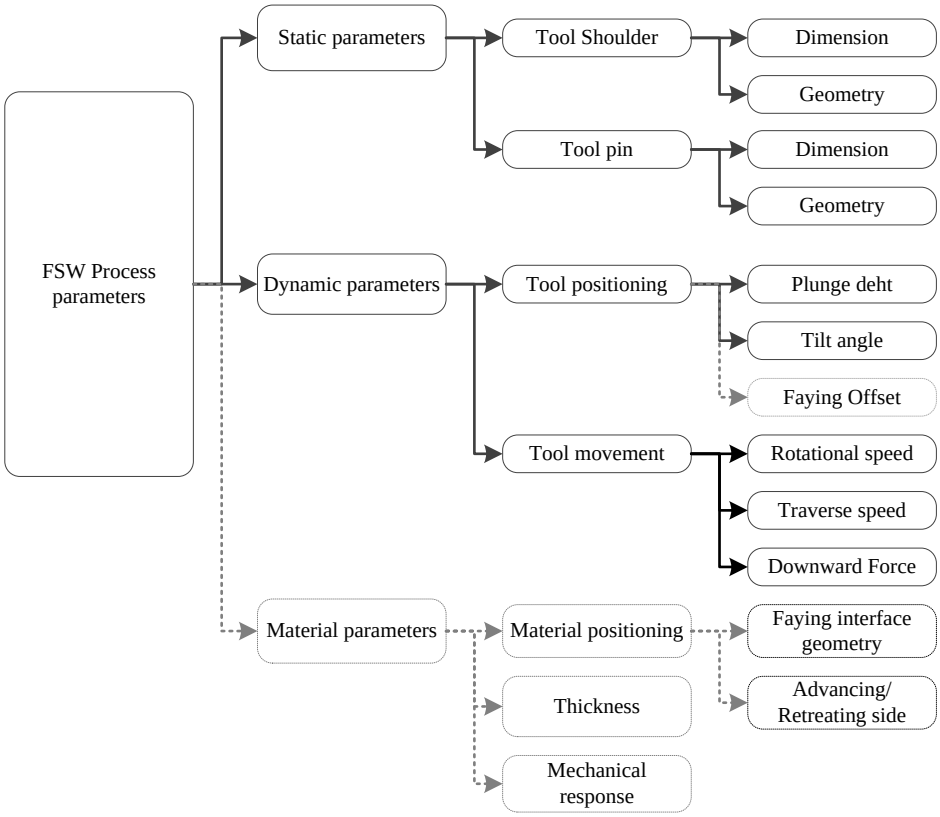

Figure 2.11 – Diagram of the FSW process parameters.

The correct combination of all these parameters is considered highly crucial on FSW, namely, to promote the optimization of the metal flow and, consequently, to improve weld quality.

Material flow during the process

The flow of material around the tool is not symmetric, relatively to the weld centreline displaying significant differences between the advancing and retreating sides (Seidel and Reynolds, 2001; Fratini *et al.*, 2006; Schmidt *et al.*, 2004; 2005a; Zhao *et al.*, 2006; Arbegast, 2008; Kumar and Kailas 2008a,b). According to several authors, vertical, straight-through and rotational flows of plasticized material take place in the vicinity or around the tool, dragging the bulk of the stirred material to a final position behind its original position (Seidel and Reynolds, 2001; Guerra *et al.*, 2002; Zhao *et al.*, 2006; Kumar and Kailas 2008b; Chen *et al.*, 2008; Reynolds, 2008). In the wake of the weld, behind the travelling tool, material deposition takes place layer-by-layer resulting in the formation of a zone with a banded structure commonly referred as the *nugget*. Spacing between banding in the *nugget* is typically the same as the distance travelled by the tool during a single rotation (Kumar and Kailas, 2008b; Krishnan, 2002; Schnneider and Nunes Jr., 2004; Chen *et al.*, 2008; Xu and Deng, 2008; Reynolds, 2008; Yang *et al.*, 2004; Chen and Cui, 2008).

With regard to the influence of the tool in the FSW flow, two different modes of tool related flows are frequently mentioned in literature: shoulder-driven flow and pin-driven flow (Kumar and Kailas, 2008a,b; Schmidt *et al.*, 2004; Zhao *et al.*, 2006; Guerra *et al.*, 2002; Chen *et al.*, 2008; Chen and Cui, 2008; Muthukumaran and Mukherjee, 2006, 2008). These two tool related flows can be depicted in the schemes of Figure 2.12. As shown in Figure

2.12a), where the shoulder driven flow is represented, this flow is promoted by the material dragged by the tool shoulder. On the other hand, the pin-driven flow, as shown in Figure 2.12b), is characterized by the material flowing from the leading side to the trailing side, on both retreating and advancing sides of the pin. Several studies, addressing the influence of pin geometry on material flow during FSW have been developed (Seidel and Reynolds, 2001; Fratini *et al*, 2006; Zhao *et al.*, 2006; Muthukumaran and Mukherjee, 2006). On the other hand, the influence of shoulder geometry on material flow can be depicted from Leal *et al.* (2008a) and Galvão *et al.* (2010). The strong influence of shoulder geometry on the microstructure and mechanical behaviour was reported by Scialpi *et al.* (2008), Elangovan and Balasubramanian (2008) and Kumar *et al.* (2008b). All of the studies referred address FSW of different plate thicknesses.

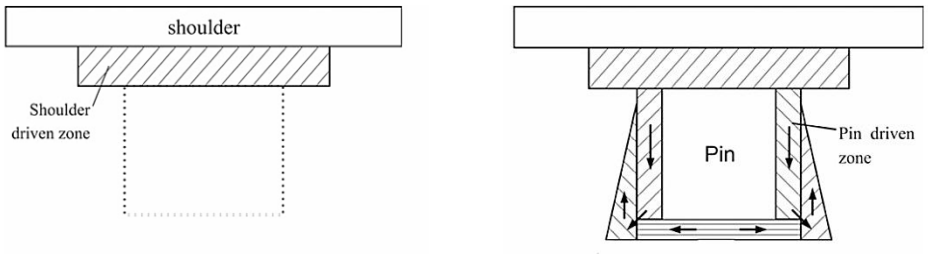

(a) (b)

Figure 2.12 – Conceptual diagrams of shoulder and pin-driven flows (adapted from Zhang *et al*., 2011b)

Arbegast (2008), in particular, studied the influence of material flow on defect formation. According to the author, the flow-related defects occur outside the acceptable processing parameter window, for welding conditions that can be considered either too hot or too cold. The author also refers that the optimum processing conditions to prevent flow related defects occur at a

temperature where stick–slip wiping flow occurs, and the material flowing from the region ahead of the pin is exactly balanced by that flowing back, into the vacated region behind the tool. According to Schmidt and Hattel (2005b), sticking conditions at the tool-workpiece interface are developed when the friction shear stress at the interface exceeds the yield shear stress of the underlying base material. When the contact shear stress is smaller than the base material yield shear stress, sliding conditions prevail. Arbegast (2008) stated that under hot processing with stick conditions, excessive material flow results in flash formation, surface galling and nugget collapse. Under cold processing with slip conditions, insufficient material flow results in surface lack of fill, wormholes or lack of consolidation on the advancing side.

According to the flow-partitioned deformation zone model proposed by Arbegast (2008), schematized in Figure 2.13, advancing (Zone I) and a retreating (Zone II) deformation zone geometries form around the pin with different volumes, velocity and flow directions. Material passing through Zone II moves downward and around the probe and converges with the material in Zone I. Material passing through Zone II may move far enough downward to enter Zone IV beneath the probe tip and again rise to merge with the materials within Zone I. The Zone III, originating from the retreating side, is dragged across the top, toward the advancing side. On the other hand, Zone III material is ‘‘interleaved’’ with the Zone III material originating on the advancing side and forced (pumped) downward to fill Zone I from the top. Excess flow of Zone III material into Zone I results in nugget collapse. Loss of material from Zones II, III or IV cause by flash formation, sheet lifting or sheet separation, will directly cause an insufficient amount of material entering in Zone I and, consequently, promoting defects such as surface lack of fill, wormhole or lack of consolidation (microvoid/scalloping) volumetric defect. The author also showed that, a critical mass flux of material must move from the front leading-edge of the tool, to the trailing-edge, through the extrusion zone cross-sectional

area, per revolution, to maintain mass balance and prevent volumetric (void) formation.

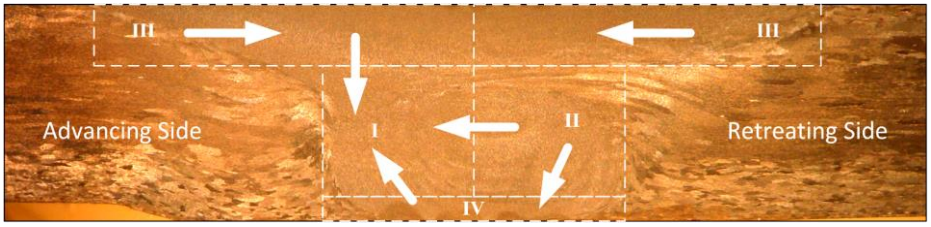

Figure 2.13 - Flow-partitioned deformation zone geometries forming within the extrusion zone. (Adapted from Arbegast 2008)

In Figure 2.14, where are schematized the different processing zones developed during the process, according to Arbegast (2007), it is possible to depict that the different thermo-mechanical history experienced by the material inside each processing zone leads to different metallurgical changes, which will directly influence the final weld microstructural and mechanical properties. Actually, weld properties are different for diverse materials/alloys, due its varied heat and cooling sensitivity and mechanical response during the process. Based on this, it is possible to conclude that the material flow during the FSW process, as to be dependent on the plastic behaviour of the base material during the process.

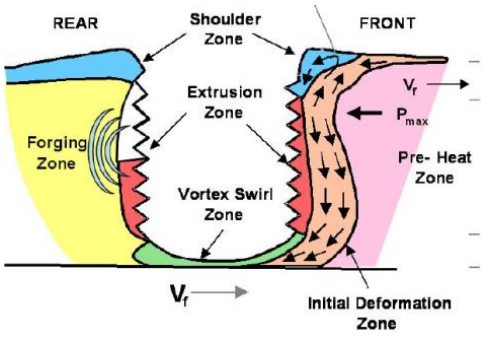

Figure 2.14 – Leading-to-trailing flow paths. (Adapted from Arbegast, 2007)

Metallurgical changes

The presence of several characteristic microstructural zones within the friction stir welds, promoted by the thermo mechanical nature of the process, is deeply explored in literature since process development. In Mishra and Mahoney (2007) review work, the following classification is used to distinguish the different weld regions, which are schematically shown in Figure 2.15,

- Thermo-mechanically affected zone (*TMAZ*): In this region, the FSW tool has plastically deformed the material, and the heat from the process also exerted influence on the material. In this zone there is generally a distinct boundary between a fully recrystallized zone (*nugget*) and a partially or non-recrystallized zone.
- Weld nugget (*nugget*): This zone is comprised in the TMAZ, characterized by an equiaxial fine grain structure, due dynamic recrystallization, caused by the severe deformation and the high temperatures registered during the process.
- Heat-affected zone (*HAZ*): This region, which lies closer to the base material, experienced a thermal cycle that has modified its microstructure and/or the mechanical properties, without any plastic deformation occurring.

It is important to emphasize that, each one of the mentioned zones presents distinct metallurgical properties, playing a key role on the final joint efficiency.

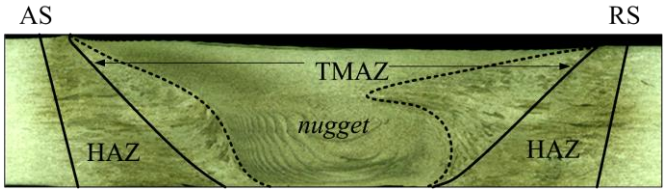

Figure 2.15 – Scheme of the different microstructural zones on a FSW cross-section.

Thermo-mechanically affected zone – TMAZ

The TMAZ experiences both temperature and deformation during the process. Inside this zone, as can be depicted from Figure 2.16, where a TMAZ micrograph is shown, it is possible to distinguish two different subzones: a partially or un-recrystallized zone and a full recrystallized zone, also known as nugget.

In the non-recrystallized zone, the base material is deformed according to a flowing pattern around the nugget. In this sub-zone, recrystallization doesn't occur due the insufficient deformation. This fact was depicted by Sato *et al.* (1999a, b), analysing a heat-treatable alloy, where the interface between the recrystallized sub-zone and the nugget, was constituted by partially recovered grains, containing a high density of sub-boundaries. According to the authors, in this interfacial zone, the high density of sub-boundaries promotes a hardness value increase up to that registered in the nugget. However, being the dissolution of precipitates the main mechanism governing the mechanical properties of the heat treatable alloys welds, the value registered in this zone is much lower than the registered in the base material.

In Figure 2.17 is shown the precipitates distribution as well as the thermal cycles registered for each weld microstructural zone. For the thermal cycle corresponding to the TMAZ (cycles 1 and 2) the maximum temperature is higher than the registered in the HAZ, which leads to the total dissolution of the precipitates. This fact can be assessed by comparing Figure 2.18a) and Figure 2.18b), which corresponds to the un-recrystallized zone of TMAZ and, to the regions situated closest to the HAZ and to the nugget, respectively, as shown in the scheme of this figure. In this last region (see Figure 2.18b) it is also possible to observe the absence of precipitates.

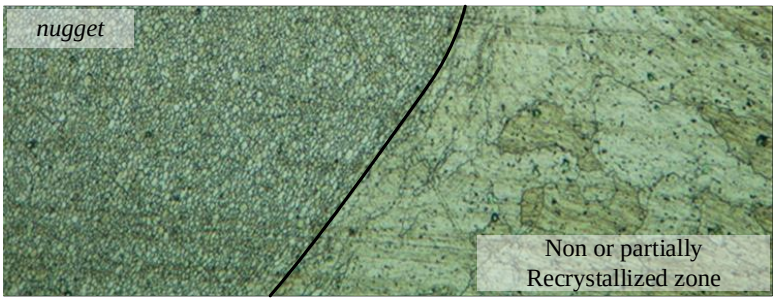

Figure 2.16 – Detail of a cross-section of a FSW: Interface between the TMAZ sub-zones.

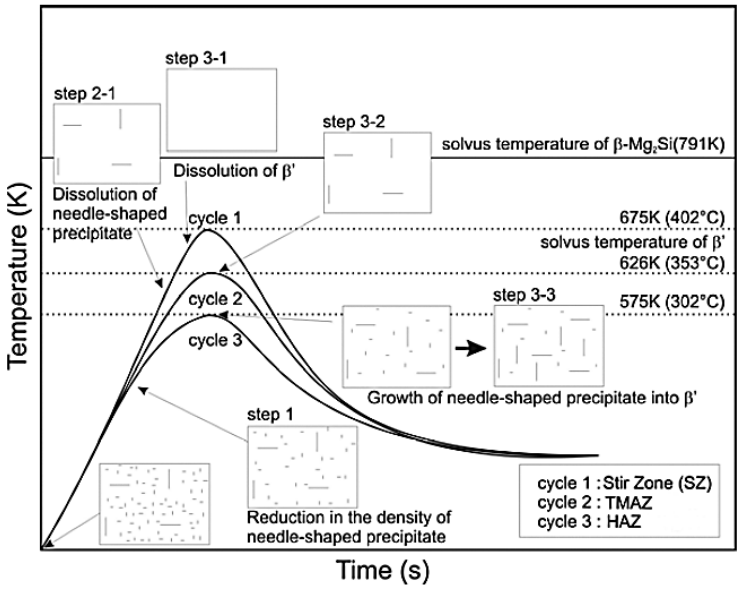

Figure 2.17 – Precipitates distribution according to the thermal cycle registered for each weld characteristic microstructural zone. (Sato *et al.* 1999b)

According to Sato *et al.* (1999a) the hardness value registered close to the recrystallized zone of TMAZ (*nugget*) is higher than that registered in the HAZ/TMAZ boundary. This can be explained by the smaller grain size and the higher density of sub-boundaries observed in the nugget. On the other hand, as can be assessed in Nandan *et al.* (2008), the precipitates dissolute will re-enter in solution when the temperature peak is sufficiently high (see cycle 1 in

Figure 2.17). However, the re-precipitation may occur during the cooling part of the thermal cycle.

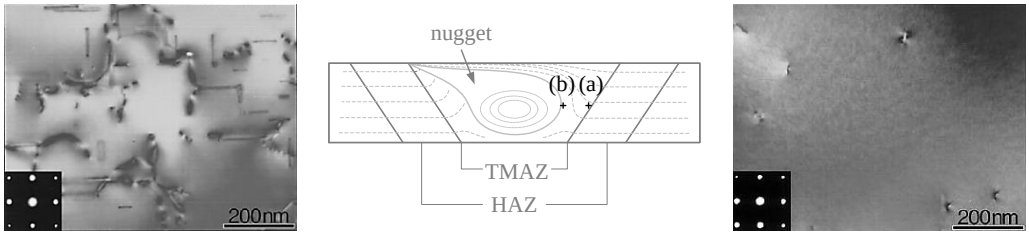

(a) (b)

Figure 2.18 – TEM micrographs of precipitates distribution in the un-recrystallized TMAZ at HAZ (a) and in the nugget (b) boundaries.(Adapted from Sato *et al.*,1999a)

From Figure 2.19 it is possible to observe a scheme of the precipitates dissolution and re-precipitation influences on hardness evolution along half of a weld cross-section. Thus, considering the entire cross-section of a weld produced using a precipitation strengthened aluminium alloy, the hardness profile displays a typical *"W"* shape (Murr *et al.*, 1998; Sato *et* al., 1999a,b; Heinz and Skrotzi, 2002; Lee *et al*,.2003, 2004; Lim *et al*., 2004; Simar, 2006; Scialpi *et al.*, 2007; Cabibbo *et al*., 2007), from where it is possible to register the high contribution of the re-precipitation phenomena on the hardness value of the TMAZ.

On the other hand, for the non-heat treatable alloy welds, the mechanical properties of the TMAZ, depend mainly on the grain size and on the density of the dislocations after plastic deformation and recrystallization occurring during welding. When the non-heat treatable alloy is used in the annealed condition the microstructure is stable and usually no softening occurs in the TMAZ and HAZ. In contrast, when this type of aluminium alloys are used in the strain hardened condition the work hardened structure will readily recover and/or

recrystallize during welding and, softening may occur. (Murr *et al.*, 1998; Shigematsu *et al.*, 2003; Miles *et al.*, 2004,2005; Peel *et al.*, 2006; Etter *et al.*, 2007).

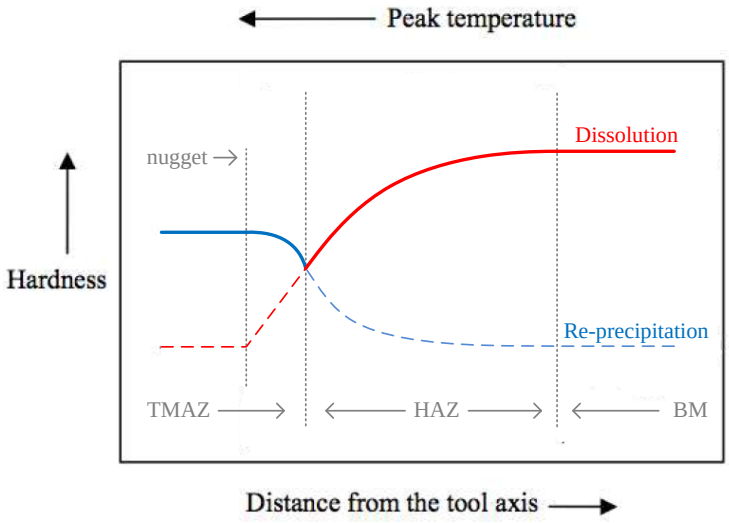

Figure 2.19 – Schematic diagram showing the weight of dissolution and re-precipitation on age-hardenable aluminium alloys, in a typical "W" shape hardness profile. (Adapted from Nandan *et al.*, 2008)

Nugget zone – NZ

This sub-zone of the TMAZ, the nugget, is constituted by small equiaxed grains when compared with base material grains, which, according to Lee *et al.*, (2003) doesn't affects strongly the mechanical properties of the TMAZ, particularly on precipitation strengthened alloys, due the re-precipitation phenomena (see Figure 2.19).

One of the main characteristics of the nugget, under determined conditions, is the formation of onion-ring shaped forms within it. According to

Leal *et al*. (2008a), in dissimilar welding, the onion rings can be attributed to the combined effect of two modes of metal transfer, i.e., it can be attributed to the interaction of the pin and shoulder material flow volumes, which are stored layer by layer, in the trailing side of the tool. In similar welding, according to Kumar and Kailas (2008b), argued that the onion ring pattern, which is evidenced by differential etching, results from the difference in the degree of deformation within the layers, or to the difference in stored energy between them, which can lead to changes in precipitates concentration and size.

However, since the pin and shoulder driven material flows are strongly affected by the tool geometry, the onion ring morphology in the nugget is not always observed. Leal (2011) compared the cross-section of welds obtained by using different tool geometries, which are shown in Figure 2.20, and concluded that the onion rings only were visible when a tool with conical shoulder tool was used.

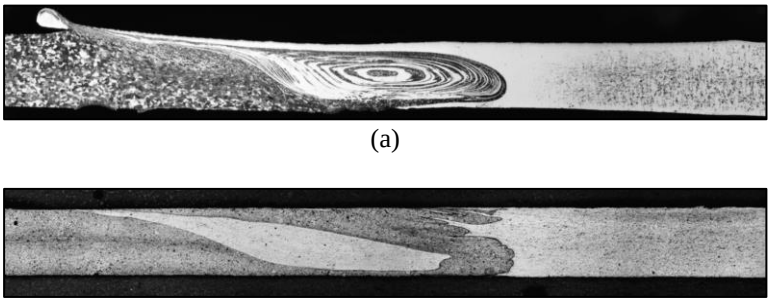

(a)

(b)

Figure 2.20 – Nugget morphology of dissimilar welds obtained using a concave (a) and a scrolled (b) shoulder (Adapted from Leal, 2011).

Kwon *et al.* (2009) reported that the onion-ring structure become wider by increasing the rotational speed, and almost imperceptible at the high rotational speeds, as can be depicted from Figure 2.21.

At a microstructural level, Hassan *et al.* (2003), considering welds performed using the AA7010 alloy, argue that the nugget grain size varies along the weld depth and is affected by the process parameters, mainly, the rotational speed. In fact, as shown in Figure 2.22a), where is plotted grain size variation through the depth, it is possible to depict a grain size decrease of 10μm from the crown to the root. Moreover, the authors also argue that the variation in grain size is not so significant when the rotational speed is varied (approximately 4.5μm), as evidenced in Figure 2.22b).

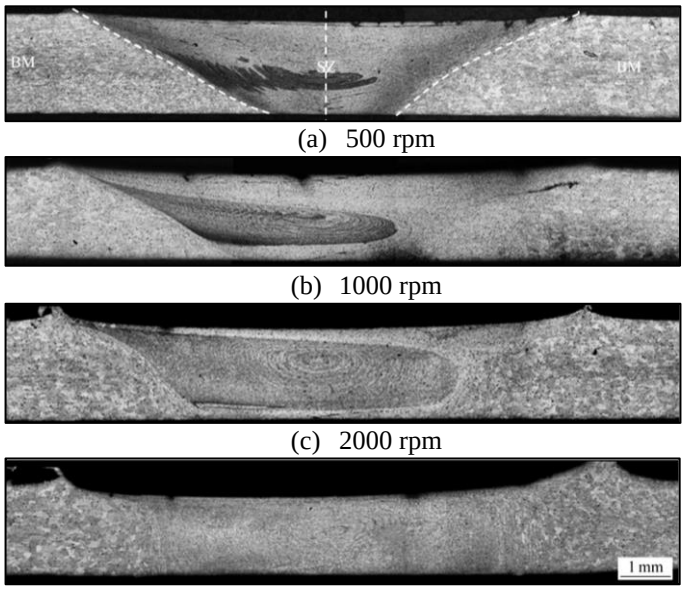

(a) 500 rpm

(b) 1000 rpm

(c) 2000 rpm

(d) 3000 rpm

Figure 2.21 - Macrographs of the FS weld cross-sections at the tool different rotation speeds. (Adapted from Kwon *et al.*, 2009)

Tronci *et al.* (2011) performed a TEM microstructural analysis, in order to understand the causes of the differences in yield strength of AA5182 welds produced using different weld parameters. Based on this analysis, the authors concluded that the base material had an annealed microstructure, free of dislocations and with a large number of precipitates dispersed inside the grains,

meanwhile, in the nugget, despite the reduced grain size, it was depicted a rearranged dislocations mesh inside the grains. According to the authors, the sub-grain structure plays a major role in determining the welds strength.

Based on the facts previously presented, in this point, it is important to emphasize that both nugget morphology and onion ring structure formation are strongly dependent of the tool and welding parameters.

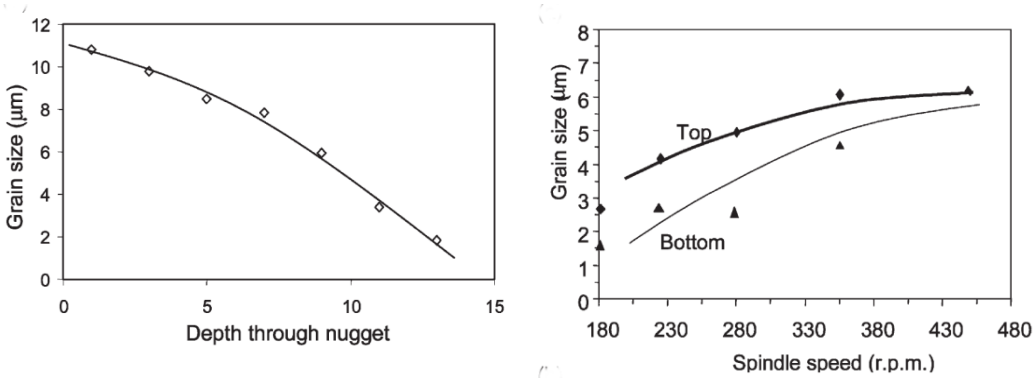

(a) (b)

Figure 2.22 - Variation in nugget zone grain size through the depth of the plate (a) and, the effect of spindle speed on the nugget zone grain size (b). (Adapted from Hassan *et al.*, 2003)

Heat affected zone - HAZ

The HAZ is the weld zone where the material does not undergo any plastic deformation. This zone presents metallurgical changes, which can also promote different mechanical properties, relatively to the base material.

Sato *et al.*, (1999a), when analysing welds in 6xxx series of heat treatable alloys have shown that despite the almost imperceptible differences in grain shape and size, between the HAZ and BM, even for a wide range of welding conditions, the HAZ presents the lowest mechanical properties. Similar HAZ

strength loss can be also found for other precipitation hardened alloys, such as, the AA7xxx (Mahoney *et al*., 1998) and AA2xxx (Yang *et al*., 2004).

In Figure 2.23 are shown TEM micrographs corresponding to BM, HAZ centre and HAZ near to the TMAZ zones of an AA6063-T5 FS weld (Sato *et al*, 1999b). Observing these figures it is possible to depict an increase in precipitates size (see Figure 2.23b and c) and a decrease in precipitates density in the HAZ relatively to the base material (see Figure 2.23a). Indeed, in the zone closest to the BM, it is registered a high density of needle-shaped precipitates and a few rod-shaped precipitates, whereas, in the zone closest to the TMAZ, the presence of both types of precipitates, is not perceptible. In the HAZ subzone comprised between the two former subzones, the authors also observed that the needle-shaped precipitates were dissolved and that only a low density of rod-shaped precipitates remained. Similar observations were also performed by other authors for the AA6xxx family alloys (Simar, 2006; Liu and Ma, 2008).

In Figure 2.24 is plotted the variation in yield strength with temperature, along different weld zones for the AA6061-T6 alloy (Olea, 2008). According to the figure, the yield strength of the HAZ is approximately 60% of that of the BM. The author also reveals that, depending on the alloy, the yield strength decrease in the HAZ can be even higher.

However, in some welding conditions, no differences in mechanical properties, relatively to the base materials, are depicted in the HAZ. In fact, Rodrigues *et al.*, (2009), analysing AA6016-T6 welds, performed under different welding conditions, namely tool design and rotational speed, realised that, hot weld conditions promoted even-match welds, i.e, similar mechanical properties than those observed in the base material in all weld zones, inclusively, in the HAZ.

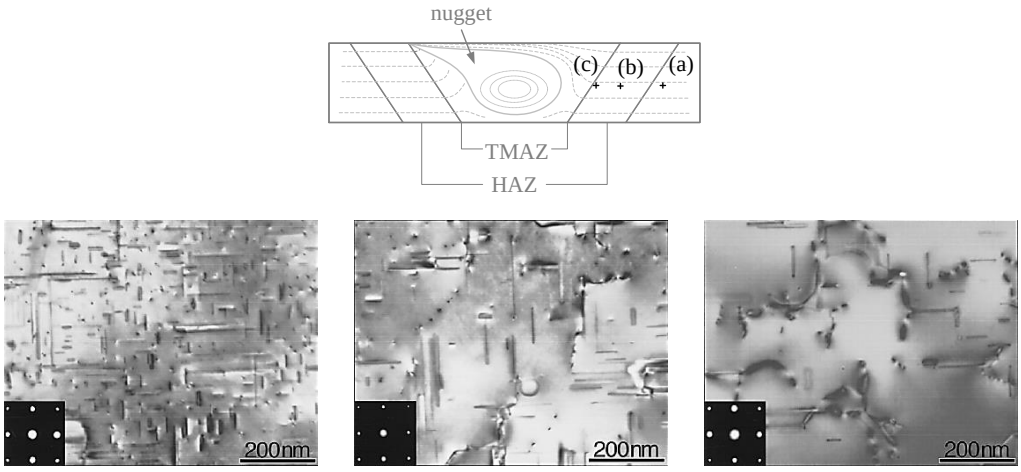

(a) (b) (c)

Figure 2.23 – TEM micrographs of Precipitates distribution in the BM (a), HAZ centre (b) and HAZ near to the TMAZ (c).(Adapted from Sato *et al.*, 1999a)

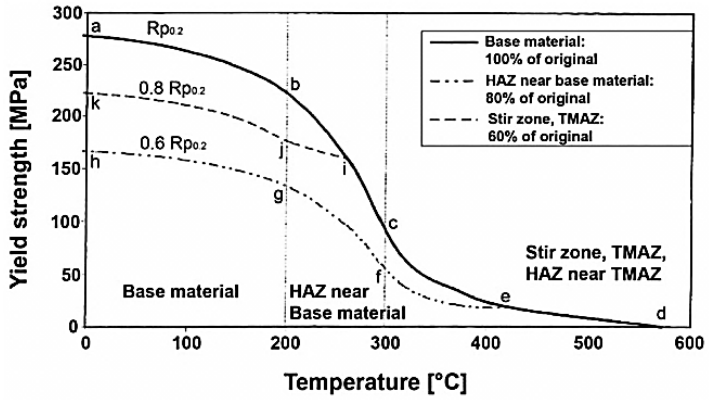

Figure 2.24 – Yield strength variation with temperature in three weld zones. (Olea, 2008)

The strong effect of the precipitates shape, size and/or distribution on HAZ mechanical properties is not verified for the non-heat treatable alloys, due to its different strengthening mechanism. In fact, Lim *et al.* (2005) observed that the hardness registered by within the HAZ of AA5083-H32 welds, presents a decrease of less than 10%, which much lower than those commonly registered for heat-treatable alloys. Treadgill *et al.* (2009), analysing the cold

work condition alloys (e.g. H1xx, H2xx or H3xx), have also depicted a hardness decrease and concluded that as the weld is approached, the heat from the process causes annealing and recovery takes place, leading to a drop on hardness. However, the authors did not register any hardness variation in HAZ of annealed non-heat treatable aluminium welds (O condition). This trend was already shown in Leal *et al.* (2008b), who did not observed any hardness variation in this zone, considering welds performed using the AA5182-H111 alloy, which presents the closest mechanical behaviour to the O condition alloy.

Influence of process parameters on weldability and weld mechanical properties

Static parameters

The static parameters are directly related to the tool, comprising the tool geometry, as well as, the dimensions and plates thickness. As previously shown in Figure 2.10a), the tool is constituted by two main parts: the shoulder and the pin.

According to several authors, the tool shoulder is the responsible for the majority of the heat produced during the process, however, it strongly depends on contact conditions between the tool and the workpiece (Song and Kovacevic, 2003; Schmidt and Hattel, 2005a,b; Colegrove *et al.*, 2007; Arora *et al.*, 2009; Assidi *et al.*, 2010; Jamshidi *et al.*, 2011). It is also consensual that the shoulder is also responsible for the downward forging action, which is

important for weld consolidation. According to Schmidt *et al.* (2004) and Kumar *et al*., (2008), the concave tool shoulder helps establishing the necessary pressure under the shoulder, but also acts as an escape volume for the material displaced by the probe during the plunge action (see Figure 2.6a).

Arora *et al.* (2011) proposed a method, to determine an optimal shoulder diameter, based on the torque values registered during welding. According to the authors, the total torque can be decomposed in two components, corresponding to the sticking and sliding components of the tool-workpiece contact, called *MT* and *ML*, respectively. In Figure 2.25a), are plotted the total torque and its components for three different shoulder diameters. From the graph, it is possible to conclude that while the sticking torque component increases, for increasing shoulder diameters, the sliding component, after a maximum value, starts decreasing. In the same work, the authors emphasize that the sticking torque component represents the resistance of the plasticized material against flow around the tool, and the optimum amount of material flow around the tool with minimum resistance improves weld quality and tool lifetime. In this way, the author proposes the following optimization function,

$$O(f) = \frac{MT \times ML}{\left(MT + ML\right)^2}. \tag{2.1}$$

Therefore, the optimum shoulder diameter is the one that maximizes the referred function. In Figure 2.25b, are shown the curves corresponding to the optimized function ($O(f)$) values considering different rotation speeds and shoulder diameters. From the figure, it is possible to observe that optimization function varies with the rotational speed, being the optimal shoulder diameter also determined by the rotational speed. However, the analysis performed by Arora *et al.* (2011), which is based on the torque values registered during welding, considering different shoulder diameters and rotational speeds,

showed that the torque is dependent of the amount of material stirred by the tool. Consequently, the torque is also dependent on the plate thickness and material properties, which restricts the applicability of the proposed method.

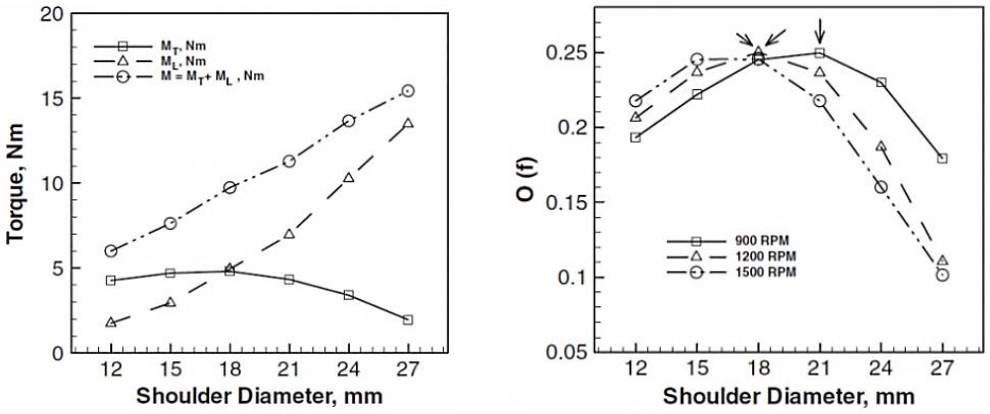

(a) (b)

Figure 2.25 – Optimum Shoulder diameter. Torque components versus tool shoulder (a) and optimization function versus shoulder diameter (b). (Arora *et al.*, 2011)

The pin geometry depends on its playing role during the process, which comprises the disrupting of the faying surfaces and the shearing of the material in front of the tool. Moreover, the pin length (L_p) is directly related to the thickness of the plate, being limited by the work piece thickness. The pin tip should not fully penetrate the work piece in order to avoid the damage of the backing plate. The pin diameter, for an efficient material transport and heat generation, is usually determined as a function of the shoulder diameter. Theoretical relationships, between pin and shoulder diameters and plate thickness, were established in Zhang *et al.* (2012) for both similar and dissimilar welds, produced using several alloys and materials. As shown in Figure 2.26a), the author shows that the ratio between the pin (D_p) and shoulder (D_s) diameters follows the expression,

$$D_s = 2.097 D_p + 4.760. \quad (2.2)$$

Furthermore, plotting the pin and shoulder diameter values versus thickness, which is shown in Figure 2.26b), the author developed the following relations,

$$D_s = 2.199t + 7.318, \quad (2.3)$$

$$D_p = 0.834t + 2.224. \quad (2.4)$$

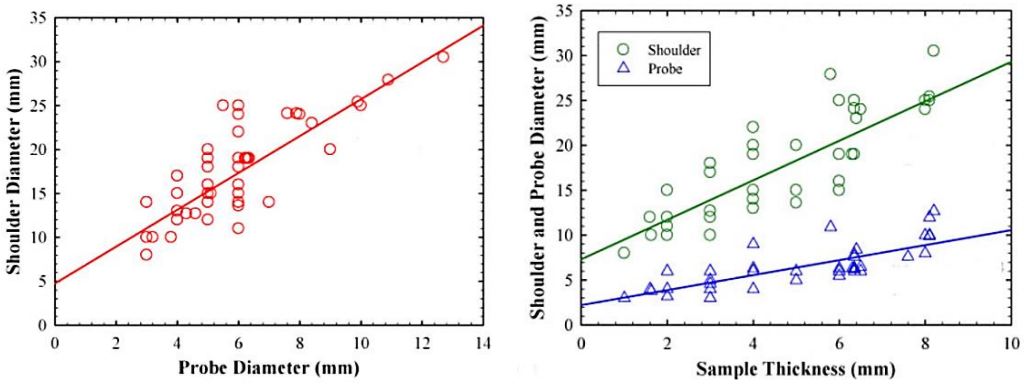

(a) (b)

Figure 2.26 – Pin (Probe) diameter versus Shoulder diameter (a) and, thickness versus shoulder and pin diameters (b). (Zhang *et al.*, 2012)

It is also important to emphasize that the assessment of the ideal tool dimension is being mainly based on try-fail analysis for a restrict range of pin and shoulder diameters and, consequently, no appropriate principle for the determination of an optimum shoulder and pin diameter was established until

now. In fact, as mentioned by Rai *et al.* (2011) the search of this principle is just beginning.

According to Rai *et al.* (2011), during the process, the tool is subjected to severe stresses at high temperatures and, consequently, the tool life depends mainly on the base material hardness. Tool life constitutes a key factor in process cost/efficiency, from an industrial perspective. Depending on the material to be welded an optimization of tool geometry and tool material is required in order to increase the tool life and guarantee the weld quality. Being a widely studied subject, several tool geometries and materials have been already proposed and can be found in many review works (Mishra and Mahoney, 2007; Çam, 2011; Rai *et al.*, 2011; Zhang *et al.*, 2012). From these works, the tool constituted by a concave flat shoulder and a threaded pin, which is schematized in Figure 2.10a), is the simplest and the most used FSW tool geometry. The popularity of this tool is related to its easy production and replication. Depending on the base material mechanical properties, the materials commonly used in tool construction are the tool steels, the tungsten carbides (WC), the polycrystalline cubic boron nitrides (pcBN) and the commercially pure tungsten (cp-W). The tool steel widely used, namely for aluminium welding, because it is cheaper and allows a faster reproduction. According to Zhang *et al.* (2012) review work, the remaining materials are more appropriate for welding harder alloys, such as Steel, Titanium and Composites, due to its improved hardness and thermal conductivity.

Dynamic parameters

Positioning parameters

According to Figure 2.11, the positioning parameters are exclusively responsible for tool positioning during the process. Until now, the influences of the plunge depth (l_{dz} in Figure 2.10) and tilt angle (α in Figure 2.10) on weld quality and mechanical properties are widely referenced in the literature (Kumar and Kailas, 2010; Zhang *et al.* 2011), considering both similar and dissimilar FSW. Simultaneously, references to the importance of faying surface offset (l_{dy}) comes mainly from works focused on dissimilar welding. In fact, the main handicaps of dissimilar FSW are the different deformation characteristics and the chemical affinity of the base materials at the welding temperature. According to Lee *et al.* (2006), the better dissimilar FSW configuration is obtained when the welding tool is plunged into the softer base material. This fact was reinforced in the work of Chen and Lin (2010), where the toughness of the dissimilar aluminium (AA6061) – steel (SS400) joints was analysed, showing that by moving the pin towards the aluminium side (0.1 to 0.2 mm), the quality of the welds was improved gradually.

Considering the tool offset in similar FSW, Kumar and Kailas (2008a) analysed the effect of the faying interface position on the tensile strength of a similar friction stir welded aluminium alloy. From their work, the authors concluded that the tool can be allowed to deviate from the interface, to either the advancing or retreating sides, but better weld quality is obtained when the interface is positioned in the advancing side of the tool. However, during similar FSW, the harmful differences in base material are not present and, due to this fact, tool offset does not affect considerably the weld quality.

On the other hand, contrarily to the effect of the tool offset, the plunge depth has a direct influence on weld quality. In fact, according to Leonard and Locker (2003), the correct depth of the pin penetration avoids root void formation, due to its strong influence on the material forging beneath the shoulder and around the pin. As shown by Longhurst *et al.* (2010), the increase of the plunge depth also promotes an increase of the downward force, due the changes on physical contact between the tool and the workpiece. Zhao *et al.* (2007) proposed the following empirical expression, between downward force (F_z) and the plunge depth (l_{dz}):

$$F_z = 0.204 \cdot l_{dz}^{1.8}. \quad (2.5)$$

This relation was developed using AA6061 aluminium alloy FSW results, obtained at constant rotational and traverse speed, which shorts its range of applicability.

However, excessive plunge depths are also harmful since it can promote a high flash amount, resulting from the excessive heat-input during the welding process (Kim *et al.*, 2006; Arbegast, 2008). It is also important to emphasize that, an excessive plunge depth can cause the direct contact between the pin and the backing plate promoting both pin and backing plate damage. In fact, due to its high relevance on weld consolidation, the tool plunge depth is widely used in process control, especially when force control is not possible.

The tilt angle (α) is also considered an important factor affecting the forging effect of the tool on the flow of plasticised metal behind the pin. Zhang *et al.* (2011) showed that the maximum volume of plasticised material extruded into the groove left, behind the pin, increases significantly by increasing the tool tilt angle. This enables to conclude that there is a direct influence of the tilt angle on defect formation. In fact, the authors noticed that for the joints

produced without tilt angle, void defect tended to appear at the advancing side, close to the weld root. These void defects had considerable width, while no void appeared within the cross-section of the joint produced with tilt angle. It was also realised that a small pin and considerable tool tilt angle are beneficial in eliminating weld voids. The results obtained by the author were shown to be improved by using a featureless shoulder. Actually, using a featured shoulder eliminates the need of tilt angle (Leal *et* al., 2008; Leitão *et al.*, 2009; Zhang *et al.*, 2012), which makes possible to conclude that the tilt angle depends strongly on shoulder geometry. As a matter of fact, from former expositions, the influence of the faying surface offset (l_{dy}), the plunge depth (l_{dz}) and the tilt angle (α) was always assessed considering specific material characteristics and welding parameters. In this way, it is important to emphasize that, when other weld conditions are considered, which varies the thermal and mechanical solicitation conditions, the influence of the positioning parameters may also varies.

Movement parameters

As previously stated, the movement parameters, which are represented in the scheme of Figure 2.10, are the rotational speed (ω), the traverse speed (v) and the downward force (F_z), rule all the tool movement during welding. This family of parameters have a strong influence on final welding results due to its strong influence on heat generation and material transport during the entire process. Actually, according to Zhao *et al.* (2007), it may be controversial to classify the downward force as a movement parameter. In fact, this is only possible when the welding is performed in force control. During the force-controlled process, in order to maintain a constant downward force value, the

plunge depth (l_{dz}) is increased and/or decreased, during the process, promoting the vertical tool movement. On the other hand, during the position control of the process, the downward force is considered as a process output, depending mainly on the plunge depth applied.

The use of the downward force to control the process is an important process improvement, since the continuous adjustment of the plunge depth enables the correction of positioning errors, avoiding defect formation due to any thickness variation and/or plate wrapping. Longhurst *et al.* (2010) reveals that insufficient downward force conducts to inadequate forging pressure beneath the tool, which difficult the formation of sound joints. Kumar and Kailas (2008a,b) have already observed this trend, referring that, above a minimum downward force value, it was possible to produce defect free welds. However, according to Louro *et al.* (2008), when an excessive downward pressure is applied, the over-storage of plasticised material beneath the tool shoulder is promoted, resulting in a high amount of flash and high thickness reduction.

Moreover, some authors have analysed the influence of other welding parameters on downward force. For example, Kumar *et al.* (2012) analysed the influence of each FSW parameter, and its possible combinations, on the downward force, by performing 12mm thick welds in AA5083-H112 aluminium. The welds were produced, in position control, using an instrumented milling machine and several tool diameters, weld speeds and rotational speeds. In Figure 2.27 is plotted the evolution of the downward force, considering each one of the parameters and/or combinations. From the figure it is possible to conclude that F_z increases for increasing shoulder diameters (see Figure 2.27b), welding speed (see Figure 2.27c) and, for decreasing rotational speeds (see Figure 2.27d). Trimble *et al.* (2012), observed the same trends in welds performed using an AA2024 alloy, and concluded that it can be attributed to a thermal softening reduction of the work piece, due to a

reduced heat generation, which increases the resistance acting on the tool as it traverses along the joint line. Furthermore, increasing the rotational speed has the opposite effect due to an increase in the heat generation.

Based on Kumar *et al.* (2012) study, considering the specific welding conditions used, it is proposed the following empirical expression,

$$F_Z = 17412 + 2426 \cdot D_p - 551 \cdot \omega + 531 \cdot v \tag{2.6}$$

to predict the optimum F_z. This expression, which was conceived for a particular set of welding conditions, clearly shows the complementarity between the movement parameters.

In fact, during the process, the rotational speed is usually referred as the most crucial parameter for heat generation, due to its high influence on tool/work piece contact conditions (Song and Kovacevic, 2003; Schmidt and Hattel, 2005a,b; Colegrove *et al.*, 2007; Arora *et al.*, 2009; Assidi *et al.*, 2010; Jamshidi *et al.*, 2011). Actually, the higher the number of tool rotations, the higher the frictional heat generated at the shoulder/work-piece contact surface (Flores *et al.*, 1998). On the other hand, the weld speed rules the number of rotations in the same place of the work piece. Considering this fact, it is possible to depict that, weld speed works as a heat dissipation regulator, strongly affecting the heat-history (Khandkar *et al.*, 2003; Colegrove and Shercliff, 2006; Sutton *et al.*, 2006; Ren *et al.*, 2007; Cabibbo *et al.*, 2007; Hwang *et al.*, 2008).

As was already discussed, the rotational and travel speeds are indirectly responsible for material transport during the process, due its influence on heat input and dissipation and, consequently, on the contact condition between the tool and the work-piece, which, as previously mentioned, assumes a significant importance on weld quality. In fact, according to Schmidt and Hattel (2008),

sound welds are only obtained when predominantly sticking contact conditions are developed. Sticking conditions allows the correct material deformation and transport, beneath the shoulder and around the pin. Thus, high levels of heat input, promoted by excessive tool rotational speed, can conduct to conditions. The sliding contact conditions, which is usually attributed to low levels of heat input, doesn't allow the material to be correctly transported beneath and around the tool shoulder and pin, leading to the production of defective welds.

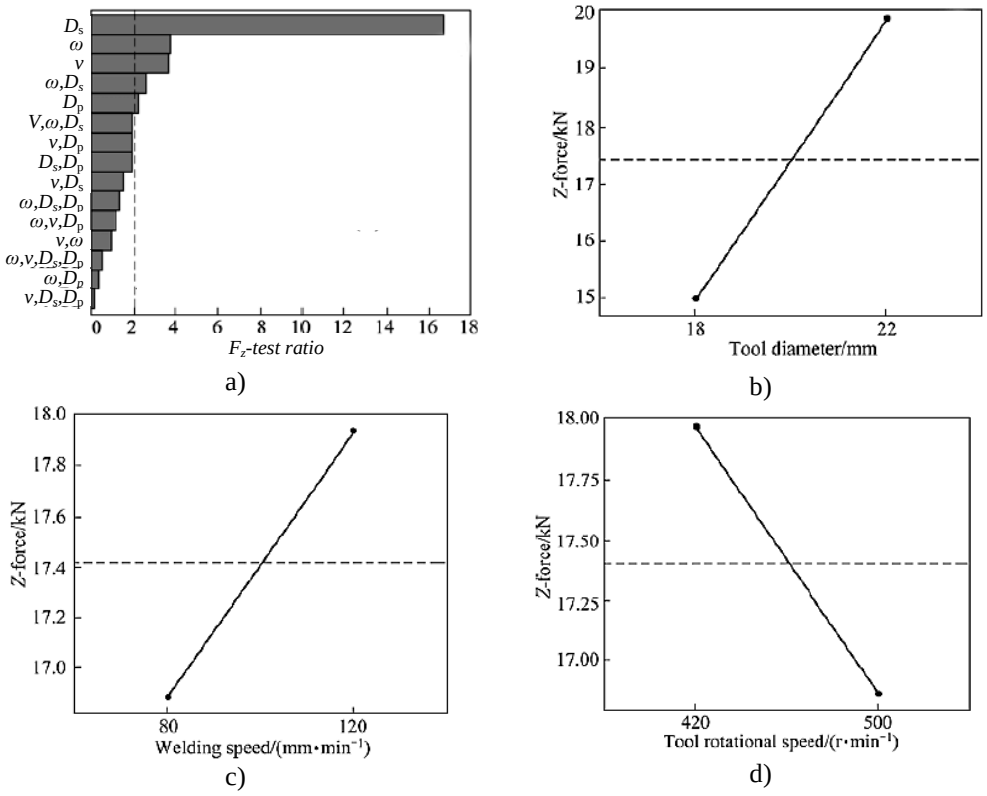

Figure 2.27 – Weight of process parameters on downward force (a), namely, tool diameter (b), travel speed (c) and rotation speed (d). (Adapted from Kumar *et al.*, 2012)

In fact, Selvaraj *et al.* (2013), studying welds produced using the AA6061-T6 alloy, concluded that defect size increases for increasing welding speeds, as shown in Figure 2.28a). From this figure is also possible to depict

that sound welds were produced at moderate rotational speeds (400 to 1200 rpm). Observing the Figure 2.28b), where the weld parameters window is plotted, it is possible to depict the direct influence of rotational and welding speeds on flow regulation and, consequently, on defects formation. The authors argue that these tool parameters influence the tool-workpiece interface temperature and, consequently, the contact conditions in the interface.

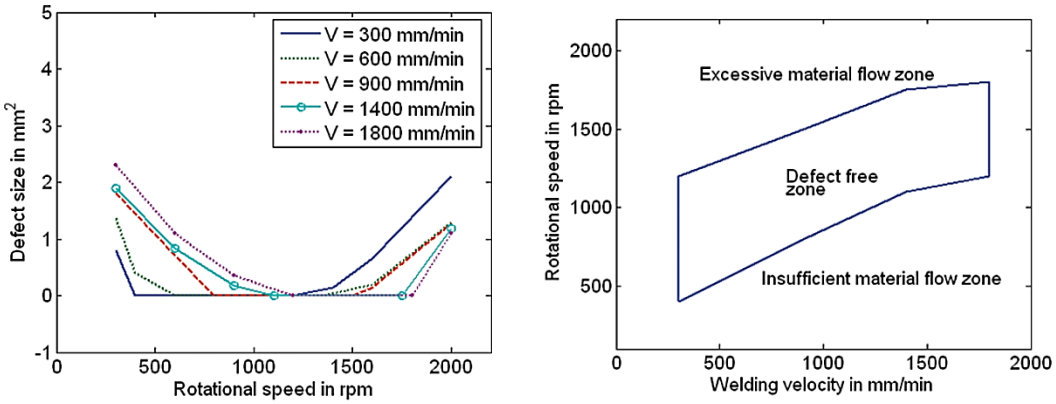

(a) (b)

Figure 2.28 – Influence of rotational and weld speeds on defect size (a) and, parameters window (b) fot FSW of an AA6061-T6 alloy. (adapted from Selvaraj *et al.*, 2013)

The increased friction per surface unit, caused by the use of a low weld speed conducts to a high heat-input during the process. On the other hand, elevated weld speed values are appellative to the industrial application of the process. However, if excessive, a lower heat input level is promoted, affecting directly the base material plastic behaviour and the contact conditions between tool and workpiece. Low heat inputs decrease the capability of moving the material beneath and around the tool, leading to the formation of defective welds.

The influence of rotational and welding speeds on welds microstructure and mechanical properties is a widely explored subject in FSW literature. According to Figure 2.29, by Cavaliere *et al.* (2008), the nugget average grain-

size decreases for increasing welding speeds, for a given rotational speed. The average nugget grain-size decreases, with the increasing travel speed, but until a certain value, from which it stabilizes. As stated by Ren *et al.* (2007) and Cavaliere *et al.* (2008), considering Al-Mg-Si alloys, the weld speed influence the yield stress of 4mm AA6082 thick friction stir welds. Observing the graphic shown in Figure 2.30, where the evolution of the yield stress values with the weld speed are plotted, it is possible to conclude that, considering the same rotational speed, the yield strength decreases for increasing weld speeds.

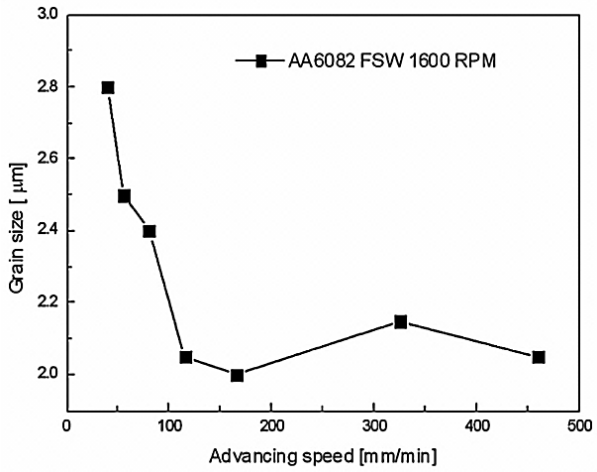

Figure 2.29 – Mean grain size as a function of welding speed. (Cavaliere et al., 2008)

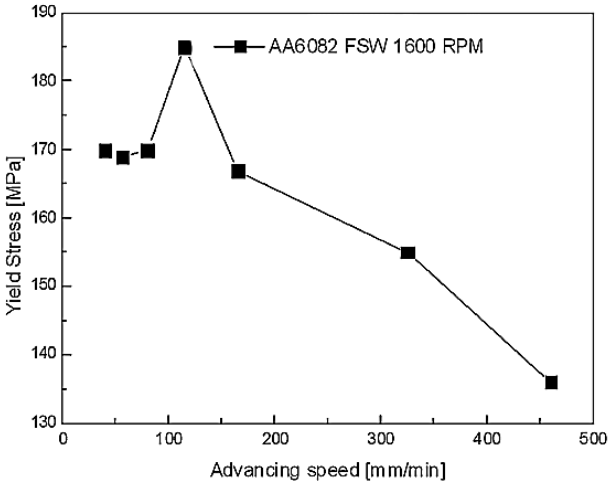

Figure 2.30 – Weld speed versus Elongation (a) and yield stress (b). (Cavaliere *et al.*, 2008)

Rajakumar and Balasubramanian (2012) performed a broader range study then previous authors, by analysing the mechanical properties of welds performed using several aluminium alloys (AA1100, AA2024-T3, AA2219-T87, AA6061-T6, AA7039-T4 and AA7075-T6) and, under several welding conditions. The quality analysis and statistical treatment of weld results data, the authors proposed the empirical expressions,

$$\omega_{opt} = 31.6 \cdot \sigma_0^{\,0.66}, \tag{2.7}$$

$$\omega_{opt} = 4.13 \cdot Hv^{1.21}, \tag{2.8}$$

$$\omega_{opt} = 17074 \cdot E_l^{\,-0.8822}, \tag{2.9}$$

in order to calculate the optimal rotational speed (ω_{opt}) using mechanical properties of the base material, at room temperature, such as: the Yield stress(σ_0), Hardness (Hv) and Elongation (E_l). Similar analysis was performed, by the authors, in order to determine the optimal weld speed (v_{opt}). The authors propose the equations,

$$v_{opt} = 1116.8 \cdot \sigma_0^{\,-0.458}, \tag{2.10}$$

$$v_{opt} = 2816.72 \cdot Hv^{-0.74}, \tag{2.11}$$

$$v_{opt} = 12.045 \cdot E_l^{\,0.67}, \tag{2.12}$$

to calculate the travel speed for which the best weld results are obtained. However, it is important to emphasize that, despite the fact of some materials show similar room temperature mechanical properties, different weld results are obtained due to its different mechanical behaviours at high temperatures and strain rate sensitivities. Considering this fact, Qian *et al*. (2013), using an analytical approach, proposed the following expressions for optimal weld and rotational speeds determination,

$$\omega_{\text{opt}} = \frac{\left(120\pi\sigma_8 SC\eta\right)\times\left(n\sinh^{-1}\left(\frac{\dot{\varepsilon}}{A}\exp\left(\frac{Q}{RT_{\text{opt}}}\right)\right)^{\frac{1}{n}}\right)^2}{kr^2}\times 10^{-\left(\frac{\left(\frac{T_{\text{opt}}-T_0}{T_s-T_0}-0.097\right)}{0.151}\right)} \tag{2.13}$$

$$v_{\text{opt}} = \frac{1000r\omega}{n\sinh^{-1}\left(\frac{\dot{\varepsilon}}{A}\exp\left(\frac{Q}{RT_{\text{opt}}}\right)\right)^{\frac{1}{n}}} \tag{2.14}$$

where, σ_8 is the yield stress of the base material at 80% of solidus temperature (T_s), S the pin cross-section area, C is the specific heat capacity of the work-piece material, k is the work-piece thermal conductivity, η is the ratio according to which heat generated at the shoulder/work-piece interface is transported between the tool and work piece, n and A are material constants, $\dot{\varepsilon}$ is the strain rate, Q is the activation energy, R is the universal gas constant, T is the absolute temperature, and T_0 refers to the initial temperature. According to Qian *et al*. (2013), the obtained results present high concordance with the results from previously published works by the same author and co-workers, and by other authors (Li *et al.*, 2012; Lim *et al.*, 2004), namely, for the AA1100, AA2024, AA6061 and AA7050 aluminium alloys. However, in the proposed model, the effects of the tool dimension, the plunge depth, downward

force and the tilt angle were not considered, which, according Qian *et al*. (2013) were relevant for defect formation assessment. In a matter of fact, the author considers that the actual model requires further improvements, in order to comprise those parameters.

The expressions proposed by Qian *et al*. (2013) and by Rajakumar and Balasubramanian (2012) show the important role of the material thermic and mechanical properties on rotational and weld optimal speeds calculation. However, some of the variables present in these models, for example σ_8, which is the yield stress of the base material at 80% of solidus temperature, may be difficult to obtain using conventional methods and, consequently, becomes a handicap.

Base Material parameters

As early referred by Mishra and Ma (2005), the material properties are a crucial factor to setup the welding parameters, in order to perform defect-free welds. Some works, had already correlated the material properties and weld parameters (Balasubramanian, 2008; Rajakumar *et al.*, 2011a, b; Rajakumar and Balasubramanian, 2012). Most of these studies are restrictive due the fact that they are mainly based on heat-treatable and commercial pure aluminium alloys. In fact, Lim *et al.* (2005) found differences, when welding aluminium alloys with different strengthening mechanisms (AA6061-T651, AA7075-T6 and AA5083-H32), using several process parameters. In his study, the authors clearly show that the AA6061-T651 alloy has a quite large range of process parameters available for friction stir welding, while the AA7075-T6 and AA5083-H32 have a very narrow bend of welding parameters combination available for sound welding. It is also demonstrated that, each alloy showed a slightly different trend regarding the effect of different welding parameters on

the tensile properties. According to these observations, it is plausible to corroborate the strong influence of base material mechanical behaviour during the process in obtaining sound welds, which, is clearly affected by the strengthening mechanism.

However, any possible influence of the plastic properties of the materials on friction stir weldability is not fully explored and/or understood. In fact, establishing relation between plastic behaviour and material flow during FSW is a very difficult task, either by experimental means or by numerical simulation, due the high difficulty in characterizing the plastic behaviour of the materials at temperatures and strain rates attained during FSW.

Thesis framework

From the exposed in this section, it is possible to stress the high maturity of the research encompassing FSW. The simplicity of the process and its advantages relatively to the commonly used fusion welding processes increased the interest by it inside both the scientific and industrial communities. In fact, FSW was initially developed for joining aluminium alloys, which present several issues when welded by using the conventional fusion wielding processes. However, the versatility of the process to join other materials beyond aluminium alloys, including dissimilar joining, turns the FSW research field even more attractive.

In the last few decades, several studies were performed in order to understand the process, intending to reach the necessary maturity for its full-range application on industry. These studies were initially focused on production of sound welds and further, on the mechanical and microstructural characterization of the welds, mainly obtained from trial-error approaches. On the other hand, the thermo-mechanical roots of the process lead to the heat

input and flow mechanics assessments. At the same time, several works including numerical approaches have been also developed, in order to complement the experimental approaches.

Nowadays, the scientific contributions showed the influence of welding parameters on weldability and weld mechanical properties, for several types of materials. However, due to the differences between each material/alloy, it is not completely consensual about which is the optimal set of parameters, aiming a wide range application of FSW.

Thus, knowing the base material plastic behaviour at high temperatures and strain rates, and, establishing direct relations with the weldability results and the weld mechanical properties, constitutes an innovative approach in FSW research field. It was, under this context that the present PhD thesis, named *"Influence of base material plastic properties and process parameters on friction stir weldability"*, was written.

Aims and Objectives

The main objectives of this work were:

- *To characterise the plastic behaviour of the base materials under different temperatures and loading conditions;*
- *To analyse the influence of base material plastic properties and process parameters on friction stir weldability;*
- *To assess weldability through an extensive weld defect analysis;*
- *To perform a torque sensitivity analysis under varying welding conditions;*

- *To analyse welds local properties using varying testing conditions and strain data acquisition by DIC (Digital Image Correlation).*

3
Experimental Procedure

In this chapter, it is intended to contextualize the readers in relation to the experimental techniques applied during this investigation. The chapter is divided in two distinct parts: the first part includes the description of all process and tool parameters used in welds production and, the second part includes a description of the laboratorial techniques applied in analysing the welds, with special emphasis on the mechanical characterization techniques developed under the scope of current work.

This Page Intentionally Left Blank

Overview

In Figure 3.1 is shown the experimental framework. According to the figure, the first stage of the work consisted in welds fabrication. In this chapter are described the welding parameters used to fabricate the welds analysed in the thesis. Then, the welds were analysed by using conventional laboratorial practices. The majority of these techniques, such as hardness tests, metallographic practices and uniaxial tensile tests, followed common procedures. However, some innovative approaches were also used during present study. These new approaches committed in the use of shear testing to assess weld local mechanical and the use of *Digital Image Correlation* (DIC), in order to register the local strain, in different weld zones, during mechanical testing.

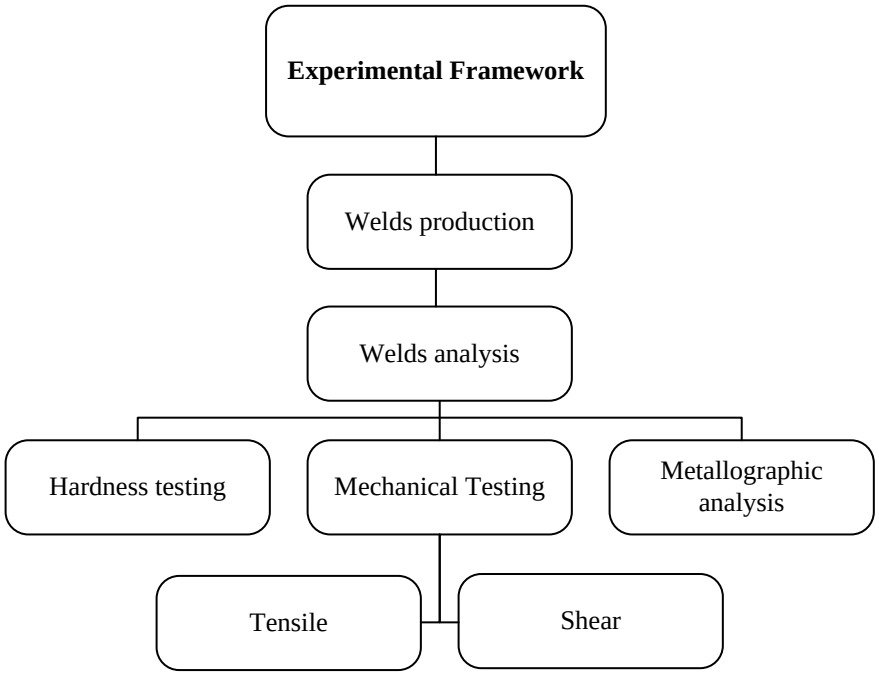

Figure 3.1 – Experimental framework structure.

Welding Procedures

The two base materials used in this study ware supplied in two different thicknesses: 6mm and 4mm, for the AA5083-H111, and 6mm and 3 mm, for the AA6082-T6 alloy. Bead-on-plate welds were produced in order to avoid any influence of sheet positioning and clamping on weld quality. Tools with conical shoulders, with a cone angle of 5º, and cylindrical threaded pins, were used in all welding tests. Although the geometry was maintained, the tool dimensions, namely, the pin (D_p) diameter, shoulder (D_s) diameter and pitch angle (α), were varied. For each tool tested, the welding speeds (v), the rotating speeds (ω) and the vertical forces (F_z) were different according to the values displayed in Table 3.1. Using the parameters identified as *Set 1*, *Taguchi analysis* was performed in order to establish a testing plan for each base material and plate thickness, as described in Louro *et al.* (2010), which determined a total of 144 welding tests to be performed. After analysing *Set 1* welding results, some supplementary tests were scheduled for both base materials (identified as *Set 2*, in Table 3.1), in order to accomplish a more comprehensive analysis of their welding behaviour.

Table 3.1 - Welding parameters.

Alloy	Thickness (mm)		*Process parameters*			*Tool Parameters*		
			v (mm/min)	ω (rpm)	F_z (kN)	D_s (mm)	D_p (mm)	α (º)
AA5083-H111	4 mm	*set 1*	300	400	7	13	5	1
			400	500	11	15	6	2
			500	600	15	18		3
		set 2	300 to 700	400 to 1100	15	15	6	3
	6 mm	*set 1*	200	300	10	15	6	1
			275	400	15	18	7	2
			350	500	20	21		3
		set 2	50 to 350	300 to 1000	20	21	7	3
AA6082-T6	3 mm	*set 1*	800	1000	5	10	4	1
			950	1150	7	12	5	2
			1100	1300	9	15		3
	6 mm	*set 1*	200	300	10	15	6	1
			275	400	15	18	7	2
			350	500	20	21		3
		set 2	200 to 1000	500 to 1000	20	21	7	3

Laboratory techniques

Metallographic practices

After welding, all sheets were visually inspected for surface defects like excessive flash and surface flaws. Base material and transverse weld specimens for metallographic analysis were cut, cold mounted, polished, etteched with modified *Poultons reagent* (12ml *HCl*, 31ml HNO_3, 1ml *HF*, 1g H_2CrO_4 and 11ml distiled water) and observed using the *Zeiss Stemi 2000-C* and *Zeiss Axiotech 100HD* microscopes, in order to detect large and very small internal flaws as well as to analyse welds morphology.

Grain-size measurements were performed according to the ASTM E112-96 standard. However, for some cases, in order to depict the grain-size distribution within a particular area of interest, *ImageJ software* was used for digital image processing, according the practices proposed in Ferreira and Rasband (2012).

Mechanical testing

Hardness

During this work, the micro-hardness measurements, in selected areas of the mechanical testing samples and of the welds, were performed, according to the ASTM E384 standard, using a *Shimadzu - Micro-Hardness Tester*, with 200gf load during 30s.

Overageing tests

In order to analyse the sensitivity of the AA6082-T6 heat-treatable aluminium alloy to overageing, at very high heating rates, very small samples, shown in Figure 3.2a), were heated at 30ºC/s using a *Theta 5528 vertical infra-red furnace* (see Figure 3.2b). As shown in Figure 3.2a), the volume of each sample was approximately 90mm^3 with a cross-section of 3x3mm and, the tests, were performed at temperatures from 240ºC to 600ºC. The use of very small samples and very fast heating conditions intended to simulate the very small volume of material processed during FSW, at each tool revolution, and the fast heating conditions experienced during welding.

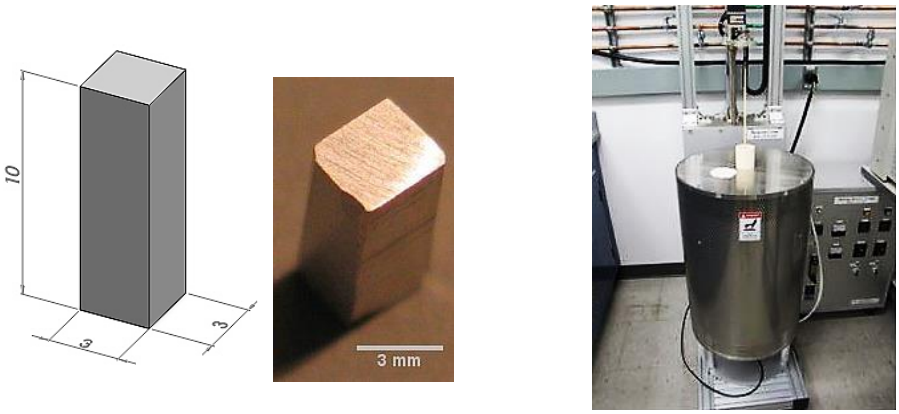

(a) (b)

Figure 3.2 – Overageing testing sample (a) and testing equipment (b).

Tensile and Shear testing

The plastic behaviour of the base materials and welds was analysed by performing tensile and shear tests under *quasi-static* and *quasi-dynamic* conditions, in accordance with the ASTM E8M and ASTM E21 standards.

The testing speed, used on *quasi-static* tests, was 5 mm/min and, the testing temperatures ranged from room temperature to 500ºC. The temperature was controlled by using a thermocouple placed inside the convection oven, directly in contact with the surface of the samples.

The *quasi-dynamic* tensile tests were performed by using speeds up to 3000 mm/min. Temperature data acquisition during the dynamic tests was performed using a *FLIR P Series* Infrared thermographic camera.

During tensile testing, except for the tests performed above room temperature, the strain data acquisition was performed using *ARAMIS Optical 3D Deformation & Strain measurement system*. As it is described in further sections, the use of this technique in tensile testing of transverse weld samples,

using bulk traverse samples, requires a correct methodology in order to assess efficiently the local plastic behaviour.

The shear tests were performed under *quasi-static* conditions, at room temperature, with testing speed of 5 mm/min, in an *Instron 4206* machine and strain data acquisition was performed using *ARAMIS Optical 3D Deformation & Strain Measurement system*. Being an innovative technique, the shear testing procedures will be described in detail in further sections.

Local properties assessment using uniaxial tensile tests

Method

In this section a simple procedure for the mechanical characterization of the local plastic behaviour of welds is presented. The present methodology enables to compute local tensile stress-strain curves, from local strain fields registered, using DIC, during tensile tests of transverse weld specimens, as schematized in Figure 3.3. In Figure 3.4a) is shown a picture and a scheme of a full-size transverse tensile specimen, with the weld centred in the gauge section and the loading axis normal to the welding direction. In this figure, the TMAZ, both HAZ (at AS and at the RS) and BM are respectively signalized. In Figure 3.4b) is possible to observe an image of the major logarithmic strain (ε_1) distribution after maximum load, acquired using DIC, in the surface and in the thickness of a 6mm thick weld tensile sample. Observing the figure it is possible to verify the non-uniform strain distribution across the sample and where the largest

strain values are registered, which corresponds to the zone where the rupture probably occurs.

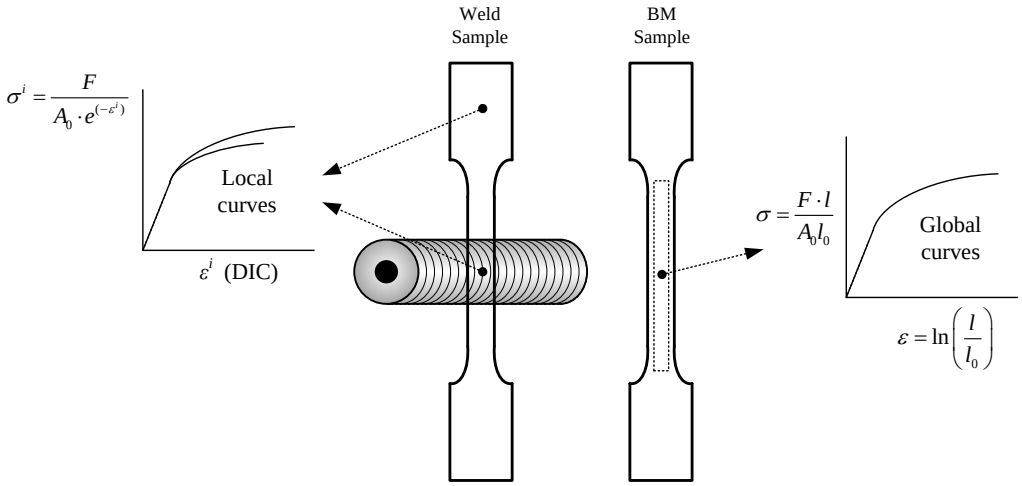

Figure 3.3 – Base material and weld transverse tensile specimen scheme.

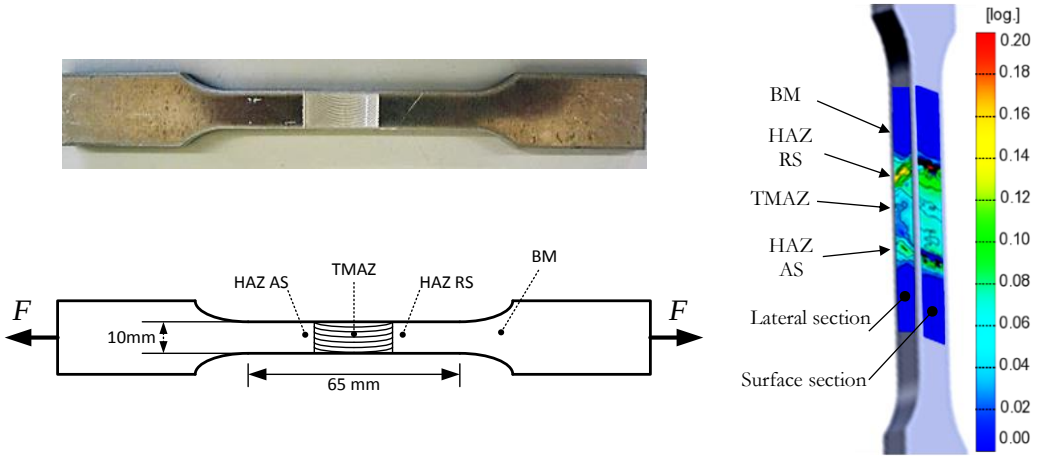

(a) (b)

Figure 3.4 – Weld transverse tensile sample picture and scheme (a), and DIC strain maps registered during testing (b).

Knowing the local strain values, it is possible to determine the evolution of the cross sectional area of a specific part of the sample, A^i, using the following relation

$$A^i = A_0^i \exp(-\varepsilon^i), \tag{3.1}$$

in which A_0^i is the initial cross-section of the specimen in the zone under study, calculated after evaluating specimen dimensions across the samples, and ε^i is the local axial strain registered using DIC.

The local stress in this area is obtained by dividing the applied load, F, by the actual cross sectional area, A^i, of the part of the sample under study:

$$\sigma^i = \frac{F}{A^i}. \tag{3.2}$$

Expressions (3.1) and (3.2) can be used as long as the sample part under analysis is subjected to uniaxial loading conditions. In order to evaluate if the local microstructural heterogeneities and geometric discontinuities, across the transverse weld samples, such as thickness variations across the weld, had any influence in the local strain fields, the evolution of local principal logarithmic strains ε_1^i and ε_2^i with plastic deformation should be analyzed before calculating the stress-strain curves. This analysis allows determining the occurrence of any local change of the deformation path during the tensile test. More precisely, it is possible to evaluate the existence of any local stress triaxiality and if it had any influence on the local stress-strain curves registered for each sample part. The proposed method was tested and validated in the mechanical characterization of very thin welds (1mm) in Leitão *et al.* (2012) – *Annex A*. The following case study exemplifies the application of this method to the mechanical characterization of the welds tested in present work.

Case study – A 6mm thick AA6082weld sample

For the sample used in the demonstration case study, local tensile stress-strain curves were calculated for all sample regions identified in Figure 3.4b) (HAZ AS, HAZ RS, TMAZ and BM). Before computing the local cross-section area evolution, from eq. (3.1), the local loading conditions are always analysed by plotting the evolution of the local principal logarithmic strains (ε_1^i and ε_2^i) with plastic deformation. The results obtained for sample areas corresponding to different weld zones, for the specimen analysed in this case, are shown in Figure 3.5. It is important to emphasize that, when the lateral section of the tensile sample (see Figure 3.4b) is considered, only ε_1^i and ε_3^i are measured, as shown in the scheme of Figure 3.5. In this case, ε_2^i can be calculated assuming volume constancy, i.e.,

$$\varepsilon_1 + \varepsilon_2 + \varepsilon_3 = 0. \tag{3.3}$$

The logarithmic strain values plotted in this figure correspond to an average of the strain values registered for all the points located inside the areas under study, calculated using *Aramis* software (GOM mbH, 2009). In the same figure it is also plotted the strain path corresponding to pure uniaxial loading conditions for isotropic materials ($\varepsilon_2/\varepsilon_1 = -0.5$). Analysing the major and the minor strain evolution in Figure 3.5, it is possible to verify that linear strain paths were registered in the weld zone, for all the weld zones before maximum load was attained. In fact, in Figure 3.5, is possible to verify that deformation path corresponding to the HAZ RS zone, started changing after maximum load had been attained (signalised in the figure by necking).

Comparing the strain paths corresponding to the AS and RS HAZ zones, with those representing isotropic uniaxial loading conditions, it is

possible to conclude that the slopes $(\varepsilon_2/\varepsilon_1)$ corresponding to the HAZ strain paths are higher than -0.5. This type of behaviour can be attributed to the existence of constraints in the very narrow deformed area and/or severe anisotropic conditions inside it. It is also possible to observe that, the strain path corresponding to the TMAZ zone follows the uniaxial tensile path.

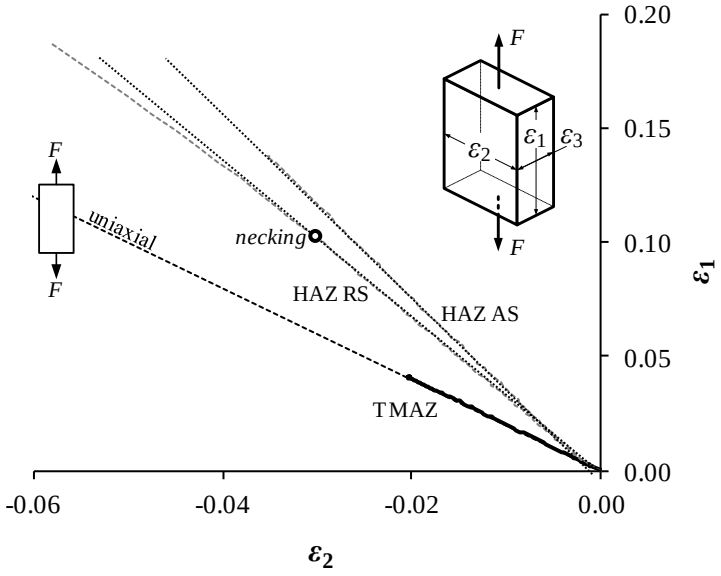

Figure 3.5 – Strain path evolution.

The local stress-strain curves corresponding to the different weld zones, plotted in Figure 3.6 were computed using average strain values, evaluated from the strain distribution inside the weld area under measurement, which are signalised in the strain maps in Figure 3.4b).

Observing the results in Figure 3.6, it is possible to conclude that, in view of the progressive gradient in properties depicted from the hardness profile, also shown in the figure, the plastic properties registered for the HAZ zone, in both retreating and advancing sides, are similar and lower than those registered in the TMAZ zone, which, in turn, is lower than those registered for the BM. These sharp differences in strength between BM and the remaining

weld zones, lead to premature strain localization in the weaker zones, avoiding, in this case, the base material to be plastically deformed during testing, which is perfectly translated by the BM curve registered using DIC.

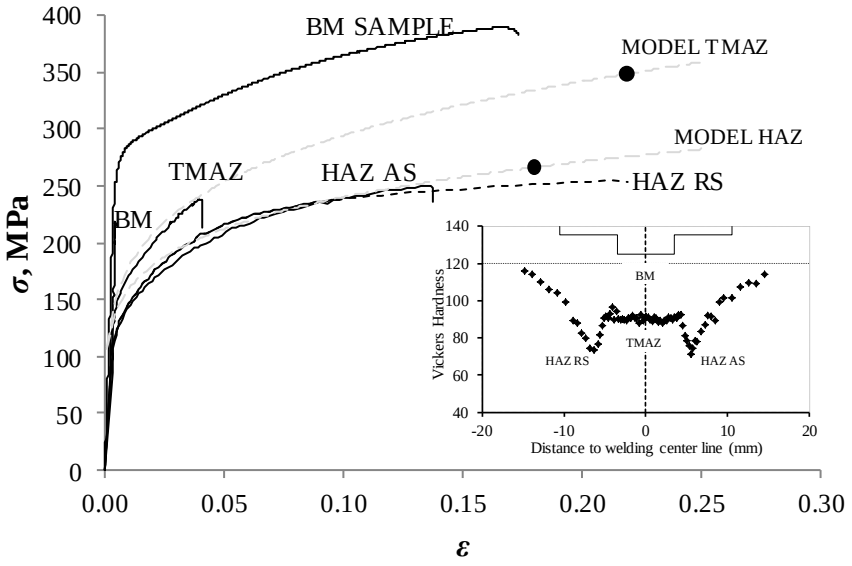

Figure 3.6 – Local tensile stress-strain curves and hardness profile.

In order to preview the plastic behaviour of the welds until high values of plastic deformation, from the local tensile stress-strain curves, the *Swift* isotropic work-hardening model

$$\sigma = k(\varepsilon_0 + \bar{\varepsilon}^{\mathrm{p}})^n \tag{3.4}$$

was adjusted to HAZ_AS and TMAZ curves of Figure 3.6. In the previous equation, k and ε_0 are material constants, σ is the flow stress in simple tension, $\bar{\varepsilon}^{\mathrm{p}}$ the equivalent plastic strain and n the hardening coefficient. Material parameters identification was performed by using the in-house code

DD3MAT (Chaparro *et al.*, 2008). The results are shown in Table 3.2 and the stress-strain curves, plotted according to eq.(3.4), are shown in Figure 3.6 (MODEL_TMAZ and MODEL_HAZ_AS). In Table 3.2 it is also possible to observe the values of the ultimate tensile strength (σ_u), for all the weld materials, estimated using *Considère* criteria. According to this criterion, for the *Swift* equation:

$$\sigma_u = kn^n. \tag{3.5}$$

In the graphic of Figure 3.6, the maximum stress values, corresponding to each weld, are signalised by black dots in the MODEL curves.

Table 3.2 – Swift coefficients for each curve and ultimate tensile strength ($\varepsilon_0 = 0.01$).

	k, MPa	*n*	σ_u, MPa
MODEL TMAZ	483.4	0.216	347
MODEL HAZ AS	360.6	0.177	265

Local properties assessment using simple shear Tests

During this study, shear tests were performed in a universal tensile testing machine and strain data acquisition via Digital Image Correlation (DIC), using the apparatus shown in Figure 3.7a) and in Figure 3.7b). Being a non-standardized test, it was necessary to develop the shear testing tool, the shear sample geometry and the test procedures described in the next section.

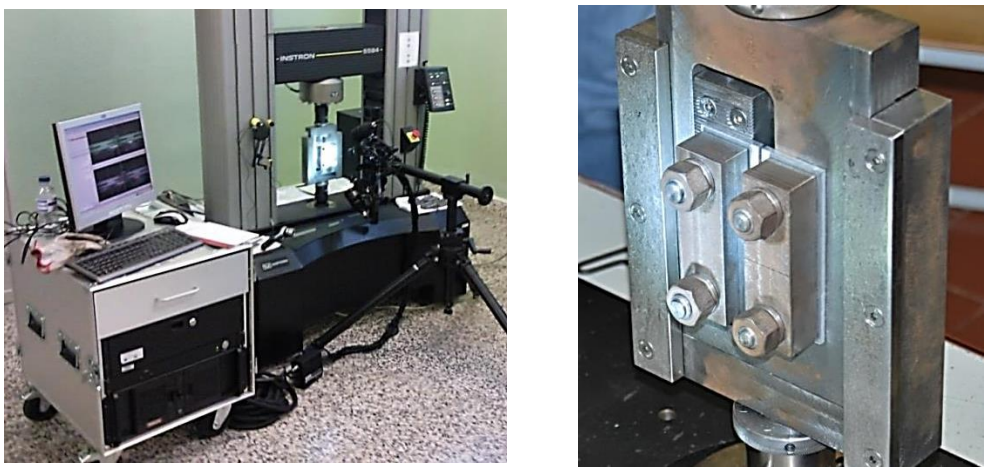

Figure 3.7 – GOM Aramis 5M apparatus (a) and tool detail (b) during shear testing.

Equipment

As referred, in present work, a special tool enabling to perform simple shear tests was developed. The shear device, illustrated in Figure 3.8a), works directly connected to a tensile testing machine (see Figure 3.7a), which promotes the parallel translation between the fixed and the moving parts of the tool, identified in the Figure 3.8a). The shear samples, whose geometry is shown in Figure 3.8b), are placed in the tool with the aid of cylindrical guides and fixed using grips. The tool design was conceived in order to avoid any rotation of the moving part of the tool, enabling the planar deformation of the sample during the test. In this way, as can be observed in Figure 3.8c), where a scheme representing *Section A* in Figure 3.8b) is shown, the vertical translation of the moving part of the tool promotes the deformation in simple shear of the central section of the sample, with lower cross-section, labelled as *shear zone* in Figure 3.8b).

The samples geometry was selected in order to avoid undesirable phenomena, such as buckling, stress concentration and abnormal strain distribution at the shear zone free-ends, which were reported by G'Sell *et al.* (1983) and Bouvier et *al*. (2006a, 2006b) in shear testing of very thin plates.

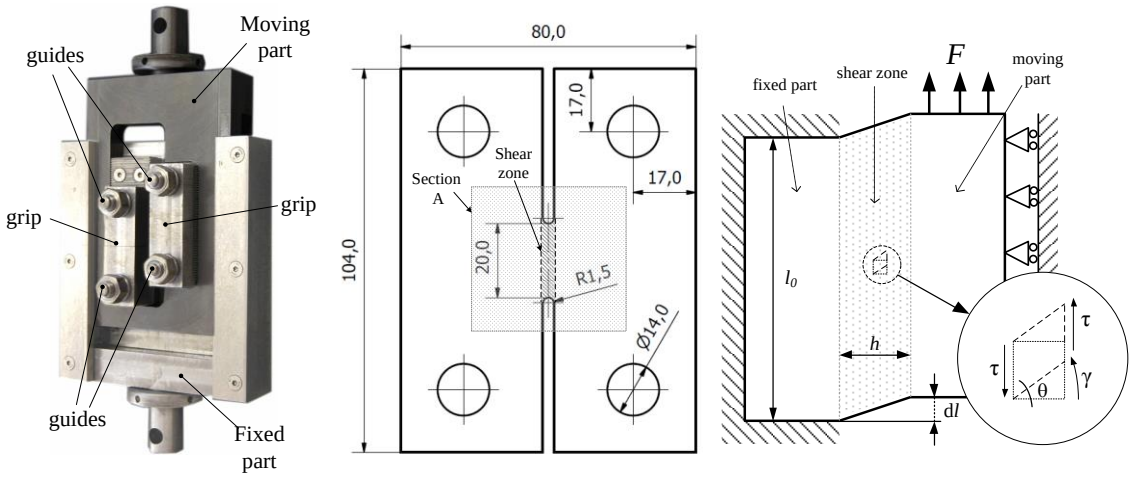

(a) (b) (c)

Figure 3.8 – Shear test tool (a), shear test sample geometry (b) and scheme of the shear zone behaviour under simple shear solicitation (c).

Due to the high relevance of the size of the homogeneous strain area, on shear testing results, several authors have already studied the influence of specimen dimensions on strain distribution. Bouvier *et al.* (2006b) stated that the size of the heterogeneous deformation area increases by decreasing the length (l_0) to width (h) ratio of the shear zone. In Figure 3.8b), where the dimensions of the different shear samples features are shown, it is possible to depict that the maximum shear area width (h) is 3 mm and the minimum shear length (l_0) is 20 mm. Actually, the circular geometry, at the free-end of the shear zone, promotes a smooth variation of the h value and the maximization of

the geometry factor (l_0/h) at the centre of the sample, which optimizes the homogeneous strain area size.

Due to its potential effect on load testing results, the friction load between the fixed and the moving parts of the shear testing tool was measured. In Figure 3.9 is compared the load versus the vertical displacement evolution for tests performed with and without sample. Observing the figure, it is possible to conclude that the load values for the test performed without sample are much lower than that registered in testing a sample, which allows to conclude that the influence of the friction between the fixed and the moving parts of the shear tool, on testing load results, is negligible.

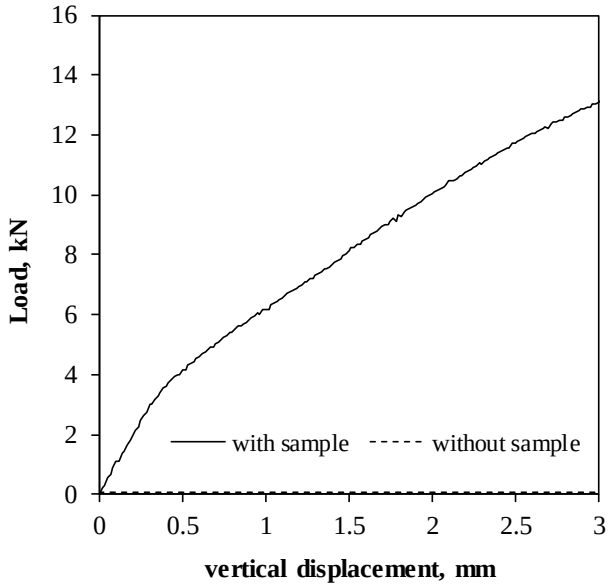

Figure 3.9 - Load (kN) versus vertical displacement (mm) evolution in tests performed with and without sample.

In Figure 3.10 is shown an image of the sample gage section before testing (Figure 3.10a) and after plastic deformation, at maximum load (Figure 3.10b). In Figure 3.10b) is also shown the corresponding vertical displacement

map, acquired by DIC. Analysing this map, it is possible to conclude that the region marked as 1, corresponding to the part of the sample clamped to the fixed part of the shear tool, displays a uniform vertical displacement of 1.32mm, indicating that the sample slipped slightly during testing. However, as stated by Bouvier *et al.* (2006b), the use of a noncontact optical technique, such as DIC, for strain data acquisition, enables to eliminate the influence of any sample slipping during the test on strain measurement.

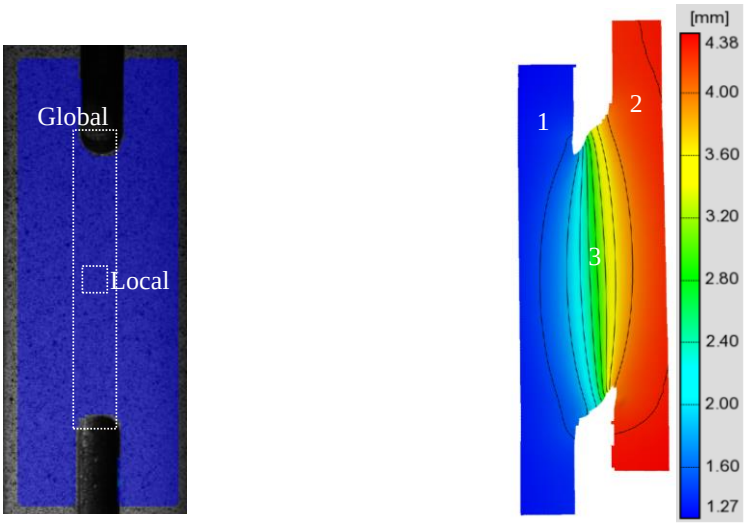

(a) (b)

Figure 3.10 - Gage section before testing (a) and vertical displacement map at maximum load(b). (Annex C)

Strain data analysis

In Figure 3.11 are shown ε_{xy} strain maps, calculated using ARAMIS software, at half of the maximum load ($F_{max}/2$) and at maximum load (F_{max}), for AA5083 and AA6082 samples, respectively. As it is possible to see in Figure 3.11, after yielding, an area of heterogeneous plastic deformation is formed along the

shear zone, symmetric relative to the loading direction and to the sample middle-plane. The gradient in strain distribution becomes sharper at maximum load, when strain localization occurs at the free-ends of the shear zone. G'Sell *et al.*(1983) reported that this strain concentration results, on one hand, from the constrain effect of the grips, reacting against the rotational moment imposed by the couple of shearing forces and, on the other hand, from the departure from ideal simple shear conditions, at the shear zone free-end, where stresses normal and parallel to the sample surfaces develop. The localized transverse tensile stresses, at the shear zone free-ends, promote the strain localization at maximum load.

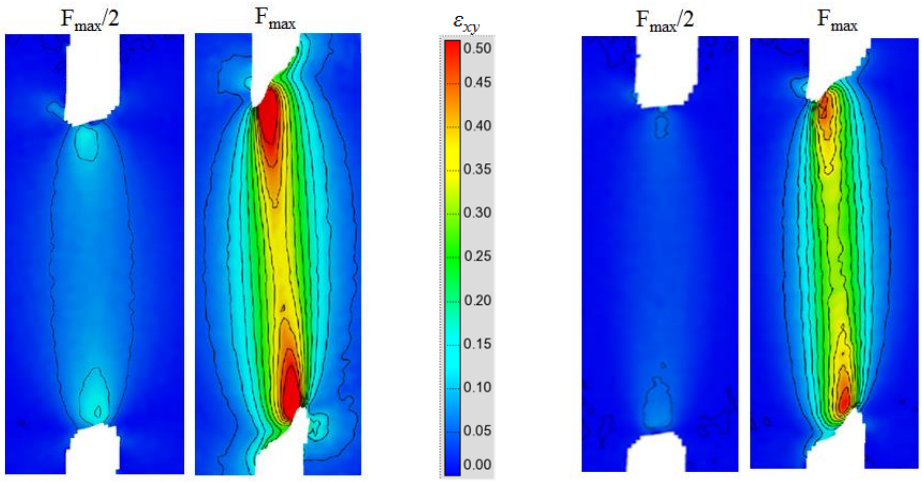

Figure 3.11 - Strain maps (ε_{xy}) at half of maximum load ($F_{max}/2$) and at maximum load (F_{max}) for the AA5083 (a) and AA6082 (b) alloys. (Annex C)

In order to evaluate the accuracy of the strain data acquisition by DIC in capturing the strain gradients across the gage section, metallographic analyses were performed in order to identify different deformation patterns across the shear zone. The microstructural evolution near the fracture zone of AA5083 and AA6082 shear samples is shown in Figure 3.12 and in Figure 3.13,

respectively. In these pictures it is possible to see the evolution in grain shape and orientation, from the non-deformed part of the sample to the fracture surface. The evolution of the angle between the initial grain orientation and the normal to the loading direction (θ) was measured, being marked in both micrographs. In both figures are also shown shear angle maps (γ), obtained by DIC, after maximum load, for the same samples. Since the shear angle (θ) and the shear strain (γ) may be related through the expression

$$\gamma = \tan\theta \cong \theta, \tag{3.6}$$

the results from the metallographic analysis were compared with DIC measurements, as is shown in the graphs of the Figure 3.14a) and Figure 3.14b), for the AA5083 and AA6082 alloys, respectively. In each of these graphs, the evolution of θ and γ with the distance to the fracture surface of the samples is plotted, considering the sample sections marked by black lines in each strain map of the Figure 3.12 and Figure 3.13. From the graphs it is possible to depict that both type of results are in very good agreement.

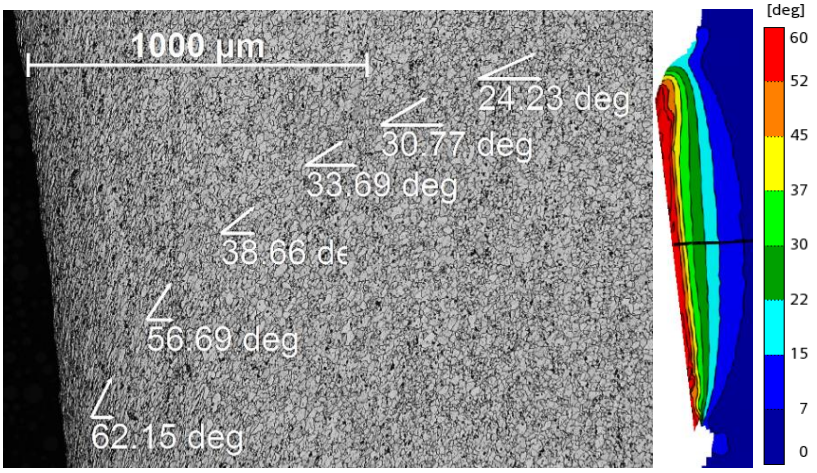

Figure 3.12 - Evolution of grain orientation (θ), from micrographic analysis, and shear strain angle (γ), assessed by DIC, for the AA5083-H111 alloy. (Annex C)

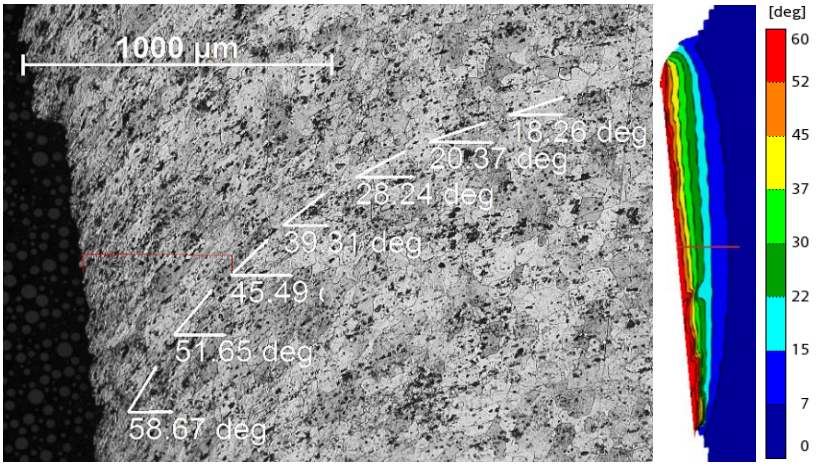

Figure 3.13 - Evolution of grain orientation (θ), from micrographic analysis, and shear strain angle (γ), assessed by DIC, for the AA6082-T6 alloy. (Annex C)

For each base material sample tested, the strain path evolution with plastic deformation, inside the shear zone, was also analysed in order to verify if the simple shear loading conditions prevail until maximum load, in spite of the non-uniform strain distribution depicted in previous figures. The major (ε_1) versus the minor strain (ε_2) evolution, which is representative of the strain path evolution during loading, is shown in Figure 3.15a) and in Figure 3.15b), for the AA5083 and AA6082 alloys, respectively. The results plotted in the graphs correspond to average strain values calculated using *Aramis* software. Two evaluation areas were considered for calculating the average strains ε_1 and ε_2, which are identified as Local and Global, in Figure 3.10a). Using the Global evaluation area, the full range of strain values registered in the shear zone is considered for computing the average strains. Using the Local evaluation area, only the strain values at the centre of the sample, where the strain fields are homogeneous, are considered in computing the average strains.

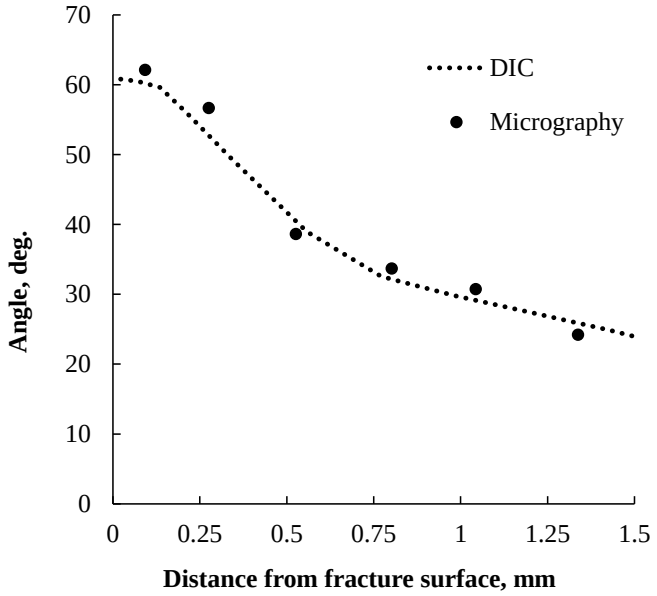

(a)

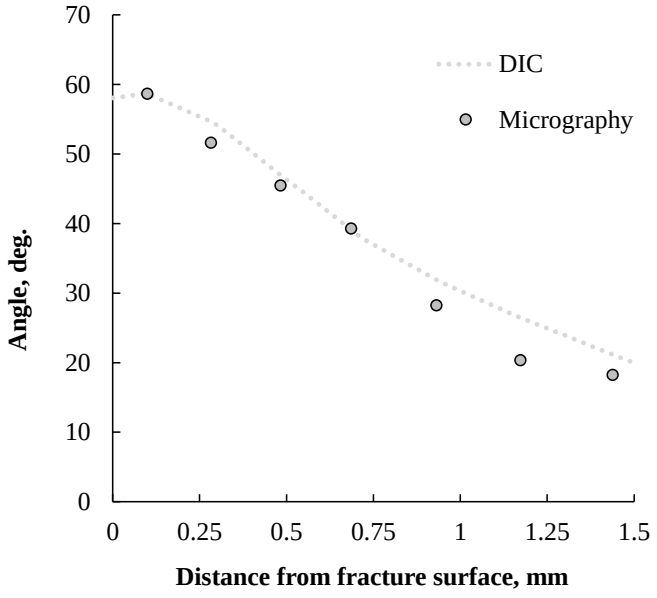

(b)

Figure 3.14 - Evolution of grain orientation (θ), from micrographic analysis, and shear strain angle (γ), assessed by DIC, for the AA5083-H111 (a) and AA6082-T6 (b) alloys. (Annex C)

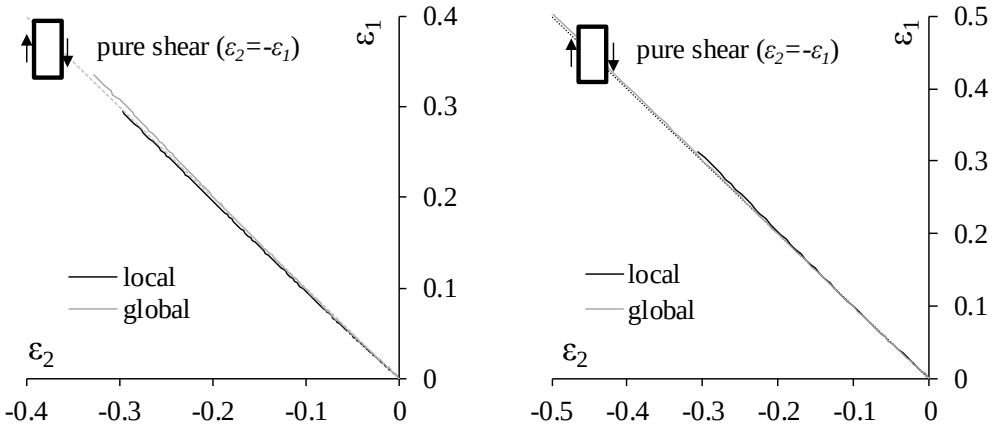

(a) (b)

Figure 3.15 - Strain path evolution, during shear testing, for AA5083 (a) and AA6082 (b) samples. (Annex C)

Analysing the results for both alloys, in Figure 3.15, it is possible to conclude that pure-shear conditions ($\varepsilon_2 = -\varepsilon_1$) prevail until maximum load, independently of the strain evaluation area considered. Actually, no strain path change is observed, even considering the global evaluation area, which allows concluding that the free-end influence on strain distribution, inside the shear zone, has no significant influence on global strain path evolution.

Shear stress-strain curves calculation

Using the strain data acquired by DIC, shear stress-strain curves (τ, γ) were computed, considering the Local and the Global strain evaluation areas, indicated in Figure 3.10a), for calculating the average strain (γ) in the shear zone. Assuming iso-stress conditions during shear testing, the shear stress

($\tau = \tau_{xy}$) was obtained by dividing the testing load (F) by the shear zone cross-section area (A), according to the equation

$$\tau = \frac{F}{A} = \frac{F}{l_0 \times t} \tag{3.7}$$

where, l_0 and t are the length and the thickness of the shear zone, respectively. In the same way, the shear strain (γ) was obtained considering the relation

$$\gamma = 2\varepsilon_{xy}. \tag{3.8}$$

The Local and the Global average shear stress-strain curves ($\tau - \gamma$) are plotted in Figure 3.16, where it is possible to depict an excellent concordance between both type of results. This shows that the non-uniform shear strain distribution, depicted in previous analysis, does not influence significantly the shape of the curves. The only difference between Local and Global results is that the strain values, corresponding to the global strain average, are significantly higher than the local average strain values, corresponding to the local area with homogeneous strain distribution, at the centre of the sample.

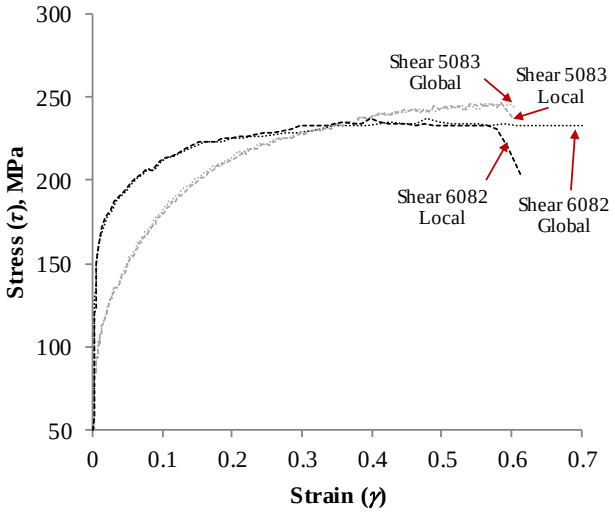

Figure 3.16 - Local and global shear stress-strain curves. (Annex C)

Analysing the shear stress-strain curves, it is possible to conclude that the AA6082 alloy, after moderate values of plastic deformation, presents an almost steady-state flow stress, which is according to that reported by Rauch *et al.*, (2002), for other aluminium alloys of the 6xxx series. On the other hand, for the AA5083 alloy, which displays lower yield strength than the AA6082 alloy, the flow stress keeps increasing with loading. Actually, the AA5083 alloy attains strength values higher than that of the AA6082 alloy, after some plastic deformation. The differences in strain-hardening behaviour determine the shape and size of the plastic deformation area, at the centre of the sample, which, as shown in Figure 3.11, is narrower for the AA6082 alloy than for the AA5083 alloy. Actually, the AA5083 alloy displays a wider plastic deformation zone, with a belly form, for the same strain range of the AA6082, due to its stronger hardening sensitivity.

Finally, in Figure 3.17 are compared the equivalent stress-strain curves corresponding to uniaxial tensile tests and shear tests, for both alloys. The equivalent stress-strain curves were obtained using the *Hill'48* plasticity criteria

$$F\left(\sigma_{yy}-\sigma_{zz}\right)^2+G\left(\sigma_{zz}-\sigma_{xx}\right)^2+H\left(\sigma_{xx}-\sigma_{yy}\right)^2+2L\tau_{yz}{}^2+2M\tau_{zx}{}^2+2N\tau_{xy}{}^2=K^2 \qquad (3.9)$$

where σ_{xx}, σ_{yy}, σ_{zz}, τ_{xy}, τ_{xz} and τ_{yz}, are the components of the *Cauchy* stress tensor, defined in the orthotropic frame, and F, G, H, L, M and N are the *Hill'48* coefficients of anisotropy. The *Hill'48* coefficients were calculated according to the equations

$$F = \frac{r_0}{r_{90}(1+r_0)} \tag{3.10}$$

$$G = \frac{1}{1+r_0} \tag{3.11}$$

$$H = \frac{r_0}{1+r_0} \tag{3.12}$$

$$N = (r_0 + r_{90})\frac{(2r_{45}+1)}{2r_{90}(1+r_0)} \tag{3.13}$$

where r_0, r_{45} and r_{90} are the anisotropy coefficients determined by performing tensile tests at 0, 45 and 90º from the rolling direction, as shown in the scheme represented in Figure 3.17, where it is also shown the *Hill'48* coefficients determined for both alloys.

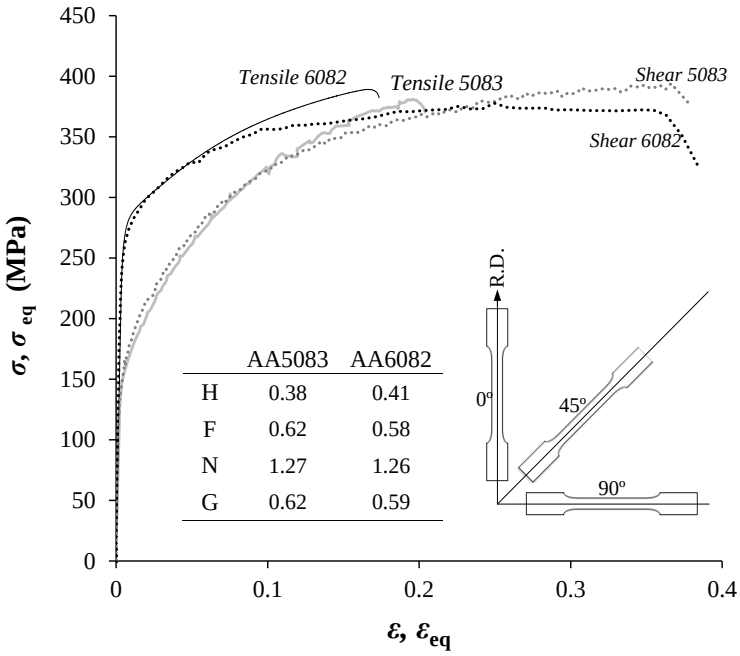

Figure 3.17 – Equivalent strain-stress (σ-ε) curves for the base material. (Annex C)

Observing Figure 3.17, it is possible to conclude that, until moderate values of plastic deformation ($\varepsilon \approx 0.1$), the tensile and shear equivalent stress-strain curves are in excellent concordance, for both alloys. However, for higher levels of plastic deformation, the tensile curves become higher than the shear curves, which points for the limitations of the *Hill'48* criteria in describing aluminium alloys behaviour, as already stated by other authors, e.g., Wang and Lee (2006).

With the foregoing, it was possible to depict the good accuracy of results obtained using DIC to evaluate the shear response for the AA5083 and AA6082 alloys, as well as the benefits of the shear test in assessing materials constitutive behaviour up to very large values of plastic deformation. The shear data was validated by comparing shear equivalent stress-strain curves, calculated using the *Hill'48* criteria, with the ones obtained in uniaxial tension. For both alloys, the concordance between shear and tensile curves, for moderate values of plastic deformation, was evident. The shear testing procedure can also be applied for the assessment of the plastic properties of thick welds, with special relevance, for the local characterization of the plastic properties, for which the limited width of the sampling area makes the mechanical characterization in tension very hard. In Chapter 8 the results of the mechanical characterization of welds will be shown.

4

Visual inspection and morphological analysis

In this chapter are shown the results of an extensive analysis, based on defects qualification and on the morphological analysis of welds performed using several welding conditions. The results are compared for each weld condition, in order to depict any important trend, aiming to establish the influence of each weld parameter on friction stir weldability.

This Page Intentionally Left Blank

Visual Inspection

In order to perform a deep analysis of the weldability in FSW of the AA5083-H111 and AA6082-T6 alloys, both base materials were welded using different tools and process parameters, according to the procedures already described in Chapter 3, i.e., bead on plate welds were produced using conical shoulder tools, with cone angle of 5º and cylindrical threaded pins. The welding speed (v), rotating speed (ω), vertical force (F_z), shoulder and pin diameters (D_s and D_p, respectively) and tool pitch angle (α) were varied according to Table 3.1. As already mentioned in Chapter 3, the friction stir welds were performed in 4 and 6 mm thick sheets of the AA5083-H111 alloy, which in the text will be labelled 5_4 and 5_6, respectively, and 3 and 6 mm thick sheets of the AA6082-T6 alloy, which will be labelled 6_3 and 6_6, respectively. Qualitative inspection of the welds was performed by visual examination to detect surface defects, followed by metallographic analysis to detect internal flaws.

Three basic types of defects were identified: excessive flash (F) (exemplified in Figure 4.1a), surface flaws (SD) (exemplified in Figure 4.1b) and internal voids (ID) (exemplified in Figure 4.1c). Under some welding conditions, the pin was broken (BP) and it was not possible to perform the weld. These situations have also been identified and reported in conjunction with the weld inspection results. Finally, it is important to enhance that the results identified as GOOD, after visual and metallographic analysis, comprise both the non-defective welds and the welds with very small defects (exemplified in Figure 4.1d) that were considered unimportant for the global strength of the welds in monotonic loading. In Table 4.1 are summarized the different weld inspection results and the symbols used along the text, in the different figures and graphs, to identify it.

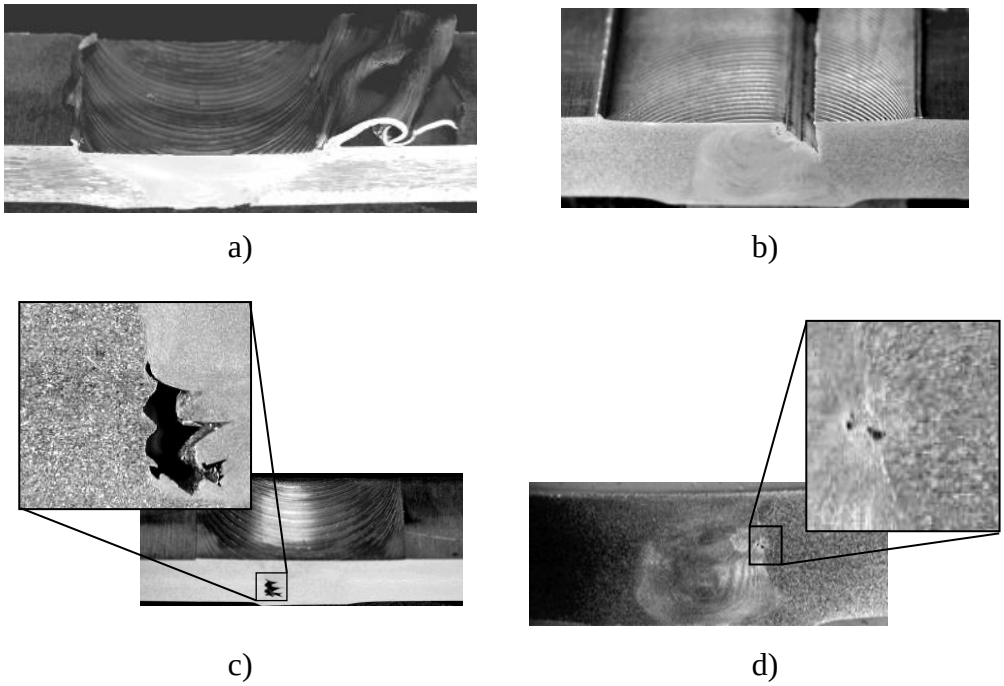

a) b)

c) d)

Figure 4.1 – Tipical welding defects: a) Flash (F), b) Surface defect (SD), c) Internal defect (ID) and d) very small defct [Annex D]

Table 4.1 – Weld inspection classification and nomenclature

weld type	acronym	symbol
No defect	GOOD	●
Flash	F	△
Surface defect	SD	◇
Internal defect	ID	◆
Broken pin	BP	■

In Table 4.2 to Table 4.9 are shown the weld inspection results for the AA5083 and the AA6082 alloys, respectively, for the full range of welding

conditions tested in this work: in Table 4.2, Table 4.3, Table 4.6 and Table 4.7, are shown the results corresponding to the 5_4 and 5_6 welds and in Table 4.4, Table 4.5, Table 4.8 and Table 4.9, are shown the results corresponding to the 6_3 and 6_6 welds. For all testing conditions the results are grouped according to the processing parameters (welding speed, rotating speed and vertical force), in Table 4.2 to Table 4.5, and according to the tool parameters (tilt angle and shoulder diameter) in Table 4.6 to Table 4.9. Welding results corresponding to *Set 1* and *Set 2* welding parameters are also clearly delimited in the Tables.

Analysing the full set of tables it is possible to conclude that for the *Set 1* range of welding parameters the AA6082 aluminium alloy presents higher weldability than the AA5083 alloy, since a larger number of acceptable welds (good and small defect welds) were obtained for both plate thicknesses. However, it is important to remark that the number of non-acceptable welds (F, SD, ID and BP) was very high for both alloys, in both plate thicknesses, showing that the process is very sensitive to the choice of tool and machine parameters.

For *Set 2* of welding parameters the number of defective welds is much lower, for both alloys, since these welding tests were planned after *Set 1* welds inspection, which enabled a comprehensive analysis of both base materials welding behaviour and the establishment of optimized welding conditions for each alloy. In this way, in the next, the weldability analysis will be performed considering separately *Set 1* and *Set 2* welds.

Table 4.2– Weld inspection AA5083-H111 (4 mm thick)

Rotational Speed (rpm)	*weld speed (mm/min)*														
	300			400			500			600			700		
	Axial load (kN)			*Axial load (kN)*			*Axial load (kN)*			*Axial load (kN)*			*Axial load (kN)*		
	7	11	15	7	11	15	7	11	15	7	11	15	7	11	15
1100			O												
1000			O												
900			O						O						O
800			O												
700			O												
600	◇	◇	O	◇	◇	◆	◇	◆	◆						
500	◇	O	O	◇	◆	◆	◆	◆	◆						
400	◇	◇	△	■	◆	O	■	■	◆						

O GOOD | △ Flash | ■ Broken Pin | ◇ Surface defect | ◆ Internal defect

Table 4.3 – Weld inspection AA5083-H111 (6 mm thick)

Rot.al Speed (rpm)	*weld speed (mm/min)*														
	50			100			200			275			350		
	Axial load (kN)			*Axial load (kN)*			*Axial load (kN)*			*Axial load (kN)*			*Axial load (kN)*		
	10	15	20	10	15	20	10	15	20	10	15	20	10	15	20
1000									◆						
900									◆						
800									◆						
700						◆			◆						
600			△			O			O			O			O
500			O			O	◇	O	O	◇	△	O	◇	◇	◇
400			O			O	◇	◇	△	◇	◇	■	◆	◆	◆
300			O			O	◇	◇	◆	◇	◆	■	◇	◆	◆

O GOOD | △ Flash | ■ Broken Pin | ◇ Surface defect | ◆ Internal defect

Table 4.4 – Weld inspection AA6082-T6 (3 mm thick)

Rotational Speed (rpm)	*weld speed (mm/min)*								
	800			950			1100		
	Axial load (kN)			*Axial load (kN)*			*Axial load (kN)*		
	5	7	9	5	7	9	5	7	9
1300	O	O	■	O	O	■	O	■	■
1150	O	O	■	O	O	■	O	O	■
1000	△	O	■	■	O	■	■	O	■

O GOOD | △ Flash | ■ Broken Pin | ◇ Surface defect | ◆ Internal defect

Table 4.5 – Weld inspection AA6082-T6 (6 mm thick)

Rot.al Speed (rpm)	*weld speed (mm/min)*																	
	200			275			350			400			600			1000		
	Axial load (kN)			*Axial load (kN)*			*Axial load (kN)*			*Axial load (kN)*			*Axial load (kN)*			*Axial load (kN)*		
	10	15	20	10	15	20	10	15	20	10	15	20	10	15	20	10	15	20
1000			O									O			O			O
900			O															
800			O															
700			O															
600			O															
500	■	O	O	■	O	O	◆	△	△									
400	◆	O	O	◆	◆	△	◆	◆	O									
300	△	△	△	■	◆	◆	◆	◆	◆									

O GOOD | △ Flash | ■ Broken Pin | ◇ Surface defect | ◆ Internal defect

Table 4.6 – Weld inspection AA5083-H111 (4 mm thick)

D_s, *mm*	F_z *(kN)*								
	7			11			15		
	α^o			α^o			α^o		
	1	2	3	1	2	3	1	2	3
13	■	△	■	◆	△	■	△	■	◆
15	◇	■	◇	◇	◆	◆	◆	O	O
18	◇	◇	■	◆	■	◆	△	◆	■

O GOOD | ○ small defect | △ F | ■ BP | ◇ SD | ◆ ID

Table 4.7 – Weld inspection AA5083-H111 (6 mm thick)

D_s, *mm*	F_z *(kN)*								
	10			15			20		
	α^o			α^o			α^o		
	1	2	3	1	2	3	1	2	3
15	◇	◇	◆	◇	◇	■	◇	◆	◇
18	◇	◇	◇	◇	◇	◆	◇	◆	O
21	◇	◇	◇	◇	◆	O	◆	O	O

O GOOD | ○ small defect | △ F | ■ BP | ◇ SD | ◆ ID

Table 4.8 – Weld inspection AA6082-T6 (3 mm thick)

D_s, *mm*	F_z *(kN)*								
	5			7			9		
	α^o			α^o			α^o		
	1	2	3	1	2	3	1	2	3
10	△	△	△	■	△	△	■	■	■
12	O	O	O	O	O	O	■	■	■
13	O	O	O	O	O	O	■	■	■
15	O	O	O	O	O	O	■	■	■

O GOOD | ○ small defect | △ F | ■ BP | ◇ SD | ◆ ID

Table 4.9 – Weld inspection AA6082-T6 (6 mm thick)

D_s, *mm*	F_z *(kN)*								
	10			15			20		
	α^o			α^o			α^o		
	1	2	3	1	2	3	1	2	3
15	◆	◆	◆	◇	△	◆	◆	■	◇
18	◆	◆	O	O	O	◆	O	◆	O
21	◆	O	◆	O	◆	O	△	O	O

O GOOD | ○ small defect | △ F | ■ BP | ◇ SD | ◆ ID

Set 1 welding conditions

In order to perform a deeper analysis of the AA5083 and AA6082 alloys weldability, *Set 1* weld inspection results are plotted in the graphs of Figure 4.2 and Figure 4.3, respectively, where the energy consumed per unit length of weld versus the ratio ω/v is shown. The energy E (in J/mm) consumed per unit length of weld was determined using the equation

$$E = T\frac{\omega}{v} \tag{4.1}$$

where T the torque registered by the welding machine during the joining operation.

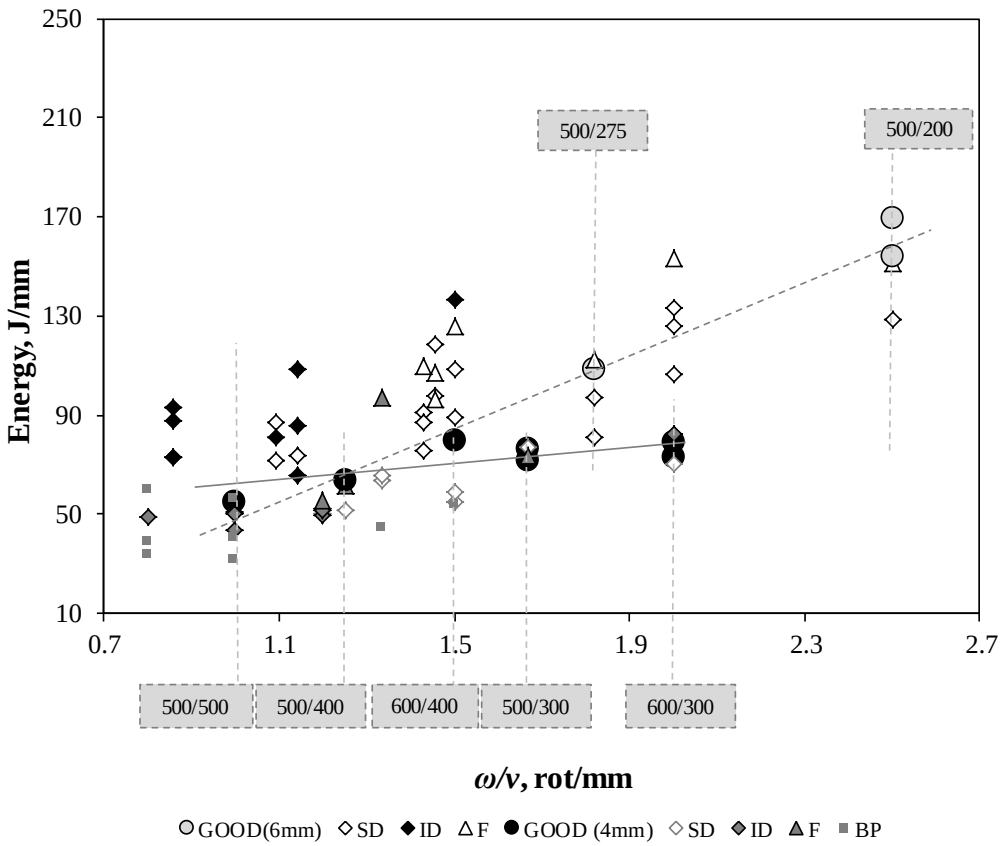

Figure 4.2 – Energy consumed per unit length of weld versus ω/v, for the 5_4 and 5_6 welds performed under Set1 welding conditions.

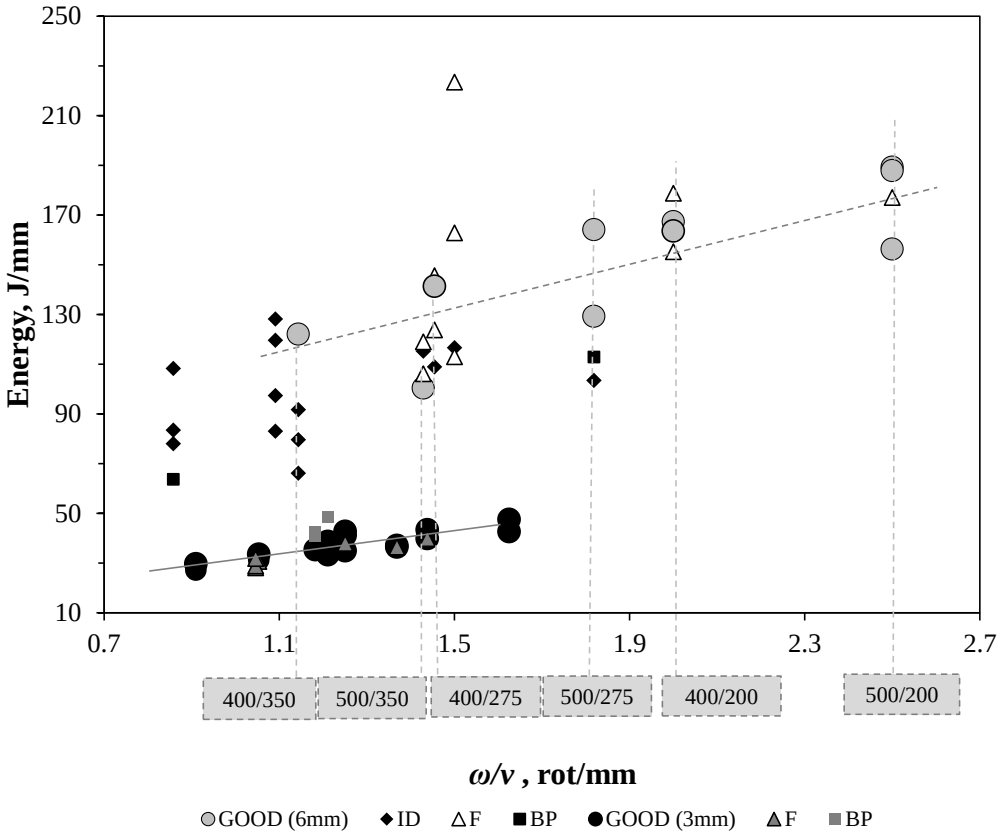

Figure 4.3 – Energy consumed per unit length of weld versus ω/v, for the 6_3 and 6_6 welds performed under Set1 welding conditions.

Looking carefully at the results presented in Figure 4.3 for the 5_6 welds, it is possible to conclude that only three GOOD welds were obtained for these plates under *Set 1* welding conditions. There were a large number of welds with internal and surface defects and also two situations in which the pin was broken. Globally the energy results are widely dispersed and it was impossible to establish any relationship between the energy consumed in the process and the process parameters. However, if only the GOOD weld energy values are considered (large grey circles), which presumably correspond to equilibrium welding conditions, a linear regression can be used to fit the results, which

indicate that the energy consumed in the process increases with increasing ω/v ratios.

For the 5_4 plates, according to Figure 4.2 more non-defective welds were achieved under the selected welding conditions. For these plates, the energy consumed in the process was lower than that for the 5_6 welds and the results are much less dispersed, indicating weld conditions closer to equilibrium. This can be also inferred by fitting the results relative to the GOOD welds. These results show that the energy increases almost linearly with ω/v, but at a much lower rate than that for the 5_6 welds, which sets an important influence of plate thickness on welding conditions. This will be discussed later in this text, when performing the torque sensitivity analysis.

Analysing the results corresponding to the AA6082 alloy, displayed in Figure 4.3, it was possible to conclude that with this base material the principal defect types were: flash formation, for both plate thicknesses, internal defects, for the 6_6 plates, and a large number of broken pin situations, for the 6_3 plates. Just as for the AA5083 alloy, the energy values for the GOOD welds can be fitted using linear interpolation, indicating increasing values with increasing ω/v ratios. For the 6_3 welds, the energy consumed is almost the same for both defective and GOOD welds, which indicates that at the higher rotation speeds used to join these plates, which corresponded to hotter welding conditions tested in this work, the process becomes very stable. On the other hand, for the 6_6 welds, the energy results are more widely dispersed, especially for the low ω/v ratios and/or ω=300 rpm, which correspond to colder welding conditions, indicating again a strong influence of plate thickness on welding conditions, as already stated when analysing the AA5083 welding results.

A more detailed analysis of the *Set 1* weld inspection results enabled some unacceptable welding parameters for each type of alloy/plate to be determined. These are identified in Table 4.10 and Table 4.11, where the unacceptable tool

(α, D_p and D_s) and process (v, ω and F_z) parameters, respectively, are identified by colouring the cells in grey. A welding parameter was considered unacceptable when all the welds produced under welding conditions including this parameter were defective. For the 5_4 plates, parameters leading to only one good weld were also considered unacceptable.

Table 4.10 – Tool parameters

		D_s (mm)			D_p (mm)		α (º)		
AA5083	4mm	13	15	18	4	5	1	2	3
	6 mm	15	18	21	6	7	1	2	3
AA6082	3 mm	10	12	15	5	6	1	2	3
	6 mm	15	18	21	6	7	1	2	3

Table 4.11– Process parameters

		v (mm/min)			ω (rpm)			F_z (kN)		
AA5083	4mm	300	400	500	400	500	600	7	11	15
	6 mm	200	275	350	300	400	500	10	15	20
AA6082	3 mm	800	950	1100	1000	1150	1300	5	7	9
	6 mm	200	275	350	300	400	500	10	15	20

Analysing the grey cells in Table 4.10, it can be seen that no acceptable welds were produced with the narrower shoulders for any of the plates. At the same time, qualitative analysis revealed that the process was relatively unaffected by changing pin dimensions. For both alloys, the main defect that

could be directly related to the small shoulder diameter was flash formation. A very small tool tilt angle (α=1º) also led to flash formation, especially for the thicker plates.

For the 5_4 plates, the 18 mm shoulder tool was also found wanting, since it only produced one good weld. However, in this case no specific defect type could be related to shoulder size. Finally, for the AA5083 alloy, in Table 4.11, it is possible to depict serious limitations in rotation speed (400 rpm for the 4 mm thick plates, and 300 and 400 rpm for the 6 mm thick plates) and traverse speed (500 mm/min for the 4 mm thick plates and 350 mm/min for the 6 mm thick plates) since no suitable welding conditions were achieved using these parameters. Independently of the plate thickness, low rotation speeds and high traverse speeds led to the formation of large internal defects, and for the 5_4 plates, they were also associated with tool destruction (BP) in many cases.

Analysing now the unacceptable welding parameters results for the AA6082 alloy, in Table 4.10 and Table 4.11, it is possible to see that this base material, for both plate thicknesses, displayed much less sensitivity to varying welding parameters than the AA5083 alloy. The only unacceptable welding parameters reported for this base material were related to the very small shoulder diameter (10 mm for the 6_3 plates and 15 mm for the 6_6 plates). For the 6 mm thick plates, the low rotation speed of 300 rpm was also found to be inappropriate.

Another important limiting factor for successful welding was the choice of the axial load (see grey cells in Table 4.11). However, the variation in welding conditions with this parameter was detected to be highly influenced by the nature of the base material. In fact, for the AA5083 alloy, it was found that using very low axial loads (7 and 11 kN, for the 4 mm thick plate, and 10 kN, for the 6 mm plate) led to significant superficial and internal welding defects, which indicates that these values are the lower axial load limits for FSW of these plates. On the other hand, for the AA6082 alloy, no clear limit for axial

load was found when welding the 6 mm thick plates. For the 3 mm plates, a maximum load of 9 kN was determined, since the pin was destroyed in all tests performed with this axial load.

Finally, the weldability results for the 5_6 and 6_6 plates, for which *Set 1* welding conditions were exactly the same, are compared in Figure 4.4 and Figure 4.5. The full range of welding inspection results are summarised in that graphs, where the pressure (P_z) versus rotation to traverse speed ratio (ω/v) are plotted. The pressure parameter, which was calculated using the equation

$$P_z = \frac{F_z}{\frac{\pi}{4}(D_s^2 - D_p^2)} \tag{4.2}$$

reflects the influence of the axial load (F_z) and tool parameters (D_s and D_p) on welding results.

In Figure 4.4 and Figure 4.5, process parameter domains, corresponding to a larger incidence of each defect type, were delimited. Comparing the pictures it is possible to conclude that, for both base materials, flash was mainly formed for the higher values of ω/v, corresponding to the higher heat input conditions, and for the higher values of pressure, P, corresponding to the use of the smaller shoulder diameter tool (D_s = 15 mm). For the lower ω/v values, internal flaws (ID) were the main type of defect detected for both alloys. However, for the AA5083 alloy, for almost the entire range of ω/v values, surface flaws (SD) were also detected for the lower pressure conditions, corresponding to the utilisation of very low axial loads (10 and 15 kN). In contrast, for the AA6082 alloy, no strong limitation in axial load was found, being possible to obtain GOOD welds for all the loads tested. Finally, defects of varying types, according to the global combination of process parameters, were detected for the welds performed with tool tilt angle α = 1º. These situations, which are not explicitly identified in Figure 4.4 and Figure 4.5, justify some dispersion of the weld inspection results in both graphs.

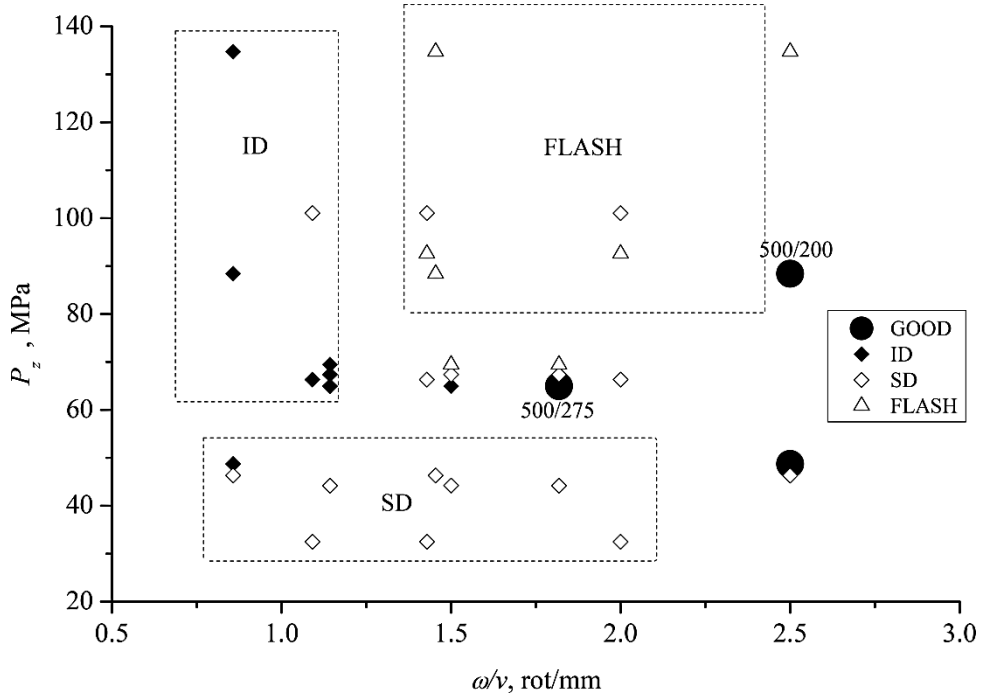

Figure 4.4 – Pressure (P_z) versus rotation to traverse speed ratio (ω/v) for the AA5083 alloy.

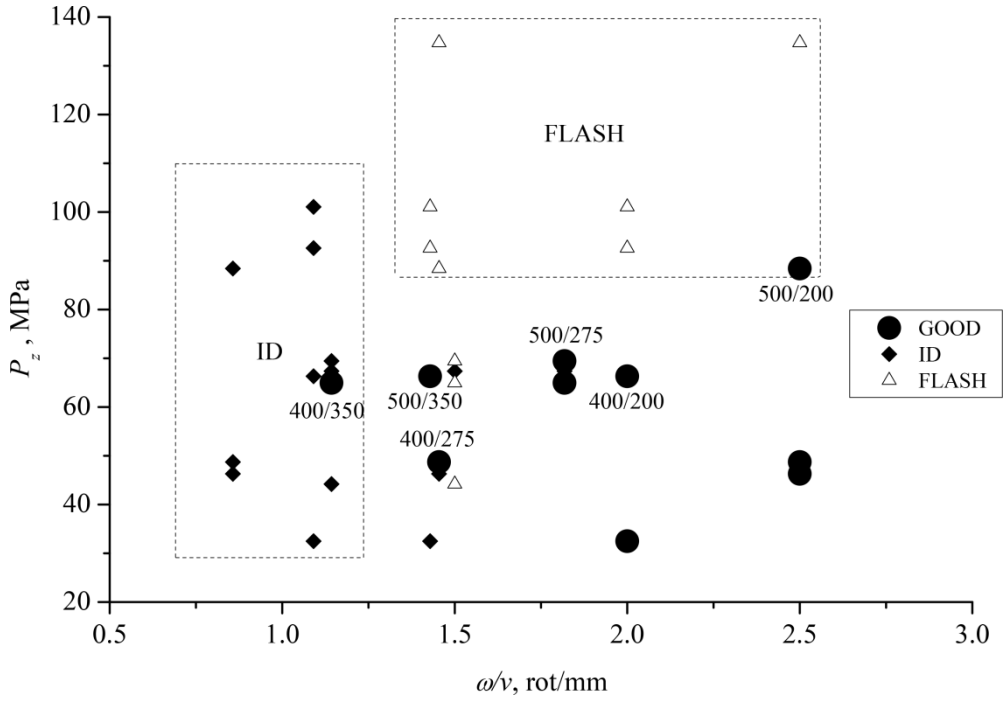

Figure 4.5 – Pressure (P_z) versus rotation to traverse speed ratio (ω/v) for the AA6082 alloy.

The same types of weld defects reported in current work were already reported by other authors (Kim *et al.*, 2006; Chen *et al.*, 2006; Iordachescu *et al.*, 2009). The origin of these defects is currently attributed to an inappropriate level of heat input and/or deficient stirring of the materials, both influenced by the utilization of inadequate process parameters and/or tool characteristics (Zhang *et al.*, 2006; Enlagovan and Balasubramanian, 2008; Padmanaban and Balasubramanian, 2009). Other authors also associated flash formation to the tool incapability to hold the material under it during the process conjugated with the selection of hot processing conditions (Kumar and Kailas, 2008). Actually, it is easy to understand that the formation of welds by FSW, and consequently, the formation of defects, is based on thermic and mechanical transformations of the base materials which are directly related to the set of selected welding parameters. However, in current work, important differences in weldability between the heat treatable and a non-heat treatable base materials were detected, which points for an important influence of base material plastic properties on material flow during FSW, and in this way, on FSW conditions.

Set 2 welding conditions

The analysis of *Set1* weld results enabled to conclude that, for the 6 mm thick plates, the AA5083 alloy displayed much lower weldability than the AA6082 alloy. For each alloy, new welding conditions were tested, after *Set1* welds inspection, which were labelled *Set2* in Chapter 3. With the new selection of welding parameters, for the AA5083 alloy, it was intended to improve the welding results, for the AA6083 alloy, which displayed good weldability, it was intended to optimize welding conditions in order to improve process productivity and weld quality. As shown in Table 3.1, for *Set2* of welding

conditions only one tool (D_s=21mm, D_p=7mm) was used and the tool tilt angle (α=3º) and the axial load (F_z=20kN) were kept constant. These parameters were considered optimum after *Set1* welds inspection.

As already performed for *Set1* results, in Figure 4.6 and Figure 4.7 is plotted the energy consumed per unit length of weld versus the ratio ω/v, for 5_6 and 6_6 welds, respectively, performed under Set 2 welding conditions. Again the symbols used in the graphs identify the weld inspection results for each test according to Table 4.1 nomenclature. Analysing Figure 4.6, where are displayed the results relative to the AA5083 alloy, it is possible to conclude that welding at 200 mm/min and increasing the tool rotation speeds from 600 to 1000 rpm, the weldability of the alloy was not improved since most of the welds obtained displayed internal defects. For this alloy, the weldability was found to be improved by reducing the welding speed, for rotation speeds equal or lower than 500 rpm. Actually, when reducing the welding speed, from 200 to 100 and 50 mm/min, GOOD welds started being consistently obtained.

Analysing now Figure 4.7, where are displayed the results relative to the AA6082 alloy, it is possible to conclude that for this alloy, using appropriate tool parameters and axial load, GOOD welds where obtained increasing the rotation speed, from 600 to 1000 rpm, and the advancing speed, from 200 to 1000 mm/min, which confirms the readiness of this alloy to be joined by FSW already depicted when analysing *Set 1* welding results.

From Figure 4.6 and Figure 4.7, where is plotted the energy input for a broader range of ω/v values than in Figure 4.2 and Figure 4.3, it is also possible to confirm that, for both alloys, the energy inputted during the process increases linearly by increasing the tool rotation speed and keeping the traverse speed constant. However, *Set2* welding results also enable to conclude that keeping the tool rotation speed constant, and varying the traverse speed, the energy input remains almost constant.

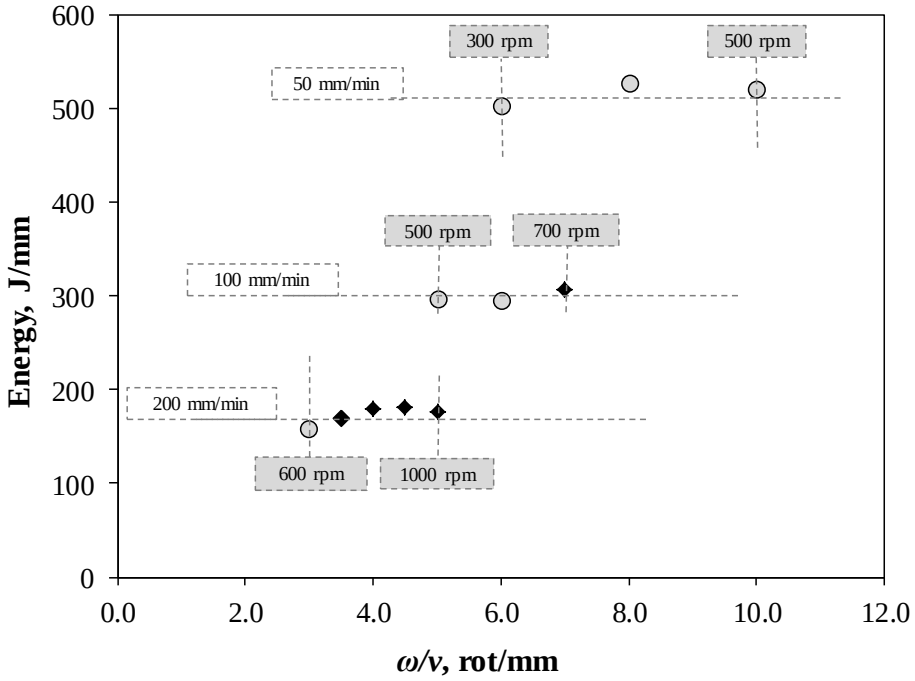

Figure 4.6 – Energy consumed per unit length of weld versus ω/v, for the 5_6 welds performed under Set2 welding conditions.

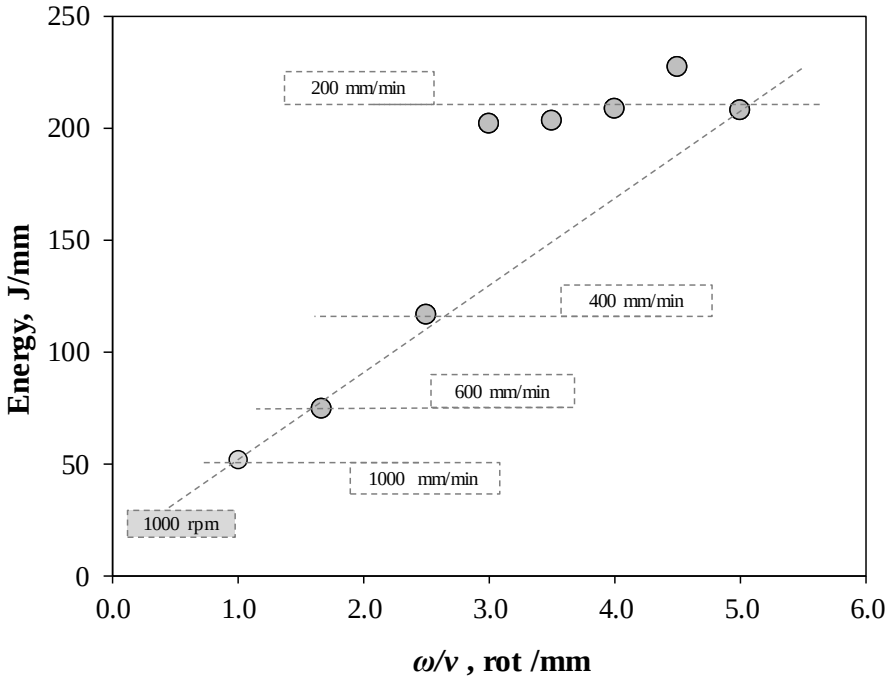

Figure 4.7 – Energy consumed per unit length of weld versus ω/v, for the 6_6 welds performed under Set2 welding conditions.

Despite similar trends were reported for the evolution of the energy inputted during welding with process parameters, for both alloys, it is important to stress that their weldability didn't evolve in the same for *Set2* welding conditions, which points again to the strong influence of base material properties in friction stir weldability. Actually, another important aspect registered in present work was the markedly different morphology of the welds obtained from the different base materials, under the same welding conditions. This aspect will be analysed in the next.

Morphological analysis

Set1 welding parameters

As already pointed in previous section, another important aspect registered in present work was the markedly different morphology of the welds obtained from the different base materials, under the same welding conditions. In order to better illustrate this aspect, 5_6 and 6_6 weld cross sections are compared in Figure 4.8a) to Figure 4.8f). In the figure, each pair of AA6082 and AA5083 welds (a and b, c and d, e and f) were performed using exactly the same welding conditions and the same welding equipment. As it is possible to observe in the figure, independently of the welding conditions, the weld cross-section is wider for the AA6082 plates, being characterized by a well-defined shoulder influence area, extending to the plate mid thickness. On the other hand, for the AA5083 weld, the TMAZ is clearly restricted to the pin influence

area with a very small evidence of material being dragged by the shoulder. In fact, at the under shoulder area, where a large portion of TMAZ material is located for the AA6082 weld, it is possible to observe the presence of undeformed AA5083 base material.

For the welds performed with very low axial load (10kN), shown in Figure 4.8e and Figure 4.8f, it is even possible to observe a regular cross-section for the AA6082 weld, despite with some evidence of incomplete tool penetration, and a large surface defect for the AA5083 weld. According to previous authors (Colegrove *et al.*, 2006,2007; Zhang *et al.*, 2008; Arora *et al.*, 2009; Rosales *et al*., 2010), the morphology and dimensions of the TMAZ, which is associated with the quantity of material dragged by the tool in each rotation, is strongly influenced by the welding parameters. However, since each pair of welds shown in Figure 4.8 was performed using exactly the same welding conditions, it is possible to say that the weld morphology also depends on base material properties.

In Figure 4.8 is also shown, for each weld, the final print left by the tool at the end of the welding operation. As it is possible to conclude from the figure, for the AA6082 weld, the shoulder mark is almost perfectly round, except for the lower axial load weld (Figure 4.8e), showing that the material was easily dragged by the shoulder. For the AA5083 weld, the final print left by the shoulder clearly shows that the shoulder-workpiece contact area was restricted to the trailing side of the tool, especially for the cold welds, performed at 400 rpm (Figure 4.8d and Figure 4.8f). Again, since the AA6082 and AA5083 welds were performed under the same welding conditions, the differences in contact conditions have to be related with intrinsic base material properties.

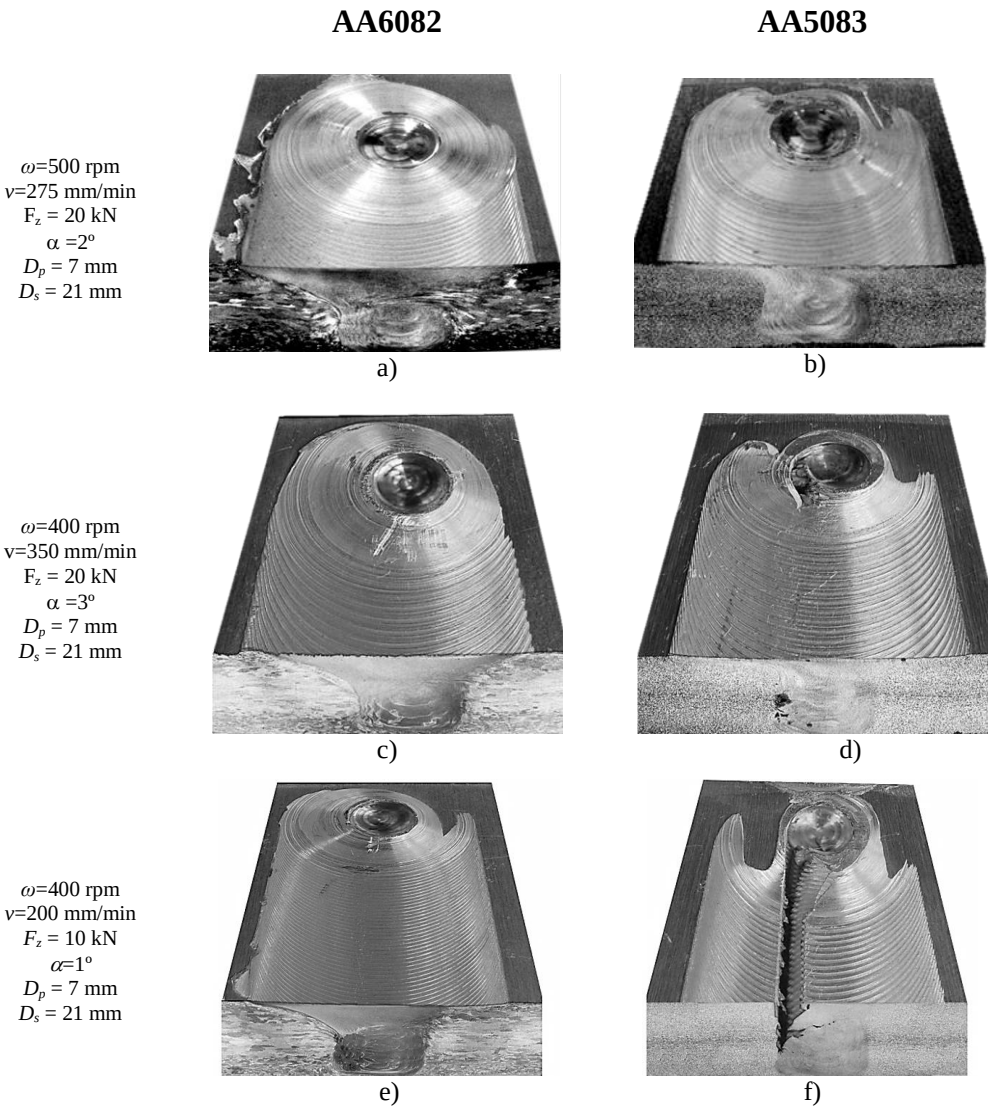

Figure 4.8 – Top views and cross-sections of AA6082 (a, c and e) and AA5083 (b, d and f) welds. (Annex D)

Intending to compare the differences between the amounts of material dragged by the tool during the weld process, and its evolution with welding parameters, for both alloys, the evolution of the pin influence zone width (L), evaluated at the welds middle thickness, is plotted in Figure 4.9 and Figure 4.10. More precisely, in Figure 4.9 is plotted the evolution of L versus the welding speed for different tool rotation speeds: 500 and 600 rpm, for the

AA5083 alloy, and 500 and 1000rpm, for the AA6082 alloy. In Figure 4.10 is plotted the evolution of *L* with the rotation speed for different traverse speeds: 50, 200 and 350 mm/min, for the AA5083 alloy, and 200 and 350 mm/min, for the AA6082 alloy. It is important to emphasize that all the results plotted in Figure 4.9 and Figure 4.10 correspond to welds which were produced using the same axial force (20kN), tool tilt angle (3º) and tool dimensions (D_s/D_p=21/7mm).

Analysing Figure 4.9 it is possible to conclude that, for each tool rotational speed, *L* strongly varies with the tool traverse speed, deeply increasing for decreasing welding speed values. For a specific welding speed value, *L* increases with the increasing of the rotation speed. Finally, under similar welding conditions (welding and rotation speeds), the amount of material dragged by the tool is much higher for the AA6082 alloy than for the AA5083 alloy, unless for the higher weld speed values, for which the width of the pin affected zone become similar for both alloys. In the figure, a cross-symbol was used for identifying, for each alloy, defective weld results. According to the figure, when the width of the pin influence zone is inferior to a value near to 7.6 mm, which corresponds to *L* values only 10 % higher than the pin diameter, internal defects were formed for both alloys.

Analysing now Figure 4.10, it is possible to conclude that, for the AA5083 alloy, the width of the pin affected zone strongly increases with the increasing of the tool rotation speed, for the lower tool traverse speed of 50mm/min. For the higher tool traverse speed values (200 and 350 mm/min), for which all the welds displayed very small or large defects, *L* remains in very small values independently of the tool rotation speed. Contrarily to this, for the AA6082 alloy, a strong increase of *L* with the increasing tool rotation speed was registered for 200 mm/min traverse speed. The differences in weld characteristics, for this particular set of welding parameters are enhanced in Figure 4.11, where *L* is plotted against the ω/v ratio, for v=200 mm/min.

Comparing the curves in the graph, it is possible to conclude that the evolution of L with ω/v is much more pronounced for the AA6082 alloy, than for the AA5083 alloy.

In Figure 4.12 and Figure 4.13 are now shown the cross-section morphologies for AA5083 and AA6082 welds, respectively, performed at increasing rotational speeds. Comparing the images in the figure it is now possible to depict the evolution of the shoulder influenced zone, with the traverse and rotational speeds of the tool, for both base materials. According to the figures, independently of the base material properties, the size of the shoulder influence zone increases for decreasing traverse speeds and decreasing tool rotational speeds. As already concluded from Figure 4.8, the size of the shoulder influenced zone is always larger for the AA6082 welds, than for the AA5083 welds.

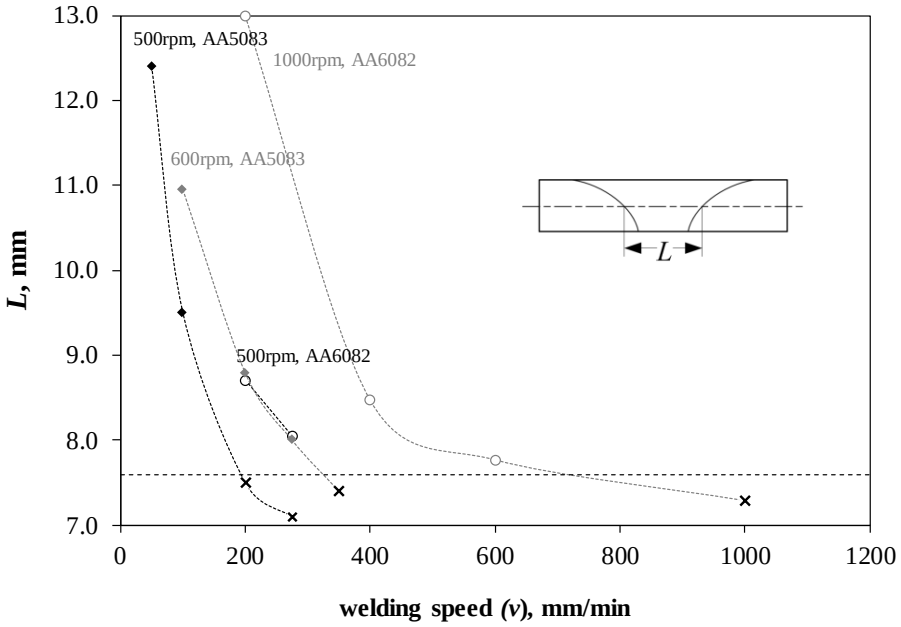

Figure 4.9 - Evolution of the pin influence zone width with the welding speed

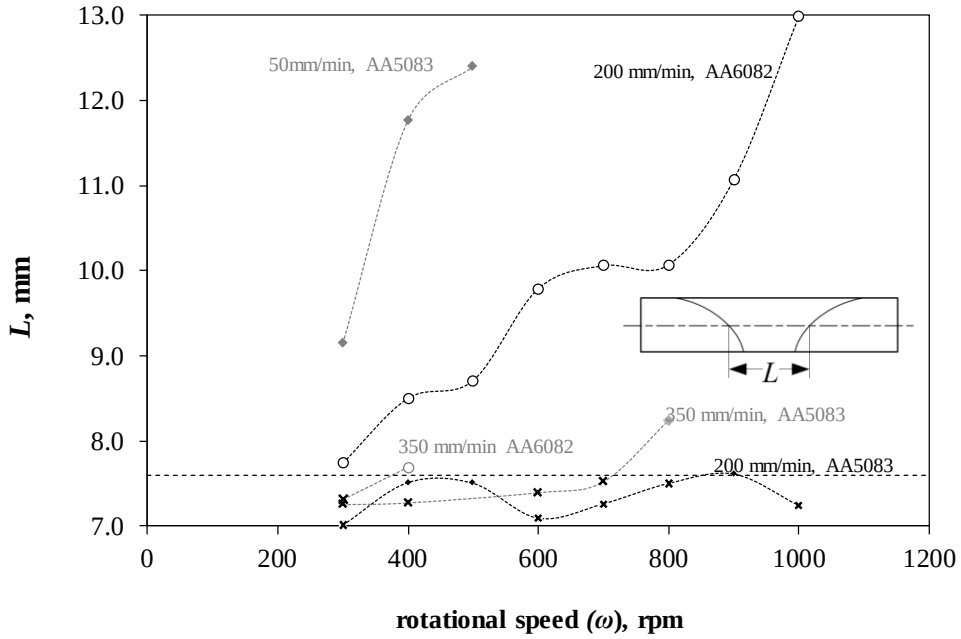

Figure 4.10 - Evolution of the pin influence zone width with the rotational

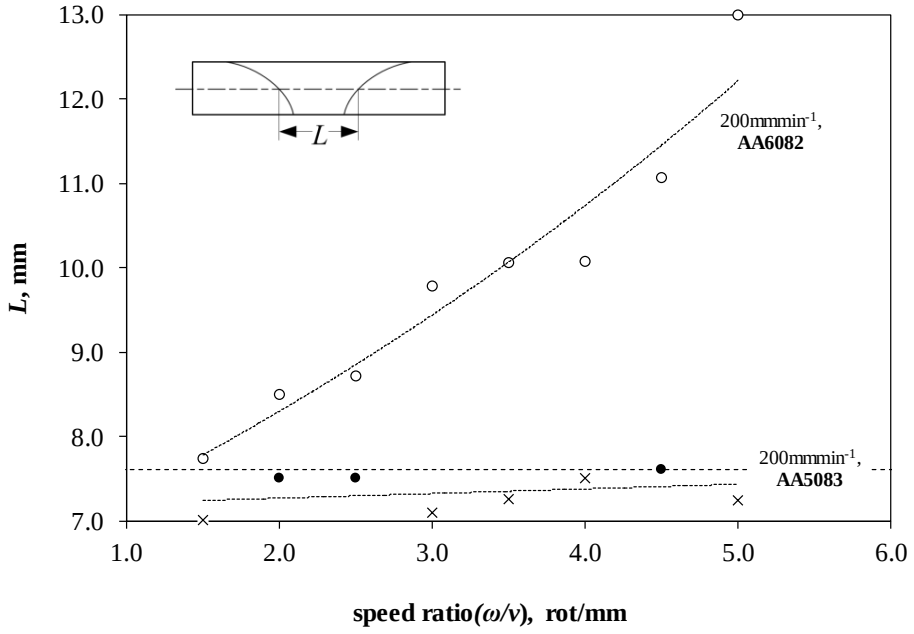

Figure 4.11 - Evolution of the pin influence zone width with *ω/v* ratio

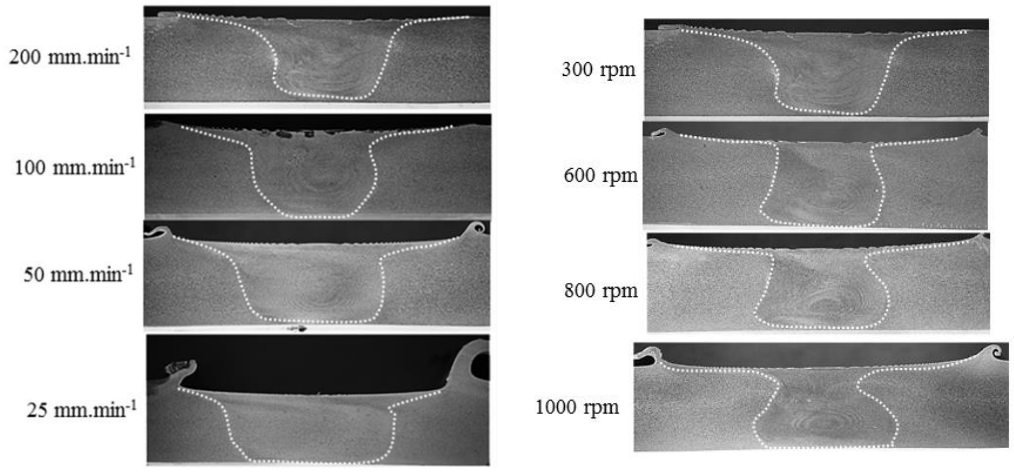

ω=300rpm v=200 mm/min

(a) (b)

Figure 4.12 - Evolution of the AA5083 welds cross-section with the traverse (a) and rotational (b) speeds. Other welding parameters: Fz=20kN, α=3º, D_s/D_p=21/7 mm (Annex E)

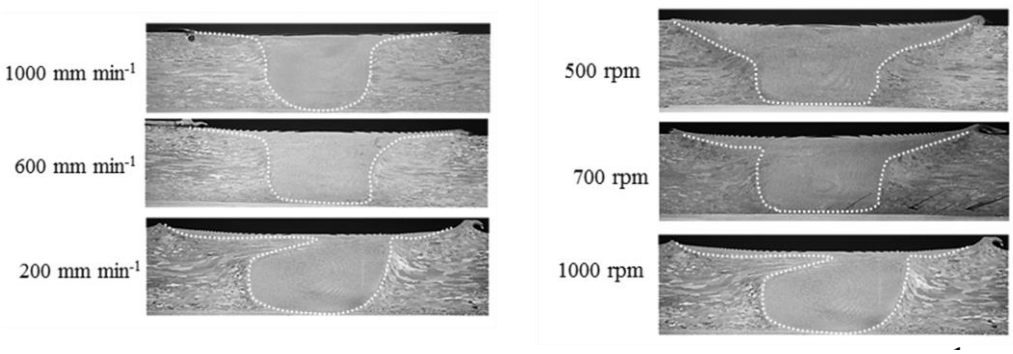

ω=1000rpm v=200 mm/min

(a) (b)

Figure 4.13 - Evolution of the AA6082 welds cross-section with the traverse (a) and rotational (b) speeds. Other welding parameters: F_z=20kN, α=3º, D_s/D_p=21/7 mm (Annex E)

According to Figure 4.8 to Figure 4.13, under the same welding conditions, the quantity of material dragged by the shoulder and pin during the

welding process was higher for the AA6082 alloy than for the AA5083 alloy, which displayed much lower weldabity than the previous one. Then, it is possible to establish a direct relation between the quantity of material dragged by the tool, in each rotation, and defect formation. It is also plausible to establish a direct relation between the quantity of material dragged by the tool and base material properties, since the welds for both alloys were performed under the same welding conditions. In Chapter 5, the plastic behaviour of both base materials will be analysed, and then, in Chapter 6, relations will be established between the plastic properties registered for both base materials and the weldability in FSW.

Set2 Welding parameters

Visual inspection of the AA6082 welds performed under *Set1* and *Set2* welding conditions revealed that using proper shoulder dimensions and axial load, this alloy has very good weldability, for a large range of tool rotation and traverse speeds. It was also found that the evolution of the welds morphology with process parameters was similar for *Set1*and *Set2* welds, and for that reason no further analysis of this welds is performed in this item.

Unlike what was registered for the AA6082 alloy, for the AA5083 welds, increasing the rotation speed, from 500 rpm to 1000 rpm, at a constant welding speed of 200 mm/min, promoted the formation of important internal defects, with non-conventional morphology. This is illustrated in Figure 4.14, where 600 and 1000 rpm welds are compared with non-defective welds produced at lower tool rotation and welding speeds. In this figure, it is possible to see that the internal defects registered for the welds produced at higher tool rotation consist of small discontinuities, at the advancing side of the tool, where the pin and shoulder governed material flows merge together. The

morphology of the discontinuities suggests that merging/mixing of the materials from the two different flow volumes was unsuccessful.

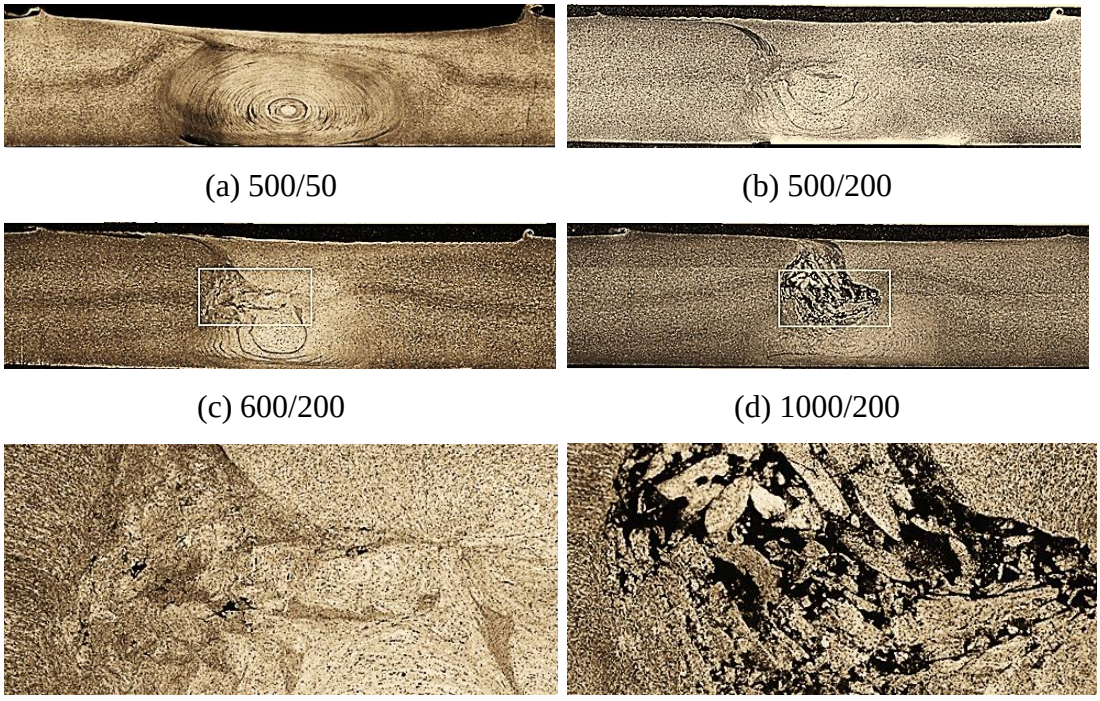

(a) 500/50 (b) 500/200

(c) 600/200 (d) 1000/200

(e) 600/200 (f) 1000/200

Figure 4.14 – Cross-sections of the 5_6 welds for rotational/weld speeds of 500/50 (a), 500/200 (b), 600/200 (c) and 1000/200 (d), and detailed view pictures of the signalized areas for the 600/200 weld (e) and 1000/200 weld (f). (Annex H)

According to Iordachescu *et al.* (2009) revision, improper merging of the material flow layers at the advancing side of the welds is associated with low heat input during welding and may be suppressed by increasing the tool rotation speed. However, comparing Figure 4.14c and Figure 4.14d, it is obvious that for the AA5083 alloy, increasing the tool rotation rate did not improved material flowability since the size and complexity of the weld defects were also increased. Actually, for this alloy, the weldability in FSW was improved by decreasing the traverse speed of the tool for the low rotation speed of 500 rpm. Comparing the non-defective welds of Figure 4.14a and

Figure 4.14b it is possible to confirm that diminishing the welding speed improved material flow, since meanwhile the weld performed at the lower welding speed (Figure 4.14a) displays a well-defined onion ring structure, the weld performed at higher welding speed (Figure 4.14b) shows much less defined material flow features and "incomplete" onion ring structure, which points for a less efficient material mixing between the shoulder and pin driving flow volumes.

Final comments

From the results displayed in this chapter it can be concluded that the weldability of both base materials in FSW is different. In fact, the visual inspection results of the welds allowed to verify that, under the same welding conditions, the number of defective welds was higher for the AA5083 alloy than for the AA6082 alloy, which indicates that, for the studied range of parameters, the AA5083 alloy displays much lower weldability than the AA6082 alloy. It was also possible to verify that, meanwhile, for the AA5083 alloy the main types of defects detected were surface and internal defects, which are commonly associated to low heat-input conditions, for the AA6082 alloy, several situations of mass flash formation were registered, which are usually associated to high heat-input conditions during the process, which reinforces the importance of the influence of base material properties on defect formation during the FSW process.

Another important conclusion is that, independently of the welding conditions, the weld cross-section is wider for the AA6082 alloy, being characterized by a well-defined shoulder influence area, extending to the plate

mid thickness, and, on the other hand, for the AA5083 weld, the TMAZ is clearly restricted to the pin influence area with a very small evidence of material being dragged by the shoulder.

It was also observed that, despite being strongly dependent of base material, weld quality also varies with plate thickness. In fact, the results prove that below certain shoulder dimensions, dependent on plate thickness, and for very low tool tilt angles, it is not possible to achieve non-defective welds whatever the process parameters in use. In order to guarantee hot weld conditions an accurate selection of tool rotation speed is also very important. In fact, the calculation of the energy consumed in the process, as well as the analysis of the welds, shows that the process becomes relatively less dependent on process and tool parameters for high tool rotation rates. The present study also shows that the establishment of accurate axial load values is also intimately related to the process parameters in use. Therefore, for cold weld conditions low axial loads led to significant internal and surface defects, whereas for hot weld conditions high axial load values led to tool destruction due to excessive plunge depth in the softened material.

5

Analysis of base materials plastic behaviour

The plastic behaviour of the non-heat-treatable (AA5083-H111) and the heat-treatable aluminium (AA6082-T6) alloys, which are characterised by markedly different strengthening mechanisms and microstructural evolution at increasing temperatures, is analysed in this chapter. As already mentioned in the Experimental Procedure chapter, the plastic behaviour of both alloys was analysed by performing tensile and shear tests at different temperatures and strain rates. In the next, the results of base materials mechanical characterization are discussed. The main conclusions from this chapter will be used to explain the differences in weldability between the two alloys, which will be performed in the next chapter.

This Page Intentionally Left Blank

Plastic behaviour at room temperature

In Figure 5.1 are shown stress–strain curves for both base materials, obtained in tension and shear, at room temperature in quasi-static conditions (5 mm/min). Analysing the curves it is possible to conclude that at room temperature the AA5083 alloy displays much lower yield strength than the AA6082 alloy, in both shear and tension. However, despite displaying much lower tensile yield strength, the AA5083 alloy exhibits strong *Portevin-Le Châtelier* (PLC) effect and pronounced hardening with plastic deformation, attaining tensile strength values very close to that of the AA6082 alloy. Complementary, comparing the shear stress-strain curves shown in Figure 5.1, for both materials, it is possible to conclude that, after moderate values of plastic deformation, the AA6082 alloy presents an almost steady-state flow stress, which is in accordance to that reported by Rauch et al., 2002, for other aluminium alloys of the 6xxx series. On the other hand, for the AA5083 alloy, which displays lower yield strength than the AA6082 alloy, the flow stress keeps increasing with loading. Actually, the AA5083 alloy attains strength values higher than that of the AA6082 alloy, after some plastic deformation. Inside the graph of Figure 5.1 is also show a smaller graph where the hardness registered for the tensile and shear samples, of both base materials, before and after plastic deformation, is compared. The hardness values for the deformed samples are that measured near the rupture section, where extreme values of plastic deformation were attained. From the graph it is possible to conclude that despite the hardness values relative to the non-deformed alloys are very different (HV^{5083} = 87 $Hv_{0.2}$ and HV^{6082} = 120 $Hv_{0.2}$), they become similar after plastic deformation. In fact, meanwhile for the AA5083 alloy, the hardness strongly increases with plastic deformation, for the AA6082 alloy, the hardness registered for the deformed and non-deformed samples is very similar. These

hardness results enhance again the higher sensitivity of the AA5083 alloy to strain hardening at room temperature.

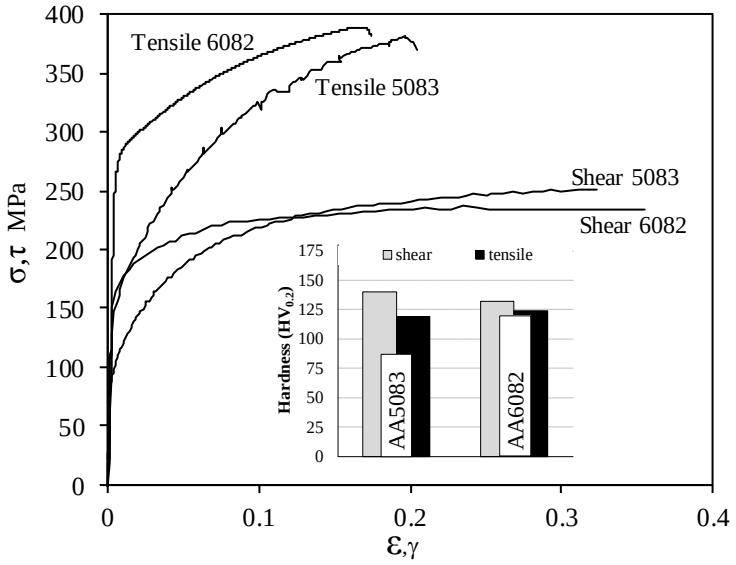

Figure 5.1 - Base materials tensile and shear stress-strain curves (T=25ºC, 5 mm/min)

Plastic behaviour at high temperatures

Since FSW involves plastic deformation at high temperatures, the plastic behaviour of the base materials was also analysed at temperatures ranging from 240ºC to 500ºC. In Figure 5.2 are shown the engineering stress–strain curves corresponding to the tensile tests performed at temperatures ranging from 240ºC to 500ºC, for the AA5083 alloy, and from 240ºC to 400ºC, for the AA6082 alloy.

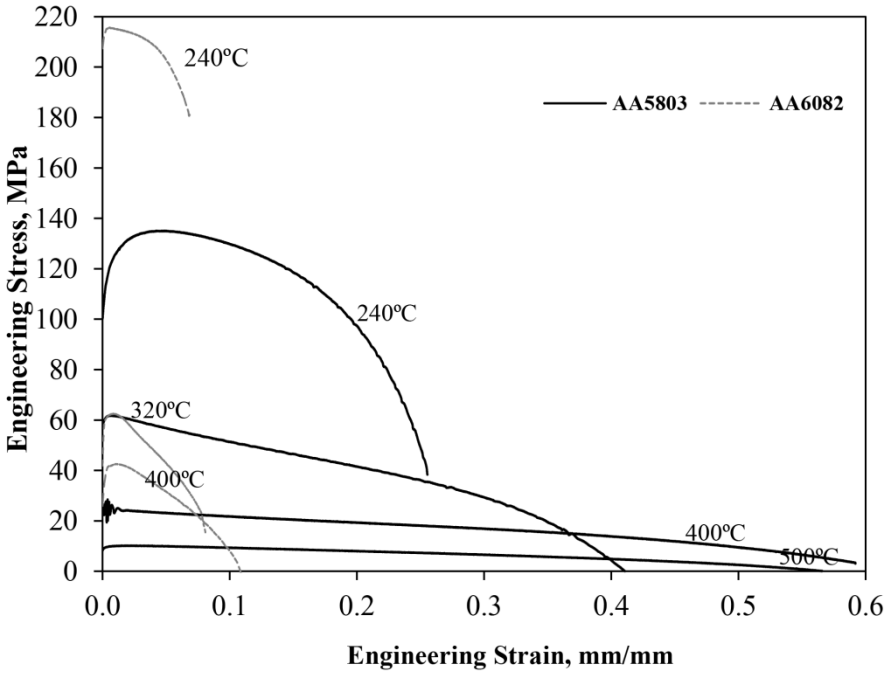

Figure 5.2 – Engineering tensile stress–strain curves at high temperatures.

In Figure 5.3 is shown the evolution of the yield stress with temperature, for both base materials. It is important to enhance that, for each base material, the mechanical properties reported from the samples of plates of different thickness were observe two be consistent, although they corresponded to different material batches. From the graphs in Figure 5.2 and Figure 5.3 it is possible to conclude that, for the tensile testing conditions analysed, the yield strength of the base materials become closer at higher temperatures. It is also possible to observe that the AA6082 alloy displays much smaller strain to failure, than the AA5083 alloy, for the entire range of temperatures.

In Figure 5.4 are plotted the hardening rates (ds/de), calculated from the tensile engineering stress-strain curves of Figure 5.2. In Figure 5.4a, which corresponds to the AA6082 alloy, is possible to conclude that, for temperatures above 240ºC, the hardening rate of this alloy sharply decreases after yielding, attaining negative values for very low values of plastic deformation (e < 2%). This result allows concluding that this material experiences strong softening

with plastic deformation at increasing temperatures. Contrarily to this alloy, as shown in Figure 5.4b, the AA5083 alloy presents hardening until 10% of plastic deformation, even at 240ºC and very small softening with plastic deformation for temperatures higher than 240ºC. Actually is important to enhance the almost perfectly plastic behaviour presented by this alloy for temperatures above 300ºC.

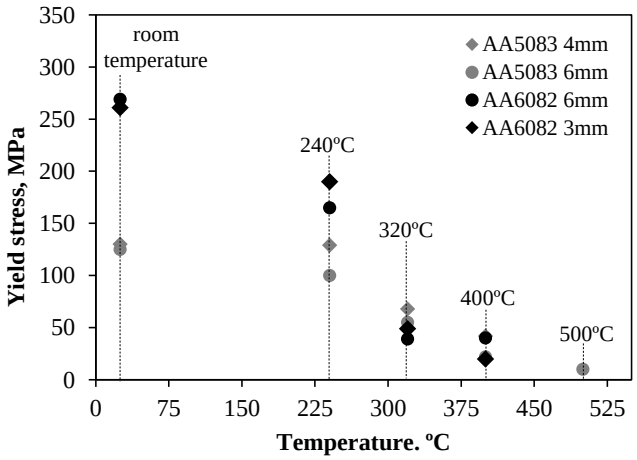

Figure 5.3 – Yield stress variation versus temperature

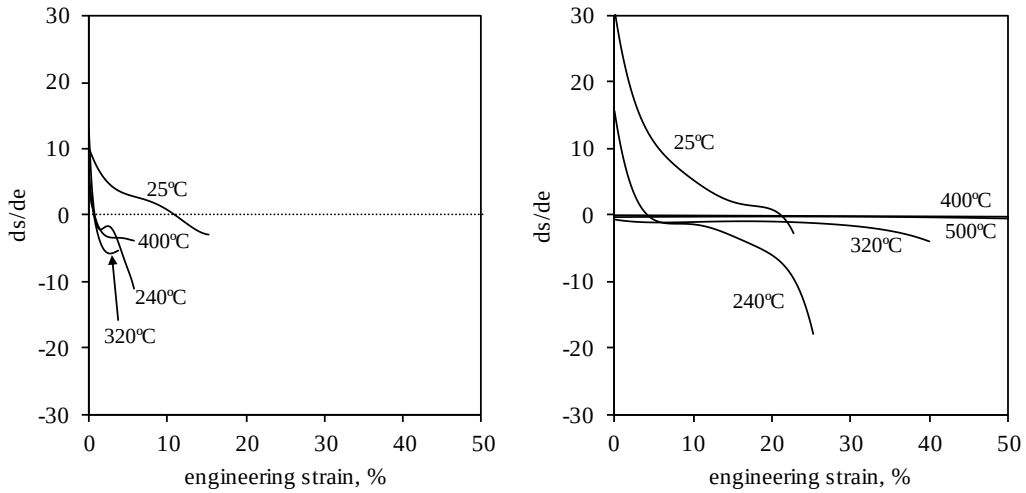

(a) (b)

Figure 5.4 - Hardening rate for the AA6082 (a) and AA5083 (b) alloys (Annex E)

The plastic behaviour reported in Figure 5.2 and Figure 5.4 can be explained based on literature. In fact, it is well reported that, for sufficiently high deformation temperatures, dynamic recovery, and in particular conditions, dynamic recrystallization, take place during plastic deformation (Zhou and Clode, 1998), promoting the steady flow stress behaviour registered in Figure 5.4, for the AA5083 non-heat treatable alloy. For the heat-treatable alloys, in artificially aged condition, like the AA6082-T6 alloy, concomitantly to dynamic recovery and/or dynamic recrystallization phenomena, dynamic precipitation also takes place during hot plastic deformation (Cerri *et al.*, 1997). Dynamic precipitation, which is faster than precipitation in static conditions, due to the increased particle diffusion coefficients in the presence of dense dislocation tangles, easily promotes overageing of the artificially aged microstructure resulting in intense softening with plastic deformation (Verlinder *et al.*, 1990), as was registered for the AA6082 alloy, in Figure 5.4. According to Wouters *et al.* (1990), the very low ductility experienced by the AA6082 alloy in the high temperature tests should also be related with intense coarsening of precipitates. The mechanisms of failure by coalescence of microvoids, due to localised strain discontinuities, such as that associated with second phase particles, grain boundaries, and dislocation pile-ups, are well documented in literature (ASM International, 1987).

Plastic behaviour in quasi-dynamic conditions

Another important subject in FSW analysis is the heat generation during the process, which is usually assumed to result from friction, at the tool-base

material interface, and plastic deformation. In fact, despite during quasi-static plastic deformation the heat generated by plastic work is lost by heat conduction and radiation, at very high strain rates, as that experienced by the material during FSW, a portion of this heat remains within the material, causing temperature increase and thermal softening. The temperature rise (ΔT) associated with plastic deformation can be directly obtained from stress-strain curves, by computing

$$\Delta T = \frac{0.9}{\rho C_p} \int_0^{\varepsilon} \sigma(\varepsilon) d\varepsilon \qquad (5.1)$$

where ρ and C_p are the density and heat capacity of the materials, respectively. In this expression it is assumed the very usual 0.9 conversion factor, which implies that 90% of the work of deformation is changed to heat.

In Figure 5.5 are shown the tensile stress-strain curves for both alloys, obtained in tensile tests performed with 5 mm/min and 3000 mm/min testing speeds, and in Figure 5.6 the temperature fields registered at maximum load for the samples tested at 3000 mm/min (quasi-dynamic conditions), acquired using a thermographic camera. It is important to point that meanwhile the strain data acquisition for the 3000 mm/min curves was performed using the *Aramis* system, the 5 mm/min curves were registered using a mechanical extensometer. According to the figure, for this range of testing speeds, both materials plastic behaviour is independent of the strain rate.

However, according to the thermographic camera measurements plotted in Figure 5.7, under the same testing conditions (3000 mm/min), the temperature rise was higher for the AA5083 alloy (ΔT_{exp}= 70 ºC), which experienced higher plastic deformation inside the necking area, than for the AA6082 alloy (ΔT_{exp}= 16 ºC). The temperature rise, for both alloys, was also calculated using Eq. (5.1) by computing the plastic work from the 3000

mm/min stress-strain curves in Figure 5.5. It is important to enhance that these stress-strain curves, are local curves, corresponding to points close to the necking region, somewhere inside the area where the maximum temperatures were registered. From Eq. (5.1) it was obtained ΔT_{Eq}= 40 ºC, for the AA 5083, alloy and ΔT_{Eq}= 22 ºC, for the AA6082 alloy. According to Figure 5.7, these values are different from that registered by the thermographic camera, which can be associated with several factors, namely, the inaccuracy of the material constants in Eq. (5.1), obtained from bibliography (ASM International, 1995b), the inaccuracy of the conversion factor used (0.9), and finally, the inability in fully capturing the strain fields in the sample until the exact moment of the records of the thermographic camera, displayed in Figure 5.6. In fact, strain data acquisition rates for the Aramis system were much smaller than that of the thermographic camera.

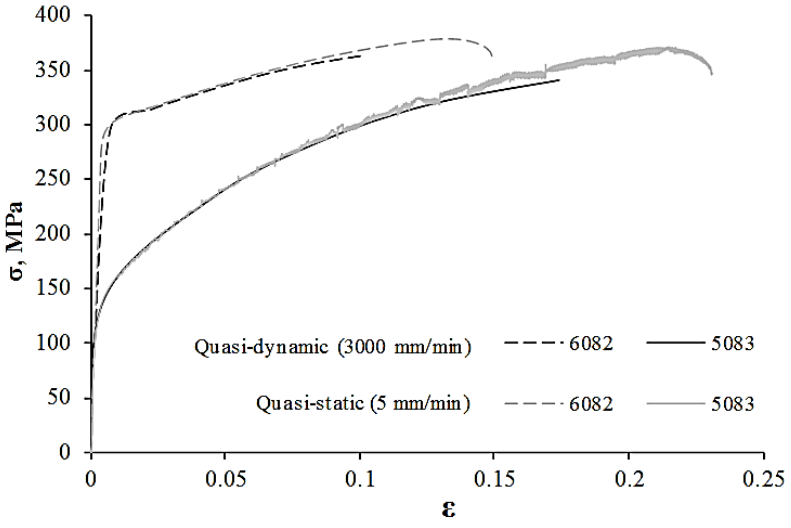

Figure 5.5 – Stress-strain curves for 5 and 3000 mm/min tensile tests.

Analysing Figure 5.6, where the temperature distribution in the samples at maximum load are plotted, it is possible to conclude that meanwhile for the AA6082 alloy, the temperature distribution is almost uniform over the entire gauge length, even for load values close to the maximum load, indicating that strain localization and rupture are almost simultaneous, for the AA5083 sample, it is possible to observe heat concentration inside a well-defined necking area, where deformation remains confined from the instant at which the maximum load is attained until rupture takes place. The very high maximum temperature value attained for this sample will be related to the very high deformation and strain rates attained in the necking area before rupture. Considering that similarly to what occurs inside the necking area, very high strain rates and deformation values are attained in the shear layer, during FSW, it is expected an important heat release due to plastic deformation, during welding, for the AA5083 alloy. According to Simar et al. (2006), the heat generated by plastic deformation is relevant on heat dissipation conditions, which has a strong influence on TMAZ morphology.

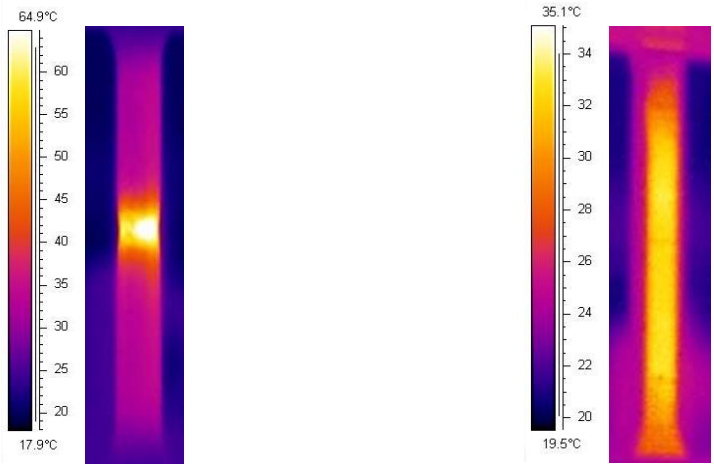

AA5083 (6mm) AA6082 (6mm)

Figure 5.6 – Temperature maps at maximum load

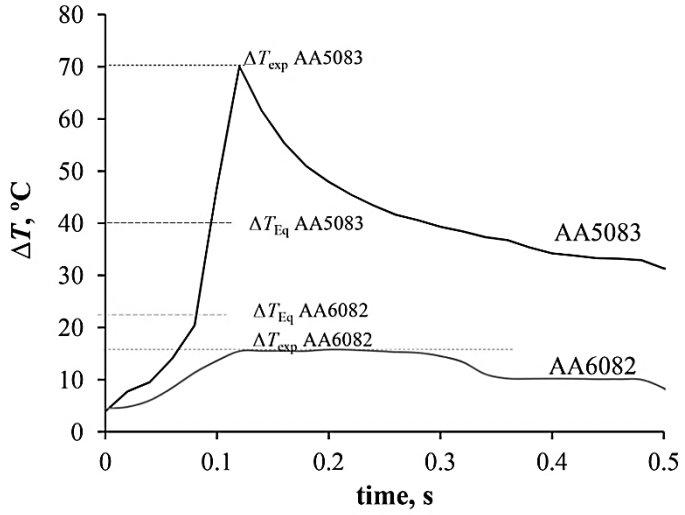

Figure 5.7 – Temperature rise registered during the quasi-dynamic tensile tests.

Final comments

From the results showed, it is possible to clearly depict important differences in base material plastic behaviours. At room temperature, the AA5083 alloy exhibits strong *Portevin-Le Châtelier* (PLC) effect and pronounced hardening with plastic deformation, attaining tensile strength values very close to that of the AA6082 alloy.

Moreover, at high temperatures, the yield strength of the base materials becomes closer. It is also possible to depict that the AA6082 alloy displays much smaller strain to failure, than the AA5083 alloy, for the entire range of temperatures. The results also allow concluding that, the AA6082 alloy experiences strong softening with plastic deformation at increasing temperatures. Contrarily to this alloy, the AA5083 alloy, presents hardening until 10% of plastic deformation, even at 240ºC and very small softening with plastic deformation for temperatures higher than 240ºC. It is also important to

enhance the almost perfectly plastic behaviour presented by this alloy for temperatures above 300ºC.

.

6

Analysis of the influence of base materials plastic behaviour on weldability

In Chapter 4, important differences in friction stir weldability between the non-heat-treatable AA5083-H111 and the heat-treatable AA6082-T6 aluminium alloys were depicted. Since both alloys were joined under similar welding conditions, for Set1 tests, the differences in base materials plastic properties were pointed as the main factor in determining the different welding behaviour. So, in Chapter 4, the plastic behaviour of the two base materials was deeply analysed based on the results of the mechanical characterisation of both alloys under varied temperatures and loading conditions. In current chapter, based on base materials mechanical characterisation analysis, weld characteristics, literature review and on previous knowledge on material flow during FSW (Leal et al., 2008) and on microstructural and mechanical characterisation of 5xxx and 6xxx friction stir welds (Rodrigues et al., 2008; Leal et al., 2008; Leitao et al., 2009), important relations between base materials plastic properties and weldability in FSW will be established.

This Page Intentionally Left Blank

Background from previous chapters

In Chapter 4 it was already concluded that the AA5083 and AA6082 alloys display important differences in weldability when joined under similar welding conditions, i.e., while for the AA6082 alloy non-defective welds were obtained for a large range of welding conditions (Table 4.5), for the AA5083 alloy, a large number of important defects were obtained under exactly the same range of welding conditions (Table 4.3). The morphological analysis of the welds, also performed in Chapter 4, revealed that these results are associated with important differences in the amount of material dragged by the tool during welding (Figure 4.8), i.e, under exactly the same welding conditions the amount of material dragged by the tool is much higher for the AA6082 alloy, than for the AA5083 alloy, which can only be related with base material intrinsic properties. Since FSW is a thermo-mechanical process in which the joining results from the stirring and mixing of the base materials under intense plastic deformation, the material properties with relevance for the process have to be the plastic behaviour at high temperatures and strain rates.

Actually, from the mechanical characterization work and literature review it was concluded that meanwhile the AA6082 alloy displays intense flow softening during tensile loading at high temperatures (Figure 5.4a), and is sensitive to dynamic precipitation and overageing under intense non-uniform deformation (Verlinder *et al.*, 1999), the AA5083 alloy, displays steady flow behaviour at increasing temperatures in quasi-static conditions (Figure 5.4b), and is sensitive to moderate hardening at high strain rates (Zhou and Clode, 1998). Important differences in the amount of heat released during plastic deformation in quasi-dynamic conditions were also recorded, between the two alloys (Figure 5.7), which would also have important influence in the thermo-mechanical conditions during welding. In the next, basic weld morphology

characteristics will be related to base materials plastic flow during welding, and in this way, to base materials weldability in FSW. Since the mechanical characterization of the base materials was performed in quasi-static and quasi-dynamic conditions, and thermal cycles during high temperature tensile testing were far from that experienced by the materials during FSW, a thermal sensitivity analysis was conducted in order to validate the analysis.

Weld morphology versus plastic properties

It is well established from literature (Nadan *et al.*, 2006) that, during friction stir welding, once steady state welding conditions are attained, the dragging action of the tool over the base material will develop under constant load. So, it is reasonable to assume that the AA6082 alloy, which experiences strong softening with plastic deformation at increasing temperatures, will have good weldability in FSW since it will easily undergo intense plastic deformation under constant load, for a large range of temperatures. In opposition, the AA5083 alloy, which displays work-hardening until 240 ºC and steady flow stress at higher temperatures, will be less efficiently deformed under constant loading conditions. Effectively, comparing the weld shapes displayed in Figure 6.1 corresponding to 6_6 and 5_6 welds performed under the same welding conditions, it can be concluded that the nugget of the welds is much broader for the AA6082 alloy, than for the AA5083 alloy, which corroborates the previous assumptions. For the AA6082 welds it is even possible to identify in the weld cross-section of Figure 6.1 a wide zone of severely deformed but non-recrystallized TMAZ material, which also evidences the intense plastic deformation of this material at temperatures and strain rates lower than that

attained in the nugget. For the AA5083 alloy, nor a deep shoulder influence zone, nor a wide non-recrystallized TMAZ, is visible in the weld cross-sections, which points for the lower efficiency of the tool in dragging this base material.

From literature it is also possible to conclude that the tool dragging action during FSW is related to the contact conditions developed at tool-workpiece interface, which in turn are determined by the plastic properties of the base materials. According to Schmidt and Hattel (2005b), during tool plunge and the first part of the dwell period, a large amount of heat is generated by frictional dissipation, increasing the temperature of the under-shoulder material. Consequently, under similar axial load conditions, the extreme thermal softening experienced by the AA6082 alloy will lead to further submerging of the tool, relatively to the AA5083 alloy, which explains the strong differences in contact area between the AA6082 and AA5083 welds, especially evident for the very low axial load situations illustrated in Figure 6.2a and Figure 6.2b. Schmidt and Hattel (2005b) also advocate that sticking conditions at the tool-workpiece interface will be developed when the friction shear stress at the interface exceeds the yield shear stress of the underlying base material. When the contact shear stress is smaller than the base material yield shear stress, sliding conditions will prevail. Present results also show that sticking conditions will easily develop during FSW of the AA6082 alloy, which presents decreasing flow stress with plastic deformation, and sliding or partial sliding/sticking conditions will prevail for the work hardenable AA5083 alloy. These assumptions are confirmed by the morphological observations in Figure 6.1 where important differences in shoulder influence area are clearly discernible in the cross-sections.

ω=500 rpm | v=275 mm/min | F_z = 20 kN | α =2º | D_p = 7 mm | D_s = 21 mm

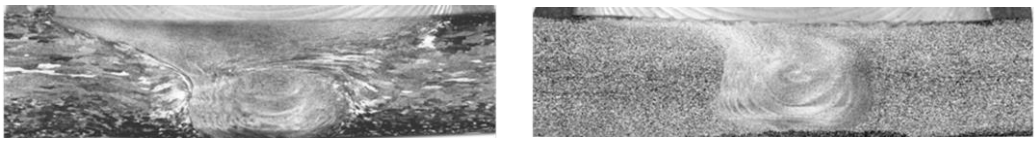

a) b)

Figure 6.1– Cross-sections of the AA6082 (a) and AA5083 (b) welds.

ω=500 rpm | v=275 mm/min | F_z = 20 kN | α =2º | D_p = 7 mm | D_s = 21 mm

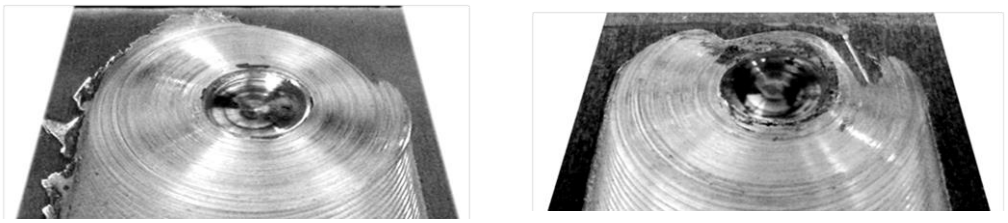

a) b)

Figure 6.2 – Contact area at the end of the AA6082 (a) and AA5083 (b) welds

.

Assuming sticking conditions at the pin-workpiece interface, for both base materials, and that under sticking conditions heat is mainly generated by plastic deformation (Schmidt and Hattel, 2005b), it is plausible to assume that heat generation by plastic dissipation will be more intense in the very narrow layer of material deformed by the pin at high strain rates, than in its surroundings. For the AA 5083 alloy, the sharp temperature increase in this very small volume of plastically deformed material will promote intense localized softening, which in addition to the sliding contact conditions at the shoulder/workpiece interface, leads to localized deformation near the pin

surface, as it is evident by the AA5083 TMAZ shape in Figure 6.1b. However, for the AA6082 alloy, the concurrent effect of sticking conditions at the shoulder/workpiece interface and pronounced softening with plastic deformation, for a large range of temperatures, results in much larger deformation areas as it is visible for the weld in Fig. 5.1a. Schmidt and Hattel (2005b) also concluded that the development of sticking contact conditions at the tool/matrix interface is important for the success of the deposition process, which is in accordance with present results.

Regarding weld material mixing inside the shear layer, and weld consolidation at the trailing side of the tool, it is also important to remark that the very low ductility of the AA6082 alloy at high temperatures, was already related in previous studies with micro-void coalescence at the grain and large particle boundaries (Verlinder *et al.*, 1999). Assuming that this micro-void coalescence mechanisms are active during FSW, due to intense plastic deformation taking place, the mixing of the materials from the pin and shoulder flow layers should be facilitated by the internal de-cohesion of the material. Again, material mixing from different flow layers, inside the stirred volume, will be much more difficult for the AA5083 alloy, which displays continuous plastic deformation and very high elongation at increasing temperatures.

Weldability Analysis

AA6082 Alloy

In Figure 6.3 are shown the transverse and longitudinal hardness profiles obtained near the end of the AA6082 weld of Figure 6.1a, where is located the

final hole left by the pin. Analysing the transverse hardness profile it is possible to conclude that the AA6082 weld display the W shape hardness profile characteristic of the heat-treatable alloys friction stir welds, which was already deeply analysed by Sato *et al.*, (2001), Upadhyay and Reynolds (2010) and other authors. From the figure it is possible to confirm that the intense hardness drop in the HAZ, relative to the initial base material hardness (HV^{6082}), extends not only to the retreating and advancing sides of the weld, but also to the front of the tool where its dragging action will be exerted. In the next a comparative analysis between the average hardness registered for the different weld zones ($nugget^{6082}$ and HAZ^{6082}), the hardness registered in the necking area for the high temperature mechanical testing samples ($tensile^{6082}$) and the hardness registered for some thermal simulation samples ($thermal^{6082}$) will be performed.

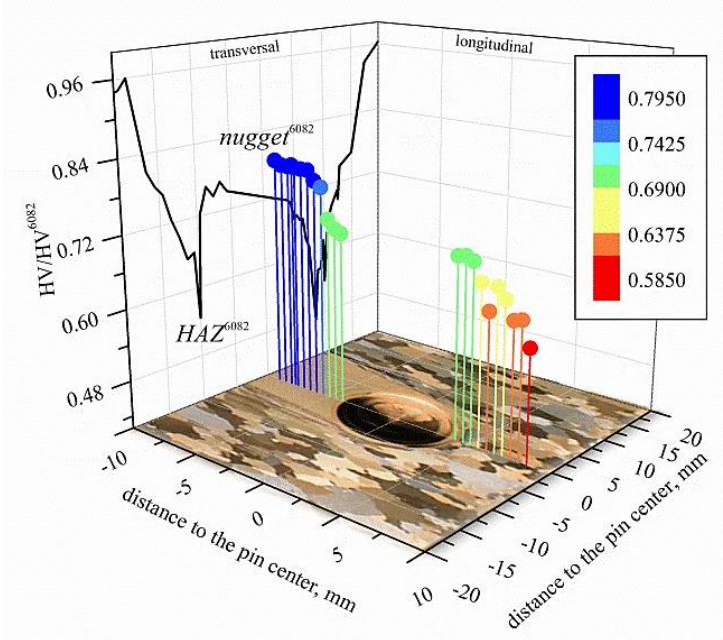

Figure 6.3 – Transverse and longitudinal hardness for a AA6082 weld. Welding conditions: ω=500rpm, v=275mm/min, Fz=20kN, α=2º, Ds/Dp=21/7 mm. HV^{6082} is the initial base material hardness. (Annex F)

Actually, despite the important differences in plastic behaviour at high temperatures depicted from the mechanical characterisation work, and the possible relation between it and the material flow behaviour during FSW pointed in the previous item, it is important to observe that the heating and cooling conditions to which the materials were subjected before and after tensile testing are much gentler than that experienced by the materials during FSW, even when the tests were performed under quasi-dynamic conditions. Actually, since the plastic behaviour of the AA6082 alloy is conditioned by solubilisation and precipitation mechanisms, which are strongly time and temperature dependent, an important question is whether at the very fast heating and cooling conditions experienced during FSW, the flow softening mechanism discussed during Figure 5.2 analysis will be active.

In order to analyse the sensitivity of the AA6082 alloy to overageing at very high heating rates, very small samples of the AA6082 alloy were heated at 30 ºC/s, following the procedure described in Chapter 3. The use of very small samples and very fast heating conditions intended to simulate the very small volume of material processed by the FSW tool at each revolution and the fast heating conditions experienced during welding. According to previous studies (Song and Kovacevic, 2003; Zhang and Zhang, 2007; Jamshidi *et al.*, 2011), the heating rates in the thermal simulation tests were even higher than that experienced during welding. After cooling and some days of natural ageing, the hardness of the thermal simulation samples was evaluated.

In Figure 6.4 is plotted the evolution of the hardness ratio HV/HV^{6082} with temperature, for all the thermal ($Thermal^{6082}$) and mechanical ($Tensile^{6082}$ and $Shear^{6082}$) testing samples studied in this work. Analysing the results corresponding to the thermal simulation samples, it is possible to conclude that for temperatures ranging from 240ºC to 400ºC, which are much lower than the solubilisation temperature of the AA6xxx alloys, which ranges from 510ºC to 595ºC, the hardness registered for the very small thermal simulation samples is

already lower than that of the base material (HV/HV^{6082} = 0.90). For the 500ºC and 600ºC thermal simulation samples, which according to references (Song and Kovacevic, 2003; Su *et al.*, 2003; Colegrove and Shercliff, 2006; Zhang and Zhang, 2007; Hwang *et al.*, 2008; Amancio-Filho *et al.*, 2008) were heated to temperatures in the range of that under the tool during FSW, the hardness is much lower than that of the base material (HV/HV^{6082} = 0.45), which point for the occurrence of overaging at heating rates much higher than that experienced in FSW.

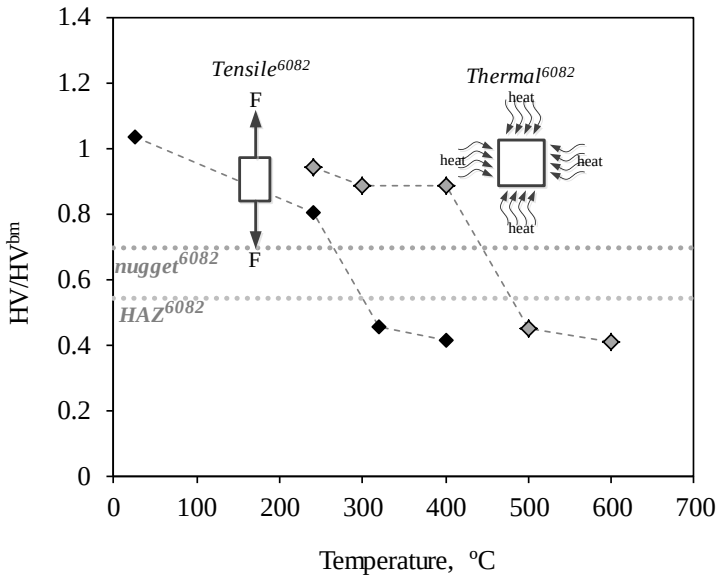

Figure 6.4 – Hardness ratio (HV/HV^{bm}) versus temperature for the AA6082 alloy (HV – average hardness corresponding to the welds and mechanical and thermal simulation samples; HV^{bm} – Initial base material hardness)

In Figure 6.4 are also plotted lines corresponding to the average hardness ratio of the nugget ($nugget^{6082}$) and HAZ (HAZ^{6082}), in front of the tool, obtained from the transverse and longitudinal harness profiles of Figure 6.3. Comparing HAZ^{6082} hardness with the average harnesses registered for the 300 and 400ºC tensile samples and for the 500ºC and 600ºC thermal simulation

samples, it is possible to conclude that all the samples display very close average hardness values. So, it is reasonable to assume that despite being subjected to different thermal cycles, the materials of the different samples are characterised for having the same overaged structure. From Figure 6.3, it is possible to conclude that the overaged HAZ domain encompasses the full perimeter in front of the tool. This material, which displays flow softening at increasing plastic deformation and temperatures, will be easily dragged by the toll into the shear layer surrounding the pin, where the weld is formed (Leal *et al.*, 2008). In the shear layer, where the overaged HAZ material in front of the tool will be subjected to intense non-uniform deformation, for one or more tool revolutions, precipitate dissolution will be facilitated by the large number of moving dislocations (Verlinden *et al.*, 1990) originating new small coherent particles which will be dispersed in the plastically deformed volume. This will contribute for improving the local strength of the nugget, relative to the surrounding HAZ, as can be depicted by comparing in Figure 6.3 and Figure 6.4 the hardness values for these two weld zones.

AA5083 Alloy

As already performed for the AA6082 alloy, in Figure 6.5 are plotted the transverse and longitudinal hardness profiles obtained near the end of the AA5083 weld of Figure 6.1b, and in Figure 6.6 is plotted the evolution of the hardness ratio HV/HV^{5083} with temperature, for all the mechanical testing samples studied in this work ($Tensile^{5083}$ and $Shear^{5083}$ results) and for the weld ($nugget^{5083}$). Analysing Figure 6.5 it is possible to conclude that, contrary to that registered for the AA6082 weld, for the AA5083 weld no important variation in hardness relative to the base material was registered, nor in the nugget, nor in the HAZ around the tool.

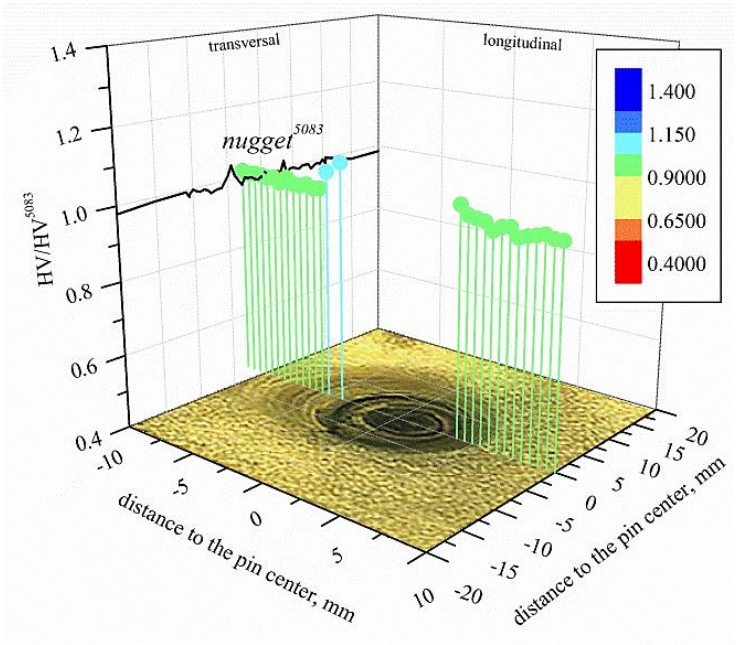

Figure 6.5 – Transverse and longitudinal hardness for a AA5083 weld. Welding conditions: ω=500rpm, v=275mm/min, Fz=20kN, α=2º, Ds/Dp=21/7 mm. HV^{5083} are the initial base material hardness of the AA5083 alloy. (Annex F)

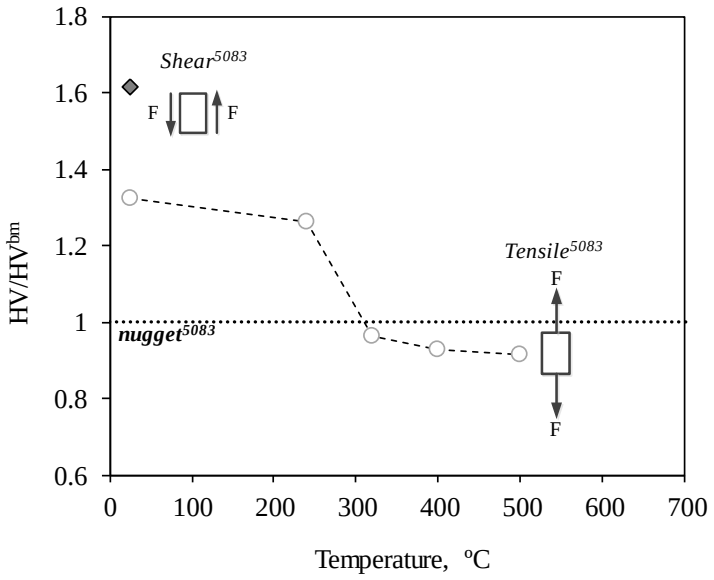

Figure 6.6 – Hardness ratio (HV/HV^{bm}) versus temperature for the AA 5083 alloy (HV – average hardness corresponding to the welds and mechanical testing samples; HV^{bm} – Initial base material hardness)

Comparing now in Figure 6.6 the hardness ratios (Hv/Hv^{5083}) corresponding to the AA5083 high temperature tensile samples ($Tensile^{5083}$ results), with the hardness ratio corresponding to the weld ($nugget^{5083}$), it is possible to conclude that, contrarily to the weld, the tensile samples display some hardness decrease relative to the base material. Actually, since this alloy displayed steady flow behaviour during the high temperature tensile tests, which is traditionally attributed to the occurrence of intense recovery during plastic deformation, after tensile testing it is expected that the recovered samples microstructure have lower hardness than the moderately strain hardened base material, in the H111 condition. It is also important to stress that during welding, despite base material is subjected to high temperature plastic deformation, the strain rates are well above the quasi-static limits (Sato *et al.*, 2005; Schmidt and Hattel, 2005; Colegrove and Shercliff, 2006; Nandan *et al.*, 2006a,b; 2007). At very high strain rates, the dislocation generation rate may rise to a level that reduces the effective time for recovery, resulting in a less recovered structure and increased flow stresses with plastic deformation (Zhou and Clode, 1998). This behaviour, which explains the higher hardness values of the weld relative to the tensile samples, also points for increased difficulties in welding the AA5083 alloy. At high strain rates, the increase in flow stress with plastic deformation would prevent intense plastic flow under constant load, which explains the very small amount of material dragged by the tool evidenced by the AA5083 weld cross-sections in Figure 6.1. However, it is also important to point that the level of hardening during plastic deformation at high temperatures and strain rates, such as in FSW, is much lower than that experienced during plastic deformation at room temperature or at 240ºC, as it is possible to deduce by comparing in Figure 6.6 the hardness ratios for the shear ($Shear^{5083}$) and tensile ($Tensile^{5083}$) samples with that of the weld ($nugget^{5083}$).

According to Long *et al.* (2007), who performed studies in FSW of aluminium alloys AA5083-O, AA2219-T87 and AA7050-T751, and Dehghani

and Chabok (2011), who performed studies in FSP of interstitial free steels, the strain rate during FSW/P increases with increasing tool rotation speeds. Therefore, it is expectable that the AA5083 weldability, which is related with the plastic behaviour of the material at high strain rates, will diminish at increasing tool rotation rates. By diminishing the tool rotation rate, diminishes the strain rate during the process, improving AA5083 flowability.

Actually, in Chapter 5, it was reported that the 5_6 plates weldability was deeply improved by simultaneously diminishing the tool rotation and welding speeds: By diminishing the tool rotation rate, diminishes the strain rate during the process, by diminishing the welding speed, as stated by Zhang et al. (2011), a more uniform temperature distribution across plate thickness is obtained. Insuring a more uniform distribution of heat between the shoulder and pin governed flow volumes, will conduct to more uniform material flow characteristics and improved material merging between the different flow layers. The longitudinal tool displacement per revolution (v/ω [mm/rot]) also becomes lower at decreasing welding speeds, diminishing the volume of material displaced by the tool at each revolution, which will also contribute for improving merging/mixing between the different material flow layers. These assumptions explain the differences in AA5083 welds morphology shown in Figure 4.14, where welds performed at the same tool rotation speed and different traverse speeds are compared in (a) and (b). Diminishing the welding speed improves the material mixing in the shear layer, and for this reason, meanwhile the weld performed at the lower welding speed (Figure 4.14a) displays a well-defined onion ring structure, the weld performed at higher welding speed (Figure 4.14b) displays an “incomplete” onion ring structure.

Final comment

The influence of the high temperature plastic behaviour, of the AA6082 and AA5083 aluminium alloys, on friction stir weldability, was analysed in this chapter. It was found that the AA6082 alloy, which according to the base materials mechanical characterisation results, is sensitive to intense flow softening during high temperature plastic deformation, displays good weldability in FSW. For the AA5083 alloy, which according to the base materials mechanical characterisation results, displays steady flow behaviour at increasing temperatures, a very poor weldability was registered under the same welding conditions of the AA6082 alloy. This behaviour results from the strong influence of the plastic properties of the base materials, at high temperatures, on material flow during welding, as well as on contact conditions at the tool workpiece interface. The very important influence of base material plastic properties on friction stir weldability depicted in this work, was never addressed before in FSW literature, which traditionally relates material flow during welding, as well as welds morphology and defects, with tool geometry and/or processing conditions.

7
Torque sensitivity analysis

In spite of being well established in literature the strong relation between torque and welding/processing conditions, all the studies reported to date are focused on a limited range of processing parameters, and most of them analyse results for a very specific material, tool geometry or plate thickness. This chapter intends to provide some further insight on this subject by discussing the relations between a broad range of processing conditions, classified as independent variables, and the corresponding welding results, classified as dependent variables, using torque sensitivity analysis. The welding conditions tested included not only testing varied processing parameters, which enabled to compare present data with previous studies from other authors, but also analysing the relation between base materials properties, plate thickness, welding results and torque evolution, which constitutes a novelty relative to the previous studies on this subject.

This Page Intentionally Left Blank

Torque evolution with plate's thickness and process parameters

In Figure 7.1 and Figure 7.2 are plotted the average torque values versus the rotational to weld speed ratio (ω/v), corresponding to *Set1* and *Set2* welding tests, for the AA5083 and AA6082 alloys, respectively. As already done in Chapter 4, the results plotted in the figures are categorised according to the classification adopted after weld inspection, summarized in Table 4.1. Analysing both graphs it is possible to conclude that, for the lower ω/v range, corresponding to *Set1* parameters, for which a large number of defective welds were produced for both alloys, which is evidenced by the large number of very small symbols almost randomly distributed, no clear tendency in the evolution of the torque results with process parameters can be found, in the same way as it was already reported when analysing the evolution of the energy input during the process with ω/v (Figure 4.2 and Figure 4.3). This shows that the torque registered during welding is very sensitive to non-equilibrium welding conditions conducting to the formation of very large weld defects. It is also possible to conclude that for a same range of ω/v values, independently of the base material, much lower torque values, were registered in thinner than in thick plates welding. For the 6_3 plates, contrary to that registered for the 6_6, 5_6 and 5_4 plates, only very small torque variations were registered, even using a broad range of welding conditions conducting to both GOOD and defective welds.

Some trend-lines were schematized in Figure 7.1 and Figure 7.2, fitting the torque evolution with ω/v, for some selected welding and rotational speeds corresponding mostly to GOOD welding conditions. More precisely, the torque values fitted by each trend line correspond to welds performed using *Set2* parameters, which correspond to a unique tool and axial load, but varying

welding and rotational speeds. Analysing the trend lines plotted for the 5_6, 6_6 and 5_4 welds, it is possible to conclude that, independently of the base material, and plate's thickness, for a constant welding speed, the torque values strongly decrease with increasing rotational speed. For a constant rotational speed, and varying welding speeds, no important changes in torque were registered. On the other hand, from the figure it is also possible to conclude that for the lower range of ω/v values, corresponding to *Set1* of testing conditions, i.e., welding tests performed using different tools and axial loads, the torque values corresponding to the GOOD welds also display strong variations, even for welding conditions corresponding to equal rotational and welding speeds (same ω/v).

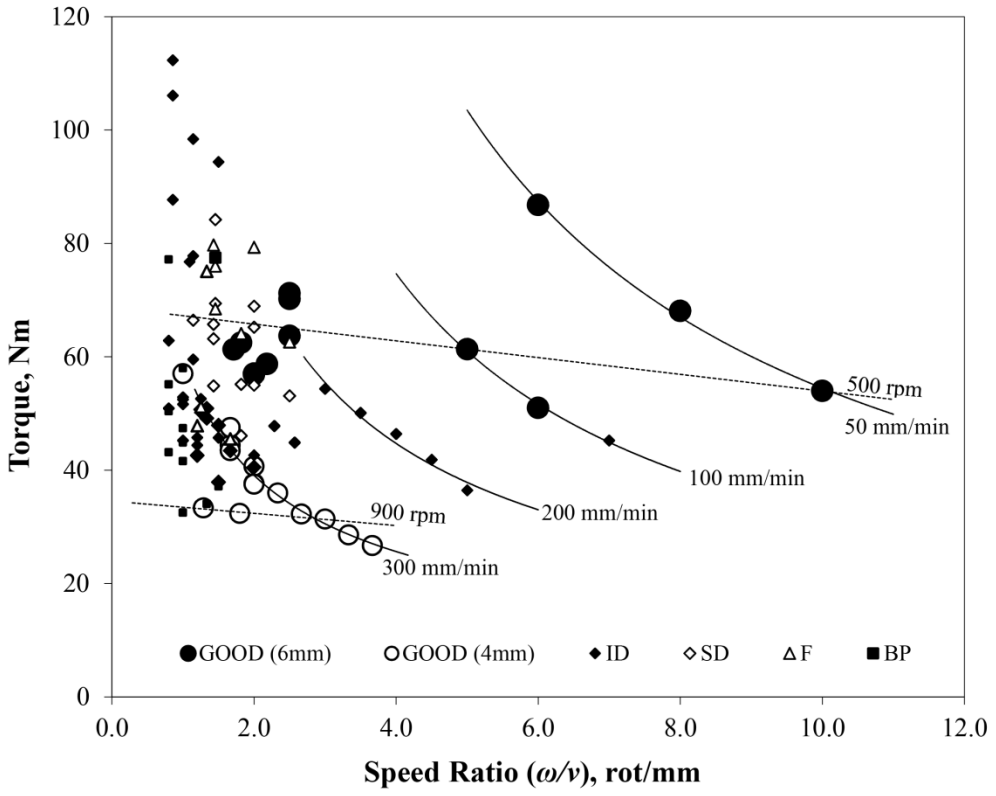

Figure 7.1 – Torque evolution with (ω/v) and weld inspection results for the AA5083 welds. (Annex H)

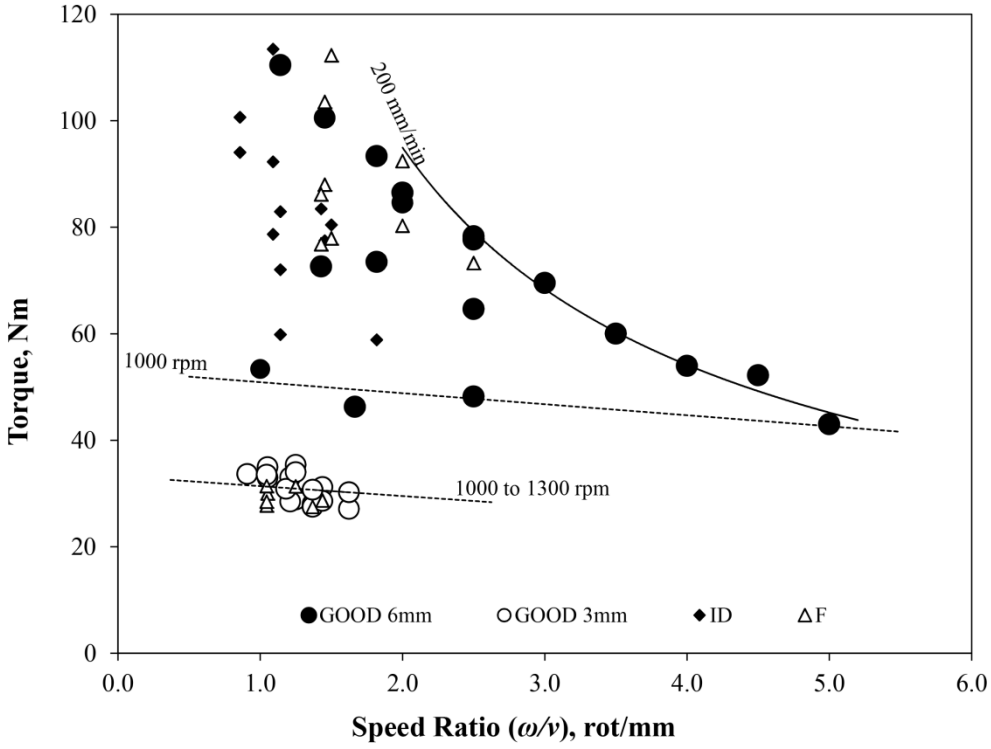

Figure 7.2 – Torque evolution with (ω/v) and weld inspection results for the AA6082 welds. (Annex H)

In order to better illustrate this aspect, in Figure 7.3 and Figure 7.4, are plotted some torque results, corresponding to selected GOOD welding conditions, together with an explicit identification of the shoulder diameter (D_s) and axial load (F_z) corresponding to each test. Since previous analyses of welding results from Chapter 3 showed that varying the pin diameter (D_p) had no influence on welding results, and tool tilt angles (α) lower than 3º conducted mostly to defective welding, no influence of these two parameters on GOOD welding torque results was reported. Figure 7.3 and Figure 7.4 show that, for both base materials, higher torque sensitivity to varying welding conditions was registered in thicker plates welding (5_6 and 6_6) than in thinner plates welding (5_4 and 6_3), since higher variations in torque values

were registered for the former tests by varying a single welding parameter. The figure also shows that, despite the strong influence of the shoulder diameter (D_s) on weld quality, depicted in previous analyses of the welding results, this parameter had a very small influence on registered torque since, independently of the plate thickness and of the base material, very similar torque values were registered when the only parameter varied was the shoulder diameter. Contrary to this, important differences in torque results were reported when varying the axial load. This is in accordance with Longhurst *et al.* (2010) who proposed the use of the spindle torque registered by the welding machines as a process control parameter for FSW, instead of displacement or force control devices, pointing for the extreme sensitivity of this parameter to varying tool position, and consequently, varying axial load.

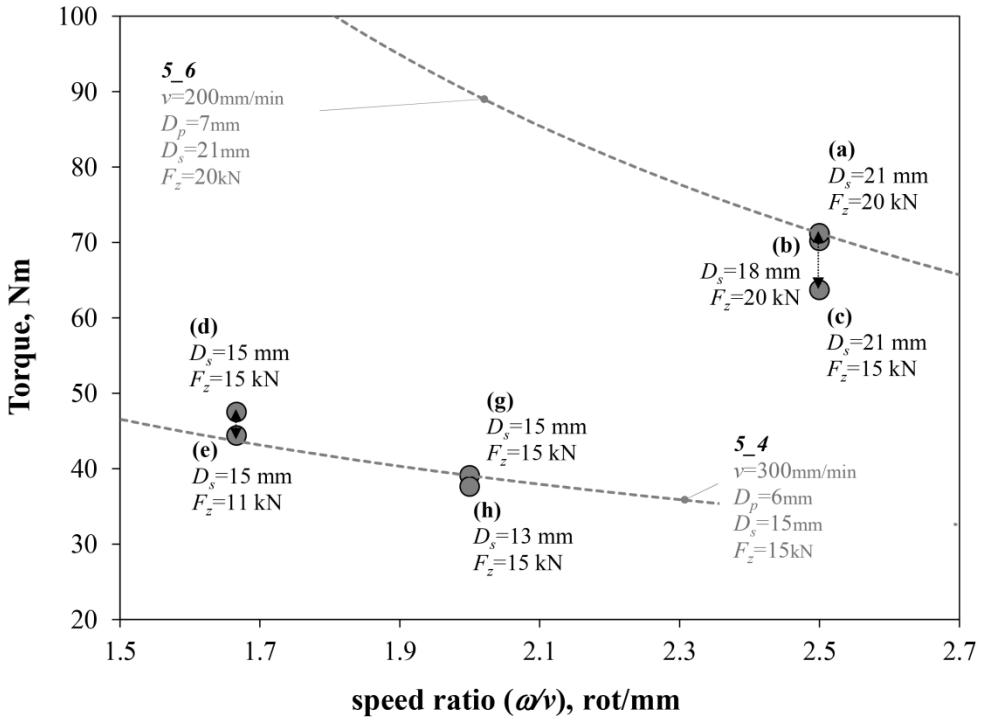

Figure 7.3 – Influence of vertical force, tilt angle and shoulder diameter on torque for the AA5083 welds. (Annex H)

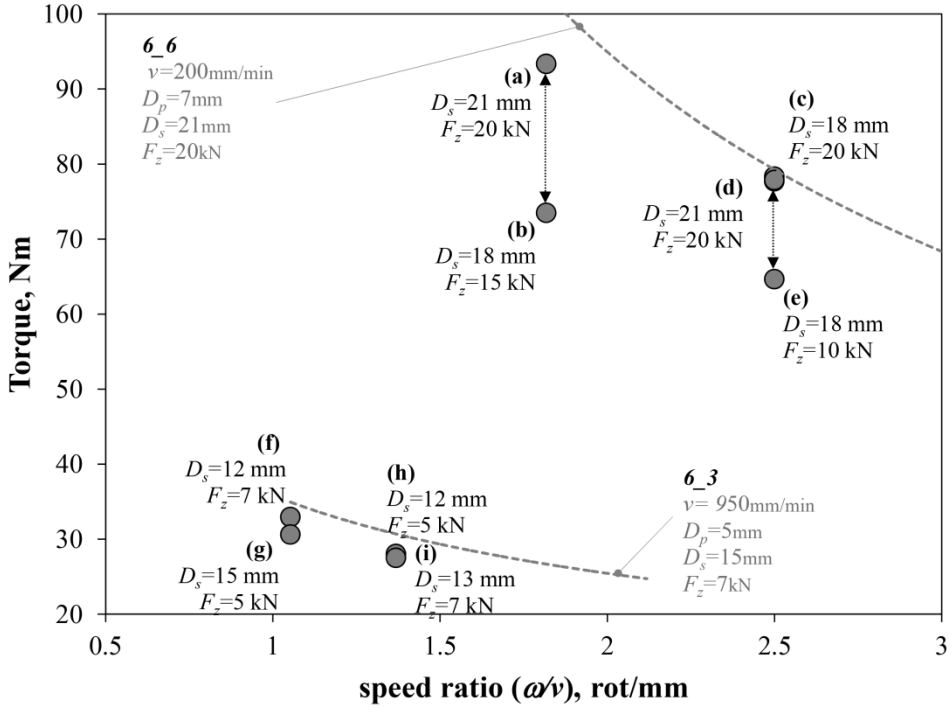

Figure 7.4 – Influence of vertical force, tilt angle and shoulder diameter on torque for the AA6082 welds. (Annex H)

Torque evolution with base materials properties

In order to analyse the influence of base material properties on torque results, in Figure 7.5 are plotted the torque values corresponding to a similar range of welding conditions (*Set1* parameters), for both base materials and same plate

thickness (5_6 and 6_6 welds), and also torque results corresponding to optimized welding conditions for each alloy (*Set2* parameters). The figure shows very similar torque evolution for both alloys, at constant welding speed (200mm/min) and increasing rotation speeds. However, as is also clearly evidenced in the figure, the welding results under these welding conditions were drastically different for both alloys. Meanwhile, for the AA6082 alloy, only GOOD welds were obtained for the full set of rotation speeds plotted in the figure, for the AA5083 alloy, several welds with internal defects were produced using exactly the same welding parameters.

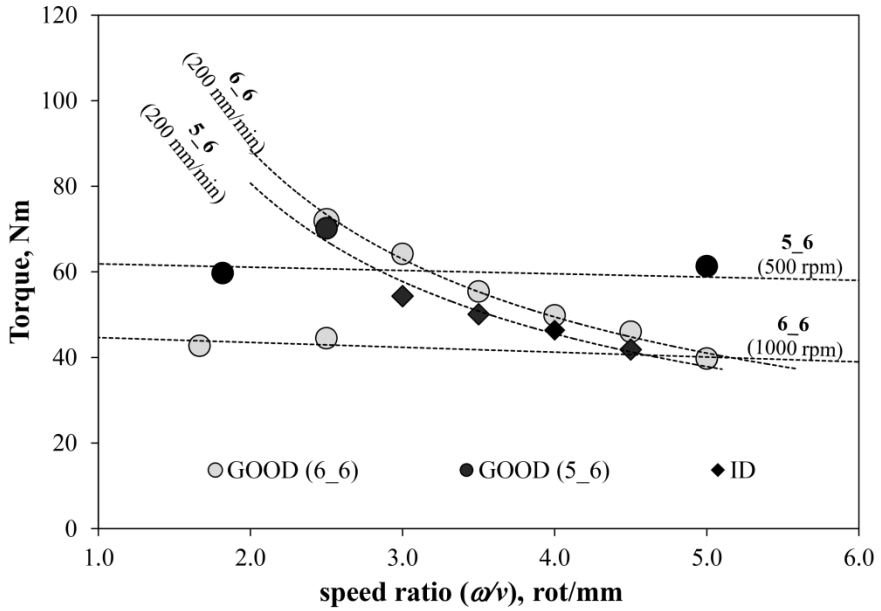

Figure 7.5 – Torque evolution with speed ratio for constant rotational and weld speeds. (Annex H)

The results in Figure 7.1 and Figure 7.2 also show that for the AA5083 alloy the torque values corresponding to the optimized welding parameters (*Set2* parameters) are, in a general manner, higher than those corresponding to

AA6082 GOOD welding conditions. Actually, for the AA5083 alloy, it was already pointed that welding at increasing tool rotation speeds, which is the main factor in reducing the torque values, the welds obtained displayed internal defects. For this alloy, as can be depicted by analysing the 100 and 50 mm/min curves plotted in Figure 7.1, welding results were improved by using rotation speeds equal or lower than 500rpm and welding speeds lower than 200mm/min. On the other hand, for the AA6082 alloy, once optimized the tool geometry and axial load (*Set1* tests), non-defective welds were produced by simultaneously increasing the tool rotation and traverse speeds (*Set 2* tests), which according Mononen *et al.* (2003) is very interesting in terms of industrial productivity. Naturally, increasing the tool rotation speed, decreases the spindle torque, which enabled performing non-defective welding at much lower torque than that required for AA5083 non-defective welding.

Since in Figure 7.5, in spite of the very different welding results obtained in 5_6 and 6_6 welding, very similar torque evolution was registered for both base materials, the following equation was used for adjusting the torque results corresponding to both alloys:

$$T = a \cdot \omega^{-b} \tag{7.1}$$

In this equation, *a* and *b* are constants, depending on process parameters, plate thickness and base material characteristics, which were found as the main factors in affecting the welding conditions.

From current and previous analyses performed in Chapter 3, it was possible to conclude that both the tool parameters and tool axial load are very restrictive parameters, which should be carefully selected before optimizing tool traverse and rotation speeds, namely, shoulder diameter should not be less than 3.5 times plate thickness, tool tilt angle should not be less than 3º and optimal axial load should also be estimated before welding by, for example, performing welding tests in position control. After that, tool rotation and

traverse speeds should be optimized in order to provide the better compromise between weld quality and productivity. Based on this assumptions, constants *a* and *b* in eq. (7.1) were determined considering the plate thickness and the tool rotation and traverse speeds as the main independent variables in the process. For each alloy, both constants were identified by adjusting the equation, using simple log-linearization, to the torque values corresponding to *Set2* welding conditions, i.e., unique tool parameters and axial load and varying rotation and welding speeds. The results obtained are shown in Figure 7.6, where it is possible to see that meanwhile the constant *a* was found to vary mainly with plate thickness, being almost independent of base material characteristics, the constant *b* it was found to strongly vary with welding speed, following similar evolution for both alloys, but with consistently higher values for the AA5083 alloy. This indicates that torque sensitivity to welding speed can be directly related to the material properties.

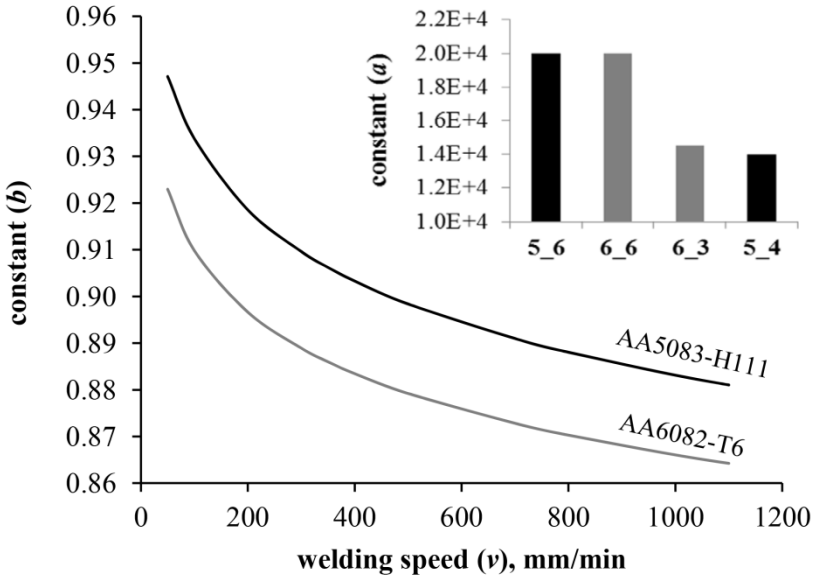

Figure 7.6 – Influence of the base material and weld speed on constant *b* and thickness effect on constant *a*. (Annex H)

In Figure 7.7 and Figure 7.8 are plotted, for the AA5083 and AA6082 alloys, respectively, the torque results corresponding to GOOD welding conditions as function of the rotation and traverse speeds. In the same figures are shown the curves corresponding to equation (7.1), calculated using the welding parameters for each set of experimental results plotted in the figure. It is possible to see that the equation satisfactorily fits all the experimental results shown in the graph. From the figure it is also possible to see that the AA5083 alloy displays much higher torque variation with tool welding speed than the AA6082 alloy. Actually, for the 6_3 welding conditions, almost no evolution of the torque results with varying welding speed was registered.

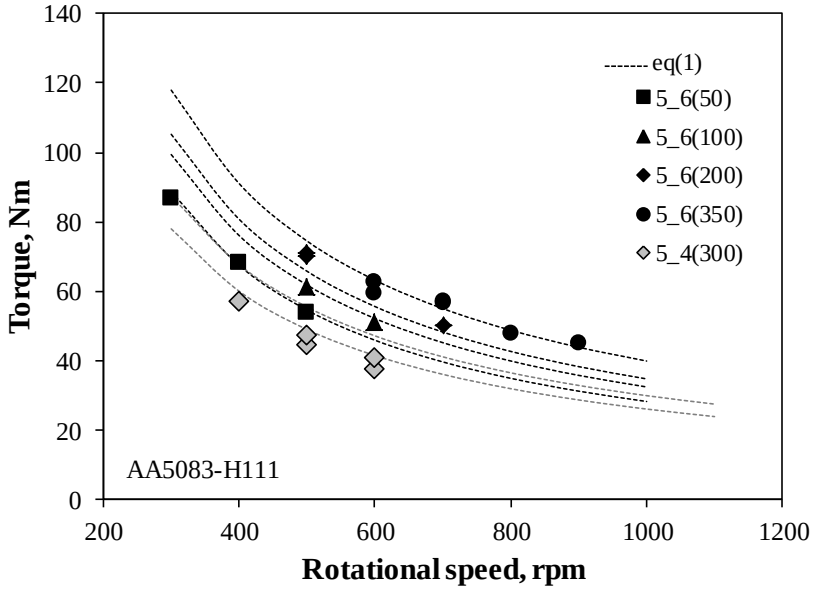

Figure 7.7 – Theoretical and Experimental torque comparison for the AA5083 welds. (Annex H)

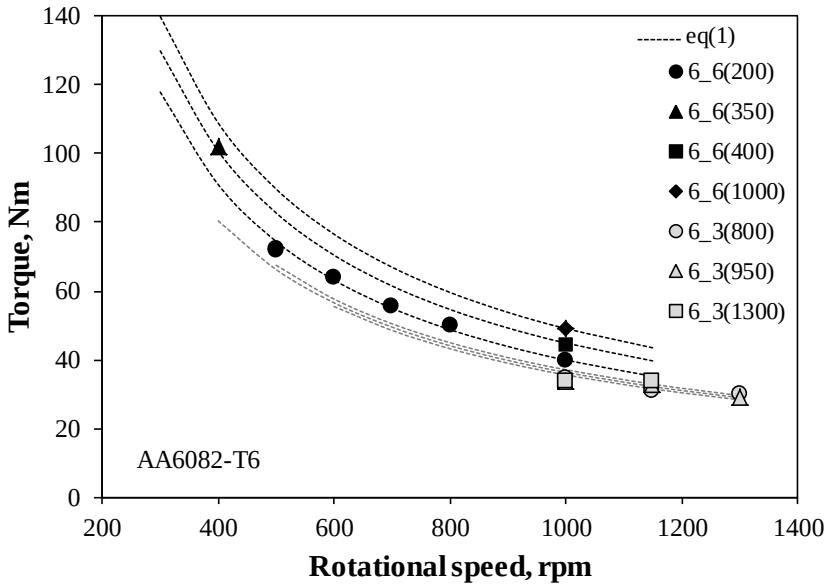

Figure 7.8 – Theoretical and Experimental torque comparison for the AA6082 welds. (Annex H)

Global analysis of torque evolution with welding conditions

From Figure 7.3 and Figure 7.4, it was concluded that using optimized tool parameters and axial force, conducting to non-defective welds production, the evolution of the torque with tool rotation and traverse speed is very similar for both base materials, in spite of higher torque values being registered for non-defective welding of the AA5083 alloy, than for the AA6082 alloy.

Arora *et al*. (2009) stated that increasing the tool rotation speed, increases the temperature, decreasing the flow stresses associated to material stirring during the process, which decreases the spindle torque. So, the differences in

torque levels for the AA5083 and AA6082 alloys must be related to the use of lower rotation rates for non-defective FSW of the AA5083 alloy. In Chapters 5 and 6 it was analysed the plastic behaviour of both base materials at high temperatures, and its relation with their weldability in FSW. The differences in plastic behaviour at high temperatures also justify the differences in base materials sensitivity to the tool rotation and traverse speeds depicted from the torque sensitivity analyses.

It is also important to enhance that when welding the AA5083 alloy in the lower plate thickness, non-defective welding results were obtained even at high tool rotation rates. This behaviour should be related with a more uniform temperature distribution, as well as improved trough thickness material flow with decreasing plate thicknesses. Actually, Figure 7.9 shows, for both base materials, that the interface between the shoulder and pin governed flow volumes become less evident by diminishing the plate thickness, indicating a more efficient through thickness material mixing, which deeply contributed in diminishing the amount of defects for both alloys.

The strong influence of plate thickness on welding conditions was also patent from the torque sensitivity analysis, since much higher differences in torque values were reported in thicker than in thinner plates welding by changing the processing conditions. Actually, for each base material, at similar rotation rates, the torque values registered in thinner plates welding were much lower than those registered in thicker plates welding. This should be related to the lower amount of material being processed at each revolution, as well as to more favourable material flow across the thickness under the more uniform through thickness temperature in thinner plates welding. The strong influence of plate thickness on welding conditions and torque evolution was also patented by adjusting the torque governing eq. (7.1) to the experimental results, when it was found that constant a value is mainly influenced by plate thickness.

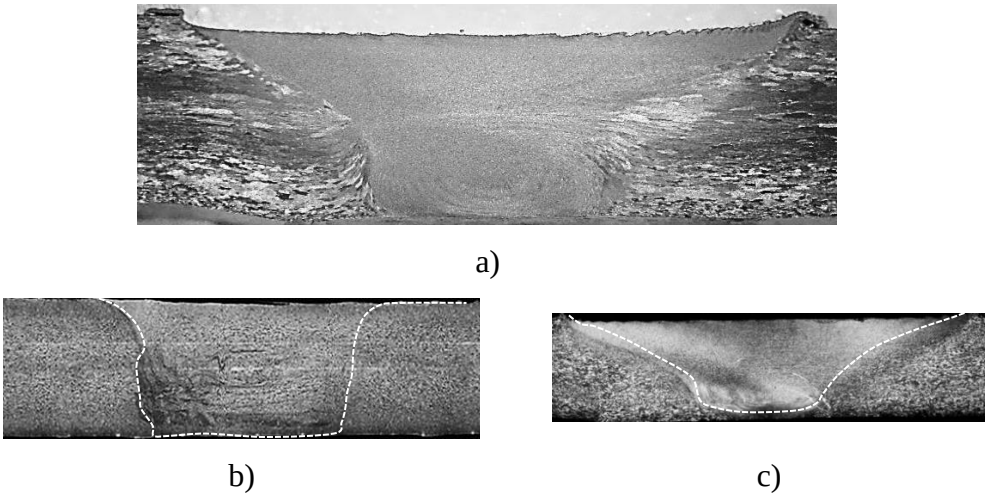

a) b) c)

Figure 7.9 - Cross-sections of 6_6, 5_4 and 6_3 welds corresponding to rotational/weld speeds of 500/200(a), 900/700 (b) and 1150/800 (c), respectively. (Annex H)

Finally, strong variations in torque results were also registered in thick plates welding by varying the axial load, which also has a strong influence on through thickness material flow and heat generation during welding. Very small axial load values conducted to inadequate material flow, with important surface or internal defects being formed, and very high axial load values promoted material expulsion from the stirring volume, conducting to massive flash formation. Torque results and weld inspection revealed that there is a much narrow interval for optimal axial load than for the tool traverse and rotational speeds.

Final comment

From the current chapter, it is possible to conclude that, in non-defective welding conditions, the evolution of torque with tool traverse and rotation speeds is independent of base material properties, being satisfactorily described by a power law equation.

Other important conclusion is that, tool rotation speed, axial load and plate's thickness are the main factors in determining torque values, due to its strong influence on heat generation and through thickness heat distribution and material flow.

Finally, it also possible to conclude that, base materials plastic properties have a strong influence on welding behaviour, and consequently, in defining optimum processing conditions.

8

Mechanical Characterization of the welds

In previous chapters the weldability of the AA5083 and AA6082 alloys was thoroughly discussed based on the morphological and microstructural analysis of the welds performed under a broad range of welding conditions. The study enabled to establish, for each alloy, a set of welding conditions under which it is possible to obtain non-defective welds. In this chapter, the results of the mechanical characterization of the non-defective welds of both alloys will be shown and the evolution in mechanical properties with process parameters will be discussed.

.

This Page Intentionally Left Blank

Introduction

In this chapter, de mechanical characterization results are organized in two chapter sections. In the first section, named "Mechanical strength evolution", the mechanical performance of the welds performed under *Set2* welding conditions, for each alloy, will be analysed individually, in order to provide an accurate understanding on the influence of process parameters on welds strength. In this way, the mechanical testing results will be labelled in order to identify the specific set of welding conditions under which each weld was obtained. This section is divided in two subsections, corresponding to each base material, named "Mechanical Characterization of AA5083 welds" and "Mechanical Characterization of AA6082 welds".

In the "Mechanical Characterization of AA5083 welds" subsection, the analysis of welds mechanical performance will be performed based on tensile and shear testing results. Since the shear samples, as well as the shear testing procedures, used for the mechanical characterization of the welds were developed under the scope of the thesis, details of testing validation procedures will be described and discussed together with the welds mechanical strength analysis. In "Mechanical Characterization of AA6082 welds" subsection only tensile testing results will be shown. Some hardness measurement results will be also displayed across the chapter in order to provide a more detailed analysis of welds mechanical heterogeneity.

In the second section, named "Global strength analysis", the mechanical strength and plastic behaviour of the GOOD welds produced under *Set1* welding conditions, for both alloys and two plate thicknesses, are compared. With this study a global overview on welds performance is provided, as well as a comparative analysis of the weld mechanical efficiency for both alloys. The test results displayed in this section will be labelled according to the alloy type

and plate thickness to which they refer, i.e., 5_4, 5_6, 6_3 and 6_6, as already performed in Chapter 4.

Mechanical strength evolution

Mechanical characterization of AA5083 welds

In Table 8.1 are summarized the welding conditions used for producing the specific set of welds analysed in this chapter section. As is shown in the table, in the next, the mechanical testing results will be labelled using the rotational and welding speeds used for producing the welds. In order to assess the evolution in mechanical strength of the 6mm thick AA5083 welds, performed under varying welding conditions, hardness measurements were performed across the welds. In Figure 8.1 are plotted the hardness ratios (Hv^{weld}/Hv^{BM}), i.e., the ratio between the average hardness registered for each weld in the pin influence zone (Hv^{weld}) and the average hardness of the base material (Hv^{BM}). Due to the strong relation between grain size, and materials strength, attributed to this alloy, the average grain sizes (GS) for all the welds and base material are also shown in the same figure. The graph clearly shows that, in spite of the varying welding conditions, no important differences in grain size and hardness were reported for the different welds. Actually, almost all the welds were in even-matched, or even in a slight under-match, relative to the base material hardness, in spite much smaller grain sizes were measured for the welds.

In order to confirm the absence of any relation between grain size and weld strength, for this alloy, at least for the range of grain sizes reported in

current work, shear and tensile tests were performed in order to more accurately analyse welds strength and plastic properties.

Table 8.1- AA5083 set*2* welds Friction stir welding parameters

Sample	Rot. Speed, (rpm)	Weld speed, (mm/min)	Shoulder diameter, (mm)	Pin diameter, (mm)	Axial Load, (kN)	Tilt Angle, (º)
300_100	300	100				
400_100	400	100				
500_100	500	100				
600_100	600	100				
700_100	700	100				
600_350	600	350	21	7	20	3
600_275	600	275				
600_50	600	50				
500_50	500	50				
400_50	400	50				
300_50	300	50				

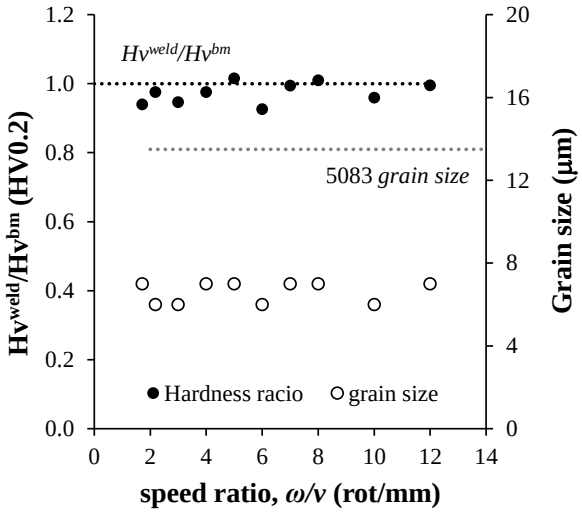

Figure 8.1 – Hardness ratio (Hv^{weld}/Hv^{bm}) and average grain sizes (GS) for all the welds tested and AA5083 base material.

Tensile tests

Tensile testing of transverse weld samples was performed according to the procedures described in Chapter 3. Strain data acquisition by DIC, with Aramis system, enabled to access the local strain fields for each weld sample, as shown in Figure 8.2, where are shown strain maps at half of the maximum load ($F_{max}/2$) and at maximum load (F_{max}), for the samples 600_100 and 300_50. The strain maps, registered at the weld cross-section, enable to conclude that, in spite of the microstructural heterogeneity in the weld zone, where a very refined microstructure was detected in the metallographic analysis, plastic deformation across the samples was almost uniform until maximum load. This enhances the even-matched mechanical properties of the AA5083 welds, relative to the base material, already depicted when analysing the hardness results of Figure 8.1.

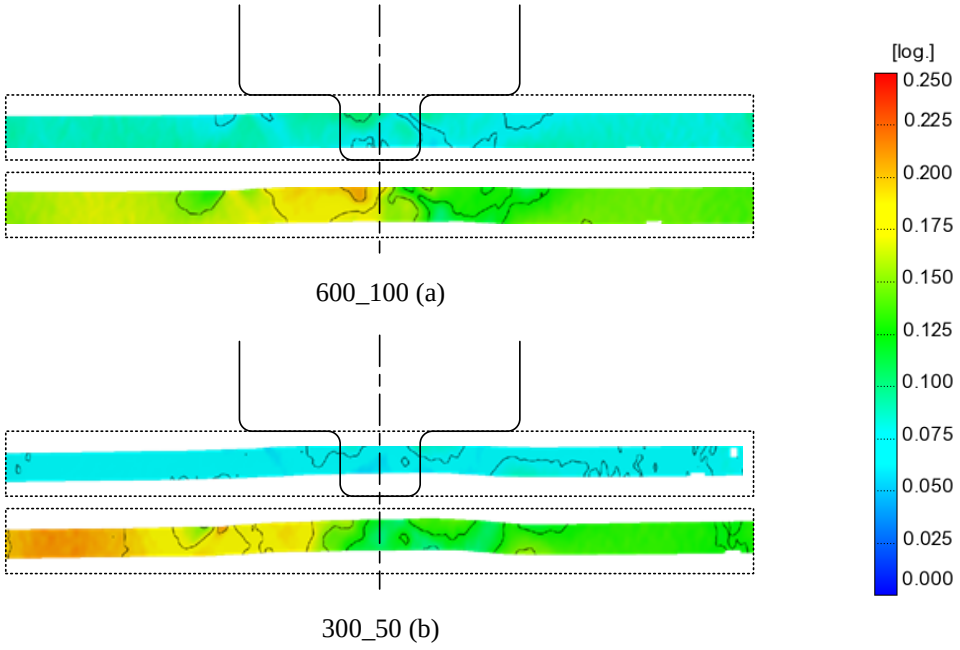

Figure 8.2 - Strain maps at half of the maximum load ($F_{max}/2$) and at maximum load (F_{max}), for the samples 600_100 (a) and 300_50 (b)

In order to check if the strain path, during tensile testing, remained linear and uniaxial, until maximum load, in spite of the microstructural and morphological weld discontinuities, the major versus minor strain (ε_1 versus ε_2) evolution with plastic deformation, for the different zones of each of the transverse weld samples tested in current work was analysed. The analysis performed is exemplified in Figure 8.3a) where are plotted ε_1 versus ε_2, for the TMAZ and BM parts of a 600_100 sample. In the same graph are plotted the strain paths corresponding to pure uniaxial loading conditions, for isotropic ($\varepsilon_2 = -0.5\varepsilon_1$) materials, and also, considering the anisotropy of the base material, calculated following the procedures described in Annex A and using the AA5083 anisotropic coefficients shown in Figure 3.17. It is also important to stress that the logarithmic strain values plotted in the graph correspond to an average of the strain values registered for all the points located inside the areas under study (exemplified in the figure), calculated using *Aramis* software. Analysing the figure it is possible to confirm that the strain path inside the TMAZ, remained linear during the test, falling over the isotropic uniaxial path. The same was registered for the base material, but in this case, the strain path followed the anisotropic uniaxial path. These results indicate that the recrystallized TMAZ has anisotropic properties.

In Figure 8.3b) are now plotted the local stress-strain curves corresponding to the TMAZ of the welds performed at 500, 600 and 700 rpm, and 100 mm/min, and at 300, 400 and 500 rpm, and 50 mm/min, which according to Table 4.3 were all non-defective welds. In the same graph is also plotted the stress strain curve corresponding to the base material (BM). Comparing the curves plotted in the graph, it is possible to confirm that the AA5083 welds were in even-match relative to the base material.

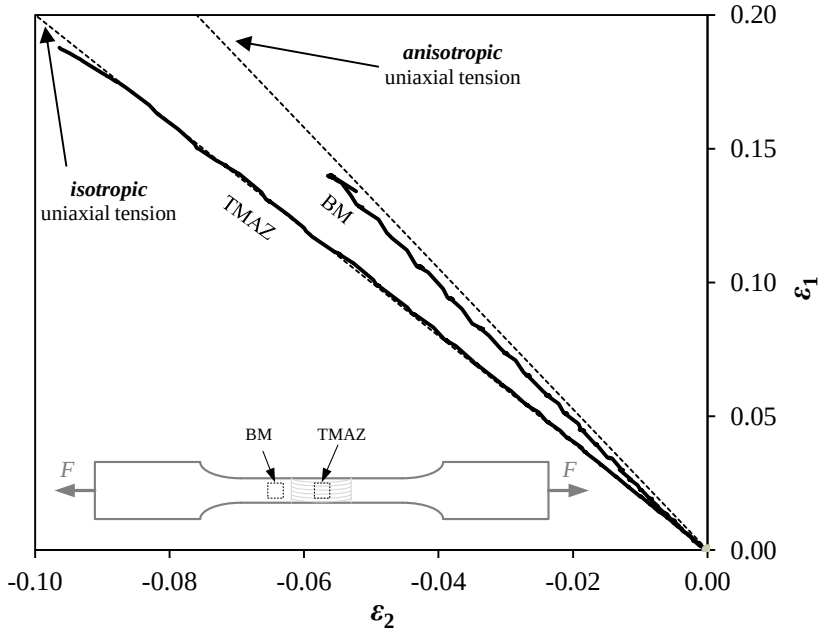

(a)

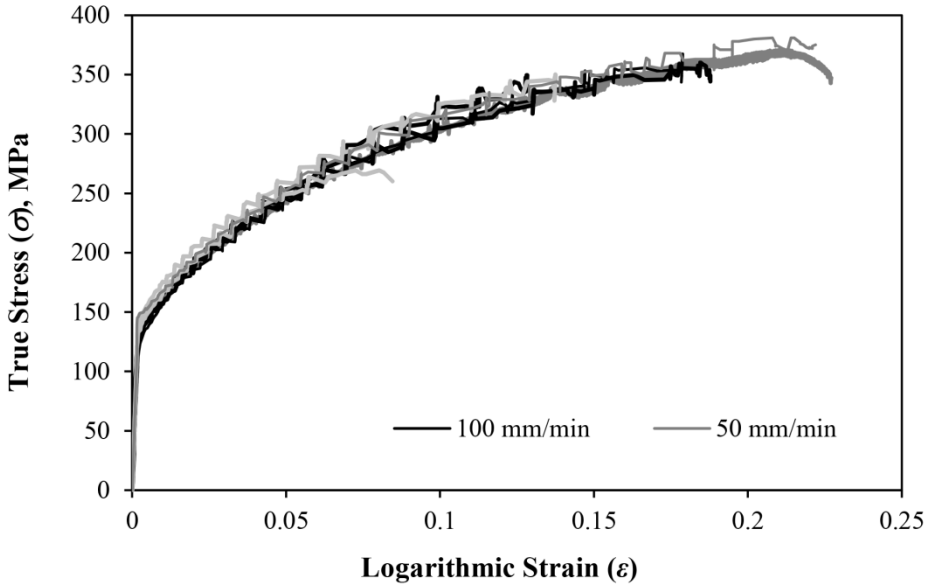

(b)

Figure 8.3 – Strain path evolution (a) and true stress-strain curves (b)

Shear Test

It is important to enhance that the results that will be shown in the next correspond to tests performed with the aim of developing and validating a shear test procedure for the mechanical characterization of welds. In this way, the shear testing were accomplished using the samples, and following the procedures, already described in Chapter 3. In Figure 8.4 is shown a scheme of a shear sample of a weld (Figure 8.4a), together with a cross-section of a friction stir weld (Figure 8.4b), where the weld region to be tested is shown, i.e., the shear zone for all the samples tested corresponded to the centre of the pin influence zone.

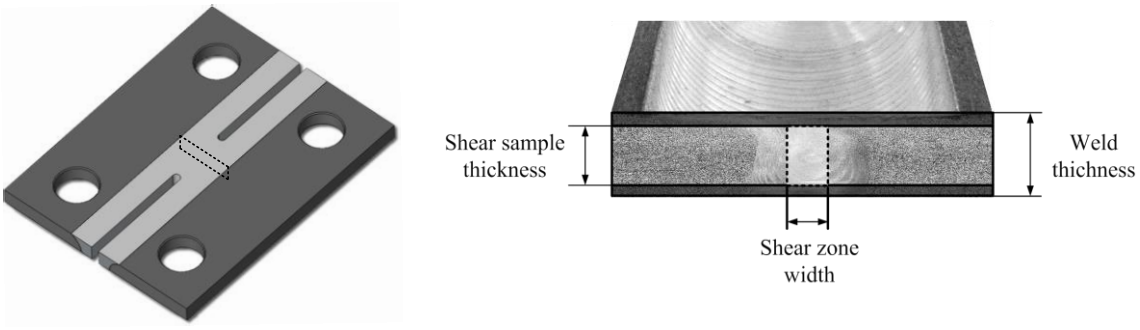

(a) (b)

Figure 8.4 – Weld shear test sample scheme (a) and cross-section (b).

From Figure 8.5a) to Figure 8.5d) are shown the ε_{xy} strain maps, at half of the maximum load ($F_{max}/2$) and at maximum load (F_{max}), for four different shear samples. As it is possible to see in the figure, after yielding, plastic deformation spreads along the weld. The deformed area is symmetric relative to the loading direction and to the sample middle-plane. The gradient in strain distribution becomes sharper at maximum load, when strain localisation occurs at the free-ends of the shear zone. Before plotting the stress-strain curves, for each sample tested, the strain path evolution with plastic deformation, inside the shear zone, was analysed in order to verify if simple shear loading conditions prevail until

maximum load, in spite of the non-uniform strain distribution depicted in Figure 8.5.

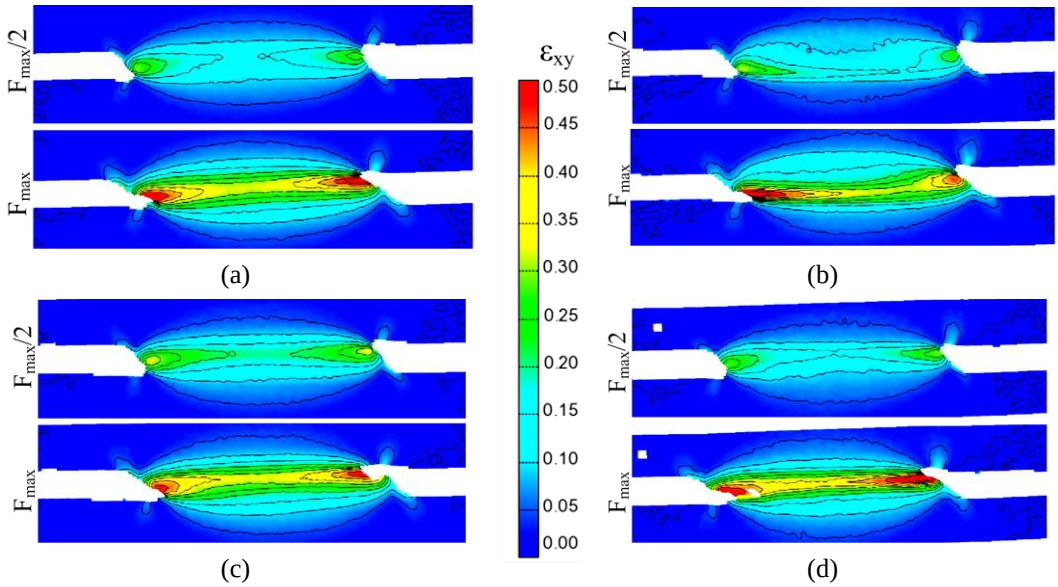

Figure 8.5 – Strain maps (ε_{xy}) obtained at half of maximum load ($F_{max}/2$) and maximum load (F_{max}) for the 300_100 (a), 700_100 (b), 600_350 (c) and 600_50 (d) welds. (Annex B)

The major (ε_1) versus minor strain (ε_2) evolution is shown in Figure 8.6a) and in Figure 8.6b), for all the samples studied. The strains plotted in the graphs, correspond to average strain values calculated using Aramis software. As already shown in Chapter 3, two different evaluation areas were considered for calculating the average strains ε_1 and ε_2, which are represented and identified as Global and Local in the auxiliary schemes of Figure 8.6a) and of Figure 8.6b), respectively. Using the Global evaluation area, the full range of strain values registered in the shear zone is considered for computing the average strains. Using the Local evaluation area, only the strain values at the centre of the sample, where the strain fields are homogeneous, are considered

in computing the average strains. Analysing Figure 8.6a) and Figure 8.6b), it is possible to conclude that pure-shear conditions ($\varepsilon_1 = -\varepsilon_2$) prevail until maximum load, independently of the strain evaluation area considered. Actually, no important strain path change is observed, even considering the global evaluation area, which allows concluding that the free-end influence on strain distribution, inside the shear zone, has no significant influence on global strain path evolution.

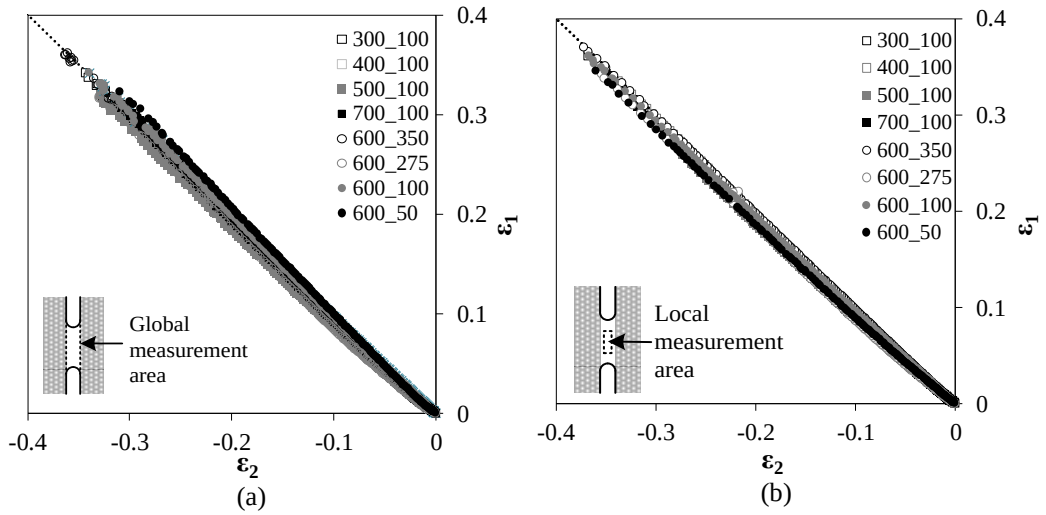

Figure 8.6 – Strain path evolution within shear zone, during shear testing, considering a global (a) and local (b) strain measurement areas. (Annex B)

Using the strain data acquired by DIC, shear stress–strain curves (τ, γ) were computed for all the welds. In order to illustrate the reproducibility of results, Local and Global average shear stress–strain curves, for three different welds, are shown in Figure 8.7. The Local and Global shear stress–strain curves were plotted using average ε_{xy} values, computed over the same local and global measurement areas already shown in Figure 8.6. Observing the

figure it is possible to depict the excellent concordance between the results obtained for each weld when testing three samples, for the sample 600_350, respectively, and two samples, for the other two welds. At least two samples were tested for each weld of Table 8.1, being always found good reproducibility of results. It is also important to observe that no significant differences can be noticed between the Local and Global stress–strain curves plotted in Figure 8.7, which shows that the non-uniform shear strain distribution, depicted in Figure 8.6, does not influence significantly the global stress–strain results. In this way, in the next figures, only the Global stress–strain curves will be plotted.

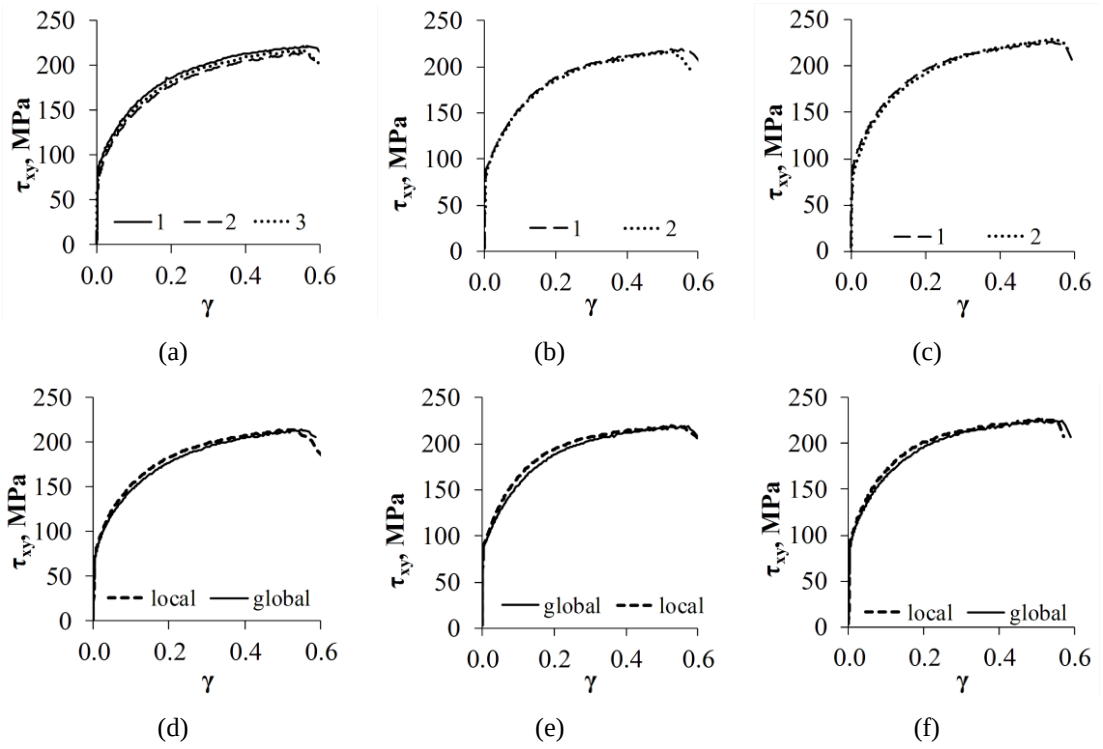

Figure 8.7 – Shear stress-strain curves (τ-γ) for the welds 600_350 (a and d), 600_100 (b and e) and 600_50 (c and f). (Annex B)

In Figure 8.8, the shear stress–strain (τ–γ) curves for the samples of Figure 8.5 are compared with the stress–strain curves obtained for the base material, by testing in shear two types of samples: samples in the rolling direction of the plate (0º) and samples transverse to the rolling direction (90º). Analysing the figure it is possible to depict the anisotropic behaviour of the base material, as well as some differences in stress–strain behaviour for the different weld samples. However, in spite of the differences, all the weld curves almost fall between the two curves of the base material.

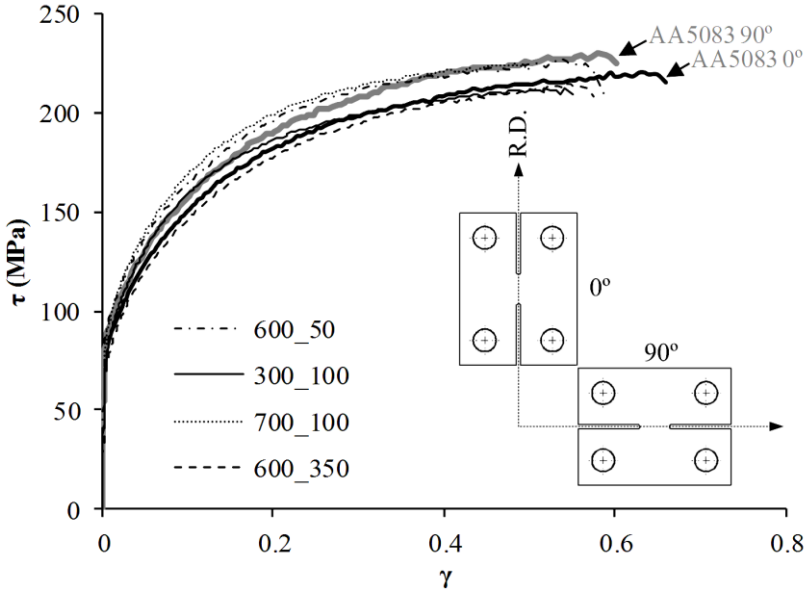

Figure 8.8 – Global shear stress strain curves (τ-γ) for the base material and some of the weld samples. (Annex B)

In Figure 8.9 are now compared the maximum shear stress and strain values, registered for all the weld samples and for the base material. It is possible to conclude that no important mis-match in maximum shear strength or maximum shear strain, relative to the base material, was registered for any

of the weld samples. Actually, the maximum difference between the results in Figure 8.9 was never higher than 18 MPa. In the same way, when analysing Figure 8.1, no important differences in grain size and hardness were reported for the different welds, which is in accordance with the small differences in plastic behaviour depicted from the shear tests. However, it is also important to enhance that in spite of the similarities reported in the microstructural and mechanical analysis, strong differences in weld morphology were obtained by changing the welding conditions. It is also important to remark that in spite of the considerable grain size reduction in the weld, relative to the base material, which can be depicted in Figure 8.6b), no important differences in strength and/or plastic behaviour were reported in any of the tests performed.

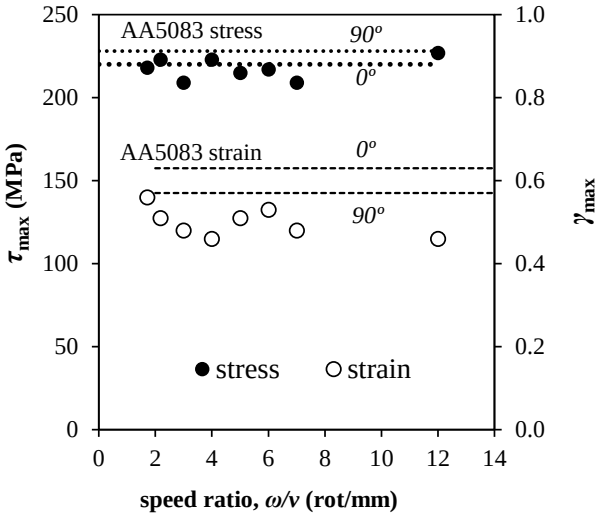

Figure 8.9 – Maximum shear stress and strain for all the welds tested and base material. (Annex B)

Finally, in Figure 8.10 are plotted tensile stress–strain curves (σ-ε) for the base material (at 0º and 90º with the rolling direction), a local tensile stress strain curve, corresponding to one of the welds (600_100), already analysed in

previous section, and equivalent stress–strain curves computed from the shear testing results for both the weld and base material parts of the sample. For the base material, the equivalent stress-strain curve was plotted using the *Hill'48* criteria, and for the welds, the equivalent stress–strain curve was calculated using the *Von Mises* criteria.

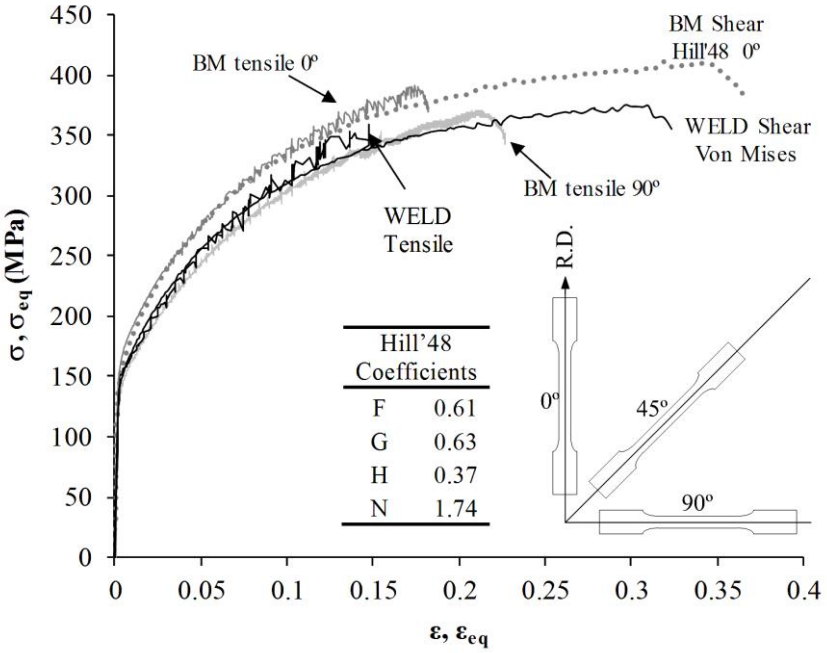

Figure 8.10 – Equivalent strain-stress (σ-ε) curves for the base material and 600_100 weld. (Annex B)

In Figure 8.10 it is possible to observe that, as already observed in Figure 8.9, the weld material is in even-match with the base material, since the weld tensile stress–strain curve follows between the tensile curves of the base material (0º and 90º). It is also important to notice the excellent concordance, until relatively high values of plastic deformation ($\varepsilon \cong 0.15$), between the weld tensile curve and the *Von Mises* equivalent curve, computed from the weld shear testing results. These results are again indicative that the recrystallized

weld nugget has isotropic behaviour in plastic deformation. In any case, characterising the anisotropy of the weld would be very hard, due the difficulty in performing tensile or shear testing transverse to the weld direction. Current results show that using *Von Mises* would give satisfactory results in describing the weld material plastic behaviour and that the method developed for the mechanical characterization of welds is trustful.

Mechanical characterization of AA6082 welds

In Table 8.2 are summarized the welding parameters used for producing the specific set of AA6082 welds analysed in this section, which correspond to welds performed in 6 mm thick plates. In the next, the mechanical testing results will be labelled using the rotational and welding speeds used for producing the welds, as was already done when analysing the AA5083 material characterization results.

Table 8.2- AA6082 set*2* welds parameters

Sample	Rot. Speed, (rpm)	Weld speed, (mm/min)	Shoulder diameter, (mm)	Pin diameter, (mm)	Axial Load, (kN)	Tilt Angle, (º)
500_200	500	200				
600_200	600	200				
700_200	700	200				
800_200	800	200				
900_200	900	200	21	7	20	3
1000_200	1000	200				
1000_400	1000	400				
1000_600	1000	600				
1000_1000	1000	1000				

In Figure 8.11 are shown, for all the welds tested, the global engineering stress-strain (*s*-*e*) curves, computed using the force-displacement records from the tensile test of transverse samples, by considering a 50mm gauge length. Since all the stress-strain curves corresponding to the welds obtained at a constant welding speed of 200 mm/min, and varying tool rotational speeds, are very similar, they are identified in the graph using this welding speed value. Actually, as can be depicted from the graph, by comparing the 200 mm/min and the 1000_400, 1000_600 and 1000_1000 curves, differences in weld strength were only reported for the welds produced at increasing traverse speeds, until a maximum traverse speed of 600 mm/min. For welding speed values higher than that, the curves became again very similar, indicating very small differences in weld strength. It is also important to remark that all welds failed for very small strain values (always lower than 5%), which points for the existence of a strong under-match in mechanical strength in the weld zone.

In order to understand the evolution in tensile behaviour reported in Figure 8.11, hardness measurements were performed across the welds, at the middle plate thickness, for the 500_200, 1000_200 and 1000_1000 samples, which, as shown in Table 8.2, correspond to the welds performed at the maximum and minimum values of tool rotational and traverse speeds tested. The hardness profiles for the 500_200 and 1000_200 and for the 1000_200 and 1000_1000 samples are compared in Figure 8.12 and Figure 8.13, respectively.

Analysing the hardness profiles in Figure 8.12 it is possible to conclude that by changing the rotational speed, at constant tool traverse speed, didn't change significantly the weld characteristics. For both welds, the traditional "W" shape hardness profile characteristic of heat treatable aluminium alloy welds was registered, being possible to depict a significant hardness decrease in the TMAZ and HAZ, with small differences in minimum hardness for both

welds. On the other hand, from the hardness profiles in Figure 8.13, it is possible to conclude that, by increasing the tool traverse speed at constant tool rotational speed, decreased the width of both TMAZ and HAZ, and increased the hardness values on each of these zones. These features were already reported bay other authors, being related to the higher heating and cooling rates experienced at increasing tool traverse speeds. By comparing the hardness results and the engineering stress-strain curves of Figure 8.11 it is possible to understand the differences in tensile strength. Higher tensile strength values were registered for the welds with higher hardness values and lower weld width.

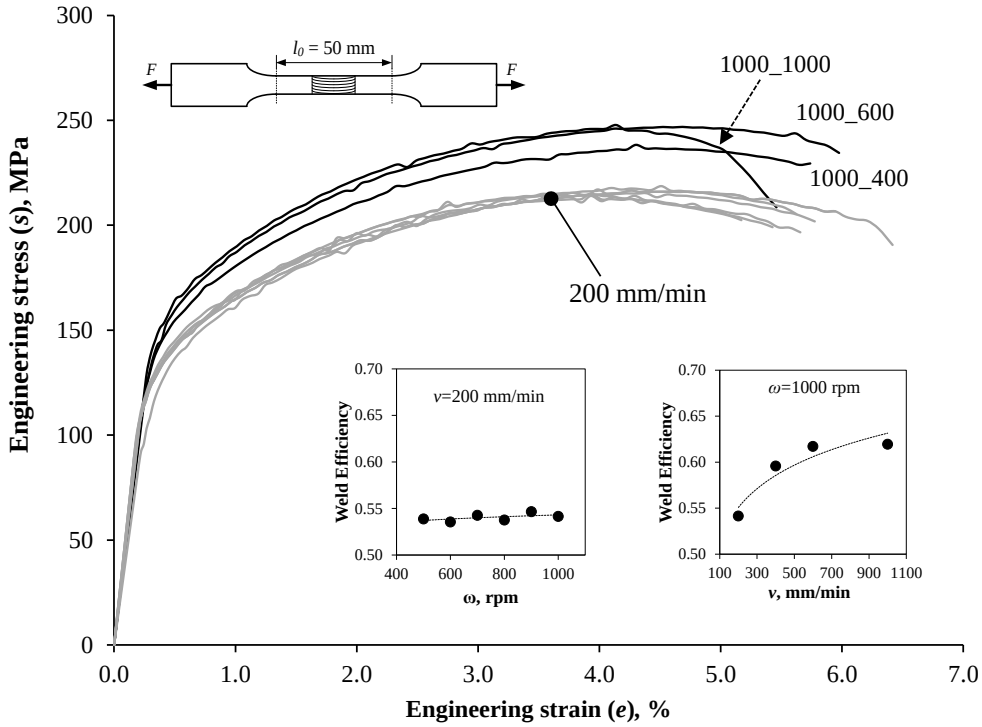

Figure 8.11 – Engineering stress-strain (*s*-*e*) curves for the 6082 *set2* welds.

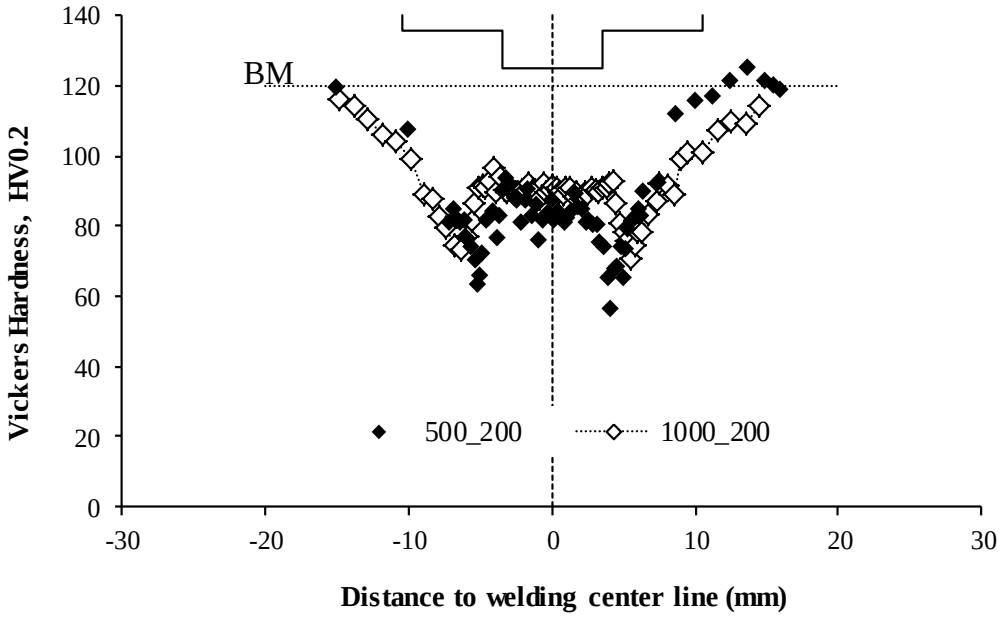

Figure 8.12 – Hardness profiles of the 500_200 and 1000_200 welds.

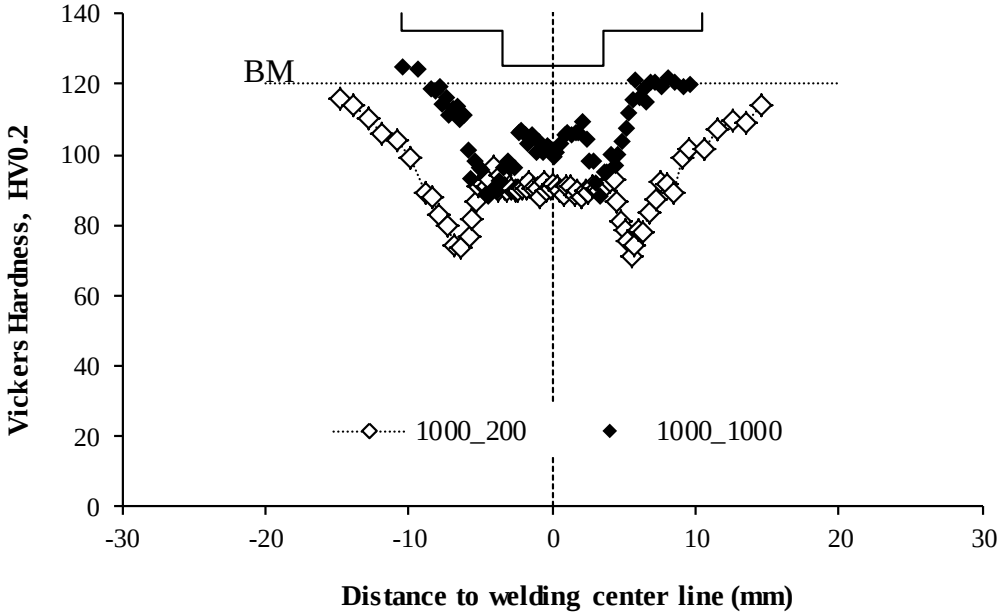

Figure 8.13 – Hardness profiles of the 500_200 and 1000_200 samples.

In Figure 8.14a) to c), are shown the major strain (ε_1) maps, at half of the maximum load ($F_{max}/2$) and at maximum load (F_{max}), for the 500_200, 1000_200 and 1000_1000 tensile samples, respectively. Analysing these maps it is possible to conclude that the 500_200 and 1000_200 samples failed in the HAZ, where the lower hardness values were registered, before any plastic deformation took place in the base material. On the other hand, for the 1000_1000 weld, it can be observed that the sample failed in the TMAZ, where a very small defect, not reported in welding inspection analysis of chapter 4, was detected by observing the fracture surface of the tensile samples. Also for this sample, for which a small defect was observed, rupture occurred before the base material was plastically deformed. The strain maps in Figure 8.14 also show that the width of the welds (plastically deformed area) increased when decreasing the tool traverse speed, as already reported when analysing the hardness profiles in Figure 8.13.

Using the procedures explained in Chapter 3, local stress-strain curves were calculated for the TMAZ and HAZ of all the welds. In Figure 8.15a) are shown the true stress-strain curves, relative to the TMAZ, and in Figure 8.15b) is shown the evolution of local principal logarithmic strains (ε_1 against ε_2), with plastic deformation, for each test. This graph enables to confirm that, for all the welds except the 1000_1000, the strain path in the TMAZ remained linear until the end of the test, coinciding with the uniaxial tension strain path. For the 1000_1000 sample, which failed in the TMAZ, the deformation path started deviating from linearity, but only after maximum load, when necking starts. The stress-strain curves, shown in Figure 8.15a), are plotted for plastic deformation values inside the ε_1-ε_2 linear domain. Analysing the curves plotted in the figure it is possible to confirm that all the samples failed for very small values of plastic deformation. It is also possible to conclude that the local strength of the TMAZ follows the same evolution with process parameters

already reported in Figure 8.11, when analysing the global strength of the welds.

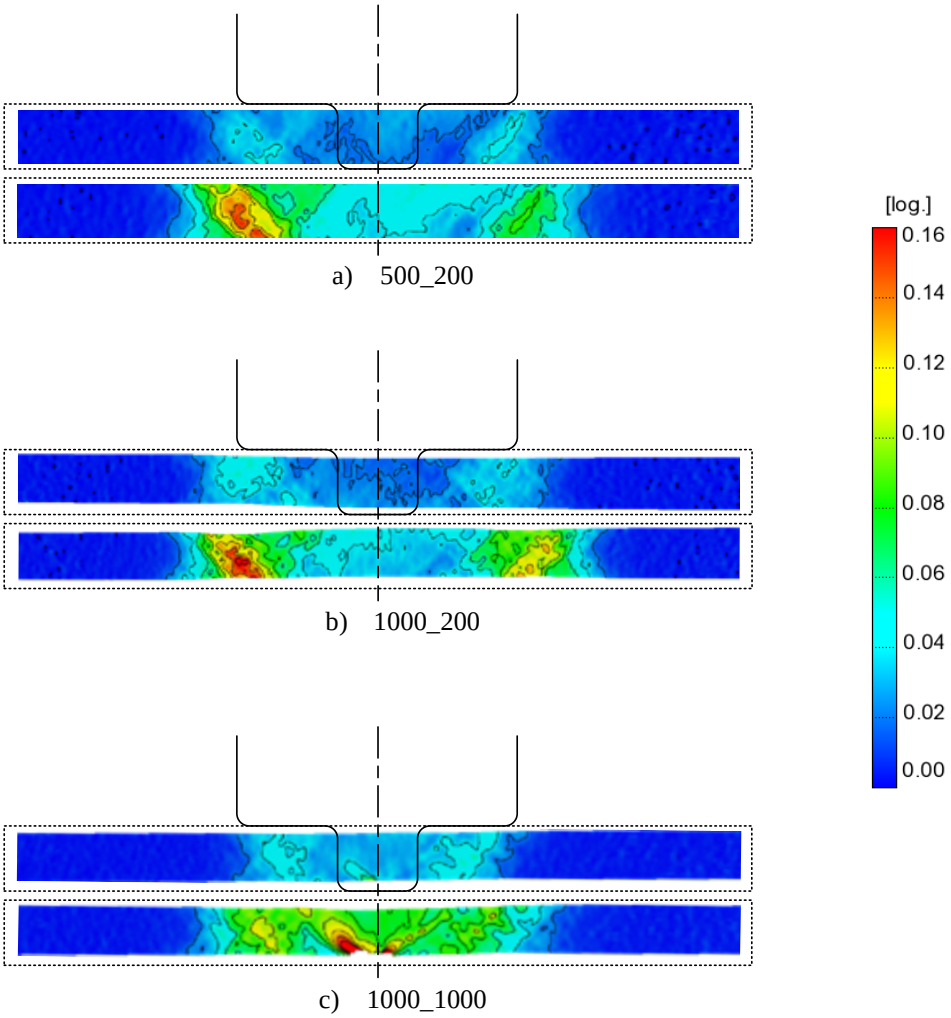

Figure 8.14 – Strain maps obtained at half of maximum load ($F_{max}/2$) and at maximum load (F_{max}), for the 500_200 (a), 1000_200 (b) and 1000_1000 (c) samples.

In order to understand the evolution of local strength, with processing parameters, a deeper analysis of local stress-strain behaviour was performed

for the welds shown in Figure 8.14. In Figure 8.16a) are shown, for the 500_200 and 1000_200 samples, the true stress-strain curves, relative to the TMAZ and HAZ, and in Figure 8.16b) is shown the evolution of local principal logarithmic strains (ε_1, ε_2),with plastic deformation. In order to enable analysing the local plastic behaviour, until high values of plastic deformation, in the graph of Figure 8.16a), in addition to the experimental curves, were also plotted analytical curves obtained by adjusting the experimental ones with the *Swift* equation (eq. 3.3). In the analytical curves, the tensile strength, estimated using the *Considére* criteria (eq. 3.4), is also indicated by a dot. In Table 8.3 are summarized the Swift equation parameters, and the calculated tensile strength, for each weld.

In the graph of Figure 8.16b) it is possible to see that, meanwhile the strain path for the TMAZ of both welds coincided to uniaxial tension until the end of the test, for HAZ, the strain path deviated from uniaxial tension, falling in the domain between it and biaxial loading. Actually, looking at the strain maps in Figure 8.14 it is possible to see that the deformed HAZ evolves along a region that makes 45º with the tensile axis of the sample. In this way, it is possible to assume that the natural morphology of the HAZ promoted some local shearing during tensile loading.

Comparing the curves in Figure 8.16a) it is possible to confirm that the plastic properties of the TMAZ are very similar, for both welds, being in under-match relative to the base material until maximum load. For the HAZ, it is possible to observe some differences in the stress-strain curves plotted for both welds. Both HAZs display similar yield strength, but at increasing values of plastic deformation, the 500_200 HAZ displays higher strength. Since Figure 8.16b) shows that the strain paths in the HAZ were very similar, for both samples, the differences in stress-strain behaviour can only be attributed to local differences in HAZ characteristics. Actually, from the hardness profile of Figure 8.12 it is possible to depict small differences in minimum hardness

and width, for both samples, which points for a different microstructural evolution in the HAZ.

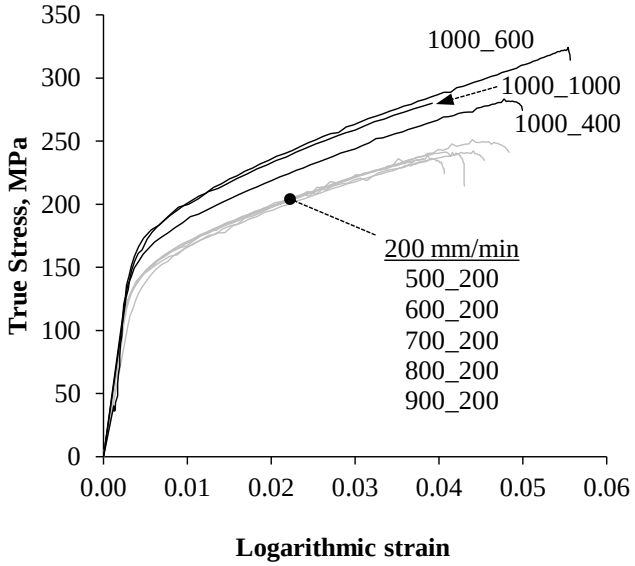

(a)

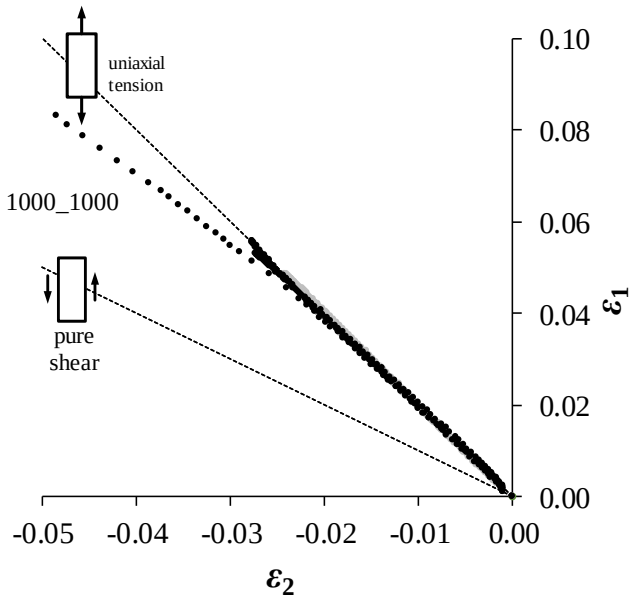

(b)

Figure 8.15 – True stress-strain curves (a) and strain path evolution (b) in TMAZ.

Table 8.3 – *Swift* equation parameters

weld	k		n		σ_{uts}	
	HAZ	TMAZ	HAZ	TMAZ	HAZ	TMAZ
500_200	480.4	540.9	0.253	0.269	337.4	382.1
1000_200	392.0	507.2	0.207	0.229	282.9	361.9
1000_1000	485.0	576.4	0.237	0.220	344.7	413.1

In Figure 8.17 are show the same type of results plotted in the previous figure, but now for the 1000_1000 and 1000_200 welds. In the graph of Figure 8.17 b) it is possible to see that the strain path, for the TMAZ and HAZ, are similar for both welds, obeying to the same characteristics already reported when analysing Figure 8.16. However, comparing the local curves relative to the TMAZ, unlike that registered in the previous figure, it is possible to depict strong differences in tensile strength for both welds. According to the graph, the tensile strength of the 1000_1000 TMAZ is of the same order of magnitude of that of base material. On the other hand, the 1000_200 TMAZ displays under-matched characteristics, relative to the base material, in both yield and tensile strength. Actually, the stress-strain curve for the 1000_200 TMAZ is very similar to that of the 1000_1000 HAZ, for which similar hardness values were registered in Figure 8.13. Finally, for the 1000_200 HAZ, which according to Figure 8.13 had the lower hardness values, were also registered the lower values of yield and tensile strength of all the weld parts.

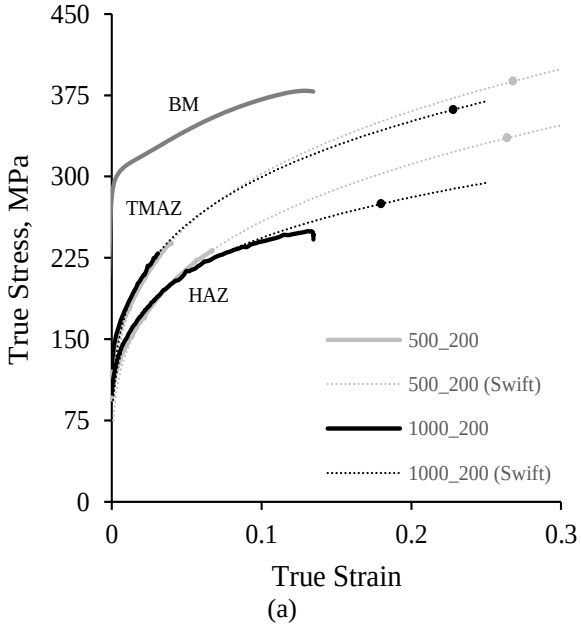

(a)

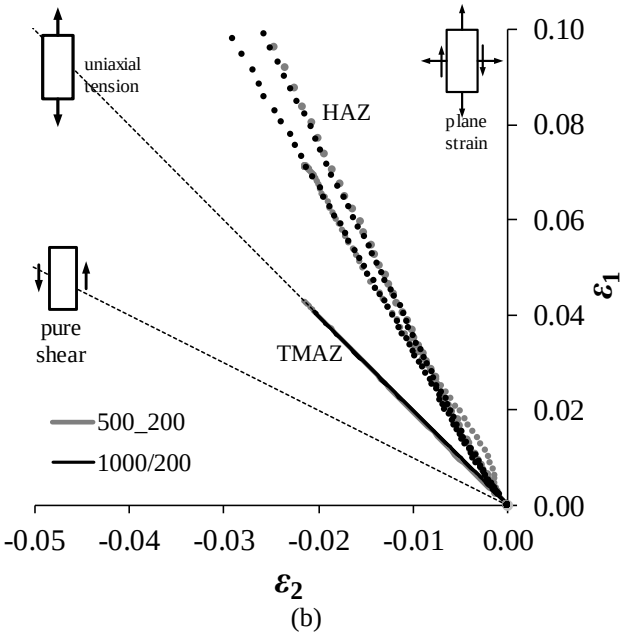

(b)

Figure 8.16 – Local true strain-stress curves (a) and strain paths (b) for the 500_200 and 1000_200 welds.

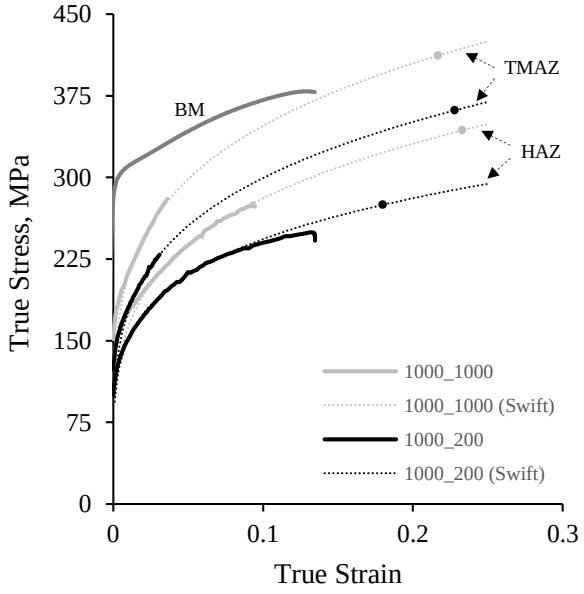

(a)

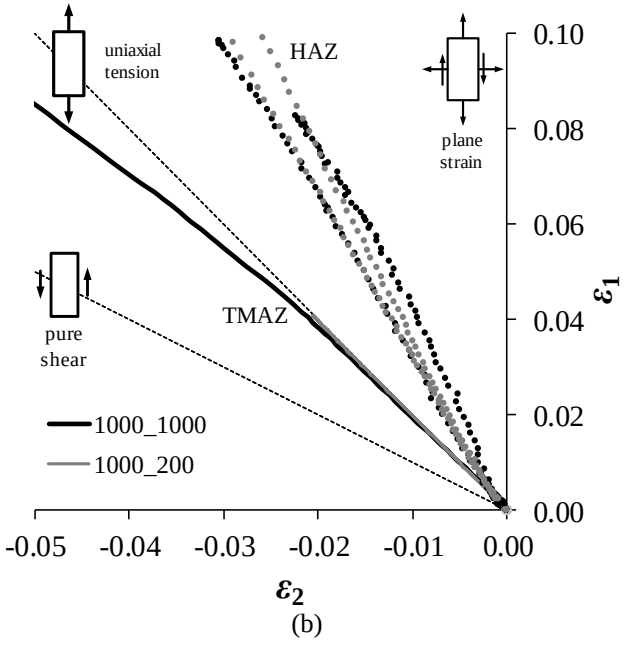

(b)

Figure 8.17 – Local true strain-stress curves (a) and strain paths (b) for the 1000_200 and 1000_1000 welds.

Global strength analysis

In Table 4.10 and Table 4.11 are summarized the welding conditions used for producing the specific set of welds analysed in this chapter section, i.e., the welds classified as GOOD in Chapter 4. The mechanical efficiency of the welds was analysed by calculating the yield (η_{ys}) and the tensile strength coefficients (η_{uts}), defined as the ratio between the yield or tensile strength of transverse weld samples (considering a 50 mm gauge length) and the same properties of the parent materials. An elongation coefficient (η_e), which is the ratio between the elongation of the weld samples and base materials at maximum load, was also calculated. The results obtained for the AA5083 and AA6082 welds are summarised in Figure 8.18 and in Figure 8.19, respectively. As shown in Figure 8.18, the 5_6 and 5_4 welds were almost in yield and tensile strength even-match ($\eta_{ys} \cong 1$ and $\eta_{uts} \cong 1$) relative to the parent plates, except in two situations where the welds had very small defects. However, even for these small defect welds the tensile strength efficiency was almost 85%. Despite the good strength of the welds, its elongation is lower than that of the base plates, never exceeding 80% efficiency and falling to 35% for the small defect welds. This behaviour is a result of slight overmatch conditions of weld material relative to base material, as exemplified in Figure 8.20.

Table 8.4 – Tool parameters

		D_s (mm)		D_p (mm)		α (º)		
AA5083	4mm	15		4	5	2		3
	6 mm	18	21	6	7	2		3
AA6082	3 mm	12	15	5	6	1	2	3
	6 mm	18	21	6	7	1	2	3

Table 8.5– Process parameters

		v (mm/min)			ω (rpm)			F_z (kN)		
AA5083	4mm	300		400	500		600	15		
	6 mm	200		275	400		500	15		20
AA6082	3 mm	800	950	1100	1000	1150	1300	5		7
	6 mm	200	275	350	400		500	10	15	20

In Figure 8.20 is shown the local tensile stress–strain curves, obtained by DIC, according to the procedure explained in Chapter 3, for the welds and parent plates, in tensile tests of 5_4 and 5_6 transverse samples, and the hardness profiles across the same welds (it is important to point out that in order to plot the two different types of results on the same graph, the logarithmic strain values were multiplied by 100 as indicated above the *x* axis). The images in the left of the figure also shows the longitudinal strain distribution, after maximum load, for both samples. It is possible to see that necking occurred in the base material, for the 5_6 sample, and in the weld, for the 5_4 sample, which actually corresponded to a small defect sample. The two welds were deformed but to a lower extent than the base material, which led to lower global elongation levels for the transverse welded samples, even for the non-defective welds. The stress–strain curves of the welds and their hardness profiles confirm the slight overmatch behaviour of the welds. It is important to highlight that very similar mechanical performance was registered for all the GOOD welds although they were obtained using different process parameters.

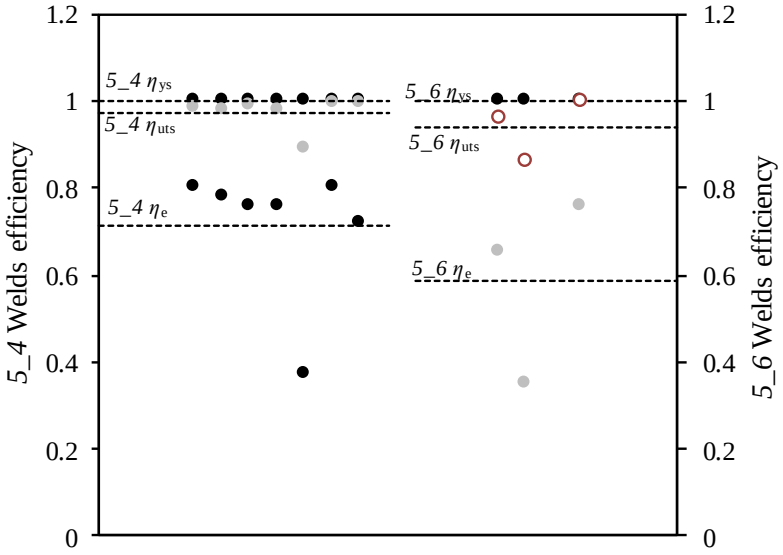

Figure 8.18 - Mechanical efficiencies for 5_6 and 5_4 welds.

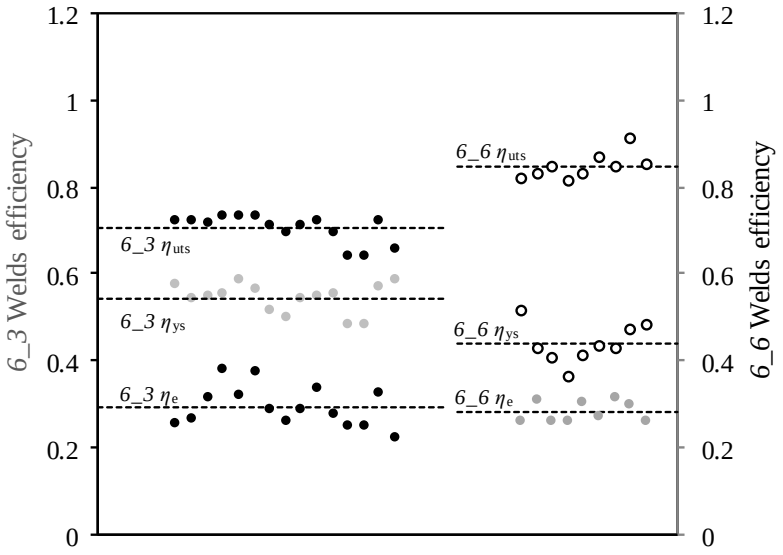

Figure 8.19 - Mechanical efficiencies for 6_6 and 6_3 welds.

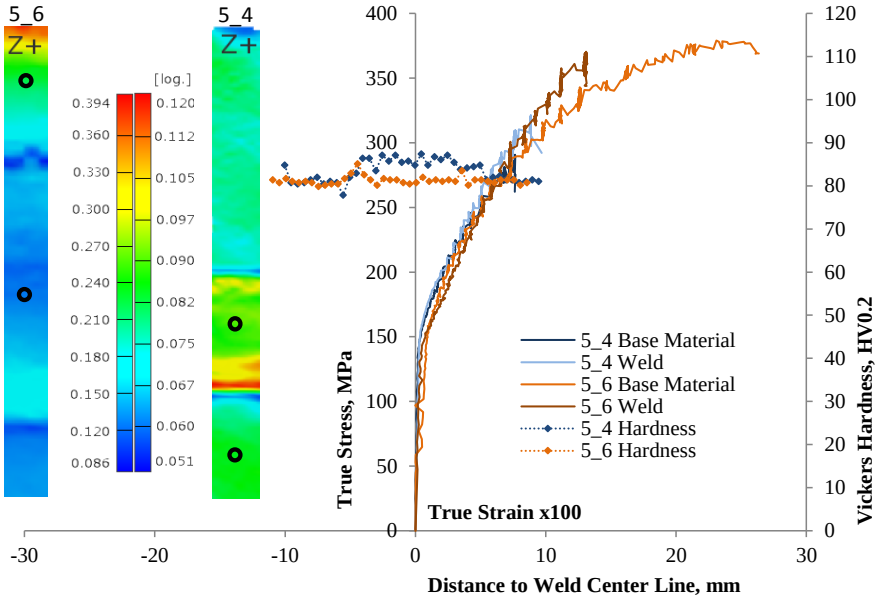

Figure 8.20 - Hardness and tensile test results for 5_4 (ω=600 rpm, v=400 mm/min, D_s=18 mm, F_z=15 kN) and 5_6 (ω=500 rpm, v=250 mm/min, D_s=21 mm, F_z=20 kN) weld samples: small circles in sample images indicate location of points for which stress–strain curves were plotted. (Annex D)

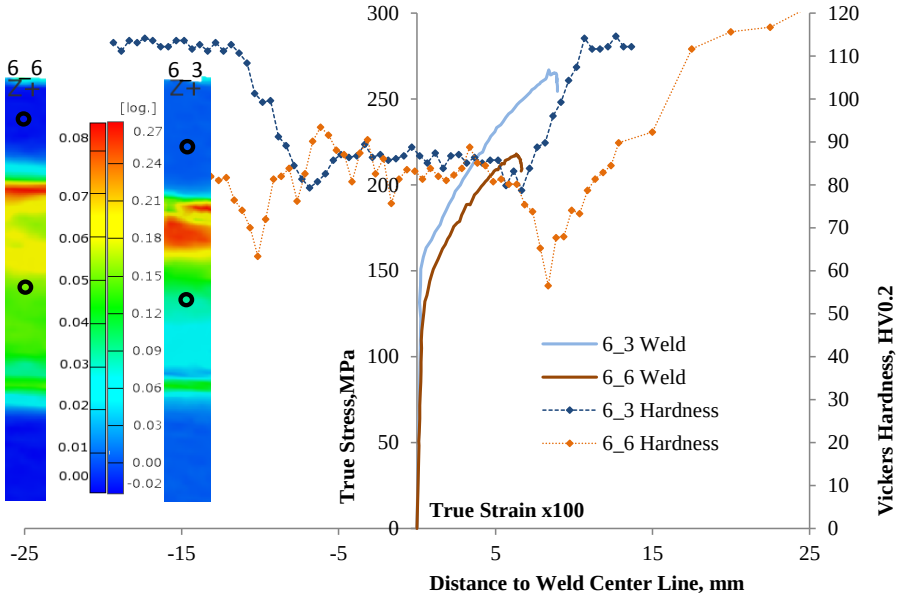

Figure 8.21 – Hardness and tensile test results for 6_3 (ω=1300 rpm, v=1100 mm/min, D_s=15 mm, F_z=5kN) and 6_6 (w=400 rpm, v=200 mm/min, D_s=18 mm, F_z=15 kN) welds. The small circles in the sample images indicate the location of the points for which the stress-strain curves were plotted. (Annex D)

Analysisng now the mechanical efficiency results for the AA6082 alloy, plotted in Figure 8.19, it is possible to conclude that all the 6_3 and 6_6 welds were in undermatch relative to the base material since the weld efficiency was always lower than 1. However, although a slightly lower yield stress undermatch was registered for the 6_6 welds (averaging 60%) than for the 6_3 welds (averaging 50%), the 6_6 welds displayed slightly higher tensile strengths. The average elongation efficiency is similar for both weld types, averaging 30%. These results can be understood by analysing the curves in Figure 8.21, where the same type of results of Figure 8.20, are plotted for the 6_3 and 6_6 welds. From the graph it is possible to see that both tensile samples failed in the weld, where the material is in undermatch condition relative to the base material, as confirmed by the low hardness values registered in the welds. Significantly, in the HAZ, the 6_6 weld exhibits lower hardness values than the 6_3 weld, which led to lower yield stress efficiencies for these welds. Since the maximum load was attained in the welds without plastic deformation of the base material, the corresponding tensile stress–strain curves are not presented in Figure 8.21. It is also important to note that the 6_3 curve indicates greater strength than that of the 6_6 weld, which is in disagreement with the results shown in Figure 8.19. Since the tensile tests (results in Figure 8.21) were performed several months after the tests used to calculate the mechanical efficiency, it is reasonable to assume that natural age hardening of the weld material occurred.

Final comment

From this chapter, it was possible to conclude that, for the AA5083 alloy, the mechanical properties of the non-defective welds are relatively independent of the welding conditions, even for higher levels of deformation. On the other hand, for the AA6082 alloy, the increasing of the welding speed showed to be very effective in avoiding extra softening in the HAZ, with positive consequences in weld yield strength efficiency. However, the welds performed using this alloy, were always undermatched, relatively to the base material mechanical strength.

In spite of this, the AA5083 welds presented optimal weld speeds much lower comparatively to those allowed for the AA6082 welds. However, contrarily to the AA6082 welds, the AA5083 alloy allowed the production of welds without any loss in mechanical properties.

9
Outputs and future research

In this last chapter are stressed the main remarks from the previous chapters of this thesis.

This Page Intentionally Left Blank

Outputs

As it is well known, the research on Friction Stir Welding process, in order to fully understand the welding mechanisms involved remains up-to-date. Particularly, the very important influence of base material plastic properties on friction stir weldability, depicted in this work, was never addressed before in FSW literature, which traditionally relates material flow during welding, as well as welds morphology and defects, with tool geometry and/or processing conditions.

The main conclusions of this work, which comprised the production of friction stir welds, using several welding parameters and using two aluminium alloys (AA5083-H111 and AA6082-T6), are:

- The AA6082 alloy, which displays intense flow softening during tensile loading at high temperatures, and is sensitive to dynamic precipitation and overageing under intense non-uniform deformation, displays good weldability in FSW. Under the same welding conditions, the AA5083 alloy, which in quasi-static conditions displays steady flow behaviour at increasing temperatures, and is sensitive to moderate hardening at high strain rates, displays poor weldability.

- For constant tool parameters and axial load, the evolution of torque with tool traverse and rotation speed was found to be independent from both factors, being described by a unique power law equation. Modelling of torque results enabled to conclude that meanwhile the tool rotation speed and plate's thickness are the main factors in determining torque values, due to its strong influence on heat generation and

through thickness heat distribution and material flow, the welding speed had no strong influence on average torque levels. Base material plastic properties also have a strong, but indirect, impact on torque results. Torque results were also found to be very sensitive to varying axial load, mainly in thicker plates welding, due to the above-mentioned reasons. No influence of varying shoulder diameter on torque results was reported. Analysing the torque evolution for a wide range of parameters, it was possible to conclude that, in non-defective welding conditions, the evolution of torque with tool traverse and rotation speeds is independent of base material properties, being satisfactorily described by a power law equation.

- It was possible to conclude that, for the AA5083 alloy, the mechanical properties of the non-defective welds are relatively independent of the welding conditions, even for higher levels of deformation. On the other hand, for the AA6082 alloy, the increasing of the welding speed showed to be very effective in avoiding extra softening in the HAZ, with positive consequences in weld yield strength efficiency. However, the welds performed using this alloy, were always undermatched, relatively to the base material mechanical strength.

Future research

The conclusions obtained from this work allowed a complete understanding on the influence of AA5083-H111 and AA6082-T6 base materials plastic behaviour, at high temperatures and strain rates, on weldability in Friction Stir

Welding (FSW). However, a wider understanding of this subject would require a coupled experimental and numerical analysis, using the numerical simulation to cover the widest possible number of material properties and welding conditions. Developing a 3D thermo-mechanical model enabling to run an extensive parametric analysis would be very important as a future research. Actually, the numerical approach would allow the analysis of the plastic behaviour of the base materials, under loading conditions closer to that experienced during FSW, which, as is well-known, is not possible by using conventional mechanical tests. Complementarily, an accurate calibration of the thermo-mechanical model, using experimental results, such as the experimental data as well as the welding results obtained in current work.

Bibliography

Amancio-Filho, S.T., Sheikhi, S., dos Santos, J.F. and Bolfarini, C. (2008). "Preliminary study on the microstructure and mechanical properties of dissimilar friction stir welds in aircraft aluminium alloys 2024-T351 and 6056-T4." Journal of Materials Processing Technology 206(1-3): 132-142.

Alvarez, P., Janeiro, G., da Silva, A.A.M., Aldanondo, E. and Echeverria, A. (2010). "Material flow and mixing patterns during dissimilar FSW." Science and Technology of Welding and Joining 15(8): 648-653.

Aonuma, M. and Nakata, K. (2009). "Effect of alloying elements on interface microstructure of Mg-Al-Zn magnesium alloys and titanium joint by friction stir welding." Materials Science and Engineering B-Advanced Functional Solid-State Materials 161(1-3): 46-49.

Arbegast, W.J. (2007). Friction stir welding: after a decade of development.

Arbegast, W.J. (2008). "A flow-partitioned deformation zone model for defect formation during friction stir welding." Scripta Materialia 58(5): 372-376.

Arora, A., DebRoy, T. and Bhadeshia, H.K.D.H. (2011). "Back-of-the-envelope calculations in friction stir welding - Velocities, peak temperature, torque, and hardness." Acta Materialia 59(5): 2020-2028.

Arora, A., Nandan, R., Reynolds, A.P. and DebRoy, T. (2009). "Torque, power requirement and stir zone geometry in friction stir welding through modeling and experiments." Scripta Materialia 60(1): 13-16.

Ashby, M.F. and Jones, D.H.R. (1998). Engineering Materials 2: An Introduction to Microstructures, Processing and Design.

Assidi, M., Fourment, L., Guerdoux, S. and Nelson, T. (2010). "Friction model for friction stir welding process simulation: Calibrations from welding experiments." International Journal of Machine Tools & Manufacture 50(2): 143-155.

ASM International (1995). Aluminium - Properties and Physical mettalurgy, ASM-International.

ASM International (1987). Fractography, ASM-International.

ASTM (1996). E112-96 Standard Test Methods for Determining Average Grain Size.

ASTM (1999). E384-99 Standard Test Method for Microindentation Hardness of Materials.

ASTM (2003). E21-03a Standard Test Methods for Elevated Temperature Tension Tests of Metallic Materials.

ASTM (2004). E8M-04 Standard Test Methods for Tension Testing of Metallic Materials [Metric].

Balasubramanian, V. (2008). "Relationship between base metal properties and friction stir welding process parameters." Materials Science and Engineering A - Structural Materials Properties Microstructure and Processing 480(1-2): 397-403.

Bang, K.-S., Lee, K.-J., Bang, H.-S. and Bang, H.-S. (2011). "Interfacial Microstructure and Mechanical Properties of Dissimilar Friction Stir Welds between 6061-T6 Aluminum and Ti-6%Al-4%V Alloys." Materials Transactions 52(5): 974-978.

Benavides, S., Li, Y., Murr, L.E., Brown, D. and McClure, J.C. (1999). "Low-temperature friction-stir welding of 2024 aluminum." Scripta Materialia 41(8): 809-815.

Benedyk, J.C. (2010). International Temper Designation Systems for Wrought Aluminium alloys: PartII - Thermally Treated (T Temper) Aluminium alloys. Light Metal age.

Bouvier, S., Gardey, B., Haddadi, H. and Teodosiu, C. (2006). "Characterization of the strain-induced plastic anisotropy of rolled sheets by using sequences of simple shear and uniaxial tensile tests." Journal of Materials Processing Technology 174(1-3): 115-126.

Bouvier, S., Haddadi, H., Levee, P. and Teodosiu, C. (2006). "Simple shear tests: Experimental techniques and characterization of the plastic anisotropy of rolled sheets at large strains." Journal of Materials Processing Technology 172(1): 96-103.

Cabibbo, M., McQueen, H.J., Evangelista, E., Spigarelli, S., Di Paola, M. and Falchero, A. (2007). "Microstructure and mechanical property studies of AA6056 friction stir welded plate." Materials Science and Engineering a-Structural Materials Properties Microstructure and Processing 460: 86-94.

Çam, G. (2011). "Friction stir welded structural materials: beyond Al-alloys." International Materials Reviews 56(1): 1-48.

Cavaliere, P., Nobile, R., Panella, F.W. and Squillace, A. (2006). "Mechanical and microstructural behaviour of 2024-7075 aluminium alloy sheets joined by friction stir welding." International Journal of Machine Tools & Manufacture 46(6): 588-594.

Cavaliere, P., Squillace, A. and Panella, F. (2008). "Effect of welding parameters on mechanical and microstructural properties of AA6082 joints produced by friction stir welding." Journal of Materials Processing Technology 200(1-3): 364-372.

Cerri, E., Evangelista, E. and Ryum, N. (1997). "On the effect of plastic deformation on the coarsening of theta-phase precipitation in an Al-Cu alloy." Metallurgical and Materials Transactions a-Physical Metallurgy and Materials Science 28(2): 257-263.

Chao, Y. J. and Qi, X. (1998). "Thermal and thermo-mechanical modeling of friction stir welding of aluminum alloy 6061-T6." Journal of materials processing and manufacturing science 7: 215-233.

Chaparro, B.M., Thuillier, S., Menezes, L.F., Manach, P.Y. and Fernandes, J.V. (2008). "Material parameters identification: Gradient-based, genetic and hybrid optimization algorithms." Computational Materials Science 44(2): 339-346.

Chen, H.-B., Yan, K., Lin, T., Chen, S.-B., Jiang, C.-Y. and Zhao, Y. (2006). "The investigation of typical welding defects for 5456 aluminum alloy friction stir welds." Materials Science and Engineering A - Structural Materials Properties Microstructure and Processing 433(1-2): 64-69.

Chen, Z.W. and Cui, S. (2008). "On the forming mechanism of banded structures in aluminium alloy friction stir welds." Scripta Materialia 58(5): 417-420.

Chen, Z.W., Pasang, T. and Qi, Y. (2008). "Shear flow and formation of Nugget zone during friction stir welding of aluminium alloy 5083-O." Materials Science and Engineering: A 474(1–2): 312-316.

Chen, T. (2009). "Process parameters study on FSW joint of dissimilar metals for aluminum-steel." Journal of Materials Science 44(10): 2573-2580.

Chen, T.P. and Lin, W.B. (2010). "Optimal FSW process parameters for interface and welded zone toughness of dissimilar aluminium-steel joint." Science and Technology of Welding and Joining 15(4): 279-285.

Cheng, C.P., Lin, H.M. and Lin, J.C. (2010). "Friction stir welding of ductile iron and low carbon steel." Science and Technology of Welding and Joining 15(8): 706-711.

Choi, D.H., Ahn, B.W., Yeon, Y.M., Park, S.H.C., Sato, Y.S., Kokawa, H. and Jung, S.B. (2011). "Microstructural Characterizations Following Friction Stir Welding of Dissimilar Alloys of Low- and High-Carbon Steels." Materials Transactions 52(7): 1500-1505.

Ciliberto, S., Astarita, A. and Squillace, A. (2013). "FSW of T joints in overlap configuration: process optimization in joining dissimilar aluminium

alloys for the aeronautic application." Surface and Interface Analysis 45(10): 1631-1637.

Coelho, R.S., Kostka, dos Santos, J.F. and Kaysser-Pyzalla, A. (2012). "Friction-stir dissimilar welding of aluminium alloy to high strength steels: Mechanical properties and their relation to microstructure." Materials Science and Engineering A - Structural Materials Properties Microstructure and Processing 556: 175-183.

Colegrove, P.A. and Shercliff, H.R. (2006). "CFD modelling of friction stir welding of thick plate 7449 aluminium alloy." Science and Technology of Welding and Joining 11(4): 429-441.

Colegrove, P. A., Shercliff, H. R. and Zettler, R. (2007). "Model for predicting heat generation and temperature in friction stir welding from the material properties." Science and Technology of Welding and Joining 12(4): 284-297.

Dong, H.-H., Liu, J.-H., Du, H.-B. and Wu, X.-X. (2003). "Numerical simulation research&development on welding stresses, strains and distortion." Electric Welding Machine 9: 005.

Dehghani, K. and Chabok, A. (2011). "Dependence of Zener parameter on the nanograins formed during friction stir processing of interstitial free steels (vol 528, pg 4235, 2011)." Materials Science and Engineering A - Structural Materials Properties Microstructure and Processing 528(21): 6652-6652.

Eberl, I., Hantrais, C., Ehrtsrom, J.C. and Nardin, C. (2010). "Friction stir welding dissimilar alloys for tailoring properties of aerospace parts." Science and Technology of Welding and Joining 15(8): 699-705.

Edwards, P.D. and Ramulu, M. (2009). "Investigation of microstructure, surface and subsurface characteristics in titanium alloy friction stir welds of varied thicknesses." Science and Technology of Welding and Joining 14(5): 476-483.

Elangovan, K. and Balasubramanian, V. (2008). "Influences of tool pin profile and tool shoulder diameter on the formation of friction stir processing zone in AA6061 aluminium alloy." Materials & Design 29(2): 362-373.

Esmaeili, A., Givi, M.K.B. and Rajani, H.R.Z. (2012). "Experimental Investigation of Material Flow and Welding Defects in Friction Stir Welding of Aluminum to Brass." Materials and Manufacturing Processes 27(12): 1402-1408.

Etter, A.L., Baudin, T., Fredj, N. and Penelle, R. (2007). "Recrystallization mechanisms in 5251 H14 and 5251 O aluminum friction stir welds." Materials Science and Engineering A - Structural Materials Properties Microstructure and Processing 445: 94-99.

Ferreira, T. and Rasband, W. (2012). ImageJ User Guide.

Firouzdor, V. and Kou, S. (2009). "Al-to-Mg Friction Stir Welding: Effect of Positions of Al and Mg with Respect to the Welding Tool." Welding Journal 88(11): 213S-224S.

Firouzdor, V. and Kou, S. (2010). "Al-to-Mg Friction Stir Welding: Effect of Material Position, Travel Speed, and Rotation Speed." Metallurgical and Materials Transactions a-Physical Metallurgy and Materials Science 41A(11): 2914-2935.

Firouzdor, V. and Kou, S.D. (2012). "Al-to-Cu Friction Stir Lap Welding." Metallurgical and Materials Transactions a-Physical Metallurgy and Materials Science 43A(1): 303-315.

Flores, O.V., Kennedy, C., Murr, L.E., Brown, D., Pappu, S., Nowak, B.M. and McClure, J.C. (1998). "Microstructural issues in a friction-stir-welded aluminium alloy." Scripta Materialia 38(5): 703-708.

Fratini, L., Buffa, G., Filice, L. and Gagliardi, F. (2006). "Friction stir welding of AA6082-T6 T-joints: process engineering and performance measurement." Proceedings of the Institution of Mechanical Engineers Part B-Journal of Engineering Manufacture 220(5): 669-676.

Galvao, I., Leal, R.M., Loureiro, A. and Rodrigues, D.M. (2010). "Material flow in heterogeneous friction stir welding of aluminium and copper thin sheets." Science and Technology of Welding and Joining 15(8): 654-660.

Galvao, I., Leal, R.M., Rodrigues, D.M. and Loureiro, A. (2013). "Influence of tool shoulder geometry on properties of friction stir welds in thin copper sheets." Journal of Materials Processing Technology 213(2): 129-135.

GOM, mbH. (2009). Aramis - User Manual: Software Braunschweig, Germany.

Gould, J.E. and Feng, Z.L. (1998). "Heat flow model for friction stir welding of aluminum alloys." Journal of Materials Processing & Manufacturing Science 7(2): 185-194.

Gsell, C., Boni, S. and Shrivastava, S. (1983). "Application of the plane simple shear test for determination of the plastic behaviour of solid polymers at large strains." Journal of Materials Science 18(3): 903-918.

Guerra, A., Schmidt, C., McClure, J.C., Murr, L.E. and Nunes, A.C. (2002). "Flow patterns during friction stir welding." Materials Characterization 49(2): 95-101.

Guo, J., Gougeon, P. and Chen, X.G. (2012). "Microstructure evolution and mechanical properties of dissimilar friction stir welded joints between AA1100-B4C MMC and AA6063 alloy." Materials Science and Engineering A - Structural Materials Properties Microstructure and Processing 553: 149-156.

Hassan, K.A.A., Norman, A.F., Price, D.A. and Prangnell, P.B. (2003). "Stability of nugget zone grain structures in high strength Al-alloy friction stir welds during solution treatment." Acta Materialia 51(7): 1923-1936.

Heinz, B. and Skrotzki, B. (2002). "Characterization of a friction-stir-welded aluminum alloy 6013." Metallurgical and Materials Transactions

B-Process Metallurgy and Materials Processing Science 33(3): 489-498.

Huang, Y.X., Han, B., Tian, Y., Liu, H.J., Lv, S.X., Feng, J.C., Leng, J.S. and Li, Y. (2011). "New technique of filling friction stir welding." Science and Technology of Welding and Joining 16(6): 497-501.

Hwang, Y.-M., Kang, Z.-W., Chiou, Y.-C. and Hsu, H.-H. (2008). "Experimental study on temperature distributions within the workpiece during friction stir welding of aluminum alloys." International Journal of Machine Tools and Manufacture 48(7-8): 778-787.

Iordachescu, M., Iordachescu, D., Ocana, J.L., Vilaça, P. and Scutelnicu, E. (2009). "FSW - Characteristic flaws in aluminium alloys joints." Metalurgia International 14: 135-138.

Jamshidi Aval, H., Serajzadeh, S. and Kokabi, A.H. (2011). "Evolution of microstructures and mechanical properties in similar and dissimilar friction stir welding of AA5086 and AA6061." Materials Science and Engineering: A 528(28): 8071-8083.

Jana, S., Hovanski, Y. and Grant, G.J. (2010). "Friction Stir Lap Welding of Magnesium Alloy to Steel: A Preliminary Investigation." Metallurgical and Materials Transactions a-Physical Metallurgy and Materials Science 41A(12): 3173-3182.

Jata, K.V. (2000). Friction stir welding of high strength aluminum alloys. Aluminium Alloys: Their Physical and Mechanical Properties, Pts 1-3. Starke, E.A., Sanders, T.H. and Cassada, W.A. 331-3: 1701-1712.

Jin, H., Ko, C., Saimoto, S. and Threadgill, P.L. (2000). Microstructure of friction stir welded joints in AA5182. Aluminium Alloys: Their Physical and Mechanical Properties, Pts 1-3. Starke, E.A., Sanders, T.H. and Cassada, W.A. 331-3: 1725-1730.

Khandkar, M.Z.H., Khan, J.A. and Reynolds A.P. (2003). "Prediction of temperature distribution and thermal history during friction stir

welding: input torque based model." Science and Technology of Welding and Joining 8(3): 165-174.

Kim, Y.G., Fujii, H., Tsumura, T., Komazaki, T. and Nakata, K. (2006). "Three defect types in friction stir welding of aluminum die casting alloy." Materials Science and Engineering A - Structural Materials Properties Microstructure and Processing 415(1-2): 250-254.

Krishnan, K.N. (2002). "On the formation of onion rings in friction stir welds." Materials Science and Engineering A - Structural Materials Properties Microstructure and Processing 327(2): 246-251.

Kumar, K. and Kailas, S.V. (2008). "On the role of axial load and the effect of interface position on the tensile strength of a friction stir welded aluminium alloy." Materials & Design 29(4): 791-797.

Kumar, K. and Kailas, S.V. (2008). "The role of friction stir welding tool on material flow and weld formation." Materials Science and Engineering A - Structural Materials Properties Microstructure and Processing 485(1-2): 367-374.

Kumar, K., Kailas, S.V. and Srivatsan, T.S. (2008). "Influence of tool geometry in friction stir welding." Materials and Manufacturing Processes 23(2): 189-195.

Kumar, K. and Kailas, S. V. (2010). "Positional dependence of material flow in friction stir welding: analysis of joint line remnant and its relevance to dissimilar metal welding." Science and Technology of Welding and Joining 15(4): 305-311.

Kumar, R., Singh, K. and Pandey, S. (2012). "Process forces and heat input as function of process parameters in AA5083 friction stir welds." Transactions of Nonferrous Metals Society of China 22(2): 288-298.

Kwon, Y.-J., Shim, S.-B. and Park, D.-H. (2009). "Friction stir welding of 5052 aluminum alloy plates." Transactions of Nonferrous Metals Society of China 19, Supplement 1(0): s23-s27.

Leal, R.M., Chaparro, B.M., Antunes, J.M., Vilaça, P., Rodrigues, D.M. and Loureiro, A. (2008). Mechanical Behaviour of FSW Aluminium Tailored Blanks. Advanced Materials Forum Iv. Marques, A.T., Silva, A.F., Baptista, A.P.M. et al. 587-588: 961-965.

Leal, R.M., Leitao, C., Loureiro, A., Rodrigues, D.M. and Vilaça, P. (2008). "Material flow in heterogeneous friction stir welding of thin aluminium sheets: Effect of shoulder geometry." Materials Science and Engineering A - Structural Materials Properties Microstructure and Processing 498(1-2): 384-391.

Leal, R.M. (2011). Soldadura por Fricção Linear de Elementos de baixa espessura. PhD, University of Coimbra.

Lee, W.-B., Schmuecker, M., Mercardo, U.A., Biallas, G. and Jung, S.-B. (2006). "Interfacial reaction in steel-aluminum joints made by friction stir welding." Scripta Materialia 55(4): 355-358.

Lee, W.B., Yeon, Y.M. and Jung, S.B. (2003). "Evaluation of the microstructure and mechanical properties of friction stir welded 6005 aluminum alloy." Materials Science and Technology 19(11): 1513-1518.

Lee, W.B. and Jung, S.B. (2004). "Void free friction stir weld zone of the dissimilar 6061 aluminum and copper joint by shifting the tool insertion location." Materials Research Innovations 8(2): 93-96.

Leitao, C., Leal, R.M., Rodrigues, D.M., Loureiro, A. and Vilaça, P. (2009). "Mechanical behaviour of similar and dissimilar AA5182-H111 and AA6016-T4 thin friction stir welds." Materials & Design 30(1): 101-108.

Leonard, A.J. and Lockyer, S.A. (2003). Flaws in Friction Stir Welding. 4th Symposium on friction stir welding, Park City, Utah, USA.

Li, W., Zhang, Z., Li, J. and Chao, Y.J. (2012). "Numerical Analysis of Joint Temperature Evolution During Friction Stir Welding Based on Sticking Contact." Journal of Materials Engineering and Performance 21(9): 1849-1856.

Li, Y., Murr, L.E. and McClure, J.C. (1999). "Flow visualization and residual microstructures associated with the friction-stir welding of 2024 aluminum to 6061 aluminum." Materials Science and Engineering A - Structural Materials Properties Microstructure and Processing 271(1-2): 213-223.

Li, Y., Murr, L.E. and McClure, J.C. (1999). "Solid-state flow visualization in the friction-stir welding of 2024 Al to 6061 Al." Scripta Materialia 40(9): 1041-1046.

Liang, Z. Y., K. Chen, X. N. Wang, J. S. Yao, Q. Yang, L. T. Zhang and A. D. Shan (2013). "Effect of Tool Offset and Tool Rotational Speed on Enhancing Mechanical Property of Al/Mg Dissimilar FSW Joints." Metallurgical and Materials Transactions a-Physical Metallurgy and Materials Science 44A(8): 3721-3731.

Lim, S., Kim, S., Lee, C.G. and Kim, S. (2004). "Tensile behavior of friction-stir-welded Al 6061 T651." Metallurgical and Materials Transactions a-Physical Metallurgy and Materials Science 35A(9): 2829-2835.

Lim, S., Kim, S., Lee, C.G. and Kim, S.J. (2005). "Mechanical properties of friction stir welded Al alloys with different hardening mechanisms." Metals and Materials International 11(2): 113-120.

Liu, G., Murr, L.E., Niou, C.S., McClure, J.C. and Vega, F.R. (1997). "Microstructural aspects of the friction-stir welding of 6061-T6 aluminum." Scripta Materialia 37(3): 355-361.

Liu, F.C. and Ma, Z.Y. (2008). "Influence of tool dimension and welding parameters on microstructure and mechanical properties of friction-stir-welded 6061-T651 aluminum alloy." Metallurgical and Materials Transactions a-Physical Metallurgy and Materials Science 39A(10): 2378-2388.

Liu, P., Shi, Q.Y., Wang, W., Wang, X. and Zhang, Z.L. (2008). "Microstructure and XRD analysis of FSW joints for copper T2/aluminium 5A06 dissimilar materials." Materials Letters 62(25): 4106-4108.

Long, T., Tang, W. and Reynolds, A.P. (2007). "Process response parameter relationships in aluminium alloy friction stir welds." Science and Technology of Welding and Joining 12(4): 311-317.

Longhurst, W.R., Strauss, A.M., Cook, G.E., Cox, C.D., Hendricks, C.E., Gibson, B.T. and Dawant, Y.S. (2010). "Investigation of force-controlled friction stir welding for manufacturing and automation." Proceedings of the Institution of Mechanical Engineers Part B-Journal of Engineering Manufacture 224(B6): 937-949.

Louro, R., Gouveia, H. and Brioso, P. (2008). Effect of Tool Geometry in the Friction Stir Welding of AA6082-T651. Advanced Materials Forum IV. Marques, A.T., Silva, A.F., Baptista, A.P.M. et al. 587-588: 976-980.

Louro, R., Leitao, C., Gouveia, H., Loureiro, A. and Rodrigues, D. (2010). Taguchi Analysis of the Effect of Process Parameters in Friction Stir Welding. Advanced Materials Forum V. Rosa. L.G. and Margarido, F., 636-637: 1150-1156.

Mahoney, M.W., Rhodes, C.G., Flintoff, J.G., Spurling, R.A. and Bingel, W.H. (1998). "Properties of friction-stir-welded 7075 T651 aluminum." Metallurgical and Materials Transactions a-Physical Metallurgy and Materials Science 29(7): 1955-1964.

Miles, M.P., Decker, B.J. and Nelson, T.W. (2004). "Formability and strength of friction-stir-welded aluminum sheets." Metallurgical and Materials Transactions a-Physical Metallurgy and Materials Science 35A(11): 3461-3468.

Miles, M. P., Melton, D.W. and Nelson, T.W. (2005). "Formability of friction-stir-welded dissimilar-aluminum-alloy sheets." Metallurgical and Materials Transactions a-Physical Metallurgy and Materials Science 36A(12): 3335-3342.

Mishra, R.S. and Ma, Z.Y. (2005). "Friction stir welding and processing." Materials Science & Engineering R-Reports 50(1-2): 1-78.

Mishra, R.S. and Mahoney, M.W. (2007). Friction Stir Welding and Processing, ASM International.

Mononen, J., Sirén, M. and Hänninen, H. (2003). "Cost comparison of FSW and MIG welded aluminium panels." Welding in the World 47: 32-35.

Morishige, T., Kawaguchi, A., Tsujikawa, M., Hino, M., Hirata, T. and Higashi, K. (2008). "Dissimilar welding of Al and Mg alloys by FSW." Materials Transactions 49(5): 1129-1131.

Murr, L.E., Liu, G. and McClure, J.C. (1997). "Dynamic recrystallization in friction-stir welding of aluminium alloy 1100." Journal of Materials Science Letters 16(22): 1801-1803.

Murr, L.E., Li, Y., Trillo, E.A., Flores, R.D. and McClure, J.C. (1998). "Microstructures in friction-stir welded metals." Journal of Materials Processing & Manufacturing Science 7(2): 145-161.

Murr, L.E. (2010). "A Review of FSW Research on Dissimilar Metal and Alloy Systems." Journal of Materials Engineering and Performance 19(8): 1071-1089.

Muthukumaran, S. and Mukherjee, S.K. (2006). "Two modes of metal flow phenomenon in friction stir welding process." Science and Technology of Welding and Joining 11(3): 337-340.

Muthukumaran, S. and Mukherjee, S.K. (2008). "Multi-layered metal flow and formation of onion rings in friction stir welds." International Journal of Advanced Manufacturing Technology 38(1-2): 68-73.

Nandan, R., Roy, G. and Debroy, T. (2006). "Numerical simulation of three-dimensional heat transfer and plastic flow during friction stir welding." Metallurgical and Materials Transactions A 37(4): 1247-1259.

Nandan, R., Roy, G.G., Lienert, T.J. and DebRoy, T. (2006). "Numerical modelling of 3D plastic flow and heat transfer during friction stir welding of stainless steel." Science and Technology of Welding and Joining 11(5): 526-537.

Nandan, R., Prabu, B., De, A. and Debroy, T. (2007). "Improving reliability of heat transfer and materials flow calculations during friction stir welding of dissimilar aluminum alloys." Welding Journal 86(10): 313S-322S.

Nandan, R., Roy, G.G., Lienert, T.J. and Debroy, T. (2007). "Three-dimensional heat and material flow during friction stir welding of mild steel." Acta Materialia 55(3): 883-895.

Nandan, R., DebRoy, T. and Bhadeshia, H.K.D.H. (2008). "Recent advances in friction-stir welding - Process, weldment structure and properties." Progress in Materials Science 53(6): 980-1023.

NDT Resource Center. Retrieved 8 October, 2013, from http://www.ndt-ed.org/EducationResources/CommunityCollege/Materials/Structure/strengthening.htm.

Okane, M., Takami, Y., Miyagawa, K., Yasui, T. and Fukumoto, M. (2010). "Fatigue Behaviors of Aluminum Alloy/Steel Dissimilar Joint by Friction Stirring." Steel Research International 81(9): 1120-1123.

Olea, C.A.W. (2008). Influence of Energy Input in Friction Stir Welding on Structure Evolution and Mechanical Behaviour of Precipitation-Hardening in Aluminium Alloys (AA2024-T351, AA6013-T6 and Al-Mg-Sc). PhD, GKSS-Forschungszentrum Geesthacht GmbH.

Padmanaban, G. and Balasubramanian, V. (2009). "Selection of FSW tool pin profile, shoulder diameter and material for joining AZ31B magnesium alloy - An experimental approach." Materials & Design 30(7): 2647-2656.

Peel, M. J., Steuwer, A., Withers, P. J., Dickerson, T., Shi, Q. and Shercliff, H. (2006). "Dissimilar friction stir welds in AA5083-AA6082. Part I: Process parameter effects on thermal history and weld properties." Metallurgical and Materials Transactions a-Physical Metallurgy and Materials Science 37A(7): 2183-2193.

Qian, J., Li, J., Sun, F., Xiong, J., Zhang, F. and Lin, X. (2013). "An analytical model to optimize rotation speed and travel speed of friction stir welding for defect-free joints." Scripta Materialia 68(3-4): 175-178.

Rai, R., De, A., Bhadeshia, H.K.D.H. and DebRoy, T. (2011). "Review: friction stir welding tools." Science and Technology of Welding and Joining 16(4): 325-342.

Rajakumar, S., Muralidharan, C. and Balasubramanian, V. (2010). "Establishing empirical relationships to predict grain size and tensile strength of friction stir welded AA 6061-T6 aluminium alloy joints." Transactions of Nonferrous Metals Society of China 20(10): 1863-1872.

Rajakumar, S., Muralidharan, C. and Balasubramanian, V. (2010). "Optimization of the friction-stir-welding process and tool parameters to attain a maximum tensile strength of AA7075-T-6 aluminium alloy." Proceedings of the Institution of Mechanical Engineers Part B-Journal of Engineering Manufacture 224(B8): 1175-1191.

Rajakumar, S., Muralidharan, C. and Balasubramanian, V. (2011). "Influence of friction stir welding process and tool parameters on strength properties of AA7075-T-6 aluminium alloy joints." Materials & Design 32(2): 535-549.

Rajakumar, S. and Balasubramanian, V. (2012). "Establishing relationships between mechanical properties of aluminium alloys and optimised friction stir welding process parameters." Materials & Design 40: 17-35.

Rauch, E.F., Gracio, J.J., Barlat, F., Lopes, A.B. and Duarte, J.F. (2002). "Hardening behavior and structural evolution upon strain reversal of aluminum alloys." Scripta Materialia 46(12): 881-886.

Reed-Hill, R.E. (1972). Physical metallurgy principles, Van Nostrand New York.

Ren, S.R., Ma, Z.Y. and Chen, L.Q. (2007). "Effect of welding parameters on tensile properties and fracture behavior of friction stir welded Al-Mg-Si alloy." Scripta Materialia 56(1): 69-72.

Reynolds, A.P. (2008). "Flow visualization and simulation in FSW." Scripta Materialia 58(5): 338-342.

Rhodes, C.G., Mahoney, M.W., Bingel, W.H., Spurling, R.A. and Bampton, C.C. (1997). "Effects of friction stir welding on microstructure of 7075 aluminum." Scripta Materialia 36(1): 69-75.

Rodrigues, D.M., Leitao, C. and Menezes, L.F. (2010). "A multi-step analysis for determining admissible blank-holder forces in deep-drawing operations." Materials & Design 31(3): 1475-1481.

Rodrigues, D.M., Loureiro, A., Leitao, C., Leal, R.M., Chaparro, B.M. and Vilaça, P. (2009). "Influence of friction stir welding parameters on the microstructural and mechanical properties of AA 6016-T4 thin welds." Materials & Design 30(6): 1913-1921.

Russell, M. J. and Shercliff, H. (1999). "Analytical modelling of friction stir welding." Analytical modelling of friction stir welding, R Inalco 98: 197-207.

Sayer, S., Yeni, C. and Ertugrul, O. (2011). "Comparison of mechanical and microstructural behaviors of tungsten inert gas welded and friction stir welded dissimilar aluminum alloys AA 2014 and AA 5083." Kovove Materialy-Metallic Materials 49(2): 155-162.

Sato, Y.S., Kokawa, H., Enomoto, M. and Jogan, S. (1999). "Microstructural evolution of 6063 aluminum during friction-stir welding." Metallurgical and Materials Transactions a-Physical Metallurgy and Materials Science 30(9): 2429-2437.

Sato, Y.S., Kokawa, H., Enomoto, M., Jogan, S. and Hashimoto, T. (1999). "Precipitation sequence in friction stir weld of 6063 aluminum during aging." Metallurgical and Materials Transactions a-Physical Metallurgy and Materials Science 30(12): 3125-3130.

Sato, Y.S., Park, S.H.C. and Kokawa, H. (2001). "Microstructural factors governing hardness in friction-stir welds of solid-solution-hardened Al alloys." Metallurgical and Materials Transactions a-Physical Metallurgy and Materials Science 32(12): 3033-3042.

Sato, Y.S., Takauchi, H., Park, S.H.C. and Kokawa, H. (2005). "Characteristics of the kissing-bond in friction stir welded Al alloy 1050." Materials Science and Engineering: A 405(1-2): 333-338.

Schmidt, H., Hattel, J. and Wert, J. (2004). "An analytical model for the heat generation in friction stir welding." Modelling and Simulation in Materials Science and Engineering 12(1): 143-157.

Schmidt, H. and Hattel, J. (2005). "A local model for the thermomechanical conditions in friction stir welding." Modelling and Simulation in Materials Science and Engineering 13(1): 77-93.

Schmidt, H. and Hattel, J. (2005). "Modelling heat flow around tool probe in friction stir welding." Science and Technology of Welding and Joining 10(2): 176-186.

Schmidt, H.B. and Hattel, J.H. (2008). "Thermal modelling of friction stir welding." Scripta Materialia 58(5): 332-337.

Schneider, C., Weinberger, T., Inoue, J., Koseki, T. and Enzinger, N. (2011). "Characterisation of interface of steel/magnesium FSW." Science and Technology of Welding and Joining 16(1): 100-106.

Schneider, J.A. and Nunes, A.C. (2004). "Characterization of plastic flow and resulting microtextures in a friction stir weld." Metallurgical and Materials Transactions B-Process Metallurgy and Materials Processing Science 35(4): 777-783.

Scialpi, A., De Giorgi, M., De Filippis, L.A.C., Nobile, R. and Panella, F.W. (2008). "Mechanical analysis of ultra-thin friction stir welding joined sheets with dissimilar and similar materials." Materials & Design 29(5): 928-936.

Seidel, T.U. and Reynolds, A.P. (2001). "Visualization of the material flow in AA2195 friction-stir welds using a marker insert technique."

Metallurgical and Materials Transactions a-Physical Metallurgy and Materials Science 32(11): 2879-2884.

Selvaraj, M., Murali, V. and Rao, S.R.K. (2013). "Mechanism of Weld Formation during Friction Stir Welding of Aluminum Alloy." Materials and Manufacturing Processes 28(5): 595-600.

Shigematsu, I., Kwon, Y. J., Suzuki, K., Imai, T. and Saito, N. (2003). "Joining of 5083 and 6061 aluminum alloys by friction stir welding." Journal of Materials Science Letters 22(5): 353-356.

Simar, A. (2006). A multiscale multiphysics investigation of aluminium friction stir welds - from thermal modelling to mechanical properties through precipitation evolution and hardening. PhD, Universite Catholique de Louvain.

Smallman, R. E. and Bishop, R. J. (1999). Modern physical metallurgy and materials engineering, Butterworth-Heinemann.

Song, M. and Kovacevic, R. (2003). "Thermal modeling of friction stir welding in a moving coordinate system and its validation." International Journal of Machine Tools and Manufacture 43(6): 605-615.

Song, S. W., Kim, B. C., Yoon, T. J., Kim, N. K., Kim, I. B. and Kang, C. Y. (2010). "Effect of Welding Parameters on Weld Formation and Mechanical Properties in Dissimilar Al Alloy Joints by FSW." Materials Transactions 51(7): 1319-1325.

Su, J.Q., Nelson, T.W., Mishra, R. and Mahoney, M. (2003). "Microstructural investigation of friction stir welded 7050-T651 aluminium." Acta Materialia 51(3): 713-729.

Sutton, M.A., Reynolds, A.P., Yan, J.H., Yang, B.C. and Yuan, N. (2006). "Microstructure and mixed mode I/II fracture of AA2524-T351 base material and friction stir welds." Engineering Fracture Mechanics 73(4): 391-407.

Tavares, S. M. O., Castro, R. A. S., Richter-Trummer V., Vilaça P., Moreira P. and de Castro, P. (2010). "Friction stir welding of T-joints with

dissimilar aluminium alloys: mechanical joint characterisation." Science and Technology of Welding and Joining 15(4): 312-318.

Thomas, W.M. and Nicholas, E.D. (1997). "Friction stir welding for the transportation industries." Materials & Design 18(4-6): 269-273.

Threadgill, P.L., Leonard, A.J., Shercliff, H.R. and Withers, P.J. (2009). "Friction stir welding of aluminium alloys." International Materials Reviews 54(2): 49-93.

Totten, G. E. and MacKenzie, D. S. (2003). Handbook of Aluminum: Vol. 1: Physical Metallurgy and Processes, CRC Press.

Trimble, D., Monaghan, J. and O'Donnell, G.E. (2012). "Force generation during friction stir welding of AA2024-T3." Cirp Annals-Manufacturing Technology 61(1): 9-12.

Tronci, A., McKenzie, R., Leal, R.M. and Rodrigues, D.M. (2011). "Microstructural and mechanical characterisation of 5XXX-H111 friction stir welded tailored blanks." Science and Technology of Welding and Joining 16(5): 433-439.

Upadhyay, P. and Reynolds, A.P. (2010). "Effects of thermal boundary conditions in friction stir welded AA7050-T7 sheets." Materials Science and Engineering A - Structural Materials Properties Microstructure and Processing 527(6): 1537-1543.

Wang, L. and Lee, T.C. (2006). "The effect of yield criteria on the forming limit curve prediction and the deep drawing process simulation." International Journal of Machine Tools & Manufacture 46(9): 988-995.

Wouters, P., Verlinden, B., McQueen, H.J., Aernoudt, E., Delaey, L. and Cauwenberg, S. (1990). "Effect of homogenization and precipitation treatments on the hot workability of an aluminium alloy AA2024." Materials Science and Engineering: A 123(2): 239-245.

Xu, S. and Deng, X. (2008). "A study of texture patterns in friction stir welds." Acta Materialia 56(6): 1326-1341.

Yang, B.C., Yan, J.H., Sutton, M.A. and Reynolds, A.P. (2004). "Banded microstructure in AA2024-T351 and AA2524-T351 aluminum friction stir welds - Part I. Metallurgical studies." Materials Science and Engineering A - Structural Materials Properties Microstructure and Processing 364(1-2): 55-65.

Zhang, H., Lin, S.B., Wu, L., Feng, J.C. and Ma, S.L. (2006). "Defects formation procedure and mathematic model for defect free friction stir welding of magnesium alloy." Materials & Design 27(9): 805-809.

Zhang, Z. and Zhang, H. (2007). "Material behaviors and mechanical features in friction stir welding process." The International Journal of Advanced Manufacturing Technology 35(1): 86-100.

Zhang, G.F., Su, W., Zhang, J. and Zhang, J.X. (2011). "Visual observation of effect of tilting tool on forging action during FSW of aluminium sheet." Science and Technology of Welding and Joining 16(1): 87-91.

Zhang, Y.N., Cao, X., Larose, S. and Wanjara, P. (2012). "Review of tools for friction stir welding and processing." Canadian Metallurgical Quarterly 51(3): 250-261.

Zhao, X., Kalya, P., Landers, R.G., Krishnamurthy, K. and IEEE (2007). Design and implementation of a Nonlinear axial force controller for friction stir welding processes. 2007 American Control Conference, Vols 1-13: 3559-3564.

Zhao, Y.H., Lin, S.B., Qu, F.X. and Wu, L. (2006). "Influence of pin geometry on material flow in friction stir welding process." Materials Science and Technology 22(1): 45-50.

Zhou, M. and Clode, M.P. (1998). "Constitutive equations for modelling flow softening due to dynamic recovery and heat generation during plastic deformation." Mechanics of Materials 27(2): 63-76.

Zhu, X. and Chao, Y. (2004). "Numerical simulation of transient temperature and residual stresses in friction stir welding of 304L stainless

steel." Journal of Materials Processing Technology 146(2): 263-272.

Annexes

Annex A

Materials and Design 33 (2012) 69–74

Contents lists available at ScienceDirect

Materials and Design

journal homepage: www.elsevier.com/locate/matdes

Determination of local constitutive properties of aluminium friction stir welds using digital image correlation

C. Leitão, I. Galvão, R.M. Leal, D.M. Rodrigues *

CEMUC, Department of Mechanical Engineering, University of Coimbra, Portugal

ARTICLE INFO

Article history:
Received 6 May 2011
Accepted 4 July 2011
Available online 14 July 2011

Keywords:
Plastic behaviour
Welding
Aluminium alloys

ABSTRACT

In this paper a simple procedure for the characterization of the constitutive behaviour of welds is presented. Digital Image Correlation (DIC) is used for accessing local strain fields in transverse weld tensile samples and the stress distribution is calculated taking into account local strain data and thickness variation across the samples. The constitutive behaviour of the welds is assessed from local tensile stress–strain curves, plotted up to moderate values of plastic deformation, by fitting an appropriate work-hardening model to the experimental results and the ultimate tensile strength of the welds is estimated using the Considère criterion. Based on this information it is possible to assess the constitutive behaviour of different weld sub-zones, which cannot be derived from the hardness measurements, as well as evaluating the mis-match in yield stress and plastic properties across the welds. The proposed methodology is validated by comparing local stress–strain curves obtained by testing transverse weld samples of friction stir welds in very thin plates with those obtained by testing longitudinal samples of the same welds.

1. Introduction

It is well known that the global strength of any weld depends on the distribution of properties across the zones affected by the welding operation. Consequently, it is important to determine the local mechanical properties of different weld sub-zones in order to understand the global strength and ductility of the bonding. Mechanical characterization has traditionally been addressed by performing hardness tests across the welds, by testing miniature samples from each region of the weld or samples obtained by weld thermal simulation, and more recently, by using digital image correlation to obtain local stress–strain curves across transverse weld samples [1,2].

Hardness testing is the most well-known and widely used technique for the mechanical characterization of welds. However, no precise relations have yet been established to determine important constitutive relations, which enable the plastic behaviour of the welds to be described, from hardness data. Testing of miniature samples, from different weld sub-regions, allows constitutive properties to be determined [3–6]. However, the production and testing of such miniature specimens is very complicated. If steep gradients in material properties exist within the welds, then even very small specimens may exhibit non-homogeneous properties. This problem can be avoided by using bulk material samples from weld thermal simulation, which allows full-size specimens to be tested and properties from yield to fracture to be determined [7,8]. However, the highly transient thermal histories experienced by the welded joints are difficult to characterize accurately and to reproduce, which makes the use of thermal simulation samples simultaneously expensive and imprecise.

One important step towards the immediate characterization of the mechanical behaviour of different weld sub-zones and of the global response of the welds is the use of digital image correlation to obtain local and global stress–strain curves. Reynolds and Duvall [9] were pioneers in applying this technique to determine the constitutive behaviour of both weld and base metal constitutive behaviour. These authors, as well as all the others who have used this technique for the mechanical characterization of friction stir welds [10–12] and laser welds [13,14], assumed iso-stress conditions during transverse tensile weld sample loading. Using this assumption, the local stress–strain curves are determined by mapping the global applied stress to the corresponding local strain fields captured using DIC. Lockwood et al. [4] analysed the viability of the iso-stress assumption by performing numerical simulations of tensile tests, using a FE model replicating experimental welds with local material properties assessed by DIC. Full correspondence between predicted and measured global weld behaviour was not achieved, which was attributed to the possible limitations of the iso-stress load assumption in mechanical characterization.

Actually, assuming iso-stress conditions implies that the various weld regions are arranged in series and the cross-section at

* Corresponding author. Tel.: +351 239 790 700; fax: +351 239 790 701.
E-mail address: dulce.rodrigues@dem.uc.pt (D.M. Rodrigues).

0261-3069/$ - see front matter © 2011 Elsevier Ltd. All rights reserved.
doi:10.1016/j.matdes.2011.07.009

any location in the specimen is homogeneous [15]. However, this is not the case in welded samples for which, depending on the welding technology in use, steep microstructural gradients and thickness variations can be registered across the samples. In friction stir welding (FSW), for example, the forging action of the tool induces a significant thickness reduction in the weld relative to parent plate [16]. In the present study, the mechanical characterization of friction stir welds was performed using a very simple procedure which enabled local stress fields to be determined, by taking into account local thickness variations in the regions under evaluation and the local strain fields acquired by DIC. Since the stress and strain ranges in different sample regions are limited by the strength of the weakest region, the constitutive behaviour of the harder sample regions was assessed by fitting an appropriate hardening model to the "incomplete" stress–strain curves. This procedure enabled the local constitutive behaviour in different sample regions to be modelled as well as allowing the maximum strength in each weld region to be estimated using the Considère criterion.

2. Computation of local stress–strain curves from local strain fields

The methodology presented in this section enables local tensile stress–strain curves to be calculated from local strain fields registered using DIC during tensile tests of transverse weld specimens. Fig. 1a shows a schematic of a full-size transverse tensile specimen, with the weld centred in the gauge section and the loading axis normal to the welding direction. In this Fig. 1 indicates the weld, 2 the heat affected zone and 3 the base material. Fig. 1b shows an image of the major logarithmic strain (ε_1) distribution after maximum load, acquired using DIC, in a tensile sample. This clearly demonstrates the non-uniform strain distribution across the sample and the occurrence of rupture in the weld, where the largest strain values were registered.

Knowing the local strain values, the evolution of the cross sectional area of a specific part of the sample, A^i, can be determined using the following relationship

$$A^i = A_0^i \exp(-\varepsilon^i), \tag{1}$$

in which A_0^i is the initial cross-section of the specimen in the zone under study, calculated after evaluating specimen dimensions across the samples, and ε^i is the local axial strain registered using DIC.

The local stress in this area is obtained by dividing the applied load, F, by the actual cross sectional area, A^i, of the part of the sample under study:

$$\sigma^i = \frac{F}{A^i}. \tag{2}$$

Expressions (1) and (2) can be used as long as the sample part under analysis is subjected to uniaxial loading conditions. In order to evaluate if the local microstructural heterogeneities and geometric discontinuities across the transverse weld samples, such as thickness variations across the weld, had any influence on the local strain fields, the evolution of local principal logarithmic strains ε_1^i versus ε_2^i with plastic deformation should be analyzed before calculating the stress–strain curves. This analysis allows the occurrence of any local change of the deformation path during the tensile test to be determined. More precisely, it is possible to evaluate the existence of any local stress triaxiality and if it had any influence on the local stress–strain curves registered for each sample part.

3. Experimental procedure

Similar and dissimilar welds, obtained by friction stir welding of 1 mm thick aluminium sheets were tested in this study. The base materials were two very popular automotive aluminium alloys, AA5182-H111 (BM5) and AA6016-T4 (BM6) alloys. The welding conditions and results of the metallographic and mechanical analysis of the welds can be found in [17,18]. From these references it can be inferred that the AA5182 similar welds (S55) and the AA5182–AA6016 dissimilar welds (D56) were in over-match relative to the base material's hardness and yield stress, but the AA6016 similar welds (S66) were in under-match. Longitudinal and transverse samples were cut from all these welds, following the sampling scheme shown in Fig. 2.

In the present investigation, the tensile tests were performed in a 10 kN universal testing machine, operating at room temperature, with a nominal initial strain rate of $1.33 \times 10^{-3}\ s^{-1}$, in accordance with the ISO6892-1 standard [19]. The global strain of the longitudinal specimens (Fig. 2) was evaluated using a 50 mm gauge length clip-on extensometer. For the transverse samples, the local strain fields were determined by DIC using Aramis 3D 5M optical system (GOM GmbH). Before testing, the specimens were prepared by applying a random black speckle pattern, over the previously mat white painted surface of the transverse samples, in order to enable data acquisition by DIC. It is also important to clarify that none of the transverse or longitudinal samples were subjected to surface smoothing in order to homogenise sample thickness across the gauge section or avoid any influence from surface roughness on plastic behaviour.

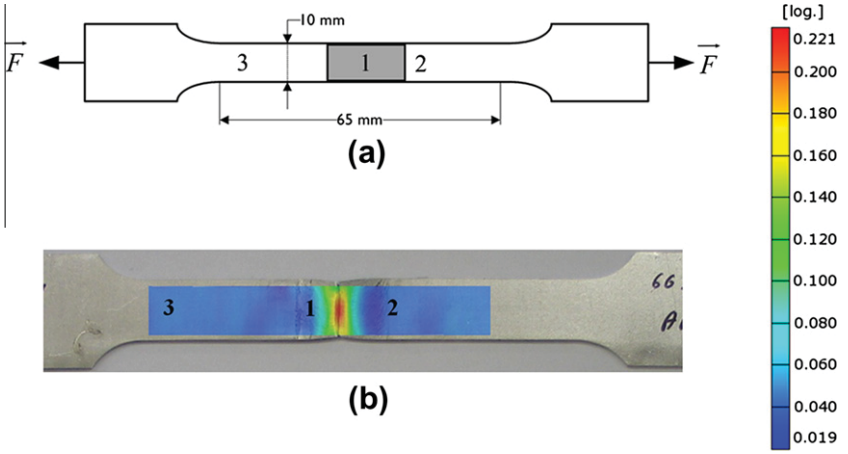

Fig. 1. Transverse tensile specimen: 1 – Weld; 2 – HAZ; 3 – BM.

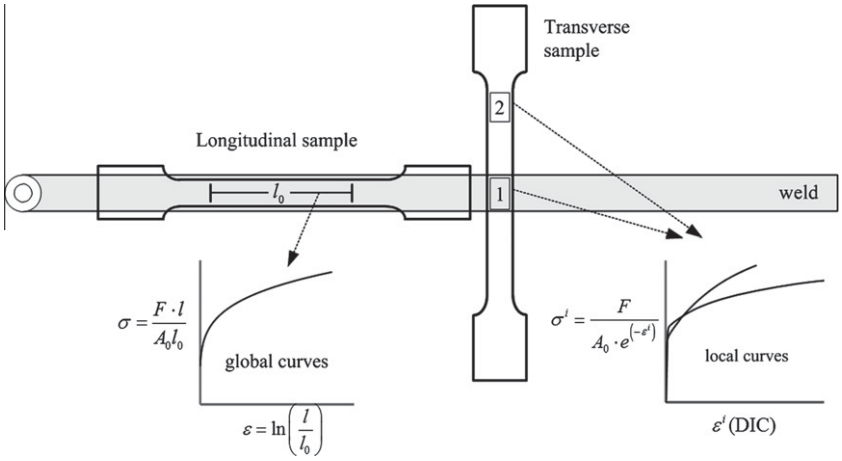

Fig. 2. Longitudinal and transverse tensile specimen scheme.

4. Results and discussion

In order to analyse the accuracy of the proposed methodology for evaluating the local mechanical behaviour of different specimen zones, the local stress–strain curves from tensile transverse weld specimens were plotted and compared with the global curves obtained from the tensile tests of longitudinal specimens, extracted from the same welds, as schematically shown in Fig. 2.

For each sample, local tensile stress–strain curves were calculated for sample regions corresponding to the weld (zone 1) and base material (zone 3) areas schematized in Fig. 1. Before computing the local cross-section area evolution, from Eq. (1), the local loading conditions were analysed by plotting the evolution of local principal logarithmic strains ε_1^i against ε_2^i with plastic deformation. The results obtained for the sample area corresponding to the weld, for all the specimens analysed in this investigation, are shown in Fig. 3. The logarithmic strain values plotted on this graph correspond to an average of the strain values registered for all the points located inside the areas under study, calculated using Aramis software [20]. The graph also shows the strain path corresponding to pure uniaxial loading conditions for isotropic materials ($\varepsilon_2 = -0.5\varepsilon_1$). By analysing the major and minor strain evolution in Fig. 3 it is possible to verify that linear strain paths were registered in the weld zone, for all the samples, before maximum load was attained. For the S66 and D56 samples, the deformation path started changing after maximum load had been attained (indicated in the figure by necking). For the samples of the overmatched S55 weld, necking occurred in the base material part of the samples and, for that reason, the strain path in the weld remained linear until the end of the test.

Comparing the strain paths corresponding to the welds, with those representing isotropic uniaxial loading conditions, it is possible to conclude that the slopes (ε_1 versus ε_2) corresponding to the welds strain paths are different from −0.5. This type of behaviour, which can be attributed to the existence of constraints in the deformed area and/or severe anisotropic conditions inside it, had no influence on mechanical characterization results, as will be shown in the next. Actually, in a previous numerical simulation study, Lockwood and Reynolds [15] established that the amount of constraint developed within the weld, during tensile loading, is primarily limited by specimen thickness. Tensile samples tested in current work were 1 mm thick, and for this reason constraint associated to thickness effects was expected to be very low.

In Fig. 4 the local stress–strain curves, for all the welds (S55,S66 and D56), obtained using Eqs. (1) and (2), and the global stress–strain curves (LONG5, LONG6 and LONG56), obtained by testing

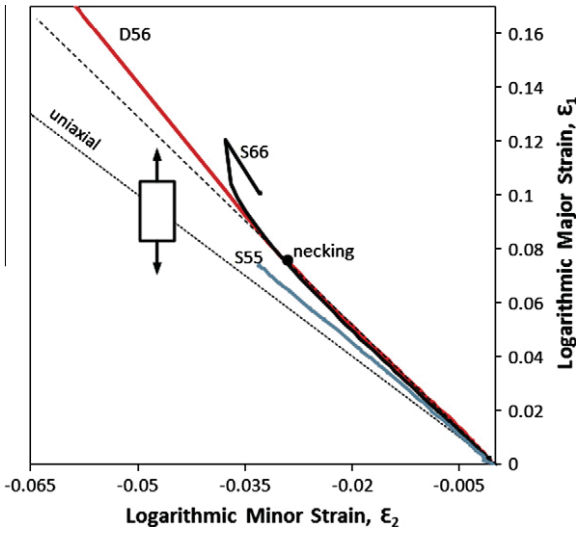

Fig. 3. Logarithmic major and minor strain evolution in the weld zone.

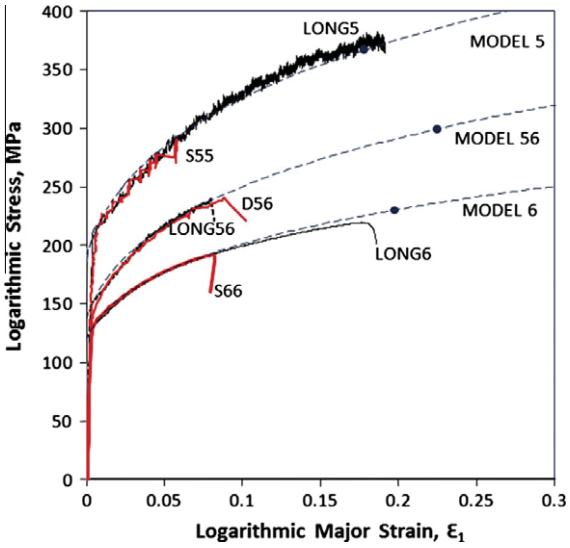

Fig. 4. Comparison of weld local strain–stress curves obtained by DIC and those corresponding to the longitudinal specimens.

longitudinal samples of each weld, are compared. This figure demonstrates that, for each weld, despite large differences in maximum strain levels, the local stress–strain curves overlap the stress–strain curves of the respective longitudinal samples. The large differences in strain at maximum load result from the strong heterogeneities in strain distribution across the transverse weld samples, as is shown in strain maps in Figs. 5–7, which correspond to two different periods during the tensile test: The right strain map in each figure corresponds to strain distribution at maximum load and the left strain map corresponds to strain distribution at an overall elongation of 50% of the elongation at maximum load. The non-homogeneous plastic deformation, which can be inferred from the strain maps, promoted local constraints that enforced premature strain localization in the transverse samples, relative to the homogeneous longitudinal samples. However, by comparing the local and longitudinal stress–strain curves in Fig. 4, for each weld, it is possible to conclude that these constraint effects had no strong influence on local loading conditions.

In order to predict the plastic behaviour of the welds up to high values of plastic deformation from the local tensile stress–strain curves, the Swift isotropic work-hardening model

$$\sigma = k(\varepsilon_0 + \bar{\varepsilon}^{p})^n \tag{3}$$

was adjusted to the S55, S66 and D56 curves in Fig. 4. In this equation, k and ε_0 are material constants, σ is the flow stress in simple tension, $\bar{\varepsilon}^{p}$ the equivalent plastic strain and n the hardening coefficient. Material parameter identification was performed by using the in-house DD3MAT code [21]. The results are shown in Table 1 and the stress–strain curves, plotted according to Eq. (3), are shown in Fig. 4 (MODEL5, MODEL6 and MODEL56 curves). Table 1 shows the values of the ultimate tensile strength (σ_u), for all the weld materials, estimated using the Considère criterion. According to this criterion, for the Swift equation:

$$\sigma_u = kn^n \tag{4}$$

The maximum stress values, corresponding to each weld, are indicated by dots in the MODEL curves shown in the graph of Fig. 4. If the values predicted by the model are compared with the LONG curves results, it is possible to confirm the satisfactory quality of the predictions. In fact, major differences between experimental and model predictions, were only found for the dissimilar weld (D56), for which very small values of ultimate tensile strength were also registered from the tensile tests of the longitudinal samples. However, it is important to point out that the longitudinal samples had very irregular surface finishing, characteristic of friction stir weld crowns, which promoted non-uniform premature failure during the tensile test [17].

The curves plotted in Fig. 4 were computed using average strain values evaluated from the strain distribution inside the weld areas under measurement, which are indicated by rectangles in the strain maps in Figs. 5–7. However, in these strain maps, it is easy to distinguish easily the presence of strong heterogeneities in the plastic deformation across the welds. This plastic heterogeneity was evaluated by plotting local stress–strain curves, corresponding to different sub-zones inside each weld, which are identified by numbers 1 and 2 in the left strain maps.

The stress–strain results from the S55, S66 and D56 welds are shown in Figs. 5–7. In order to make it easy to understand the plastic heterogeneities inside the welds which can be inferred from the maps, the hardness profiles registered across the different welds were also added to the graphs. If the stress–strain curves and strain maps from the S55 weld (Fig. 5) are analysed, it is possible to observe that this weld is made up of two sub-zones with markedly different plastic behaviour (sub-zones 1 and 2). Although the two weld sub-zones display higher tensile strength than the base material (BM5 curve), it is possible to conclude that the central part of the weld (sub-zone 2) has improved mechanical properties relative to sub-zone 1, which corresponds to the retreating side of the weld. In the hardness profile plotted on the same graph it is also possible to see a progressive decrease in hardness from the centre of the weld to the base material on the retreating side of the weld. It is also interesting to note that the stress–strain curve from weld sub-zone 2 displays higher strength levels than those registered by testing longitudinal weld samples (LONG5, Fig. 4) or considering the average strain over the entire weld (S55 curve).

If the results from the S66 weld (Fig. 6) are examined, it is possible to conclude that despite the progressive gradient in properties at the retreating side of the weld, evident from the hardness profile, the plastic properties registered for sub-zones 1 and 2 of the S66 welds are not very different, both being very close to the plastic properties calculated considering the average strain over the entire weld area (S66). However, the stress–strain curve relative to sub-zone 1, at the retreating side of the weld, is closer to that of the S66 curve. Another important result is that, despite the decrease in hardness registered for the S66 welds, the yield stress registered for all the weld sub-zones is higher than that of the 6016-T4 base material (BM6 curve). However, since the base material displays stronger hardening with plastic deformation, its strength becomes higher than that of the weld for relatively small strain values.

If Fig. 7 is analysed, relative to the D56 welds, it is possible to observe strong gradients in plastic properties and hardness across

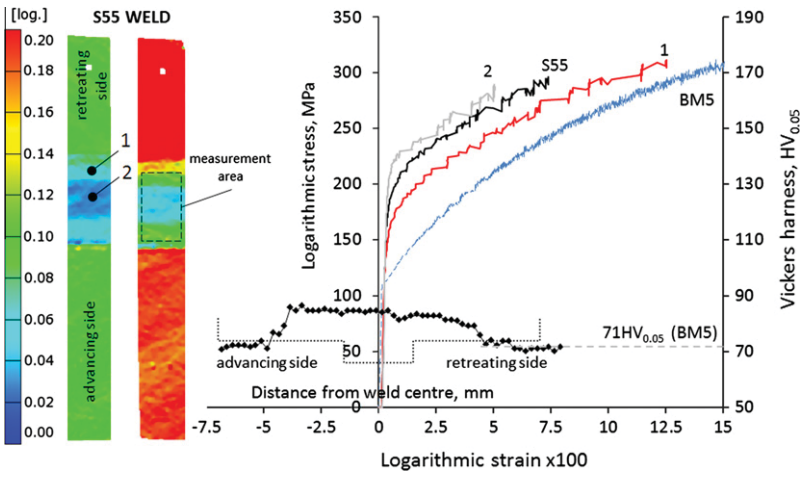

Fig. 5. Strain maps, stress–strain curves and hardness profile for the S55 weld.

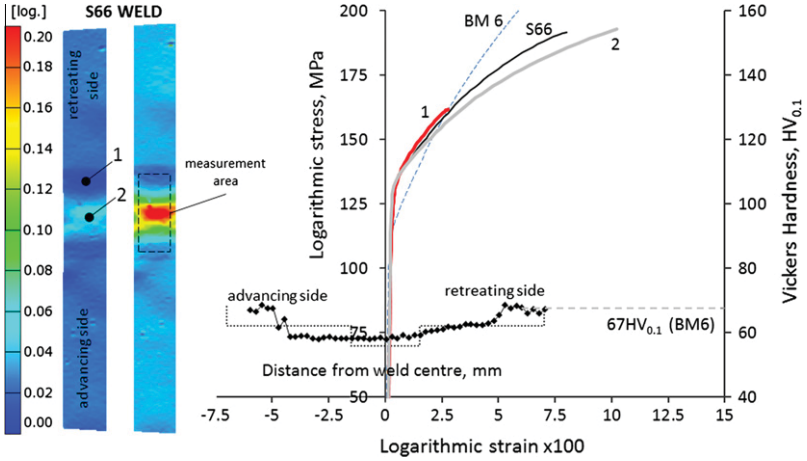

Fig. 6. Strain maps, stress–strain curves and hardness profile for the S66 weld.

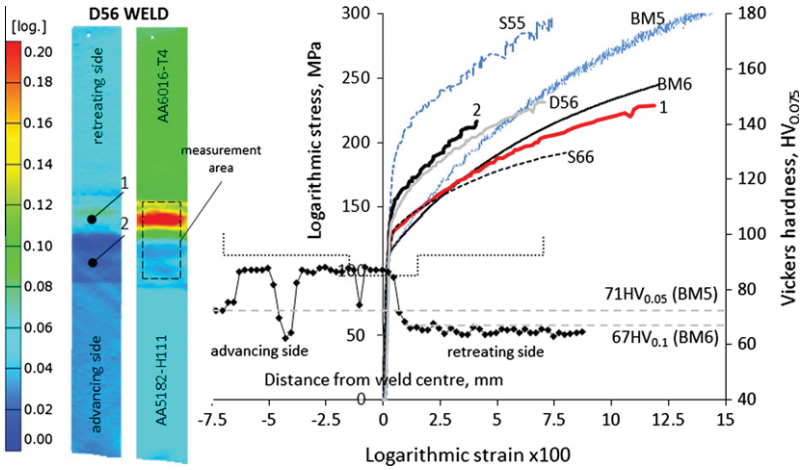

Fig. 7. Strain maps, stress–strain curves and hardness profile for the D56 weld.

Table 1
Swift coefficients for each curve and ultimate tensile strength ($\varepsilon_0 = 0.01$).

	k (MPa)	n	σ_u (MPa)
MODEL 5	520.1	0.222	372.5
MODEL 6	319.8	0.210	230.6
MODEL 56	420.0	0.233	299.1

the welds. For sub-zone 1, corresponding to the 6016-T4 side of the weld, where the hardness values registered are close to that of this base material, the stress–strain curve displays higher yield stress values but decreasing strength with plastic deformation, than the base material (BM6 curve). However, it is important to note that the mechanical properties in this sub-zone of the D56 welds are higher than those registered for the 6016-T4 similar welds (S66 curve) performed under the same welding conditions. Turning now to the results relative to the 5182-H111 (BM5) side of the weld, corresponding to sub-zone 2 in the strain map, it is possible to conclude that the local mechanical properties are higher than that of the base material here, but substantially lower than those registered for the 5182-H111 similar welds (S55 curve). This decrease in strength can be related to the strong local decrease in hardness registered on this side of the weld, which is evidenced by the hardness profile shown in the graph.

A deep characterization of local plastic heterogeneities inside the welds, as exemplified in the present investigation, is critical for the development of numerical models which can accurately predict the response of welds to various loading conditions. Several numerical studies have been devoted to modelling tailor welded blanks, with the aim of predicting forming behaviour [22], developing failure prediction models [23] or even analysing the impact of weld line modelling on numerical results [24,25]. These studies concluded that the implementation of weld details in the numerical models makes a significant contribution to the accuracy of the predictions. In the present study, local strain measurements, obtained from transversely loaded samples via DIC, enabled local stress fields to be calculated and the heterogeneity in plastic properties to be evaluated. Transverse tensile tests are simpler and quicker to perform than conventional hardness tests, which require a large number of time consuming measurements across the welds. They also provide an accurate evaluation of the constitutive behaviour of the different sub-zones of the welds, not available from the hardness measurements. Actually, in the present study, the yield stress values for the welds in hardness under-match were found to be higher than that of the corresponding base materials, which is not traditionally assumed. It was also demonstrated that it is possible to predict the plastic behaviour of the welds up to maximum load, from local tensile stress–strain curves plotted up to moderate values of plastic deformation, by adjusting an appropriate work-hardening model to the experimental results. It was even possible to estimate the ultimate tensile strength using the Considère criterion, allowing the achievement

of good quality previsions of the complete local tensile response for each zone.

5. Conclusions

The present results show the effectiveness of performing local plastic characterization of welds using digital image correlation (DIC):

- Local stress distribution was computed using strain data from tensile testing of transverse specimens.
- The constitutive behaviour of different weld regions was assessed from local tensile stress–strain curves.
- The ultimate tensile strength for all weld regions was estimated using the Considère criterion.

Acknowledgments

The authors are indebted to the Portuguese Foundation for the Science and Technology (FCT) through COMPETE program from QREN and to FEDER for the financial support.

References

[1] Lemmen HJK, Alderliesten RC, Benedictus R, Hofstede JCJ, Rodi R. The power of digital image correlation for detailed elastic–plastic strain measurements. In: WSEAS international conference on engineering mechanics, structures, engineering geology. Crate Island, Greece; 2008.
[2] Sutton MA, Yan JH, Avril S, Pierron F, Adeeb SM. Identification of heterogeneous constitutive parameters in a welded specimen: uniform stress and virtual fields methods for material property estimation. Exp Mech 2008;48:451–64.
[3] Amancio-Filho ST, Sheikhi S, dos Santos JF, Bolfarini C. Preliminary study on the microstructure and mechanical properties of dissimilar friction stir welds in aircraft aluminium alloys 2024-T351 and 6056-T4. J Mater Process Technol 2008;206:132–42.
[4] Lockwood WD, Tomaz B, Reynolds AP. Mechanical response of friction stir welded AA2024: experiment and modeling. Mater Sci Eng A 2002;323:348–53.
[5] Nielsen KL, Pardoen T, Tvergaard V, de Meester B, Simar A. Modelling of plastic flow localisation and damage development in friction stir welded 6005 A aluminium alloy using physics based strain hardening law. Int J Solids Struct 2010;47:2359–70.
[6] Molak RM, Paradowski K, Brynk T, Ciupinski L, Pakiela Z, Kurzydlowski KJ. Measurement of mechanical properties in a 316 L stainless steel welded joint. Int J Press Vessels Pip 2009;86:43–7.
[7] Bleck W, Reisgen U, Mokrov O, Rossiter E, Rieger T. Methodology for thermomechanical simulation and validation of mechanical weld-seam properties. Adv Eng Mater 2010;12:147–52.
[8] Zhang ZL, Silvanus J, Li HK, Shi QY. Sensitivity analysis of history dependent material mechanical models for numerical simulation of welding process. Sci Technol Weld Joi 2008;13:422–9.
[9] Reynolds AP, Duvall F. Digital image correlation for determination of weld and base metal constitutive behavior. Weld J 1999;78:355S–60S.
[10] Genevois C, Deschamps A, Vacher P. Comparative study on local and global mechanical properties of 2024 T351, 2024 T6 and 5251 O friction stir welds. Mater Sci Eng A – Struct 2006;415:162–70.
[11] Hatamleh O. Effects of peening on mechanical properties in friction stir welded 2195 aluminum alloy joints. Mater Sci Eng A 2008;492:168–76.
[12] Brown R, Tang W, Reynolds AP. Multi-pass friction stir welding in alloy 7050-T7451: effects on weld response variables and on weld properties. Mater Sci Eng A 2009;513–514:115–21.
[13] Boyce B, Reu P, Robino C. The constitutive behavior of laser welds in 304 L stainless steel determined by digital image correlation. Metall Mater Trans A 2006;37:2481–92.
[14] Scintilla LD, Tricarico L, Brandizzi M, Satriano AA. Nd:YAG laser weldability and mechanical properties of AZ31 magnesium alloy butt joints. J Mater Process Technol 2010;210:2206–14.
[15] Lockwood WD, Reynolds AP. Simulation of the global response of a friction stir weld using local constitutive behavior. Mater Sci Eng A 2003;339:35–42.
[16] Louro R, Leitao C, Puehringer T, Gouveia H, Loureiro A, Rodrigues DM. The relation between the plunge pressure and the mechanical properties of friction stir welded 3 mm thick AA6082-T651 Sheets. Mater Sci Forum 2010;636–637:578–84.
[17] Leitao C, Leal RM, Rodrigues DM, Loureiro A, Vilaça P. Mechanical behaviour of similar and dissimilar AA5182-H111 and AA6016-T4 thin friction stir welds. Mater Des 2009;30:101–8.
[18] Leal RM, Leitão C, Loureiro A, Rodrigues DM, Vilaça P. Material flow in heterogeneous friction stir welding of thin aluminium sheets: effect of shoulder geometry. Mater Sci Eng A 2008;498:384–91.
[19] ISO 6892-1:2009. Metallic materials – tensile testing – part1: method of test at room temperature.
[20] Gom.com. Braunschweig: GOM – optical measurement techniques, GmbH; 2011. <http://www.gom.com/home.html>.
[21] Chaparro BM, Thuillier S, Menezes LF, Manach PY, Fernandes JV. Material parameters identification: Gradient-based, genetic and hybrid optimization algorithms. Comput Mater Sci 2008;44:339–46.
[22] Veera Babu K, Ganesh Narayanan R, Saravana Kumar G. An expert system for predicting the deep drawing behavior of tailor welded blanks. Expert Syst Appl 2010;37:7802–12.
[23] Zadpoor AA, Sinke J, Benedictus R. Finite element modeling and failure prediction of friction stir welded blanks. Mater Des 2009;30:1423–34.
[24] Raymond SD, Wild PM, Bayley CJ. On modeling of the weld line in finite element analyses of tailor-welded blank forming operations. J Mater Process Technol 2004;147:28–37.
[25] Shi Y, Lin Z, Zhu P, Han S. Impact modeling of the weld line of tailor-welded blank. Mater Des 2008;29:232–8.

Annex B

Materials and Design 51 (2013) 968–974

Contents lists available at SciVerse ScienceDirect

Materials and Design

journal homepage: www.elsevier.com/locate/matdes

Assessing strength and local plastic behaviour of welds by shear testing

C. Leitão [a], M.I. Costa [a], K. Khanijomdi [a,b], D.M. Rodrigues [a,*]

[a] CEMUC, Department of Mechanical Engineering, University of Coimbra, Portugal
[b] SIIT, Sirindhorn International Institute of Technology, Thammasat University, Thailand

ARTICLE INFO

Article history:
Received 25 February 2013
Accepted 30 April 2013
Available online 14 May 2013

Keywords:
Plastic behaviour
Shear testing
Welds

ABSTRACT

In order to assess the strength and plastic properties across different weld zones, a shear testing procedure specially conceived for sampling and testing narrow weld portions, is presented in current paper. The local constitutive behaviour of the welds is assessed from local shear stress–strain curves, plotted up to large values of plastic deformation. The shear testing tool, developed in order to enable running the shear tests in a universal tensile testing machine, is described, as well as the shear sample geometry and the procedures used for strain data acquisition via Digital Image Correlation (DIC). Results of the mechanical characterisation of the nugget of AA5083 friction stir welds, produced under different welding conditions, are used to demonstrate the quality and variety of the results obtained applying the proposed mechanical characterisation technique.

1. Introduction

Developing accurate procedures for the mechanical characterisation of the local strength and/or plastic properties of highly heterogeneous material structures, such as that formed during welding, when the heat source (in fusion welding) or the severe plastic deformation (in solid state welding) promote strong, and very localised, microstructural changes of the materials being joined, remains an up-to-date research topic in the field of welding/materials science. Characterising the local mechanical properties across the different weld zones enables the full understanding of the global strength and ductility of the bonding, which is of paramount importance in structures/weld design optimization.

Performing hardness measurements had been, since long time, the most widely used/published/known technique for weld strength mis-match characterisation. The use of nanoindentation techniques, which enable plotting detailed hardness maps across the welds, is the most recent development in this field. Maier et al. [1] showed important differences between the microhardness and nanohardness measurements in coarse grained submerged arc welds. By using nanohardness tests, they found that the hardness of the grains is always smaller in the centre, increasing towards the grain boundary. In the same way, Hernandez et al. [2] used nanohardness results to reveal "softening" at nano-scale for resistance spot welds in a dual phase steel and Charitidis et al. [3] to analyse the residual stress fields in aluminium friction stir welds. A recently developed procedure for the determination of local stress–strain properties, based on instrumented indentation testing, was also proposed by Rao et al. [4]. However, in spite of these recent developments, it is well known that no precise relations still exist enabling to accurately determine the yield and tensile strength, or local plastic behaviour, from hardness data, which seriously limits the use of this technique in mechanical characterisation for weld design optimization.

In order to overcome the hardness testing limitations in characterising the plastic behaviour of welds, the use of weld thermal simulators for producing full-size specimens, replicating local weld subzones, which can be tested using standard tensile and fracture mechanics procedures, had long being tried and are still in use. An accurate description of weld thermal simulation techniques can be found in a recent paper [5] as well as examples of the application of weld thermal simulation in the microstructural and mechanical characterisation of the HAZ (heat affected zone) of steel [6] and aluminium [7] welds. However, it is also well known that the use of thermal simulation techniques displays important limitations due to the difficulty in characterising and replicating the severe transient thermal histories associated with the welding operations [8,9], which makes the use of thermal simulation samples simultaneously expensive and imprecise.

Tensile testing of miniature samples, extracted from different weld regions, is another technique widely used for local constitutive properties characterisation. Rao et al. [10], for example, analysed the asymmetric mechanical properties of aluminium friction stir welds by testing miniature specimens. In the same way, Sutton et al. [11], used micro-mechanical experiments, together with Digital Image Correlation (DIC), to quantify the material response within the periodic bands of aluminium friction stir welds. However, since the production and testing of miniature

* Corresponding author. Tel.: +351 239 790 700; fax: +351 239 790 701.
E-mail address: dulce.rodrigues@dem.uc.pt (D.M. Rodrigues).

0261-3069/$ - see front matter © 2013 Elsevier Ltd. All rights reserved.
http://dx.doi.org/10.1016/j.matdes.2013.04.100

specimens is difficult and expensive, alternative testing techniques are always being proposed. Assessing local properties by using DIC, for acquiring local strain fields during tensile testing of full-size transverse weld specimens, is a weld characterisation technique which is founding widespread application [12–20].

Reynolds and Duvall [12] were pioneers in applying DIC to determine weld and base metal constitutive behaviour of friction stir welds. Most of the following works addressing the mechanical characterisation of welds by DIC where based in tensile testing procedures for accessing the local plastic properties of friction stir welds [13–17], laser [18,19] and GMAW welds [20]. Sutton et al. [20] use two methodologies, the uniform stress and virtual fields, to estimate specific heterogeneous material properties throughout the weld zone. Leitao et al. [13] accessed the local stress–strain curves of transverse weld tensile samples using local strain data and considering local thickness variations across the samples. However, when any weld zone is in over-match relative to the base materials strength, assessing the full constitutive behaviour with transverse samples becomes impossible, since very small or no plastic deformation is registered for that zone during tensile loading. In the same way, as demonstrated by Rodrigues et al. [21], when the width of any weld zone is too small relative to the samples thickness, constraint effects prevent plastic deformation in that zone, hindering local characterisation by tensile testing of transverse specimens. In this work an alternative technique for the local mechanical characterisation of welds is presented, which enables to overcome all these limitations. This technique, based on shear testing and strain data acquisition by DIC, enables easily sampling and testing, until very large values of plastic deformation, very small weld zones.

It is well known that, due to the delay in strain localisation at maximum load, when compared to the uniaxial tensile test, the shear test allows the study of the mechanical behaviour under very large deformations [22]. Although no standards regulating shear testing procedures have already been developed, this mechanical test has already been used by several researchers, which developed distinct testing mechanisms [23,24], for characterising metallic materials. However, to the authors knowledge, this kind of test had never been applied for the mechanical characterisation of welds, as proposed in current work. In order to assess the local plastic behaviour of the welds, a shear testing tool, as well as testing samples, specially conceived for sampling narrow weld portions, were developed. During the test, strain data acquisition is performed using DIC, which also required developing and checking appropriate procedures for strain data analysis [25]. Finally, the accuracy of the developed testing procedures was evaluated by testing AA5083-H111 friction stir welds, as is shown in current paper.

2. Shear testing sample and procedures

The shear testing device used in this work, which is shown in Fig. 1a, works directly connected to a tensile testing machine that promotes the parallel translation of the moving part of the tool relative of the fixed part. The shear samples, whose geometry is shown in Fig. 1b, are placed in the tool with the aid of cylindrical guides and fixed using grips (see Fig. 1a). Tool design was conceived in order to avoid any rotation of its moving part, enabling the planar deformation of the sample during the test.

In Fig. 1c, where a scheme representing Section A in Fig. 1b is shown, it is possible to see that the vertical translation of the moving part of the tool promotes the deformation in simple shear of the central section of the sample, with lower cross-section, labelled as Shear Zone. The samples' geometry was selected in order to avoid undesirable phenomena, such as buckling, stress concentration and abnormal strain distribution at the shear zone free-ends, which were reported by several authors [26–28] in shear testing of very thin plates. It is also important to focus that, since strain data acquisition is performed using a noncontact optical technique (DIC), the influence of slight sample slipping during the test on the strain measurements is eliminated [28].

According to Bouvier et al. [28], the size of the heterogeneous deformation area increases by decreasing the length (l_0) to width (h) ratio of the shear zone. In Fig. 1b and c, where the dimensions of the different shear sample features are shown, it is possible to depict that the maximum shear area width is 3 mm (h) and the minimum shear length (l_0) is 20 mm. Actually, the circular geometry at the free-end of the shear zone, maximizes the geometry factor (l_0/h), at the centre of the sample, increasing the size of the homogeneous strain area.

In Fig. 2a is shown a scheme of a shear sample of a weld, together with a cross-section of a friction stir weld (Fig. 2b), where the weld region to be characterised in current work is shown, i.e., the shear zone for all the samples tested corresponded to the centre of the pin influence zone.

3. Experimental procedure

The accuracy of the developed shear testing procedures was assessed by testing several AA5083-H111 friction stir welds. The welds were produced in 6 mm thick plates, using a conical tool and a varied set of welding parameters, which are described in Table 1. Present work comes in the sequence of a more general investigation on weldability of heat and non-heat treatable aluminium alloys [29,30]. So, as it is possible to see in Table 1, the welding parameters tested were chosen in order to investigate the influence of varying tool rotation and advancing speeds on weld macro and microestrutural properties. As is shown in the table, across the manuscript, the shear testing results will be labelled using the rotational and welding speeds used for producing the welds to which they refer.

The shear tests were performed in an INSTRON 100 kN universal tensile testing machine. Strain data acquisition was performed using the Aramis 3D 5M optical system (GOM GmbH). Before testing, the specimens were prepared by applying a random black speckle pattern, over the previously mat white painted surface of the samples, in order to enable data acquisition by DIC. Details on the non-contact optical technique used in current work can be found in Aramis literature [31]. Reading of Chu et al. [32] and Luo et al. [33] is also advised, for a more comprehensive study on the application of DIC to experimental mechanics.

4. Results and discussion

4.1. Strain data analysis

In Fig. 3a and b are shown the ε_{xy} strain maps, at half of the maximum load ($F_{max}/2$) and at maximum load (F_{max}), for four different shear samples. As it is possible to see in the figure, after yielding, plastic deformation spreads along the shear zone (i.e., along the weld). The deformed area is symmetric relative to the loading direction and to the sample middle-plane. The gradient in strain distribution becomes sharper at maximum load, when strain localisation occurs at the free-ends of the shear zone. G'Sell et al. [26] reported that this strain concentration results, on one hand, from the constrain effect of the grips, reacting against the rotational moment imposed by the couple of shearing forces and, on the other hand, from the departure from ideal simple shear conditions, at the shear zone free-end, where stresses normal and parallel to the sample surfaces develop. The localised transverse

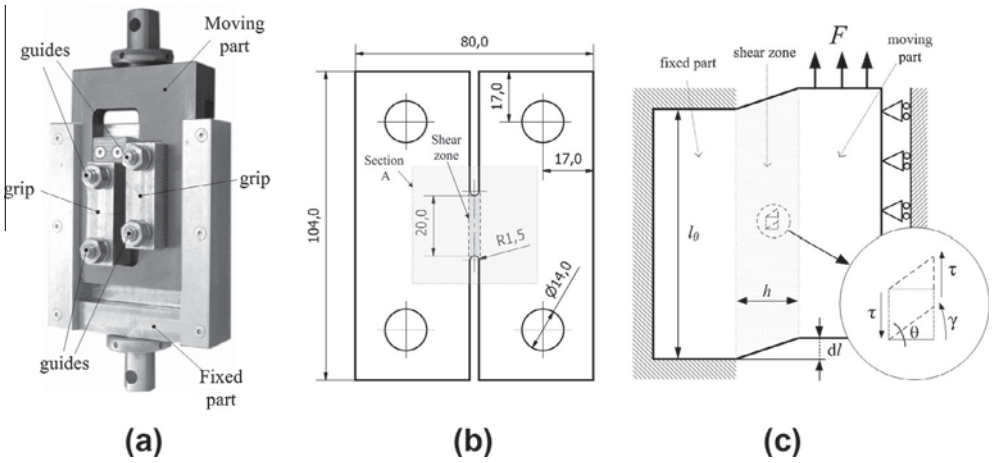

Fig. 1. Shear testing tool (a), shear testing sample geometry (b) and scheme of the shear zone deformation under simple shear (c).

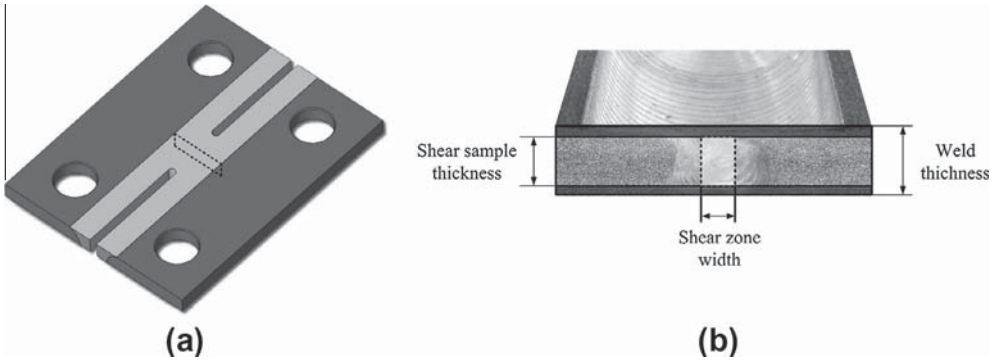

Fig. 2. Weld shear test sample scheme (a) and cross-section (b).

Table 1
Friction stir welding parameters.

Sample	Rot. speed, (rpm)	Weld speed, (mm/min)	Shoulder diameter, (mm)	Pin diameter, (mm)	Axial load, (kN)	Tilt angle, (°)
300_100	300	100	21	7	20	3
400_100	400	100				
500_100	500	100				
600_100	600	100				
700_100	700	100				
600_350	600	350				
600_275	600	275				
600_50	600	50				

tensile stresses, at the shear zone free-ends, promote strain localisation at maximum load.

For each sample tested, the strain path evolution with plastic deformation, inside the shear zone, was analysed in order to verify if simple shear loading conditions prevail until maximum load, in spite of the non-uniform strain distribution depicted in previous figures. The major (ε_1) versus minor strain (ε_2) evolution, which is representative of the strain path evolution during loading, is shown in Fig. 4a and b, for all the samples studied. The strains plotted in the graphs, correspond to average strain values calculated using Aramis software [31]. Two different evaluation areas were considered for calculating the average strains ε_1 and ε_2, which are represented and identified as Global and Local in the auxiliary schemes of Fig. 4a and b, respectively. Using the Global evaluation area, the full range of strain values registered in the shear zone is considered for computing the average strains. Using the Local evaluation area, only the strain values at the centre of the sample, where the strain fields are homogeneous, are considered in computing the average strains.

Analysing Fig. 4a and b, it is possible to conclude that pure-shear conditions ($\varepsilon_2 = -\varepsilon_1$) prevail until maximum load, independently of the strain evaluation area considered. Actually, no important strain path change is observed, even considering the global evaluation area, which allows concluding that the free-end influence on strain distribution, inside the shear zone, has no significant influence on global strain path evolution.

4.2. Stress–strain analysis

Using the strain data acquired by DIC, shear stress–strain curves (τ, γ) were computed for all the samples tested. Assuming iso-stress conditions during shear testing, the shear stress ($\tau = \tau_{xy}$) was obtained by dividing the testing load (F) by the shear zone cross-section area (A), according to the equation

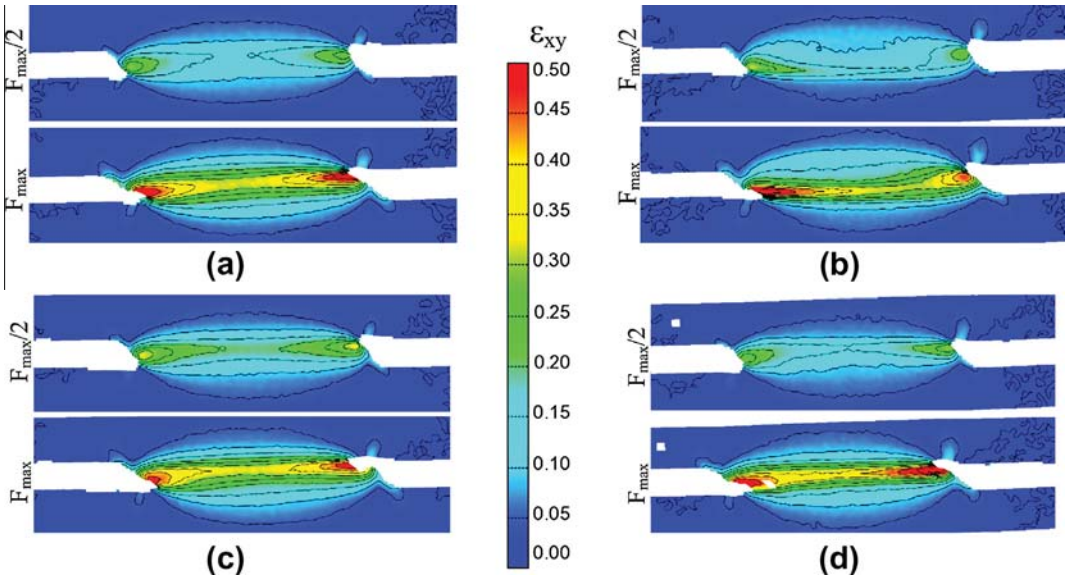

Fig. 3. Strain maps (ε_{xy}) obtained at half of maximum load ($F_{max}/2$) and at maximum load (F_{max}), for the 300_100 (a), 700_100 (b), 600_350 (c) and 600_50 (d) samples.

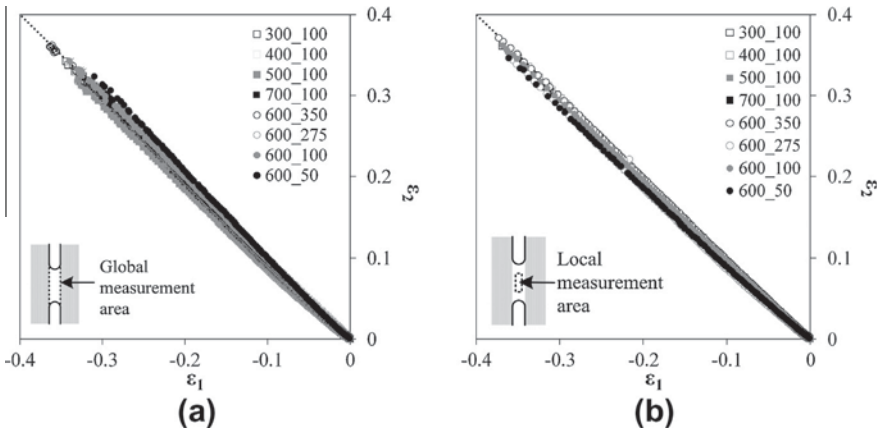

Fig. 4. Strain path evolution within the shear zone considering a global (a) and local (b) strain measurement areas.

$$\tau = \frac{F}{A} = \frac{F}{l_0 \times t} \tag{1}$$

where l_0 and t are the length and thickness of the shear zone, respectively. In the same way, the shear strain (γ) was obtained considering the relation

$$\gamma = 2\varepsilon_{xy}. \tag{2}$$

In order to illustrate the reproducibility of results, Local and Global average shear stress–strain curves (τ–γ), for three different welds, are shown in Fig. 5. The Local and Global shear stress–strain curves were plotted using average ε_{xy} values, computed over the same local and global measurement areas already shown in Fig. 4. Observing the figure it is possible to depict the excellent concordance between the results obtained for each weld when testing three samples, for the 600_350 weld, and two samples, for the other two welds. At least two samples were tested for each weld of Table 1, being always found good reproducibility of results. It is also important to observe that no significant differences can be noticed between the Local and Global stress–strain curves plotted in Fig. 5d–f, which shows that the non-uniform shear strain distribution, depicted in Fig. 4, does not influence significantly the global stress–strain results. In this way, in the next figures, only the Global stress–strain curves will be plotted.

In Fig. 6, the shear stress–strain (τ–γ) curves for the samples of Fig. 3 are compared with the stress–strain curves obtained for the base material, by testing in shear two types of samples: samples in the rolling direction of the plate (0°) and samples transverse to the rolling direction (90°). Analysing the figure it is possible to depict the anisotropic behaviour of the base material, as well as some differences in stress–strain behaviour for the different weld samples. However, in spite of the differences, all the weld curves almost follow between the two curves of the base material. In Fig. 7a are compared the maximum shear stress and strain values, registered for all the weld samples and for the base material. It is possible to conclude that no important mis-match in maximum shear strength or maximum shear strain, relative to the base material, was registered for any of the weld samples. Actually, the maximum difference between the results in Fig. 7a was never higher than 18 MPa.

In order to understand the previous results, in Fig. 7b are plotted the hardness ratios (Hv^{weld}/Hv^{BM}), i.e., the ratio between the average hardness registered for each weld in the pin influence zone (Hv^{weld}) and the average hardness of the base material (Hv^{BM}), and the average grain sizes (GS) for all the welds and base material. The

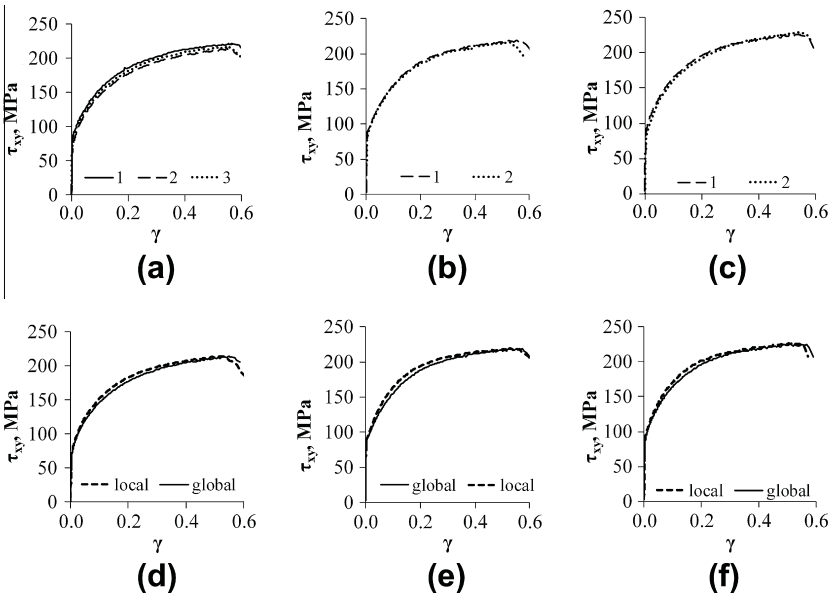

Fig. 5. Shear stress–strain curves (τ–γ) for the 600_350 (a and d), 600_100 (b and e) and 600_50 (c and f) samples.

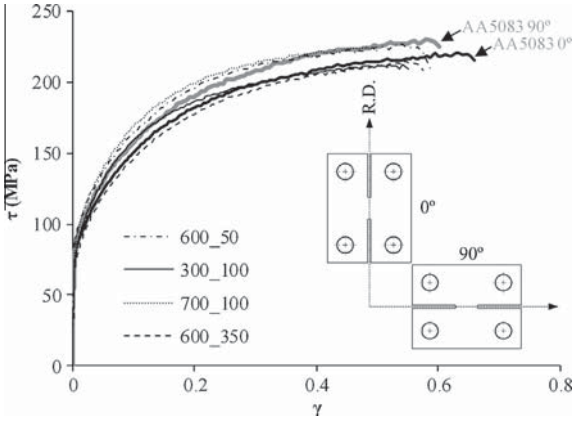

Fig. 6. Global shear stress strain curves (τ–γ) for the base material and some of the weld samples.

graph clearly shows that in spite of the varying welding conditions, no important differences in grain size and hardness were reported for the different welds, which is in accordance with the small differences in plastic behaviour depicted from the shear tests. However, it is also important to enhance that in spite of the similarities reported in the microstructural and mechanical analysis, strong differences in weld morphology were obtained by changing the welding conditions. Some of the welds sampled had important surface defects, more precisely, important thickness reduction due to flash formation. It is also important to remark that in spite of the considerable grain size reduction in the weld, relative to the base material, which can be depicted in Fig. 7b, no important differences in strength and/or plastic behaviour were reported in either shear or hardness testing.

Finally, in Fig. 8 are plotted tensile stress–strain curves (σ–ε) for the base material (at 0° and 90° with the rolling direction), a local tensile stress strain curve, corresponding to one of the welds (600_100), obtained by testing a transverse weld specimen in tension and using the procedure described in [13], and equivalent stress–strain curves computed from shear testing results for both the weld and base material. In a previous study [25], it was possible to conclude that the AA5083-H111 alloy plastic behaviour, is perfectly described using the Hill'48 plasticity criteria

$$F(\sigma_{yy}-\sigma_{zz})^2+G(\sigma_{zz}-\sigma_{xx})^2+H(\sigma_{xx}-\sigma_{yy})^2+2L\tau_{yz}^2+2M\tau_{zx}^2+2N\tau_{xy}^2=K^2 \quad (3)$$

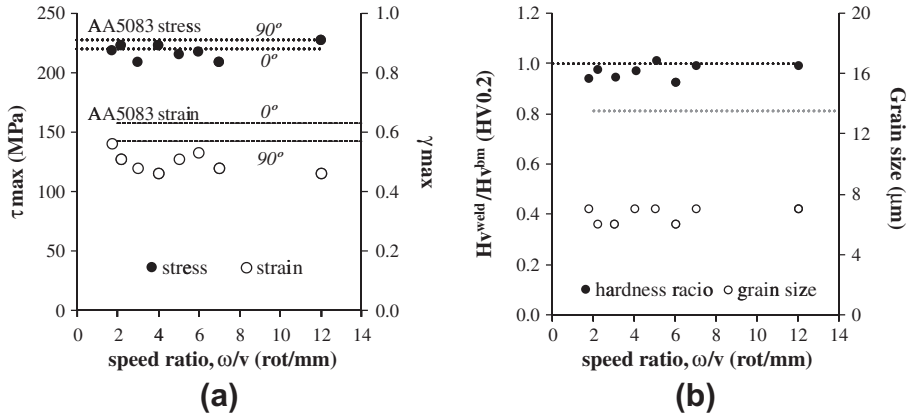

Fig. 7. Maximum shear stress and strain (a), hardness ratio (Hv^{weld}/Hv^{bm}) and average grain sizes (GS) for all the welds tested and base material.

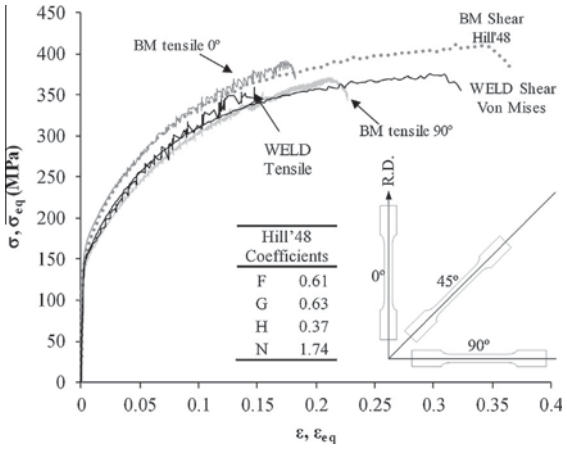

Fig. 8. Equivalent strain–stress (σ–ε) curves for the base material and 600_100 weld.

where σ_{xx}, σ_{yy}, σ_{zz}, τ_{xy}, τ_{xz} and τ_{yz}, are the components of the Cauchy stress tensor, defined in the orthotropic frame, K is the tensile yield stress in the rolling direction, and F, G, H, L, M and N are the Hill coefficients of anisotropy, which were determined in that work and are shown in the table in the graph of Fig. 8. The equivalent stress–strain curve for the weld sample was calculated using the Von Mises criteria

$$(\sigma_{yy}-\sigma_{zz})^2+(\sigma_{zz}-\sigma_{xx})^2+(\sigma_{xx}-\sigma_{yy})^2+6\tau_{yz}^2+6\tau_{zx}^2+6\tau_{xy}^2 = 2\sigma_0^2 \quad (4)$$

where σ_0 is the yield stress determined for the weld in the tensile testing of transverse weld samples.

In Fig. 8 it is possible to observe that, as already observed in Fig. 7, the weld material is in even-match with the base material, since the weld tensile stress–strain curve follows between the tensile curves of the base material (0° and 90°). It is also important to notice the excellent concordance, until relatively high values of plastic deformation ($\varepsilon \approx 0.15$), between the weld tensile curve and the Von Mises equivalent curve, computed from the weld shear testing results. Contrary to this, for the base material, the best fit was obtained using the Hill criteria. These results may be indicative that the recrystallized weld nugget has isotropic behaviour in plastic deformation. In any case, characterising the anisotropy of the weld would be very hard, due the difficulty in performing tensile or shear testing transverse to the weld direction. Current results show that using Von Mises would give satisfactory results in describing the weld material plastic behaviour.

5. Conclusions

The methodology proposed in this work allowed to accurately characterise the plastic behaviour of AA5083 friction stir welds produced under a large range of welding conditions. It was demonstrated that sample free-end influence on strain distribution, inside the shear zone, had no significant influence on global strain path evolution during shear testing nor on the global stress–strain results. The small differences in plastic behaviour, depicted from the shear tests results, were found to be in accordance with the small variations in grain size and hardness registered for the different welds. An excellent concordance was also obtained by comparing the equivalent Von Mises curves, plotted from the shear stress–strain curves, with weld tensile stress–strain curves, which states the suitability of the proposed method to be used in local mechanical characterisation of welds.

Acknowledgements

This research is sponsored by FEDER funds through the program COMPETE – Programa Operacional Factores de Competitividade – and by national funds through FCT – Fundação para a Ciência e a Tecnologia –, under the Project PEst-C/EME/UI0285/2011.

References

[1] Maier P, Richter A, Faulkner RG, Ries R. Application of nanoindentation technique for structural characterisation of weld materials. Mater Charact 2002;48:329–39.
[2] Baltazar Hernandez VH, Panda SK, Kuntz ML, Zhou Y. Nanoindentation and microstructure analysis of resistance spot welded dual phase steel. Mater Lett 2010;64:207–10.
[3] Charitidis CA, Dragatogiannis DA, Koumoulos EP, Kartsonakis IA. Residual stress and deformation mechanism of friction stir welded aluminum alloys by nanoindentation. Mater Sci Eng A – Struct Mater Prop Microstruct Process 2012;540:226–34.
[4] Rao D, Heerens J, Pinheiro GA, dos Santos JF, Huber N. On characterisation of local stress–strain properties in friction stir welded aluminium AA 5083 sheets using micro-tensile specimen testing and instrumented indentation technique. Mater Sci Eng A – Struct Mater Prop Microstruct Process 2010;527:5018–25.
[5] Samardžić I, Stoić A, Kozak D, Kladaric I, Dunđer M. Application of weld thermal cycle simulator in manufacturing engineering. In: second international conference of manufacturing engineering & management 2012, Prešov, Slovak Republic; 2012.
[6] Østby E, Kolstad GT, Akselsen OM, Thaulow C, Hauge M. Comparison of fracture toughness in real weld and thermally simulated CGHAZ of a 420 MPa rolled plate. In: 22nd international offshore and polar engineering conference, Rhodes, Greece: International Society of Offshore and Polar Engineers (ISOPE); 2012.
[7] Yang JG, Sung SH, Chen CS, Tan AH. Study of microstructural and mechanical properties of weld heat affected zones of 2024-T3 aluminium using Gleeble simulation. Mater Sci Technol 2011;27:357–65.
[8] Zhang ZL, Silvanus J, Li HK, Shi QY. Sensitivity analysis of history dependent material mechanical models for numerical simulation of welding process. Sci Technol Weld Joining 2008;13:422–9.
[9] Bleck W, Reisgen U, Mokrov O, Rossiter E, Rieger T. Methodology for thermomechanical simulation and validation of mechanical weld-seam properties. Adv Eng Mater 2010;12:147–52.
[10] Rao D, Huber K, Heerens J, Santos JF, Huber N. Asymmetric mechanical properties and tensile behaviour prediction of aluminium alloy 5083 friction stir welding joints. Mater Sci Eng A – Struct Mater Prop Microstruct Process 2013;565:44–50.
[11] Sutton MA, Yang BC, Reynolds AP, Yan JH. Banded microstructure in 2024-T351 and 2524-T351 aluminum friction stir welds – Part II. Mechanical characterization. Mater Sci Eng A – Struct Mater Prop Microstruct Process 2004;364:66–74.
[12] Reynolds AP, Duvall F. Digital image correlation for determination of weld and base metal constitutive behavior. Weld J 1999;78:355S–60S.
[13] Leitao C, Galvao I, Leal RM, Rodrigues DM. Determination of local constitutive properties of aluminium friction stir welds using digital image correlation. Mater Des 2012;33:69–74.
[14] Lockwood WD, Tomaz B, Reynolds AP. Mechanical response of friction stir welded AA2024: experiment and modeling. Mater Sci Eng A – Struct Mater Prop Microstruct Process 2002;323:348–53.
[15] Genevois C, Deschamps A, Vacher P. Comparative study on local and global mechanical properties of 2024 T351, 2024 T6 and 5251 O friction stir welds. Mater Sci Eng A – Struct Mater Prop Microstruct Process 2006;415:162–70.
[16] Hatamleh O. Effects of peening on mechanical properties in friction stir welded 2195 aluminum alloy joints. Mater Sci Eng A – Struct Mater Prop Microstruct Process 2008;492:168–76.
[17] Brown R, Tang W, Reynolds AP. Multi-pass friction stir welding in alloy 7050-T7451: effects on weld response variables and on weld properties. Mater Sci Eng A – Struct Mater Prop Microstruct Process 2009;513–14:115–21.
[18] Boyce BL, Reu PL, Robino CV. The constitutive behavior of laser welds in 304L stainless steel determined by digital image correlation. Metall Mater Trans A – Phys Metall Mater Sci 2006;37A:2481–92.
[19] Scintilla LD, Tricarico L, Brandizzi M, Satriano AA. Nd:YAG laser weldability and mechanical properties of AZ31 magnesium alloy butt joints. J Mater Process Technol 2010;210:2206–14.
[20] Sutton MA, Yan JH, Avril S, Pierron F, Adeeb SM. Identification of heterogeneous constitutive parameters in a welded specimen: uniform stress and virtual fields methods for material property estimation. Exp Mech 2008;48:451–64.
[21] Rodrigues DM, Menezes LF, Loureiro A, Fernandes JV. Numerical study of the plastic behaviour in tension of welds in high strength steels. Int J Plast 2004;20:1–18.
[22] Atkins AG. Fracture in forming. J Mater Process Technol 1996;56:609–18.
[23] Bao YB, Wierzbicki T. On fracture locus in the equivalent strain and stress triaxiality space. Int J Mech Sci 2004;46:81–98.

[24] Reyes A, Eriksson M, Lademo OG, Hopperstad OS, Langseth M. Assessment of yield and fracture criteria using shear and bending tests. Mater Des 2009;30:596–608.
[25] Leitao C, Loureiro A, Rodrigues DM. Assessment of mechanical shear response using digital image correlation. In: Silva Gomes JF, Mário APV, editors. 15th international conference on experimental mechanics. Porto 2012. p. 93–4.
[26] Gsell C, Boni S, Shrivastava S. Application of the plane simple shear test for determination of the plastic behaviour of solid polymers at large strains. J Mater Sci 1983;18:903–18.
[27] Bouvier S, Alves JL, Oliveira MC, Menezes LF. Modelling of anisotropic work-hardening behaviour of metallic materials subjected to strain-path changes. Comput Mater Sci 2005;32:301–15.
[28] Bouvier S, Haddadi H, Levee P, Teodosiu C. Simple shear tests: EXPERIMENTAL techniques and characterization of the plastic anisotropy of rolled sheets at large strains. J Mater Process Technol 2006;172:96–103.
[29] Leitao C, Louro R, Rodrigues DM. Using torque sensitivity analysis in accessing friction stir welding/processing conditions. J Mater Process Technol 2012;212:2051–7.
[30] Leitao C, Louro R, Rodrigues DM. Analysis of high temperature plastic behaviour and its relation with weldability in friction stir welding for aluminium alloys AA5083-H111 and AA6082-T6. Mater Des 2012;37:402–9.
[31] ARAMIS. User manual – Software. v6.1 rev.b ed. Braunschweig, Germany: GOM mbH; 2009.
[32] Chu TC, Ranson WF, Sutton MA, Peters WH. Applications of digital-image-correlation techniques to experimental mechanics. Exp Mech 1985;25:232–44.
[33] Luo PF, Chao YJ, Sutton MA, Peters WH. Accurate measurement of 3-dimensional deformations in deformable and rigid bodies using computer vision. Exp Mech 1993;33:123–32.

Annex C

PAPER REF:3214

ASSESSMENT OF MECHANICAL SHEAR RESPONSE USING DIGITAL IMAGE CORRELATION

Carlos Leitão[1], Altino Loureiro[2] and Dulce Rodrigues[3(*)]
[1, 2, 3] CEMUC, Mechanical Engineering Department, University of Coimbra, Coimbra, Portugal
(*)*Email:* dulce.rodrigues@dem.uc.pt

ABSTRACT

In this work, a special tool, developed for running shear tests using a universal tensile testing machine is described, as well as the procedures used for strain data acquisition via Digital Image Correlation (DIC). Testing procedures were developed and verified by testing two aluminium alloys widely used in welding construction, the heat-treatable AA6082-T6 and the non-heat-treatable AA5083-H111 aluminium alloys, which are characterized by markedly different strengthening mechanisms, having completely different mechanical behaviour under large plastic deformations. Microstructural analyses were accomplished in order to evaluate the accuracy of strain data acquisition by DIC in capturing the strain gradients along the gage section of the shear samples.

Keywords: shear testing, plastic behaviour, DIC, anisotropy.

INTRODUCTION

Nowadays, the continuous development of new materials, in addition to the continuous effort in improving and/or developing innovative industrial products, makes mandatory the development of extensive and accurate techniques for assessing chemical and physical properties, as well as for characterizing the mechanical behaviour of the materials under complex loading conditions. As it is well known, several tests regarding the characterization of metallic and non-metallic materials have already been developed and standardized. The most common between them, is the uniaxial tensile test, which is widely used for the assessment of mechanical properties at both the research and industrial levels. However, despite being a test of simple execution and having easy reproducibility of results, the tensile test doesn't supply enough information when the objective is to characterize the plastic behaviour of the materials under complex and/or severe plastic deformation conditions. In order to overcome this difficulty, the shear test appeared as an alternative approach for assessing mechanical properties under this type of solicitations. In fact, due to the delay in strain localization at maximum load, when compared to the uniaxial tensile test, the shear test allows the study of the mechanical behaviour under large deformations (Atkins, 1996) and to easily perform tests under reverse loading conditions (Bouvier, 2005) as well. Although no standards regulating shear testing procedures have already been developed, this mechanical test has already been used by several researchers for characterizing metallic materials, which developed distinct testing mechanisms (Bao, 2004; Reyes, 2009).

In this paper, a testing tool and testing samples specially conceived for testing thick material plates in simple shear, using a universal tensile testing machine, are presented. The accuracy of the developed testing procedure was evaluated by testing AA5083-H111 and AA6082-T6 aluminium alloys, which, as noticed in previous works from current authors (Leitão, 2012a), present markedly different plastic behaviours in tension. During the test,

strain data acquisition was performed by using Digital Image Correlation (DIC), which also required developing and checking appropriate procedures for strain data analysis (Leitão, 2012b). Finally, in order to access the accuracy of the developed testing and strain data analysis techniques, the mechanical response registered in shear, for the AA5083 and AA6082 alloys, is compared to that registered in uniaxial tension, by plotting equivalent stress-strain curves. Microstructural analysis was also accomplished in order to evaluate the accuracy of strain data acquisition by DIC in capturing the heterogeneous strain distribution across the gage section of the shear samples.

EXPERIMENTAL PROCEDURE

Two base materials, a non-heat-treatable (AA5183-H111) and a heat-treatable aluminium (AA6082-T6) alloy, widely used in transportation industries, were characterized in this study. The plastic behaviour of the base materials, supplied in 4 and 3 mm thick plates, respectively, was analysed by performing simple shear and tensile tests, using a 100kN universal testing machine (Instron 4206) in quasi-static conditions (5 mm min^{-1}). In order to characterize the anisotropy of both materials, the monotonic tensile tests were performed at 0, 45º and 90º to the rolling direction (RD). In both the tensile and shear tests, local strain fields were acquired by DIC using the Aramis 3D 5M optical system (GOM GmbH). Before testing, the specimens were prepared by applying a random black speckle pattern, over the previously mat white painted surface, in order to enable strain data acquisition by DIC. After testing, the gage sections of the shear samples were analysed, following standard metallographic practice, enabling to identify different deformation patterns. Metallographic analysis was performed using an optical microscope ZEISS HD 100.

DESCRIPTION OF SHEAR TESTING TOOL AND SHEAR SAMPLE GEOMETRY

In this work, a special tool enabling to perform simple shear tests was developed. The shear device, shown in Fig. 1a, works directly connected to a tensile testing machine, which promotes the parallel translation between the fixed and moving parts of the tool, which are identified in the figure. The shear samples, whose geometry is shown in Fig. 1b, are placed in the tool with the aid of cylindrical guides (a in Fig. 1a) and fixed using grips (b in Fig. 1a). Tool design was conceived in order to avoid any rotation of the moving part of the tool, enabling the planar deformation of the sample during the test. In this way, as can be observed in Fig. 1c, where a scheme representing *Section A* in Fig. 1b is shown, the vertical translation of the moving part of the tool promotes the deformation in simple shear of the central section of the sample, with lower cross-section, labelled as *shear zone* in Fig. 1b. The samples' geometry was selected in order to avoid undesirable phenomena, such as buckling, stress concentration and abnormal strain distribution at the shear zone free-ends, which were reported by G'Sell, 1984, Bouvier, 2006a and Bouvier, 2006b in shear testing of very thin plates.

Due to the high relevance of the size of the homogeneous strain area, on shear testing results, several authors have already studied the influence of specimen dimensions on strain distribution. Bouvier et al. (2006b) stated that the size of the heterogeneous deformation area increases by decreasing the length (l_0) to width (h) ratio of the shear zone. In Fig. 1b, where the dimensions of the different shear samples features are shown, it is possible to depict that the maximum shear area width is 3 mm (h) and the minimum shear length (l_o) is 20 mm. Actually, the circular geometry at the free-end of the shear zone, promotes a smooth variation

of the *h* value and the maximization of the geometry factor (l_0/h), at the centre of the sample, which optimizes the homogeneous strain area size.

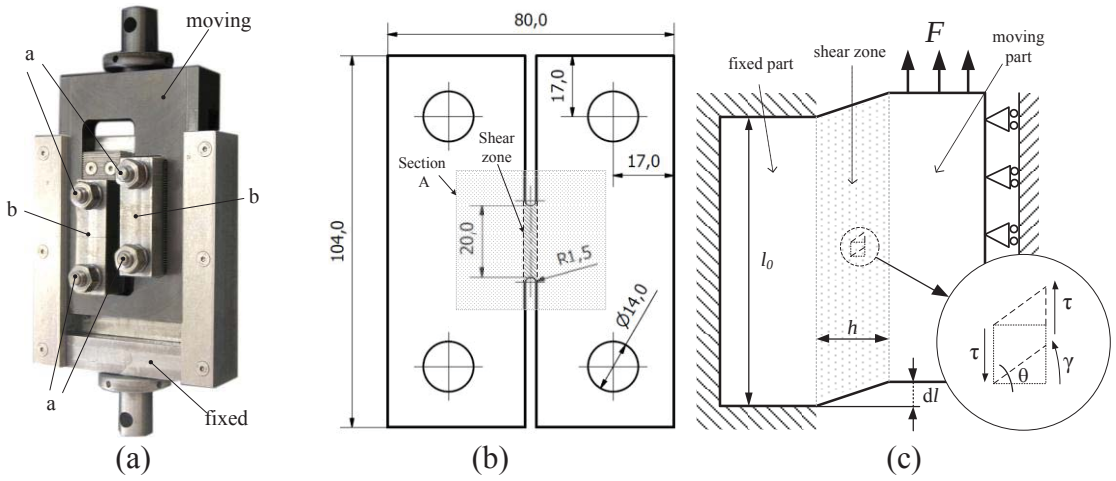

Fig. 1 Shear test tool (a), shear test sample geometry (b) and scheme of the shear zone behaviour under simple shear solicitation (c).

Due to its potential effect on load testing results, the friction load between the fixed and moving parts of the shear testing tool was measured. In Fig. 2 is compared the load versus time evolution for tests performed with and without sample. Observing the figure, it is possible to conclude that the load values for the test performed without sample are much lower than that registered in testing a sample, which allows concluding that the influence of the friction between the fixed and moving parts of the shear tool, on testing load results, is negligible.

In Fig. 3 is shown an image of the sample gage section before testing (Fig. 3a) and after plastic deformation, at maximum load (Fig. 3b). In Fig. 3b is also shown the corresponding vertical displacement map, acquired by DIC. Analysing this map, it is possible to conclude that the region marked as 1, corresponding to the part of the sample clamped to the fixed part of the shear tool, displays a uniform vertical displacement of 1.32 mm, indicating that the sample slipped slightly during testing. However, as stated by Bouvier et al. (2006b), the use of a noncontact optical technique, such as DIC, for strain data acquisition, enables to eliminate the influence of any sample slipping during the test on strain measurement.

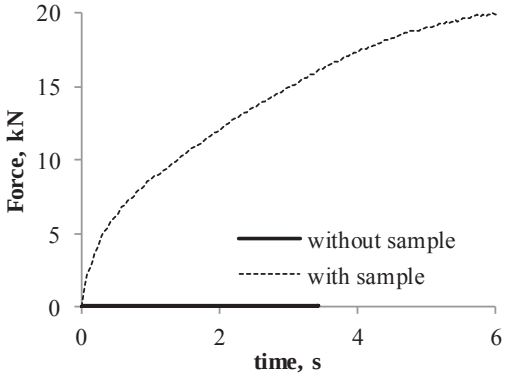

Fig. 2 Load (N) versus time (s) evolution in tests performed with and without sample.

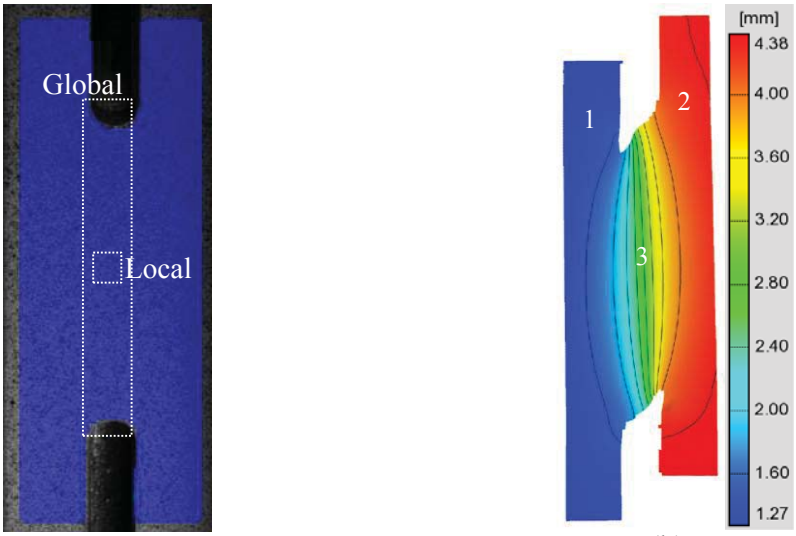

(a) (b)

Fig. 3 Gage section before testing (a) and vertical displacement map at maximum load (b).

STRAIN DATA ANALISYS

In Fig. 4a and Fig. 4b are shown ε_{xy} strain maps, calculated using ARAMIS software, at half of the maximum load ($F_{max}/2$) and at maximum load (F_{max}), for AA 5083 and AA 6082 samples, respectively. As it is possible to see in the figure, after yielding, an area of heterogeneous plastic deformation is formed along the shear zone, symmetric relative to the loading direction and to the sample middle-plane. The gradient in strain distribution becomes sharper at maximum load, when strain localization occurs at the free-ends of the shear zone. G'Sell et al.(1983) reported that this strain concentration results, on one hand, from the constrain effect of the grips, reacting against the rotational moment imposed by the couple of shearing forces and, on the other hand, from the departure from ideal simple shear conditions, at the shear zone free-end, where stresses normal and parallel to the sample surfaces develop. The localized transverse tensile stresses, at the shear zone free-ends, promote the strain localization at maximum load.

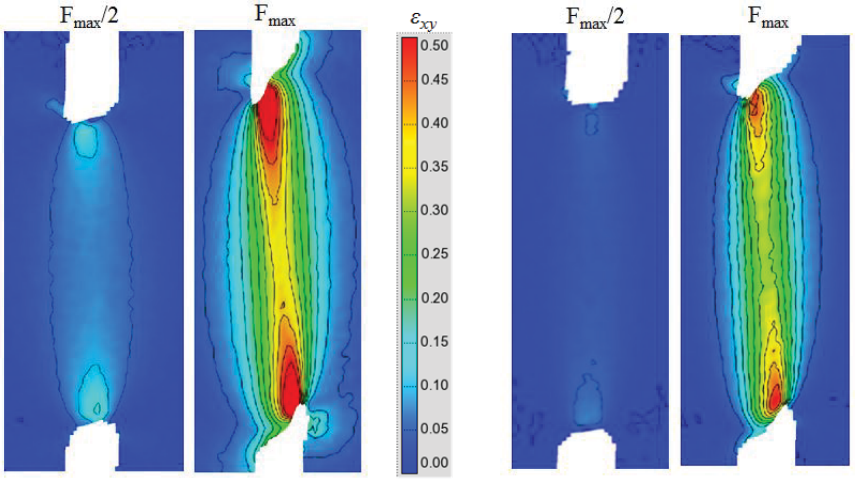

(a) (b)

Fig. 4 Strain maps (ε_{xy}) at half of maximum load ($F_{max}/2$) and at maximum load (F_{max}) for the AA5083 (a) and AA6082 (b) alloys.

In order to evaluate the accuracy of the strain data acquisition by DIC in capturing the strain gradients across the gage section, metallographic analyses were performed in order to identify different deformation patterns across the shear zone. The microstructural evolution near the fracture zone of AA5083 and AA6082 shear samples is shown in Fig. 5 and Fig. 6, respectively. In these pictures it is possible to see the evolution in grain shape and orientation, from the non-deformed part of the sample, to the fracture surface. The evolution of the angle between the initial grain orientation and the normal to the loading direction (θ) was measured, being marked in both micrographs. In both figures are also shown shear angle maps (γ), obtained by DIC, after maximum load, for the same samples. Since the shear angle (θ) and the shear strain (γ) may be related through the expression

$$\gamma = \tan\theta \cong \theta, \qquad (1)$$

the results from the metallographic analysis were compared with DIC measurements, as is shown in the graphs of Fig. 7a and Fig. 7b, for the AA5083 and AA6082 alloys, respectively. In each of these graphs, the evolution of θ and γ with the distance to the fracture surface of the samples is plotted, considering the sample sections marked by black lines in each strain map of the Fig. 5 and Fig. 6. From the graphs it is possible to depict that both type of results are in very good agreement.

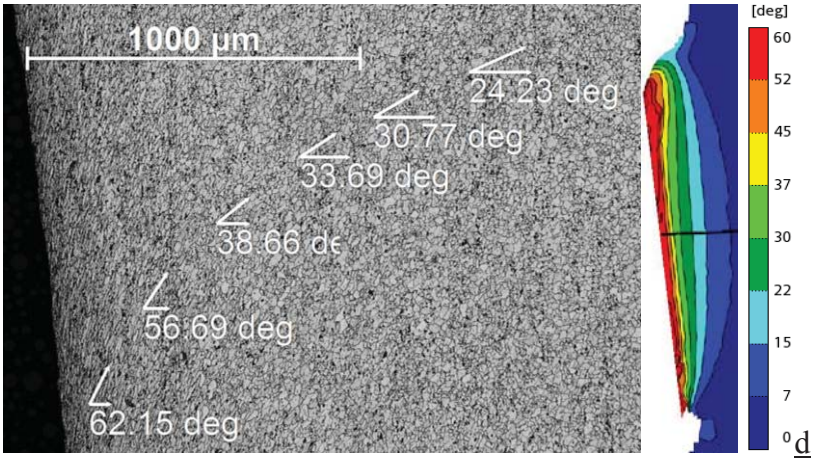

Fig. 5 Evolution of grain orientation (θ), from micrographic analysis, and shear strain angle (γ), assessed by DIC, for the AA5083-H111 alloy.

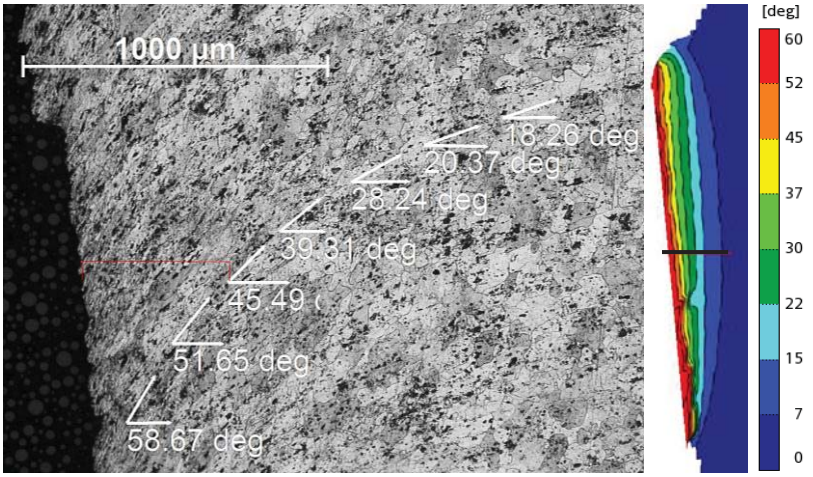

Fig. 6 Evolution of grain orientation (θ), from micrographic analysis, and shear strain angle (γ), assessed by DIC, for the AA6082-T6 alloy.

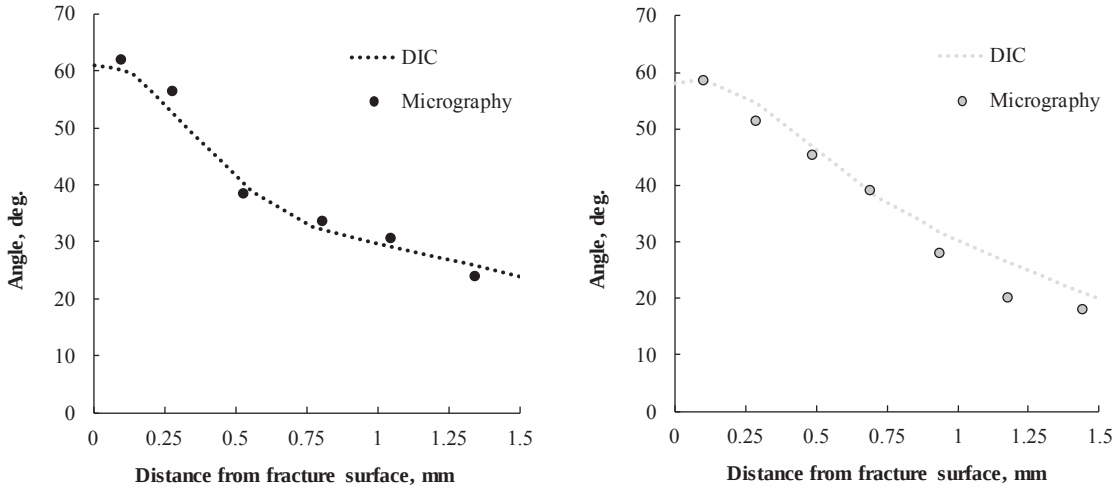

Fig. 7 Evolution of grain orientation (θ), from micrographic analysis, and shear strain angle (γ), assessed by DIC, for the AA5083-H111 (a) and AA6082-T6 (b) alloys.

For each sample tested, the strain path evolution with plastic deformation, inside the shear zone, was also analysed in order to verify if the simple shear loading conditions prevail until maximum load, in spite of the non-uniform strain distribution depicted in previous figures. The major (ε_1) versus minor strain (ε_2) evolution, which is representative of the strain path evolution during loading, is shown in Fig. 8a and Fig. 8b, for the AA5083 and AA6082 alloys, respectively. The results plotted in the graphs, correspond to average strain values calculated using Aramis software. Two evaluation areas were considered for calculating the average strains ε_1 and ε_2, which are identified as Local and Global in Fig. 3a. Using the Global evaluation area, the full range of strain values registered in the shear zone is considered for computing the average strains. Using the Local evaluation area, only the strain values at the centre of the sample, where the strain fields are homogeneous, are considered in computing the average strains.

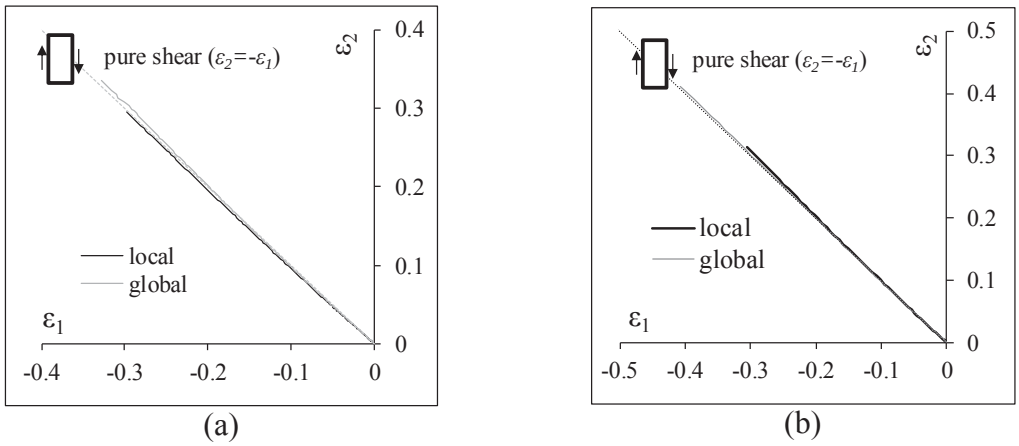

Fig. 8 Strain path evolution, during shear testing, for AA5083 (a) and AA6082 (b) samples.

Analysing Fig. 8 results, for both alloys, it is possible to conclude that pure-shear conditions ($\varepsilon_2 = -\varepsilon_1$) prevail until maximum load, independently of the strain evaluation area considered. Actually, no strain path change is observed, even considering the global evaluation area, which allows concluding that the free-end influence on strain distribution, inside the shear zone, has no significant influence on global strain path evolution.

STRESS-STRAIN ANALYSIS

Using the strain data acquired by DIC, shear stress-strain curves (τ, γ) were computed, considering the Local and Global strain evaluation areas indicated in Fig. 4a for calculating the average strain (γ) in the shear zone. Assuming iso-stress conditions during shear testing, the shear stress ($\tau = \tau_{xy}$) was obtained by dividing the testing load (F) by the shear zone cross-section area (A), according to the equation

$$\tau = \frac{F}{A} = \frac{F}{h \times t} \qquad (2)$$

where, h and t are the length and thickness of the shear zone, respectively. In the same way, the shear strain (γ) was obtained considering the relation

$$\gamma = 2\varepsilon_{xy}. \qquad (3)$$

The Local and Global average shear stress-strain curves ($\tau - \gamma$) are plotted in Fig. 9, where it is possible to depict an excellent concordance between both type of results. This shows that the non-uniform shear strain distribution, depicted in previous analysis, does not influence significantly the shape of curves. The only difference between Local and Global results is that the strain values, corresponding to the global strain average, are significantly higher than the local average strain values, corresponding to the local area with homogeneous strain distribution, at the centre of the sample.

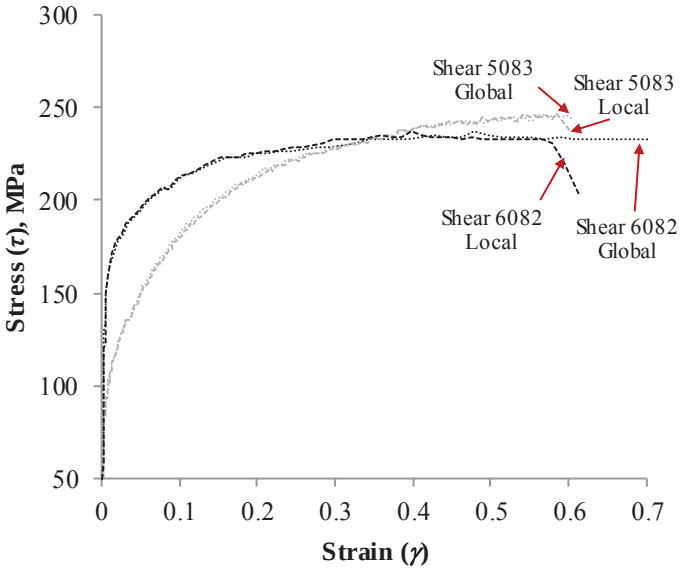

Fig. 9 Local and global shear stress-strain curves.

Analysing the shear stress-strain curves, it is possible to conclude that the AA6082 alloy, after moderate values of plastic deformation, presents an almost steady-state flow stress, which is in accordance to that reported by Rauch et al., 2002, for other aluminium alloys of the 6xxx series. On the other hand, for the AA5083 alloy, which displays lower yield strength than the AA6082 alloy, the flow stress keeps increasing with loading. Actually, the AA5083 alloy attains strength values higher than that of the AA6082 alloy, after some plastic deformation. The differences in strain-hardening behaviour determine the shape and size of the plastic deformation area, at the centre of the sample, which as shown in Fig. 4, is narrower for the AA6082 alloy, than for the AA5083 alloy. Actually, the AA5083 displays a wider plastic deformation zone, with a belly form, for the same strain range of the AA6082, due to its stronger hardening sensitivity.

Finally, in Fig. 10 are compared the equivalent stress-strain curves corresponding to uniaxial tensile tests and shear tests, for both alloys. The equivalent stress-strain curves were obtained using the Hill'48 plasticity criteria (Hill, 1948)

$$F\left(\sigma_{yy}-\sigma_{zz}\right)^2+G\left(\sigma_{zz}-\sigma_{xx}\right)^2+H\left(\sigma_{xx}-\sigma_{yy}\right)^2+2L\tau_{yz}{}^2+2M\tau_{zx}{}^2+2N\tau_{xy}{}^2=1 \tag{4}$$

where σ_{xx}, σ_{yy}, σ_{zz}, τ_{xy}, τ_{xz} and τ_{yz}, are the components of the Cauchy stress tensor, defined in the orthotropic frame, and F, G, H, L, M and N are the Hill coefficients of anisotropy. The Hill48 coefficients were calculated according to the equations

$$F=\frac{r_0}{r_{90}(1+r_0)} \tag{5}$$

$$G=\frac{1}{1+r_0} \tag{6}$$

$$H=\frac{r_0}{1+r_0} \tag{7}$$

$$N=(r_0+r_{90})\frac{(2r_{45}+1)}{2r_{90}(1+r_0)} \tag{8}$$

where r_0, r_{45} and r_{90} are the anisotropy coefficients determined by performing tensile tests at 0, 45 and 90º from the rolling direction. In Table 1 are shown the anisotropy coefficients and the Hill48 coefficients determined for both alloys.

Table 1 –Anisotropy coefficients

	r_0	r_{45}	r_{90}	***F***	***G***	***H***	***N***
AA5083	0.607	0.521	0.608	**0.621**	**0.622**	**0.378**	**1.269**
AA6082	0.681	0.576	0.699	**0.580**	**0.595**	**0.405**	**1.264**

Observing Fig. 10, it is possible to conclude that, until moderate values of plastic deformation ($\varepsilon \approx 0.1$), the tensile and shear equivalent stress-strain curves are in excellent concordance, for both alloys. However, for higher levels of plastic deformation, the tensile curves become higher than the shear curves, which points for the limitations of the Hill48 criteria in describing aluminium alloys behaviour, as already stated by other authors (Wang and Lee, 2006).

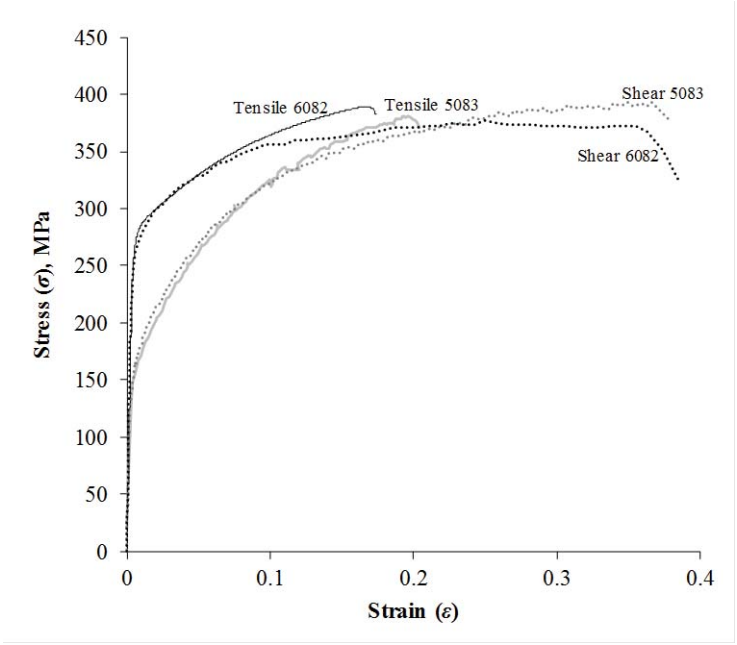

Fig. 10 Tensile and shear equivalent stress-strain curves.

CONCLUSIONS

From current study, it was possible to depict the good accuracy of results obtained using DIC to evaluate the shear response for the AA5083 and AA6082 alloys, as well as the benefits of the shear test in assessing materials constitutive behaviour until very large values of plastic deformation. The shear data was validated by comparing shear equivalent stress-strain curves, calculated using the Hill48 criterion, with the ones obtained in uniaxial tension. For both alloys, the concordance between shear and tensile curves, for moderate values of plastic deformation, was evident. The shear testing procedure developed in current work is now prone to be used in assessing the plastic properties of thick plates, with special relevance for the local characterization of the plastic properties of welds, for which the limited width of the sampling area makes the mechanical characterization in tension very hard.

ACKNOWLEDGMENTS

The authors indebted to the Portuguese Foundation for the Science and Technology (FCT) and FEDER for the financial support.

REFERENCES

Atkins AG. Fracture in forming. Journal of Materials Processing Technology. 1996, 56, p. 609-618.

Bao Y, Ghosh AK. On fracture locus in equivalent strain and stress triaxiality space. International Journal of Mechanical Sciences. 2004, 46, p. 81-98.

Bouvier S, Alves JL, Oliveira MC, Menezes LF. Modelling of anisotropic work-hardening behaviour of metallic materials subjected to strain-path changes. Computational Materials Science. 2005, 32 (3–4), p. 301-315.

Bouvier S, Gardey B, Haddadi H, Teodosiu C. Characterization of the strain-induced plastic anisotropy of rolled sheets by using sequences of simples shear and uniaxial tensile tests. Journal of Materials Processing Tecnology. 2006, 174, p. 115-126.

Bouvier S, Haddadi H, Levée P, Teodosiu C. Simple shear tests: Experimental techniques and characterization of the plastic anisotropy of rolled sheets at large strains. Journal of Materials Processing Tecnology. 2006, 172, p. 96-103.

G'Sell C, Boni S, Shrivastava S. Application of the plane simple shear test for determination of the plastic behaviour of solid polymers at large strains. Journal of Materials Science. 1983, 18, p. 903-918.

Hill R. A theory of the yielding and plastic flow of anisotropic metals. Proceedings of the Royal Society A, 1948, 193, p. 281-297.

Leitão C, Louro R, Rodrigues DM. Analysis of high temperature plastic behaviour and its relation with weldability in friction stir welding for aluminium alloys AA5083-H111 and AA6082-T6. Materials and Design. 2012, 37, p. 402-409.

Leitão C, Galvão I, Leal RM, Rodrigues DM. Determination of local constitutive properties of aluminium friction stir welds using digital image correlation. Materials and Design. 2012, 33, p. 69–74.

Rauch EF, Gracio JJ, Barlat F, Lopes AB, Duarte Ferreira J. Hardening behaviour and structural evolution upon strain reversal of aluminium alloys. Scripta Materialia. 2002, 46, p. 881-886.

Reyes A, Eriksson M, Lademo O-G, Hopperstad OS, Langseth M. Assessment of yield and fracture criteria using shear and bending tests. Materials and Design. 2009, 30, p. 596-608.

Wang L, Lee TC. The effect of yield criteria on the forming limit curve prediction and deep drawing process simulation. International Journal of Machine Tools and Manufacture. 2006, 46, p. 988-995.

Annex D

High speed friction stir welding of aluminium alloys

D. M. Rodrigues*[1], C. Leitão[1], R. Louro[2], H. Gouveia[2] and A. Loureiro[1]

In this paper, the weldability of AA 5083-H111 (non-heat treatable) and AA 6082-T6 (heat treatable) aluminium alloys, which are widely used in welding fabrication, is compared by analysing the welds obtained from both materials under a large range of welding conditions (varying tool dimensions, rotation and traverse speeds, axial loads and tilt angles) chosen to ensure high welding speeds. The differences in friction stir weldability, assessed by weld defect analysis and weld strength characterisation, will be related to the markedly different plastic behaviours of both base materials. Based on the experimental results, a methodology for determining suitable friction stir welding parameters is proposed.

Keywords: Aluminium, Weldability, Productivity, Process parameters, Plasticity

Introduction

The friction stir welding (FSW) process is commonly accepted as a promising method for joining light metallic alloys. However, the extended application of this welding process in industry still requires accurate knowledge of the joining mechanism, and the metallurgical and mechanical transformations it induces in the base materials. This knowledge will then allow the establishment of suitable welding parameters for joining a large range of materials in varied weld configurations, such as different plate thicknesses or joint types. Another important aspect is to guarantee improved levels of welding productivity. Since the welding speed has a direct influence on the process productivity,[1] in any welding operation in an industrial context, the objective behind the selection of suitable welding parameters has to be to maximise the welding speed while ensuring acceptable welding quality.

Although FSW technology has attracted significant interest from the aerospace and transportation industries, and extensive literature exists on FSW, there are few reported systematic studies on process parameter optimisation. Example of this is the extensive literature published concerning the joining of aluminium alloys, for which a deep revision can be found in Refs. 2–4 and examples of very recent works already performed in magnesium,[5] copper,[6] steel[7] and titanium.[8] On the other hand, though numerical modelling of plastic flow in FSW has provided guidelines concerning tool design and weld quality optimisation,[9] there does not appear to have been an application of these models towards the prediction of practical processing maps. The only principle globally accepted is that, for each set of welding conditions (joint type, base material and plate thickness), a specific set of welding parameters must be used to ensure acceptable process behaviour.

In this paper, the weldabilities in FSW of AA 5083-H111 (non-heat treatable) and AA 6082-T6 (heat treatable) aluminium alloys, which are widely used in welding fabrication, are compared by analysing the welds obtained from both materials under a large range of welding conditions (varying tool dimensions, rotation speeds, axial loads and tilt angles) and high welding speeds. The differences in friction stir weldability, which were evaluated based on weld defect analysis and weld strength characterisation, are related to the different mechanical and microstructural evolutions with temperature and plastic deformation of the base materials. These differences lead to drastically different welding behaviours, as has already been described in previous studies.[11–24] In fact, among the base materials already joined by FSW, the 6xxx series of aluminium alloys is the most widely analysed under a large range of welding conditions. According to these previous studies, the mechanical properties of the AA 6xxx friction stir welds depend mainly on the size, volume fraction and distribution of precipitates in the weld line and adjacent heat affected zone (HAZ). Friction stir welding of the non-heat treatable aluminium alloys, such as the AA 5xxx series, is much less studied than for the AA 6xxx alloys. However, it has already been established that the mechanical properties of the welds produced from the AA 5xxx alloys depend mainly on the grain size and on the density of the dislocations after plastic deformation and recrystallisation occurring during welding. When the AA 5xxx alloy series is used under the annealed condition, the microstructure is stable and usually no softening occurs in the weld zone and HAZ. In contrast, when these alloys are used under the strain hardened condition, the work hardened structure will readily recover and/or recrystallise during welding, and softening may occur.

[1]CEMUC, Department of Mechanical Engineering, University of Coimbra, Rua Luís Reis Santos, 3030-788 Coimbra, Portugal
[2]ISQ, Welding and Quality Institute, Avenida Cavaco Silva no. 33, 2740-120 Porto Salvo, Portugal

*Corresponding author, email dulce.rodrigues@dem.uc.pt

Science and Technology of Welding and Joining stw1709.3d 30/8/10 14:59:25
The Charlesworth Group, Wakefield +44(0)1924 369598 - Rev 7.51n/W (Jan 20 2003)

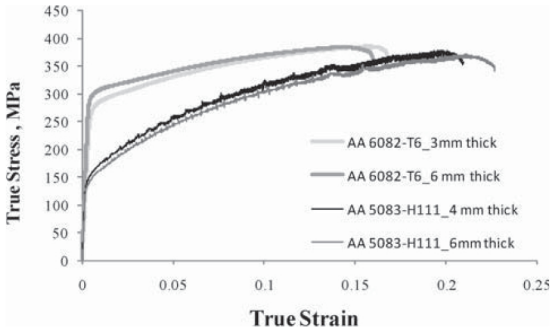

1 Base materials tensile stress–strain curves

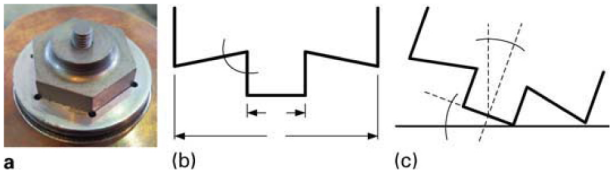

2 *a* friction stir welding tool and *b*, *c* sketches of tool geometry

Experimental

Base materials

In the current investigation, two aluminium alloys widely used in welding fabrication were studied, namely, the AA 5083-H111 (non-heat treatable) aluminium alloy, supplied in plates of 4 and 6 mm thickness, and the AA 6082-T6 (heat treatable) aluminium alloy, supplied in plates of 3 and 6 mm thickness. These base materials have markedly different mechanical behaviours, as exemplified in Fig. 1, where their corresponding tensile stress–strain curves are shown. From these curves it is possible to conclude that, for each base material, the mechanical properties are consistent although they were supplied in plates of different thicknesses, and so were from different batches. If the curves plotted in Fig. 1 are compared, it is possible to conclude that the AA 5083-H111 alloy, with 148 MPa yield strength, is much softer than the AA 6082-T6 alloy, with 290 MPa yield strength. However, despite being softer, the AA 5083-H111 exhibits strong Portevin–Le Châtelier effect and pronounced hardening with plastic deformation, attaining tensile strength values close to that of the AA 6082-T6 alloy. This pronounced difference in plastic deformation behaviour will naturally influence the FSW weldability of both types of alloys.

Welding procedure

Friction stir welds were performed in 4 and 6 mm thick sheets of the AA 5083-H111 alloy (5_4 and 5_6 respectively) and 3 and 6 mm thick sheets of the AA 6082-T6 alloy (6_3 and 6_6 respectively), under a large range of welding conditions, using a conical shoulder tool with a cylindrical threaded pin (Fig. 2). Although the geometry was maintained, tool dimensions, especially the pin diameter D_p and shoulder diameter D_s, were varied according to the plate thickness to be welded, as shown in Table 1. The pin length was set so as to guarantee that during the welding operation the lowermost surface of the pin did not come in contact with the backing bar but was never more than 0·1 mm away from it. Bead on plate welds were produced for the four different types of plates. This procedure enabled to eliminate the influence of sheet positioning and clamping on the resulting weld quality.

For the different types of tools tested in this study, the welding speed v, rotation speed w and vertical force F_z were varied, as shown in Table 2, and also the tilt angle α, as shown in Table 1. The process parameter values were selected based on bibliographic references, the capability of the available equipment and the past experience of the working group. Figure 3 shows a graph which summarises the rotation and traverse speeds (maximum values) used by other authors to perform friction stir welds in the base materials under study, and also the w–v windows considered in the current investigation for each base material and plate thickness. As shown in the graph, the maximum traverse speeds tested in the present work were always higher than those in previous studies. From Table 2 and Fig. 3 it is possible to see that for the 6 mm thick plates, similar welding parameters were established to highlight the differences in weldability between the two base materials. Testing plans were established by combining the different tool and processing parameters for each plate thickness and base material, determining a total of 144 welds to be performed. For example, the testing plan for the 6_3 plates is shown in Fig. 4.

Testing procedure

After welding, all the sheets were visually inspected for surface defects like excessive flash and surface flaws.

Table 1 Tool parameters

Plate type	Shoulder diameter D_s, mm				Pin diameter D_p, mm		Tilt angle α, °		
6_3	10	12	13	15	4	5	1	2	3
5_4	13		15	18	5	6	1	2	3
6_6	15		18	21	6	7	1	2	3
5_6	15		18	21	6	7	1	2	3

Table 2 Process parameters

Plate type	Welding speed v, mm min^{-1}			Rotation speed w, rev min^{-1}			Vertical force F_z, kN		
6_3	800	950	1100	1000	1150	1300	5	7	9
5_4	300	400	500	400	500	600	7	11	15
6_6	200	275	350	300	400	500	10	15	20
5_6	200	275	350	300	400	500	10	15	20

Science and Technology of Welding and Joining stw1709.3d 30/8/10 14:59:43
The Charlesworth Group, Wakefield +44(0)1924 369598 - Rev 7.51n/W (Jan 20 2003)

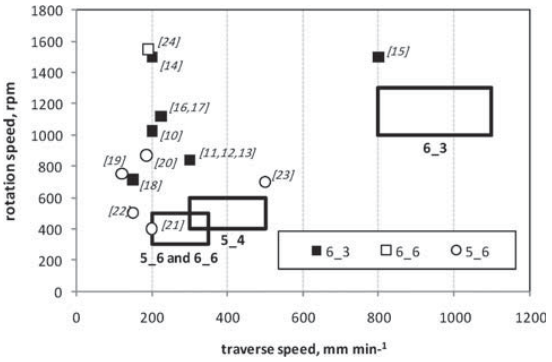

3 Rotation and traverse speeds used for friction stir welding of AA 5083 and AA 6082 alloys

Transverse specimens for metallographic analysis and hardness testing were cut from the welds with no important surface defects, using water jet cutting. For the metallographic analysis, the transverse sections of the welds were cold mounted, polished and etched with Poulton's modified reagent, and observed using Zeiss Axiotech 100 HD and Zeiss Stemi 2000-C microscopes, for detecting large and very small internal flaws respectively. The heterogeneity in mechanical properties across the welds with slight or no defects was evaluated by performing hardness measurements transversely to the weld direction, using a Shimadzu microhardness tester with 200 gf load for 15 s. Tensile tests were also performed, all of which were carried out at room temperature at a crosshead speed of 5 mm min^{-1} using an Instron computer controlled testing machine. Tensile properties were evaluated by testing three tensile specimens of each type. The tensile samples were not machined in order to eliminate weld surface roughness and its possible influence on the plastic behaviour of the samples. During testing, the global performance of the welded plates was evaluated by using a mechanical extensometer of 50 mm gauge length. The local plastic behaviour of the thermomechanically affected zone and HAZ was also analysed using optical strain data acquisition.

	D_p [mm]	D_s [mm]	a [°]	v [mm/min]	w [RPM]	F_z [kN]
1	4	10	1	800	1000	5
2	4	10	2	800	1150	7
3	4	10	3	800	1300	9
4	4	12	1	800	1000	5
5	4	12	2	800	1150	7
6	4	12	3	800	1300	9
7	5	13	1	800	1000	7
8	5	13	2	800	1150	9
9	5	13	3	800	1300	5
10	5	15	1	800	1000	9
11	5	15	2	800	1150	5
12	5	15	3	800	1300	7
13	4	10	1	950	1150	9
14	4	10	2	950	1300	5
15	4	10	3	950	1000	7
16	4	12	1	950	1150	9
17	4	12	2	950	1300	5
18	4	12	3	950	1000	7
19	5	13	1	950	1150	5
20	5	13	2	950	1300	7
21	5	13	3	950	1000	9
22	5	15	1	950	1150	7
23	5	15	2	950	1300	9
24	5	15	3	950	1000	5
25	4	10	1	1100	1300	7
26	4	10	2	1100	1000	9
27	4	10	3	1100	1150	5
28	4	12	1	1100	1300	7
29	4	12	2	1100	1000	9
30	4	12	3	1100	1150	5
31	5	13	1	1100	1300	9
32	5	13	2	1100	1000	5
33	5	13	3	1100	1150	7
34	5	15	1	1100	1300	5
35	5	15	2	1100	1000	7
36	5	15	3	1100	1150	9

4 Welding plan for 6_3 plates

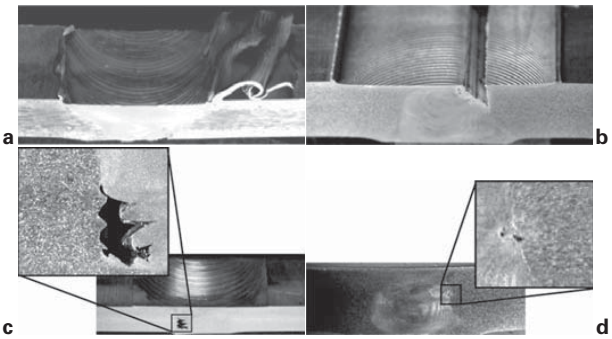

a flash (F); *b* surface defect (SD); *c* internal defect (ID); *d* very small defect

5 Tipical welding defects

Results

Visual inspection

As mentioned above, qualitative inspection of the welds was performed by visual examination to detect surface defects, followed by metallographic analysis to detect internal flaws. This inspection detected three basic types of defects: excessive flash (F) (Fig. 5*a*), surface flaws (SD) (Fig. 5*b*) and internal voids (ID) (Fig. 5*c*). Under some welding conditions, the pin was broken (BP) and it was not possible to perform the weld. These situations have also been indicated.

The energy E (in J mm^{-1}) consumed per unit length of weld, for all the weld tests, was determined by dividing the average power P by the welding velocity ($E=P/v$). The average power was obtained by multiplying the torque T, registered from the welding machine during the welding operation, by the rotation speed ($P=Tw$). Figures 6 and 7 plot the energy consumed per unit length of weld versus the ratio w/v for the 5083 and 6082 welds respectively. In the graphs, the results are grouped according to the classification of the welds after visual inspection. The results identified as GOOD comprise both the non-defective welds and the welds with very small defects (e.g. Fig. 5*d*) that were considered unimportant for the global strength of the weld. If the results from the graphs are compared, it is possible to conclude that for the range of welding parameters

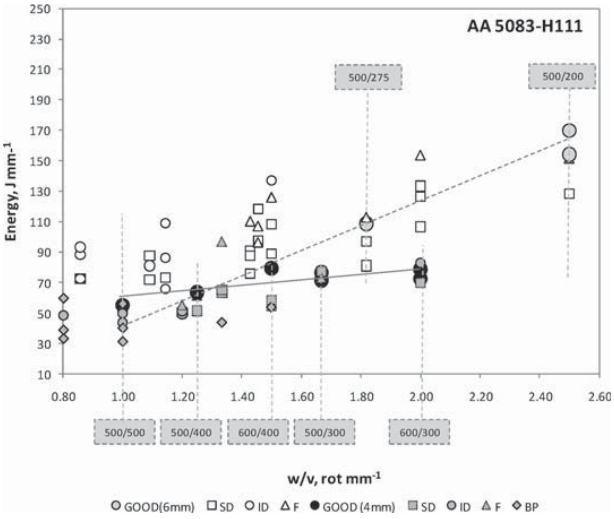

6 Energy consumed per unit length of weld versus *w/v*, for AA 5083-H1114 welds (4 and 6 mm thick plates)

Science and Technology of Welding and Joining stw1709.3d 30/8/10 14:59:48
The Charlesworth Group, Wakefield +44(0)1924 369598 - Rev 7.51n/W (Jan 20 2003)

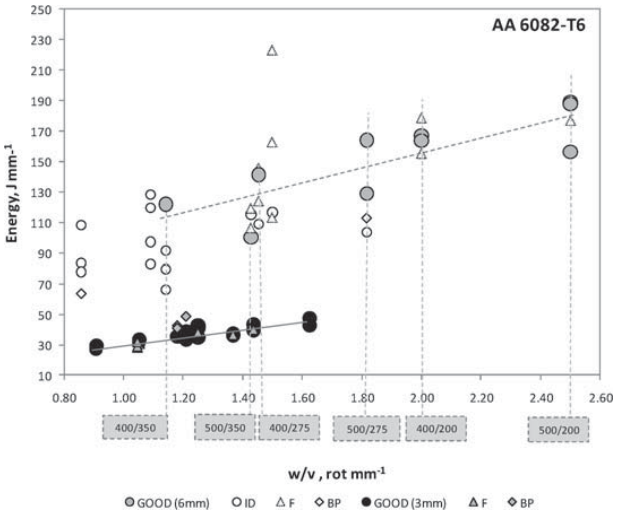

7 Energy consumed per unit length of weld versus *w*/*v* for AA 6016-T6 welds (4 and 6 mm thick plates)

tested in this study the 6082 aluminium alloy presents higher weldability than the 5083 alloy, since a large number of acceptable welds (good and small defect welds) were obtained for both plate thicknesses. However, it is important to remark that the number of non-acceptable welds (F, SD, ID and BP) was very high for all the alloys and plate thicknesses, showing that the process is very sensitive to the choice of tool and machine parameters.

A more detailed analysis of the welding results presented in Figs. 6 and 7 enabled some unacceptable welding parameters for each type of plate to be determined. These are identified in Tables 1 and 2 by colouring the cells grey. A welding parameter was considered unacceptable when all the welds produced under welding conditions including this parameter (α, D_p, D_s, v, w or F_z) were defective. For the 5_4 plates, parameters leading to only one good weld were also considered unacceptable. Analysing the grey cells in Table 1, it can be seen that no acceptable welds were produced with the narrower shoulders in any of the plates. At the same time, qualitative analysis revealed that the process was relatively unaffected by changing pin dimensions. For both alloys, the main defect that could be directly related to the small shoulder diameter was flash formation. A very small tool tilt angle ($\alpha=1^\circ$) also led to flash formation, especially for the thicker plates. For the 5_4 plates, the 18 mm shoulder tool was also found wanting, since it only produced one good weld. However, in this case no specific defect type could be related to shoulder size.

Another important limiting factor for successful welding was the choice of the axial load (*see* grey cells in Table 2). However, the sensitivity of the welds to this parameter is highly influenced by the nature of the base material. In fact, for the 5083 alloy, it was found that using very low axial loads (7 and 11 kN, for the 4 mm thick plate, and 10 kN, for the 6 mm plate) led to significant superficial and internal welding defects, which indicates that these values are the lower axial load limits for FSW of these plates. On the other hand, for the 6082 alloy, no clear limit for axial load was found when welding the 6 mm thick plates. For the 3 mm plates, a maximum load of 9 kN was determined, since the pin was destroyed in all tests performed with this axial load. Finally, for the 5083 alloy, serious limitations in rotation speed (400 rev min^{-1} for the 4 mm thick plates, and 300 and 400 rev min^{-1} for the 6 mm thick plates) and traverse speed (500 mm min^{-1} for the 4 mm thick plates and 350 mm min^{-1} for the 6 mm thick plates) were also registered. Low rotation speeds and high traverse speeds led to the formation of large internal defects, and for the 5_4 plates, they were also associated with tool destruction (BP) in many cases. Large internal defects also occurred for the 6082 alloy in 6 mm thick plates, for the low rotation speed of 300 rev min^{-1}. Previous authors[25] have already associated the formation of internal and surface defects with insufficient heat input, which in turn is usually related to low rotation speeds and high traverse speeds as in the current study.

Looking carefully at the results presented in Fig. 6, for the 5_6 plates, it is possible to conclude that only three GOOD welds were obtained for these plates. There were a large number of welds with internal and surface defects and also two situations in which the pin was broken. Globally the energy results are widely dispersed and it was impossible to establish any relationship between the energy consumed in the process and the process parameters. However, if only the GOOD weld energy values are considered (large grey circles), which presumably correspond to equilibrium welding conditions, a linear regression can be used to fit the results, which indicate that the energy consumed in the process increases with increasing w/v ratios. For the 5_4 plates, more non-defective welds were achieved under the selected welding conditions. For these plates, the energy consumed in the process was lower than that for the 5_6 welds and the results are much less dispersed, indicating weld conditions closer to equilibrium. This can be also inferred by fitting the results relative to the GOOD welds. These results show that the energy increases almost linearly with w/v, but at a much lower rate than that for the 5_6 welds.

In analysing the results from the 6082 alloy (Fig. 7), it is possible to see that with this base material the principal defect types were: flash formation, for both plate thicknesses, caused by inappropriate shoulder dimensions; internal defects, for the 6_6 plates, brought about by low tool rotation speed; and a large number of broken pin situations for the 6_3 plate, caused by excessive axial loads. Just as for the 5083 alloy, the energy values for the GOOD welds can be fitted using linear interpolation, indicating increasing values with increasing w/v ratios. For the 6_3 plates, the energy consumed is almost the same for both defective and GOOD welds, which indicates that at higher rotation speeds, which will correspond to hotter welding conditions, the process becomes very stable. On the other hand, for the 6_6 plates, energy results are more widely dispersed, especially for low w/v ratios and/or $w=300$ rev min^{-1}, which correspond to colder welding conditions. As the rotation speed increases (6_3 plates), the energy consumed in the process becomes less dependent on process parameters, and is similar for both GOOD and defective welds.

Mechanical testing results

The mechanical efficiency of the GOOD welds was analysed by calculating yield strength efficiency coefficient

Science and Technology of Welding and Joining stw1709.3d 30/8/10 14:59:55
The Charlesworth Group, Wakefield +44(0)1924 369598 - Rev 7.51n/W (Jan 20 2003)

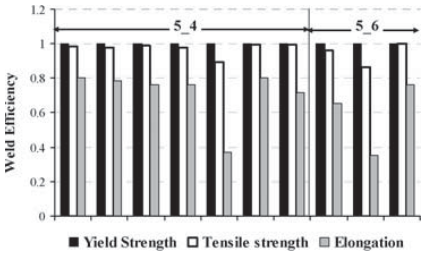

8 Mechanical efficiencies for 5_6 and 5_4 welds

1 η_{ys} and tensile strength efficiency coefficient η_{Rm} respectively, defined as the ratio between the yield or tensile strength of the transverse weld samples (considering a 50 mm gauge length) and the same properties of the parent materials. An elongation coefficient η_e, which is the ratio between the elongation of the weld samples and base materials at maximum load, was also calculated. The results obtained for the 5083 and 6082 welds are summarised in Figs. 8 and 9. As shown in Fig. 8, the 5_6 and 5_4 welds are almost in yield and tensile strength even match ($\eta_{Rm}=1$ and $\eta_{ys}=1$) relative to the parent plates, except in two situations where the welds had very small defects. However, even for these small defect welds the tensile strength efficiency is almost 85%. Despite the good strength of the welds, its elongation is lower than that of the base plates, never exceeding 80% efficiency and falling to 35% for the small defect welds. This behaviour is a result of slight overmatch conditions of weld material relative to base material, as exemplified in Fig. 10. This shows local tensile stress–strain curves for the welds and parent plates from the tensile tests of 5_4 and 5_6 transverse samples, and the hardness profiles across the same welds (it is important to point out that in order to plot the two different types of results on the same graph, the logarithm strain values were multiplied by 100 as indicated above the x axis). The figure also shows the longitudinal strain distribution, after maximum load, for both samples. It is possible to see that necking occurred in the base material, for the 5_6 sample, and in the weld, for the 5_4 sample, which actually corresponded to a small defect sample. Actually, the two welds were deformed but to a lower extent than the base material, which led to lower global elongation levels for the transverse welded samples, even for the non-defective welds. The stress–strain curves of the welds and their hardness profiles confirm the slight overmatch behaviour of the welds. It is important to highlight that very similar mechanical performance was registered for all the GOOD welds although they were obtained using different process parameters.

Turning to the mechanical efficiency results for the 6082 alloy, plotted in Fig. 9, it is possible to conclude

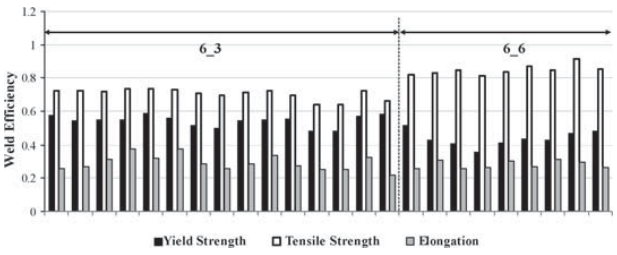

9 Mechanical efficiencies for 6_6 and 6_3 welds

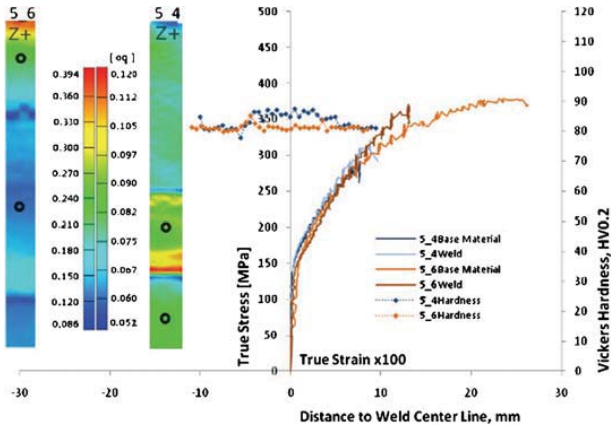

COLOUR FIGURE

10 Hardness and tensile test results for 5_4 (w=600 rev min^{-1}, v=400 mm min^{-1}, D_s=18 mm, F_z=15 kN) and 5_6 (w=500 rev min^{-1}, v=250 mm min^{-1}, D_s=21 mm, F_z=20 kN) weld samples: small circles in sample images indicate location of points for which stress–strain curves were plotted

that all the 6_3 and 6_6 welds were in undermatch relative to the base material since the weld efficiency was always <1. However, although a slightly higher yield stress undermatch was registered for the 6_6 welds (averaging 60%) than for the 6_3 welds (averaging 50%), the 6_6 welds displayed slightly higher tensile strengths. The average elongation efficiency is similar for both weld types, averaging 30%. These results can be understood by analysing the curves in Fig. 11, where the same type of results of Fig. 10 are plotted for the 6_3 and 6_6 welds. From the graph it is possible to see that both tensile samples failed in the weld, where the material is in undermatch condition relative to the base material, as confirmed by the low hardness values registered in the welds. Significantly, in the HAZ, the 6_6 weld exhibits lower hardness values than the 6_3 weld, which led to lower yield stress efficiencies for these welds. Since the maximum load was attained in the welds without plastic deformation of the base material, the corresponding tensile stress–strain curves are not presented in Fig. 11. It is also important to note that the 6_3 curve indicates greater strength than that of the 6_6 weld, which is in

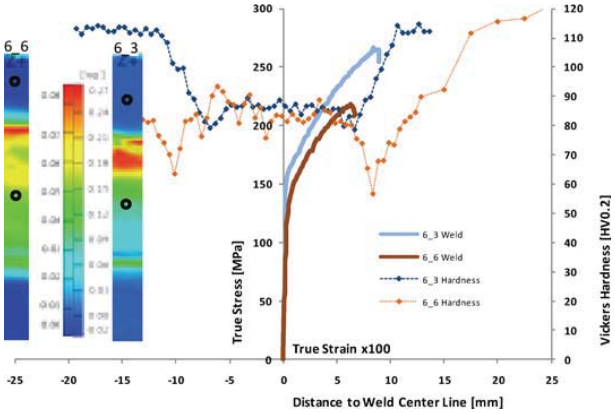

COLOUR FIGURE

11 Hardness and tensile test results for 6_3 (w=1300 rev min^{-1}, v=1100 mm min^{-1}, D_s=15 mm, F_z=5 kN) and 6_6 (w=400 rev min^{-1}, v=200 mm min^{-1}, D_s=18 mm, F_z=15 kN) welds: small circles in sample images indicate location of points for which stress–strain curves were plotted

Science and Technology of Welding and Joining stw1709.3d 30/8/10 14:59:57
The Charlesworth Group, Wakefield +44(0)1924 369598 - Rev 7.51n/W (Jan 20 2003)

disagreement with the results shown in Fig. 9. Since the tensile tests (results in Fig. 11) were performed several months after the tests used to calculate the mechanical efficiency, it is reasonable to assume that natural age hardening of the weld material occurred.

Conclusions

From the above results it can be concluded that high traverse speeds can be achieved in FSW of both base materials with carefully chosen process and tool parameters. These in turn are strongly dependent on the base material characteristics and plate thickness. In fact the study proves that below certain shoulder dimensions dependent on plate thickness, and for very low tool tilt angles, it is not possible to achieve non-defective welds whatever the process parameters in use. In order to guarantee hot weld conditions an accurate selection of tool rotation speed is also very important. In fact, the calculation of the energy consumed in the process, as well as the analysis of the welds, shows that the process becomes relatively less dependent on process and tool parameters for high tool rotation rates. However, hot weld conditions are intimately related to the characteristics of the base material, and are far more easily attained for the harder 6082 alloy, to which higher values of plastic dissipation can be associated. The present study also shows that the establishment of accurate axial load values is also intimately related to the process parameters in use. Therefore, for cold weld conditions low axial loads led to significant internal and surface defects, whereas for hot weld conditions high axial load values led to tool destruction due to excessive plunge depth in the softened material. It was also shown that establishing suitable axial load values depends strongly on base material characteristics being advisable to perform tests in position control to determine appropriate axial load values. Finally, it was determined that the mechanical properties of the non-defective welds are relatively independent of the welding conditions. In the special case of the 6082 alloy, the use of very high welding speeds proved to be very effective in avoiding extra softening in the HAZ, with positive consequences in weld yield strength efficiency.

Acknowledgement

The authors are indebted to the Portuguese Foundation for the Science and Technology through COMPETE Programme from QREN and to FEDER for the financial support.

References

1. J. Mononen, M. Sirén and H. Hänninen: 'Cost comparison of FSW and MIG welded aluminium panels', *Weld. World*, 2003, **47**, 32–35.
2. D. M. Rodrigues, A. Loureiro, C. Leitão, R. M. Leal, B. M. Chaparro and P. Vilaça: 'Influence of FSW parameters on the microstructural and mechanical properties of AA 6016-T4 thin welds', *Mater. Des.*, 2009, **30**, 1913–1921.
3. C. Leitao, R. M. Leal, D. M. Rodrigues, A. Loureiro and P. Vilaça: 'Mechanical behaviour of similar and dissimilar AA 5182-H111 and AA 6016-T4 thin friction stir welds', *Mater. Des.*, 2009, **30**, 101–108.
4. R. S. Mishra and Z. Y. Ma: 'Friction stir welding and processing', *Mater. Sci. Eng. R*, 2005, **R50**, 1–78.
5. G. Padmanaban and V. Balasubramanian: 'Selection of FSW tool pin profile, shoulder diameter and material for joining AZ31B magnesium alloy – an experimental approach', *Mater. Des.*, 2009, **30**, (7), 2647–2656.
6. H. J. Liu, J. J. Shen, Y. X. Huang, L. Y. Kuang, C. Liu and C. Li: 'Effect of tool rotation rate on microstructure and mechanical properties of friction stir welded copper', *Sci. Technol. Weld. Join.*, 2009, **14**, (6), 577–583.
7. H. K. D. H. Bhadeshia and T. DebRoy: 'Critical assessment: friction stir welding of steels', *Sci. Technol. Weld. Join.*, 2009, **14**, (3), 193–196.
8. Y. Zhang, Y. S. Sato, H. Kokawa, S. H. C. Park and S. Hirano: 'Microstructural characteristics and mechanical properties of Ti–6Al–4V friction stir welds', *Mater. Sci. Eng. A*, 2008, **A485**, (1–2), 448–455.
9. R. Nandan, T. DebRoy and H. K. D. H. Bhadeshia: 'Recent advances in friction stir welding – process, weldment, structure and properties', *Prog. Mater. Sci.*, 2008, **53**, (6), 980–1023.
10. M. Barletta, G. Buffa, L. Casamichele and L. Fratini: 'Local mechanical and morphological characterization of friction stir-welded butt joints', *Proc. IMechE B*, 2006, **220B**, 813–821.
11. A. Steuwer, M. J. Peel and P. J. Withers: 'Dissimilar friction stir welds in AA5083–AA6082: the effect of process parameters on residual stress', *Mater. Sci. Eng. A*, 2006, **A441**, 187–196.
12. M. J. Peel, A. Steuwer, P. J. Withers, T. Dickerson, Q. Shi and H. Shercliff: 'Dissimilar friction stir welds in AA5083–AA6082. Part I: Process parameter effects on thermal history and weld properties', *Metall. Mater. Trans. A*, 2006, **37A**, (7), 2183–2193.
13. M. J. Peel, A. Steuwer and P. J. Withers: 'Dissimilar friction stir welds in AA5083–AA6082 Part II: Process parameter effects on microstructure', *Metall. Mater. Trans. A*, 2006, **37A**, (7), 2195–2206.
14. L. Fratini, G. Buffa, L. Filice and F. Gagliardi: 'Friction stir welding of AA6082-T6 T-joints: process engineering and performance measurement', *Proc. IMechE B*, 2006, **220B**, (5), 669–676.
15. P. M. G. P. Moreira, M. A. V. de Figueiredo and P. M. S. T. de Castro: 'Fatigue behaviour of FSW and MIG weldments for two aluminium alloys', *Theor. Appl. Fract. Mech.*, 2007, **48**, (2), 169–177.
16. P. M. G. P. Moreira, T. Santos, S. M. Tavares, V. Richter-Trummer, P. Vilaça and P. M. S. T. de Castro: 'Mechanical characterization of friction stir welds of two dissimilar aluminium alloys of the 6xxx series', *Mater. Sci. Forum*, 2008, **587–588**, 430–434.
17. P. M. G. P. Moreira, T. Santos, S. M. O. Tavares, V. Richter-Trummer, P. Vilaça and P. M. S. T. de Castro: 'Mechanical and metallurgical characterization of friction stir welding joints of AA6061-T6 with AA6082-T6', *Mater. Des.*, 2009, **30**, 180–187.
18. L. Fratini, G. Buffa and R. Shivpuri: 'Influence of material characteristics on plastomechanics of the FSW process for T-joints', *Mater. Des.*, 2009, **30**, 2435–2445.
19. P. A. Colegrove: '3-dimensional CFD modelling of flow round a threaded friction stir welding tool profile', *J. Mater. Process. Technol.*, 2005, **169**, 320–327.
20. H. Lombard, D. G. Hattingh, A. Steuwer and M. N. James: 'Optimising FSW process parameters to minimise defects and maximise fatigue life in 5083-H321 aluminium alloy', *Eng. Fract. Mech.*, 2008, **75**, 341–354.
21. G. R. Cui, Z. Y. Ma and S. X. Li: 'Periodical plastic flow pattern in friction stir processed Al–Mg alloy', *Scr. Mater.*, 2008, **58**, 1082–1085.
22. D. G. Hattingh, C. Blignault, T. I. van Niekerk and M. N. James: 'Characterization of the influences of FSW tool geometry on welding forces and weld tensile strength using an instrumented tool', *J. Mater. Process. Technol.*, 2008, **203**, 46–57.
23. G. R. Cui, Z. Y. Ma and S. X. Li: 'The origin of non-uniform microstructure and its effects on the mechanical properties of a friction stir processed Al–Mg alloy', *Scr. Mater.*, 2009, **57**, 5718–5729.
24. T. Minton and D. J. Mynors: 'Utilisation of engineering workshop equipment for friction stir welding', *J. Mater. Process. Technol.*, 2006, **177**, 336–339.
25. M. Iordachescu, D. Iordachescu, J. L. Ocana, P. Vilaça and E. Scitelnicu: 'Characteristic flaws in aluminium alloys joints', *Metal. Int.*, 2009, **12**, (2), 135.

Annex E

International Congress on Advances in Welding Science and Technology for Construction, Energy and Transportation Systems
24-25 October 2011, Antalya, Turkey

AWST-11/28

Influence of Base Material Properties and Process Parameters on Defect Formation during FSW

C. Leitão [1,a], A. Loureiro [1,b], D.M. Rodrigues [1,c]

[1] CEMUC, Mechanical Engineering Department. – University of Coimbra. Portugal

[a]carlos.leitao@dem.uc.pt, [b]altino.loureiro@dem.uc.pt, [c]dulce.rodrigues@dem.uc.pt

Abstract

The widespread application of friction stir welding (FSW) technology in material joining requires a deep understanding of the mechanisms of defect formation. Several types of FSW defects, which are dynamically promoted during the process, were observed and classified in the literature. Concerning the analysis of defects formation, the works developed to date mainly focused on the analysis of the influence of process parameters on it. However, it is important to emphasize that each material has a particular plastic behaviour, which affects the material flow during welding and, consequently, the susceptibility for defect formation as well as the morphology of the defects. Despite this knowledge, the relation between materials plastic behaviour and defect formation, addressed in this work, was never explored.

In this study, similar aluminium welds were produced under several welding conditions, using two aluminium alloys, the Al-Mg-Si (AA6082-T6) and the Al-Mg (AA5083-H111) alloys, which are characterized by markedly different strengthening mechanisms and microstructural evolution with increasing temperatures, which conduct to markedly different viscoplatic behaviours. These two base materials were joined under varied welding conditions, using different FSW tools and welding parameters, in order to characterize their weldability in FSW. The plastic behaviour of the base materials, in tension at different temperatures, was analysed and compared. Important relations between material flow during friction stir welding, the hardening behaviour of the base materials during plastic deformation, at different temperature, and defect formation were found.

Keywords: *FSW, Defects, Material properties, Process parameters*

1. Introduction

Since the early 90's, with the development of a new solid state welding technology, the Friction Stir Welding (FSW) process, was possible to observe a large interest of the scientific community by it due the high application possibilities to the aerospace and transportation industries [1]. Due to its solid state nature, this technology allows joining several types of metals such as aluminium [2-4], magnesium [5], copper [6], steel [7] and titanium [8], presenting, in some cases, enhanced production rates relatively to conventional welding processes [9].

However, like for other well-known welding technologies, it is imperative to insure the production of good quality welds, free of defects, in order to make the process industrially reliable. The scientific community had already identified the most common defects associated with the FSW process, but had not yet established any standardization concerning their classification. The main types of defects already detected were the formation of a large mass of flash, internal and/or superficial cavities, and grooves [10-12]. The origin of these defects is currently attributed to an inappropriate level of heat input and/or deficient stirring of the materials, both influenced by the utilization of inadequate process parameters and/or tool characteristics [5, 13]. Louro et al. [14] observed that high flash amount occurs for high values of plunge pressure, which can result of excessive heat-input during the welding process [10, 15]. Other authors also associated the high amount of flash to the tool incapability to hold the material under it during the process conjugated with the selection of hot processing conditions [16]. However, defects formation can also be associated to an inadequate flow inside the stirred volume [17].

In fact, it is possible to verify that the formation of welds by FSW, and consequently, the formation of defects, is based on thermic and mechanical transformations of the base materials which are directly related to the set of selected weld parameters. So, most of the author's approaches to defect formation were focused on parameters and/or tool geometry optimization, for defect-free welds production, being developed for very specific base materials [13]. However, the influence of base material plastic behaviour on defect formation during FSW has not been set yet.

In the present work, the authors intend to define the influence of the base material plastic properties on defect

formation. To meet this objective, two different aluminium alloys were used and welds were performed using a large range of FSW parameters. During the analysis, the defects resulting from the process are classified and the weldability of both alloys is compared. Simultaneously, a relationship between the base material plastic properties, obtained under different testing conditions, and defects formation is established.

2. Experimental procedure

Two base materials, a non-heat-treatable (AA5183-H111) and a heat-treatable aluminium (AA6082-T6) alloy, widely used in welding fabrication, were used in this study. The plastic behaviour of the base materials, supplied in 6 mm thick plates, was analysed by performing tensile tests at different temperatures. The tests were performed using Instron 4206 and 8800 FastTrack machines. As show in Table 1, the tensile tests were performed at temperatures ranging from 25 to 500 ºC.

Table 1 – Tensile testing temperatures

Testing temperature [ºC]	25	240	320	400	500

In order to analyse the weldability in friction stir welding of the base materials, they were welded under varied FSW conditions. The same tool geometry, characterized by a conical shoulder with a cone angle of 5º and a cylindrical threaded pin, was used in all the welding tests. This tool geometry is the most traditional and the one with the highest industrial and research interest due to its simplicity, which reduces the number of design variables in study, and by the fact that its production is relatively simple, compared with more complicated tool designs such as scrolled shoulders, whorl pins, triflutes, etc. It is also important to enhance that the material flow mechanism during FSW with conical tools was already accurately established in literature, which is highly helpful for understanding its relation with the viscoplastic behaviour of the base materials. Despite the geometry was maintained, the tool dimensions, namely, the pin (D_p) and shoulder (D_s) diameters were varied, according to Table 2. The pin length was set so as to guarantee that, during the welding operation, the lowermost surface of the pin does not come in contact with the backing bar and that it remains at 0.1 mm or less from the backing anvil. Bead-on-plate welds were produced for both base materials. This procedure enables to eliminate the influence of sheet positioning and clamping on the resulting weld quality and eases the preparation. For the different types of tools tested in this work, the welding speed (v), rotating speed (ω), vertical force (F_z) and pitch angle (α) were also varied. Table 2 summarizes the different process and tool parameters tested in this work.

After welding, all plates were visually inspected for surface defects like excessive flash and surface flaws detection. Transverse specimens for metallographic analysis were cut from the welds, using water jet cutting, cold mounted, polished, etched with Poultons modified reagent and observed using the Zeiss Stemi 2000-C and Zeiss Axiotech 100HD microscopes, for detecting large and very small internal flaws, respectively. In the next sections, the friction stir welding results for both alloys will be compared and the main differences enhanced. Then, the differences in friction stir weldability of these alloys will be analysed and explained based in the mechanical characterization of the base materials.

Table 2 – Friction Stir Welding parameters

Tool Parameters	D_p [mm]		D_s [mm]			α [º]		
	6	7	15	18	21	1	2	3
Process parameters	v [mm/min]		ω [rpm]			F_z [kN]		
	AA5083	AA6082						
	50 to 700	200 to 1000	300 to 1000			10	15	20

3. Discussion

3.1. The base materials

The base materials used in this study (AA5083-H111 and AA6082-T6) present markedly different mechanical behaviours, as exemplified in Figure 1, where their corresponding tensile stress-strain curves are shown. Comparing the curves plotted in Figure 1, it is possible to conclude that the AA5083 alloy, with 148 MPa yield strength, is much softer than the AA6082 alloy, with 290 MPa yield strength. However, despite being softer, the AA5083 exhibits strong Portevin-Le Châtelier effect and pronounced hardening with plastic deformation, attaining tensile strength values close to that of the AA6082 alloy.

In Figure 2 are plotted the hardening rates (ds/de), calculated from the tensile engineering stress-strain curves of both alloys, registered at varying temperatures up to 500ºC. In Figure 2a, which corresponds to the AA6082 alloy, is possible to assess that, for temperatures above 240ºC, the hardening rate of this alloy sharply decreases after yielding, attaining negative values for very low values of plastic deformation (e<2%). This result allows to conclude that this material experiences strong softening with plastic deformation at increasing temperatures. Contrarily to this alloy, as shown in Figure 2b, the AA5083 alloy presents hardening until 5% of plastic deformation, even at 240ºC and very small softening with plastic deformation for temperatures higher than 240ºC. Actually is important to enhance the almost perfectly plastic behaviour presented by this alloy for temperatures above 300ºC. The pronounced differences in plastic deformation behaviour at increasing temperatures will naturally influence the FSW weldability of both types of alloys.

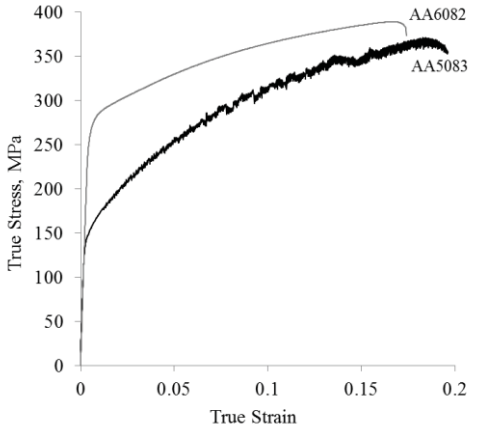

Figure 1. Base materials tensile stress-strain curves

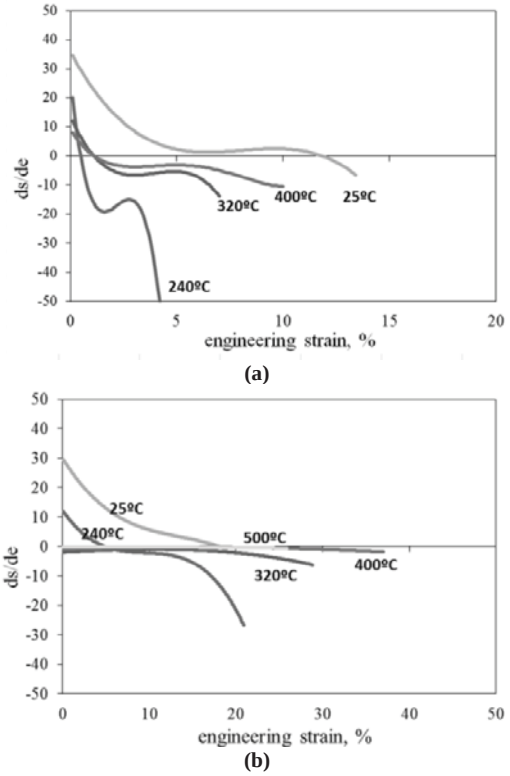

Figure 2. Hardening rate for the AA6082 (a) and AA5083 (b) alloys

3.2. Weldability and Defects formation

In Figures 3a and 3b are plotted the torque values, registered during welding, versus the ω/v ratio, which is proportional to the heat input during the process [10], for the AA5083 and AA6082 alloys, respectively. In the graphs, for each alloy, the results are grouped according to the classification of the welds after visual inspection: welds with excessive flash (F), example in Figure 4a, welds with surface flaws (SD), example in Figure 4b, and welds with internal voids (ID), example in Figure 4c. It is also important to enhance that the results identified as GOOD (large grey circles) in Figure 3 comprise both the non-defective welds and the welds with very small defects (e.g. Figure 4d), which were found to be unimportant for the global strength of the weld. Under some welding conditions, the pin was broken (BP) and it was not possible to perform the weld. These situations are also identified in Figure 3 using black squares. Comparing Figure 3a and 3b, regarding the weld inspection results, it is possible to verify that the number of defective welds is higher for the AA5083 alloy than for the AA6082 alloy, which indicates that under the same welding conditions, the AA5083 alloy displays much lower weldability than the AA6082 alloy. It is also important to observe that the range of torque values plotted in Figure 3 is very similar for both alloys despite the different characteristics of the base materials, already observed in Figures 1 and 2, and the differences in welding results.

Using the weld inspection results a set of non-acceptable parameters was identified for each alloy, which are described in Table 3. A welding parameter was considered unacceptable when all the welds produced under welding conditions including this parameter (α, D_p, D_s, v, ω or F_z) were defective. Analysing Table 3, it can be seen that no acceptable welds were produced with the narrower shoulder diameter (D_s=15mm) for any of the alloys. At the same time, the qualitative analysis revealed that the welding process results were relatively unaffected by changing pin dimensions. For both alloys, the main defect that could be directly related to the small shoulder diameter was Flash formation. The smaller tool tilt angle (α=1º) also led to Flash formation.

For the AA5083 alloy another important limiting factor for successful welding was the choice of the axial load. However, the sensitivity of the welding operation to this parameter was highly influenced by the nature of the base material. In fact, for the AA5083 alloy, it was found that using the very low axial loads of 10 kN led to significant superficial and internal welding defects, which indicates that this load value is the lower axial load limit for FSW of this alloy. On the other hand, for the AA6082 alloy, no clear lower limit for the axial load was found. Finally, for the AA5083 alloy, serious limitations in rotation speed (300 and 400 rpm) and traverse speed (350 mm min^{-1}) were also registered. Low rotation speeds and high traverse speeds led to the formation of large internal defects. For the AA6082 alloy, large internal defects also occurred, but only for the low rotation speed of 300rpm.

From the previous analysis it is possible to conclude that the AA6082 have much less welding parameter restrictions for good welds production than the AA5083 alloy which, additionally to the AA6082 alloy weld parameters restrictions, showed to be unweldable for the lower tool tilt angle (α), the higher tool traverse speed (v) and the lower axial load values (F_z).

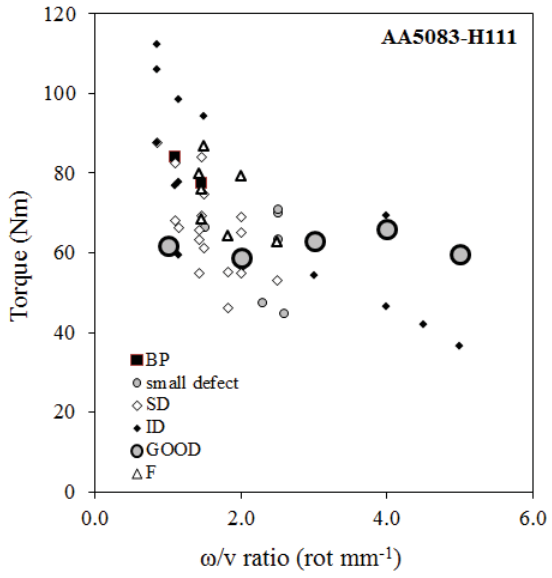

(a)

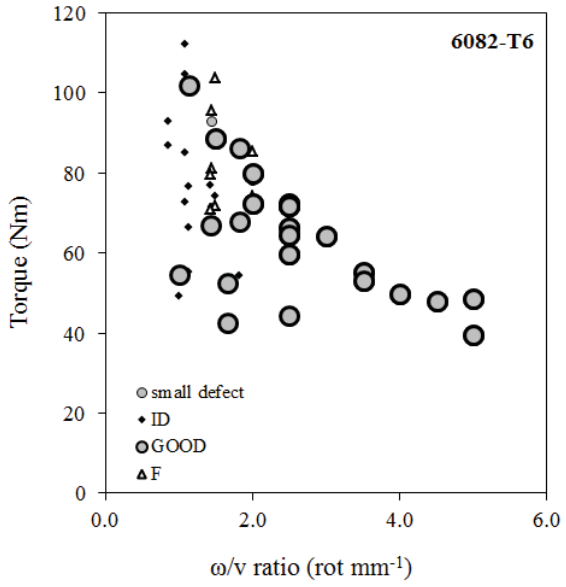

(b)

Figure 3. Torque values versus for the AA5083 (a) and AA6082 (b) welds

Table 3. Non-acceptable process parameters from the initial selection

Parameter / Alloy	D_p [mm]	D_s [mm]	α [°]	v [mm.min^{-1}]	ω [rpm]	F_z [kN]
AA5083	-	15	1	500	300 and 400	10
AA6082	-	15	-	-	300	-

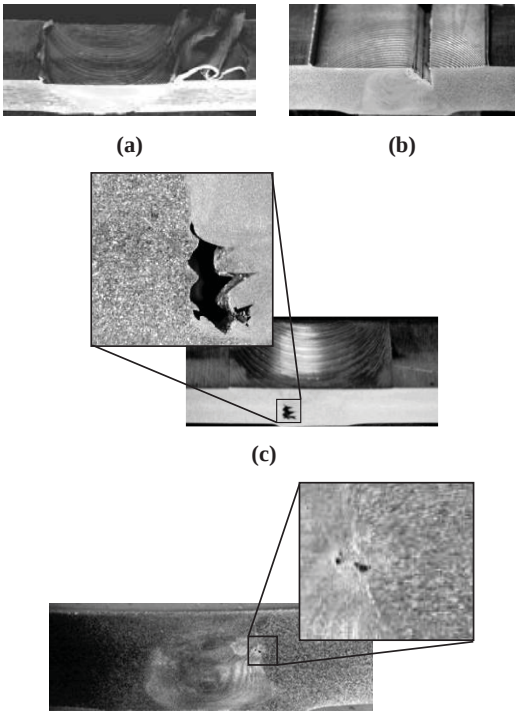

(a) (b) (c) (d)

Figure 4. Typical welding defects: a) Flash (F), b) Surface defect (SD), c) Internal defect (ID) and d) very small defect.

In Tables 4 and 5 are shown the welding inspection results for the AA5083 and de AA6082 alloys, respectively, for a selected range of welding parameters. Comparing both tables is possible to conclude again that under precisely the same welding conditions the welding results are different for both alloys. Meanwhile for the AA5083 alloy the main types of defects detected were surface and internal defects, which are commonly associated to low heat-input conditions, for the AA6082 alloy, several situations of mass flash formation were registered, which are usually associated to high heat-input conditions during the process. For the cooler welding conditions (v=275mm.min^{-1}) the main type of defects detected for the AA6082 were internal defects, meanwhile for the AA5083, the main type of defect was the surface flaw. These results point again to the strong influence of the base material characteristics on defect formation.

Another important aspect registered in present work was the markedly different morphology of the welds obtained from the different base materials, under the same welding conditions. In order to better illustrate this aspect, AA6082 and AA5083 weld cross sections are shown in Figures 5a to 5d. In the figure, each pair of AA6082 and AA5083 welds (a and b, c and d) were performed using exactly the same welding conditions and the same welding equipment. As it is possible to observe in the figure, independently of the welding conditions, the weld cross-section is wider for the AA6082 plates, being characterized by a well-defined shoulder influence area, extending to the plate mid thickness. On the other

hand, for the AA5083 weld, the TMAZ is clearly restricted to the pin influence area with a very small evidence of material being dragged by the shoulder. In fact, at the under shoulder area, where a large portion of TMAZ material is located for the AA6082 weld, it is possible to observe the presence of undeformed AA5083 base material. For the welds performed with very low axial load (10kN), shown in Figures 5a and 5b, it is even possible to observe a regular cross-section for the AA6082 weld, despite with some evidence of incomplete tool penetration, and a large surface defect for the AA5083 weld. According to previous authors [18-22], the morphology and dimension of the TMAZ, which is associated with the quantity of material dragged by the tool in each rotation, is strongly influenced by the welding parameters. However, since each pair of welds shown in Figure 5 was performed using exactly the same welding conditions, it is possible to say that the weld morphology also depends on base material properties.

Table 4. Weld Inspection – AA5083

	v=200 mm min^{-1}			*v*=275 mm min^{-1}			*v*=350 mm min^{-1}		
F_z / ω [rpm]	10 kN	15 kN	20 kN	10 kN	15 kN	20 kN	10 kN	15 kN	20 kN
1000	-	-	o						
900	-	-	o						
800	-	-	o						
700	-	-	o						
600	-	-	o						
500	◊	o	o	◊	Δ	O	◊	◊	◊
400	◊	◊	O	◊	◊	■	♦	o	o
300	◊	◊	o	◊	♦	■	◊	♦	♦

O GOOD, o small defect, Δ Flash, ■ Broken Pin, ◊ Surface defect, ♦ Internal defect

Table 5. Weld Inspection – AA6082

	v=200 mm min^{-1}			*v*=275 mm min^{-1}			*v*=350 mm min^{-1}		
F_z / ω [rpm]	10 kN	15 kN	20 kN	10 kN	15 kN	20 kN	10 kN	15 kN	20 kN
1000	-	O	O						
900	-	-	O						
800	-	-	O						
700	-	-	O						
600	-	-	O						
500	o	O	O	■	O	O	o	Δ	Δ
400	o	O	O	♦	o	Δ	♦	o	O
300	Δ	Δ	Δ	■	♦	o	♦	♦	♦

O GOOD, o small defect, Δ Flash, ■ Broken Pin, ◊ Surface defect, ♦ Internal defect

In Figure 5 is also shown, for each weld, the final print left by the tool at the end of the welding process. As it is possible to conclude from the figure, for the AA6082 weld, the shoulder mark is almost perfectly round, except for the low axial load weld (Figure 5a), showing that the material is dragged easily by the shoulder around the tool. For the AA5083 weld, the final print left by the shoulder clearly shows that the shoulder-workpiece contact area is restricted to the trailing side of the tool, especially for the cold welds, performed at 400rpm (Figures 5b and 5d).

Intending to compare the differences between the amounts of material dragged by the tool during the weld process, for both alloys, the evolution of the pin affected zone width (W), evaluated at the welds middle thickness, is plotted in Figure 6. More precisely, in Figure 6a is plotted the evolution of W versus the welding speed for different tool rotation speeds: 500 and 600 rpm for the AA5083 alloy and 500 and 1000rpm for the AA6082 alloy. In figure 6b is plotted the evolution of W with the rotation speed for different traverse speeds: 50, 200 and 350 mm.min-1 for the AA5083 alloy and 200 and 350 mm.min^{-1} for the AA6082 alloy. It is important to emphasize that all the results plotted in Figures 6a and 6b correspond to welds which were produced using the same axial force (20kN), tool tilt angle (3º) and dimensions (D_s/D_p=21/7 mm).

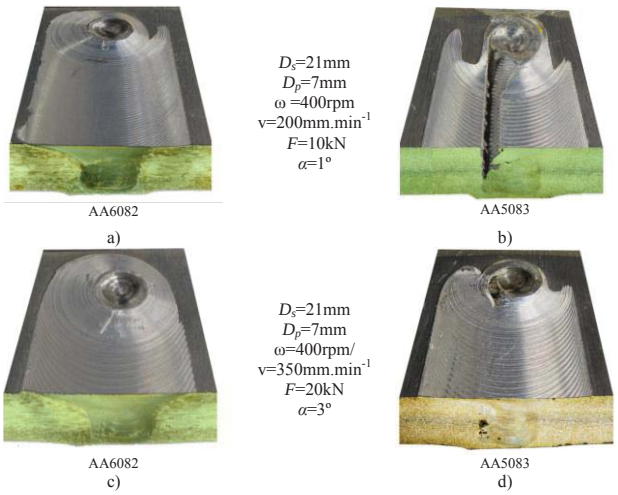

Figure 5. Cross-section and surfaces of the welds produced using both base materials

Analysing Figure 6a is possible to conclude that, for each tool rotational speed, W strongly varies with the tool traverse speed, deeply increasing for decreasing welding speed values. For a specific welding speed value, W increases with the increasing of the rotation speed. Finally, under similar welding conditions (welding and rotation speeds), the amount of material dragged by the tool is much higher for the AA6082 alloy than for the AA5083 alloy, unless for the higher weld speed values, for which the width of the pin affected zone become similar for both alloys. Actually, in the figure, a cross-symbol was used for identifying, for each alloy, defective weld results. According to the figure, when the width of the pin affected zone is inferior to a value near to 7.6 mm, which corresponds to W values only 10 % higher than the pin diameter, internal defects were formed for both alloys.

Analysing now Figure 6b, it is possible to conclude that, for the AA5083 alloy, the width of the pin affected zone strongly increases with the increasing of the tool rotation speed, for the lower tool traverse speed of 50mm.min-1. For the higher tool traverse speed values of 200 and 350 mm.min^{-1}, for which all the welds displayed

very small or large defects, W remains in very small values independently of the tool rotation speed. Contrarily to this, for the AA6082 alloy, a strong increase of W with the increasing tool rotation speed was registered for 200 mm.min^{-1} traverse speed.

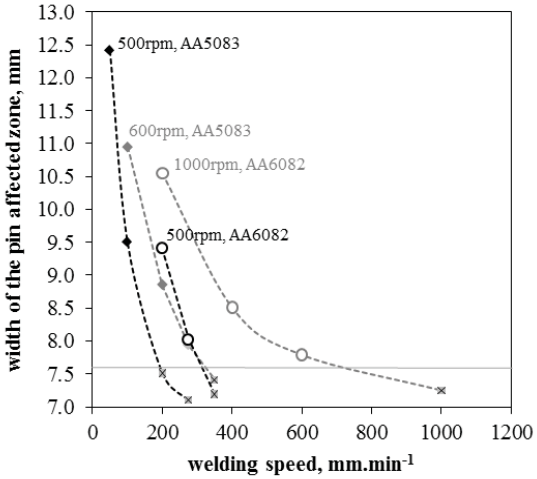

(a)

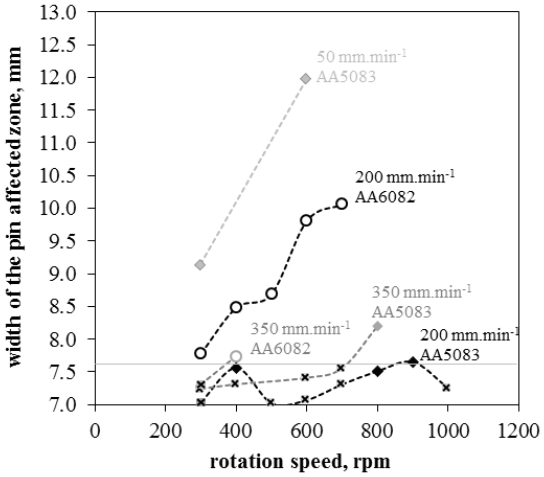

(b)

Figure 6. Evolution of the width of the pin affected zone with the traverse speed (a) and rotational speed (b).

In Figures 7 and 8 is shown the cross-section morphology for AA5083 and AA6082 welds, respectively. Comparing the images in the figure it is now possible to analyse and compare the evolution of the shoulder influenced zone, with the traverse and rotational speeds of the tool, for both base materials. According to the figures, independently of the base material properties, the size of the shoulder influence zone increases for decreasing traverse speeds and decreasing tool rotational speeds. As already concluded from Figure 5, the size of the shoulder influenced zone is always larger for the AA6082 welds, than for the AA5083 welds, despite the welds displayed in Figure 8 were performed under lower axial force values than the ones of Figure 7.

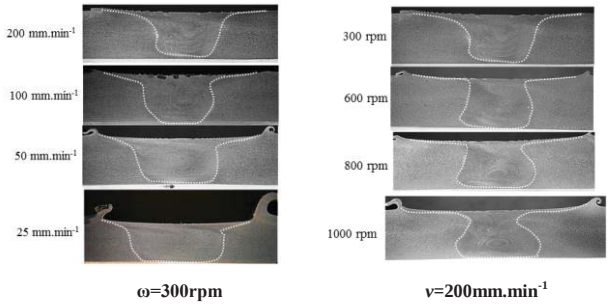

ω=300rpm **v=200mm.min^{-1}**

(a) **(b)**

Figure 7. Evolution of the AA5083 welds cross-section with the traverse (a) and rotational (b) speeds. Other welding parameters: F_z=20kN, α=3º, D_s/D_p=21/7 mm

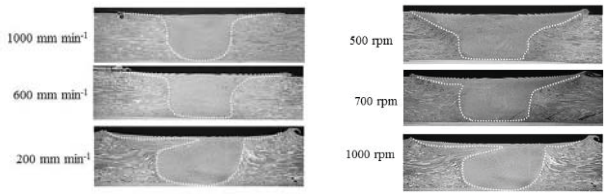

ω=1000rpm **v=200mm.min^{-1}**

(a) **(b)**

Figure 8. Evolution of the AA6082 welds cross-section with the traverse (a) and rotational (b) speeds. Other welding parameters: F_z=15kN, α=3º, D_s/D_p=21/7 mm

According to Figures 5, 6, 7 and 8, under the same welding conditions, the quantity of material dragged by the tool shoulder and pin during the welding process was higher for the AA6082 alloy than for the AA5083 alloy, which displayed much lower weldabity than the previous one. Then, it is possible to establish a direct relation between the quantity of material dragged by the tool, in each rotation, and defect formation. It is also plausible to establish a direct relation between the quantity of material dragged by the tool at each rotation and the plastic properties of the base materials at high temperatures, since the welds for both alloys were performed under the same welding conditions. Actually, based on mechanical characterization of the base materials at high temperatures, which the results are displayed on Figure 2, it was already concluded that meanwhile the AA6082 alloy displayed strong softening with plastic deformation at increasing temperatures, the AA5083 alloy display an almost perfectly plastic behaviour at increasing temperatures. Since during FSW, once steady state welding conditions are attained, the dragging action of the tool over the base material will develop under constant load, it is reasonable to expect that the AA6082 alloy, which experiences strong softening with plastic deformation at increasing temperatures, will have good weldability in FSW, since it will undergo intense plastic deformation under constant load at high temperature. On the other hand, for strongly work-hardening materials, like the AA5083 alloy, continued plastic deformation require increasing stress

levels. According to Figure 2, under constant load conditions, like that occurring in FSW, plastic deformation of the AA5083 alloy will be impossible for temperatures less than 320 ºC, and less efficient than for the AA6082 alloy, for temperatures above 320 ºC, for which this alloy display almost perfectly plastic behaviour.

The contact conditions at the tool-workpiece interface will be also determined by the plastic properties of the base materials. According to Schmidt and Hattel [23], during tool plunge and the first part of the dwell period, a large amount of heat is generated by frictional dissipation, increasing the temperature of the under-shoulder material. Consequently, under similar axial load conditions, the extreme thermal softening experienced by the AA6082 alloy will lead to further submerging of the tool, relatively to the AA5083 alloy, which explains the strong differences in contact area between the AA6082 and AA5083 welds, especially evident for the very low axial load situation illustrated in Figures 5a and b. Schmidt and Hattel [23] also advocate that sticking conditions at the tool-workpiece interface will be developed when the friction shear stress at the interface exceeds the yield shear stress of the underlying base material. On the other hand, when the contact shear stress is smaller than the base material yield shear stress, sliding conditions will prevail. According to present results, sticking conditions will easily develop during FSW of the AA6082 alloy, which presents decreasing flow stress with temperature, and sliding or partial sliding/sticking conditions will prevail for the work hardenable AA5083 alloy. These assumptions are confirmed by the morphological observations in Figure 5.

4. Conclusions

From the above results it can be concluded that the weldability of both base materials is different due the pronounced differences in plastic deformation behaviour at increasing temperatures. In fact, the visual inspection results of the welds allowed to verify that, under the same welding conditions, the number of defective welds was higher for the AA5083 alloy than for the AA6082 alloy, which indicates that the AA5083 alloy displays much lower weldability than the AA6082 alloy. It was also possible to verify that, meanwhile, for the AA5083 alloy the main types of defects detected were surface and internal defects, which are commonly associated to low heat-input conditions, for the AA6082 alloy, several situations of mass flash formation were registered, which are usually associated to high heat-input conditions during the process, which reinforces the importance of the influence of base material properties on defect formation during the FSW process.

It was also possible to verify that, independently of the welding conditions, the weld cross-section is wider for the AA6082 alloy, being characterized by a well-defined shoulder influence area, extending to the plate mid thickness, and, on the other hand, for the AA5083 weld, the TMAZ is clearly restricted to the pin influence area with a very small evidence of material being dragged by the shoulder. In fact, the amount of material dragged by the tool is much higher for the AA6082 alloy than for the AA5083 alloy, unless for the higher weld speed values, for which the width of the pin affected zone (W) become similar for both alloys. Comparing the evolution of the width of pin affected zone with the traverse speed, for welds obtained with similar force and tilt angle values, and tool dimensions, it was possible to conclude that, for each tool rotational speed, W strongly varies with the tool traverse speed, deeply increasing for decreasing welding speed values. On the other hand, when the variation of W with the rotational speed is analysed, for the AA5083 alloy, it is possible to conclude that the width of the pin affected zone strongly increases when increasing of the tool rotation speed, for the lower tool traverse speed of 50mm.min-1. For the higher tool traverse speed values of 200 and 350 mm.min-1, for which all the welds displayed very small or large defects, W remains in very small values independently of the tool rotation speed. However, for the AA6082 alloy, a strong increase of W when increasing tool rotation speed was registered for 200 mm.min-1 traverse speed. It was also possible to observe that, independently of the base material properties, the size of the shoulder influence zone increases for decreasing traverse speeds and decreasing tool rotational speeds. It is also important to emphasize that when the width of the pin affected zone is inferior to a value near to 7.6 mm, which corresponds to W values only 10 % higher than the pin diameter, internal defects were formed for both alloys.

Finally, the contact conditions at the tool-workpiece interface will be also determined by the plastic properties of the base materials. Actually, under similar axial load conditions, the extreme thermal softening experienced by the AA6082 alloy will lead to further submerging of the tool, relatively to the AA5083 alloy, which explains the strong differences in contact area between the AA6082 and AA5083 welds, especially evident for the very low axial load situations.

5. Acknowledgements

The authors are indebted to the Portuguese Foundation for the Science and Technology (FCT) through COMPETE program from QREN and to FEDER for the financial support.

References

[1] Thomas W.M., Nicholas E.D., “Friction stir welding for the transportation industries”, Mat. Des., vol. 18, pp. 269-273, 1997.

[2] Leitao C., Leal R.M., Rodrigues D.M., Loureiro A. and Vilaca P., “Mechanical behaviour of similar and dissimilar AA5182-H111 and AA6016-T4 thin friction stir welds”, Mat. Des., vol. 30, pp. 101-108, 2009.

[3] Rodrigues D.M., Loureiro A., Leitao C., Leal R.M., Chaparro B.M. and Vilaca P., “Influence of friction stir welding parameters on the microstructural and mechanical properties of AA 6016-T4 thin welds”, Mat. Des., vol. 30, pp. 1913-1921, 2009.

[4] Mishra R.S. and Ma Z.Y., “Friction stir welding and processing”, Mater. Sci. Eng. R., vol. 50, pp. 1-78, 2005.

[5] Padmanaban G. and Balasubramanian V., “Selection of FSW tool pin profile, shoulder diameter and material for joining AZ31B magnezium alloy - An experimental approach”, Mat. Des., vol. 30, pp. 2647-2656, 2009.

[6] Liu H.J., Shen J.J., Huang Y.X., Kuang L.Y., Liu C. and Li C., “Effect of tool rotation rate on microestruture and mechanical properties of friction stir welded copper”, Sci. Technol. Weld. Joining, vol. 14, pp. 577-583, 2009.

[7] Bhadeshia H.K.D.H. and Debroy T., “Critical assessment: friction stir welding of steels”, Sci. Technol. Weld. Joining, vol. 14, pp. 193-196, 2009.

[8] Zhang Y., Sato Y.S., Kokawa H., Park S.H.C. and Hirano S., “Microestructural characteristics and mechanical properties of Ti-6Al-4V friction stir welds”, Mater. Sci. Eng. A. vol. 485, pp. 448-455, 2008.

[9] Mononen J., Sirén M. and Hänninen H., “Cost comparison of FSW and MIG welded aluminium panels”, Weld. World, vol. 47, pp. 32-35, 2003.

[10] Kim Y.G., Fujii H., Tsumura T., Komazaki T. and Nakata K., “Three defect types in friction stir welding of aluminum die casting alloy”, Mat. Sci. Eng. A., vol. 415, pp. 250-254, 2006.

[11] Chen H.-B., Yan K., Lin T., Chen S.-B., Jiang C.-Y. and Zhao Y., “The investigation of typical welding defects for 5456 aluminum alloy friction stir welds”, Mat. Sci. Eng. A., vol. 433, pp. 64-69, 2006.

[12] Iordachescu M., Iordachescu D., Ocana J.L., Vilaça P. and Scitelnicu E., “Characteristic flaws in aluminium alloys joints”, Metal. Int., vol. 12, pp. 135, 2009.

[13] Elangovan K. and Balasubramanian V., “Influences of tool pin profile and welding speed on the formation of friction stir processing in AA2219 aluminium alloy”, J. Mater. Process. Tech., vol. 200, pp. 163-175, 2008.

[14] Louro R., Leitao C., Puehringer T., Gouveia H., Loureiro A. and D.M. Rodrigues, “The Relation Between the Plunge Pressure and the Mechanical Properties of Friction Stir Welded 3mm Thick AA6082-T651 Sheets”, Mater. Sci. Forum, vol. 636-637, pp. 578-584, 2010.

[15] Arbegast W.J., “A flow-partitioned deformation zone model for defect formation during friction stir welding”, Scripta Mater., vol. 58, pp. 372-376, 2008.

[16] Kumar K. and Kailas S.V., “The role of friction stir welding tool on material flow and weld formation”, Mat. Sci. Eng. A., vol. 485, pp. 367-374, 2008.

[17] Zhang H., Lin S.B., Wu L., Feng J.C. and Ma S.L., “Defects formation procedure and mathematic model for defect free friction stir welding of magnesium alloy”, Mat. Des., vol. 27, pp. 805-809, 2006.

[18] Colegrove P.A., Shercliff H.R. and Zettler R., “Model for predicting heat generation and temperature in friction stir welding from the material properties”, Sci. Technol. Weld. Joining, vol. 12, pp. 284-297, 2007.

[19] Colegrove P.A. and Shercliff H.R., “CFD modelling of friction stir welding of thick plate 7449 aluminium alloy”, Sci. Technol. Weld. Joining, vol. 11, pp. 429-441, 2006.

[20] Arora A., Nandan R., Reynolds A.P. and DebRoy T., “Torque, power requirement and stir zone geometry in friction stir welding through modeling and experiments”, Scripta Mater., vol. 60, pp. 13-16, 2009.

[21] Zhang Z. and Chen J.T., “The simulation of material behaviors in friction stir welding process by using rate-dependent constitutive model”, J. Mater. Sci., vol. 43, pp 222-232, 2008.

[22] Arora A., Zhang Z., De A. and DebRoy T., “Strains and strain rates during friction stir welding”, Scripta Mater., vol. 61, pp. 863-866, 2009.

[23] Schmidt H. and Hattel J., “A local model for the thermomechanical conditions in friction stir welding”, Model. Simul. Mater. Sc. Eng., vol.13, pp. 77-93, 2005.

[24] Colegrove P.A., “3Dimensional CFD modelling of flow round a threaded friction stir welding tool profile”, J. Mater. Process. Technol., vol.169, pp. 320-327, 2005.

[25] Rodrigues D.M., Leitao C., Loureiro A. and Louro R., “Viscoplastic materials behaviour and its infuence on friction stir weldability”, in: 8th International Friction Stir Welding Symposium, Timmendorfer Strand, Germany, 2010.

[26] Seidel T.U. and Reynolds A.P., “Two-dimensional friction stir welding process model based on fluid mechanics”, Sci. Technol. Weld. Joining, vol.8, pp. 175-183, 2003.

Annex F

Materials and Design 37 (2012) 402–409

Contents lists available at SciVerse ScienceDirect

Materials and Design

journal homepage: www.elsevier.com/locate/matdes

Analysis of high temperature plastic behaviour and its relation with weldability in friction stir welding for aluminium alloys AA5083-H111 and AA6082-T6

C. Leitão [a], R. Louro [b], D.M. Rodrigues [a,*]

[a] CEMUC, Mechanical Engineering Department, University of Coimbra, Portugal
[b] ISQ, Welding and Quality Institute, Portugal

ARTICLE INFO

Article history:
Received 13 December 2011
Accepted 16 January 2012
Available online 24 January 2012

Keywords:
Welding
Plastic behaviour
Thermal analysis

ABSTRACT

The influence of the plastic behaviour of two aluminium alloys, very popular in welding construction, on friction stir weldability, is analysed in this work. The two base materials, a non-heat-treatable (AA5083-H111) and a heat-treatable aluminium (AA6082-T6) alloy, are characterised by markedly different strengthening mechanisms and microstructural evolution at increasing temperatures. Their plastic behaviour, under different testing conditions, was analysed and compared. The two base materials were also welded under varied friction stir welding (FSW) conditions in order to characterise their weldability. The relation between weldability, material flow during FSW and the plastic behaviour of the base materials, at different temperatures, was analysed. It was found that the AA6082 alloy, which displays intense flow softening during tensile loading at high temperatures, and is sensitive to dynamic precipitation and overageing under intense non-uniform deformation, displays good weldability in FSW. Under the same welding conditions, the AA5083 alloy, which in quasi-static conditions displays steady flow behaviour at increasing temperatures, and is sensitive to moderate hardening at high strain rates, displays poor weldability.

1. Introduction

The establishment of accurate relationships between base materials plastic behaviour, process parameters and weld characteristics is still an almost unexplored topic in friction stir welding (FSW) research. Actually, despite being a solid state process, in which plastic deformation plays a major role in the joining mechanisms, studies relating the plastic behaviour of the base materials with material flow and/or heat generation during the process are still very scarce. In fact, over the past decade, most of published literature on FSW was focused on the microstructural and mechanical characterisation of the welds, on the understanding of the material flow mechanisms and on the analysis of the heat generation and dissipation during the process [1]. Concerning this last aspect, regardless of being currently accepted that heat generation during the process results simultaneously from friction and plastic deformation, there is still no consensus regarding which will be the dominant heat generation mechanism or the prevalent contact condition at the tool/workpiece interface [2–7].

Actually, establishing relations between plastic behaviour and material flow during FSW is a very difficult task, either by experimental means or by numerical simulation, due to the high difficulty in characterising the plastic behaviour of the materials at the temperatures and strain rates attained during FSW. Despite these huge difficulties, significant efforts in understanding the thermal histories and temperature distributions in the welds were already spent, using both experimental work and numerical predictions [2–5,7–15]. A common feature to almost all the numerical works was the difficulty in previewing the maximum temperature attained in the process. This problem is usually overcome by using different modelling alternatives, such as adapting the heat generation models, heat exchange coefficients and/or the tool-workpiece contact conditions. However, any possible influence of the plastic properties of the materials in heat-generation and/or friction stir weldability is not fully explored and/or understood.

Balasubramanian et al. [16,17] were the first in developing empirical relationships between base materials properties and friction stir weldability. However, their relations only take into account base material properties such as hardness, yield strength, tensile strength and maximum elongation, all at room temperature, which are not sufficient for fully characterising base material plastic behaviour in FSW conditions.

In a previous work from current authors [18], important differences in friction stir weldability between two aluminium alloys often used in welding construction, the non-heat-treatable AA5083-H111 and the heat-treatable AA6082-T6 aluminium alloys, were depicted. Since both alloys were welded under similar

* Corresponding author. Tel.: +351 239 790 700; fax: +351 239 790 701.
E-mail address: dulce.rodrigues@dem.uc.pt (D.M. Rodrigues).

0261-3069/$ - see front matter © 2012 Elsevier Ltd. All rights reserved.
doi:10.1016/j.matdes.2012.01.031

processing conditions, the differences in base materials plastic properties were pointed as the main factor in determining the different welding behaviour. So, in a subsequent work, which is described in current paper, the plastic behaviour of the two base materials was deeply analysed by performing mechanical characterisation tests under varied temperatures and loading conditions. Thermal simulation tests were also conducted, for both base materials, replicating heating conditions close to that occurring during FSW. Finally, the morphology of welds obtained for the two base materials was deeply analysed and compared. Based on base materials mechanical characterisation results, weld characteristics and on authors past experience on FSW material flow analysis [19,20] and microstructural and mechanical characterisation of 5xxx and 6xxx friction stir welds [21–24], important relations between base materials plastic properties and weld characteristics were established, which will be described in the next. First, the friction stir welding results, for both alloys, are compared, and after that, the main differences in weldability are enhanced and explained based on base materials plastic properties at high temperature.

2. Experimental procedure

2.1. Welding tests

In order to analyse the weldability of the AA5083-H111 and AA6082-T6 base materials, supplied in 6 mm thick plates, they were welded using different tools and process parameters. Since the material flow mechanisms in FSW with conical tools are already well known [19], which is important for establishing relations between it and the plastic behaviour of the base materials during welding, conical shoulder tools, with cone angle of 5° and cylindrical threaded pins, were used. The welding speed (v), rotating speed (w), vertical force (F_z), shoulder and pin diameters (D_s and D_p, respectively) and tool pitch angle (α) were varied according to Table 1. Bead-on-plate welds were produced in order to eliminate the influence of sheet positioning and clamping on welding test results.

The testing plan (Table 2), established by combining the different tool and processing parameters, determined a total of 36 welds to be performed for each base material. After welding, all welds were visually inspected for identifying surface defects like flash and surface flaws. Transverse specimens were also cut from the welds, cold mounted, polished, etteched and observed using the Zeiss Stemi 2000-C and Zeiss Axiotech 100HD microscopes, for detecting large and very small internal flaws as well as for analysing welds morphology.

2.2. Mechanical characterisation test

The plastic behaviour of the AA5083 and AA6082 alloys was analysed by performing tensile and shear tests. The tensile tests were performed using Instron 8800 FastTrack and Instron 4206 machines, in accordance with the ASTM E8 M and ASTM E21 standards [25,26]. The testing speed was 5 mm/min and the testing temperatures ranged from room temperature to 500 °C. The temperature was controlled using a thermocouple placed inside the convection oven, directly in contact with the surface of the samples. The shear tests were performed under quasi-static conditions, with 5 mm/min testing speed, in an Instron 4206 machine, by using a tool specially developed for testing thick material samples. Strain data acquisition was performed using ARAMIS Optical 3D Deformation & Strain Measurement system. Finally, microhardness measurements, in selected areas of the mechanical testing samples and of the welds, were performed using a Shimadzu – Micro-Hardness Tester with 200 gf load for 30 s.

Table 1
Friction stir welding parameters.

Tool parameters	Pin diameter (D_p) (mm)			Shoulder diameter (D_s) (mm)			Tilt angle (α (°))		
	6	7		15	18	21	1	2	3
Process parameters	Weld speed (v), mm min^{-1}			Rotational speed (w) (rpm)			Axial force (F_z) (kN)		
	200	275	350	300	400	500	10	15	20

Table 2
Welding plan.

	D_p (mm)	D_s (mm)	α (°)	v (mm min^{-1})	w (rpm)	F_z (kN)
1	6	15	1	200	300	10
2	6	15	2	200	400	15
3	7	15	3	200	500	20
4	7	18	1	200	300	10
5	6	18	2	200	400	15
6	6	18	3	200	500	20
7	7	18	1	200	300	15
8	7	18	2	200	400	20
9	6	18	3	200	500	10
10	6	21	1	200	300	20
11	7	21	2	200	400	10
12	7	21	3	200	500	15
13	6	15	1	275	400	20
14	6	15	2	275	500	10
15	7	15	3	275	300	15
16	7	18	1	275	400	20
17	6	18	2	275	500	10
18	6	18	3	275	300	15
19	7	18	1	275	400	10
20	7	18	2	275	500	15
21	6	18	3	275	300	20
22	6	21	1	275	400	15
23	7	21	2	275	500	20
24	7	21	3	275	300	10
25	6	15	1	350	500	15
26	6	15	2	350	300	20
27	7	15	3	350	400	10
28	7	18	1	350	500	15
29	6	18	2	350	300	20
30	6	18	3	350	400	10
31	7	18	1	350	500	20
32	7	18	2	350	300	10
33	6	18	3	350	400	15
34	6	21	1	350	500	10
35	7	21	2	350	300	15
36	7	21	3	350	400	20

3. Results and discussion

3.1. Friction stir welding results

Visual inspection and metallographic analysis enabled to identify non-defective welds (examples in Fig. 1a–c and e) and three main types of defects: internal flaws and flash (examples in Fig. 1d, g and h), for both base materials, and surface flaws (example in Fig. 1f), for the AA5083 welds. The full range of welding inspection results are summarised in the graphs of Fig. 2 and 3, where the pressure (P) versus rotation to traverse speed ratio (w/v), for all welding test conditions, are plotted. The pressure parameter, which was calculated using the equation:

$$P = \frac{F_z}{\frac{\pi}{4}(D_s^2 - D_p^2)} \quad (1)$$

reflects the influence of the axial load (F_z) and tool parameters (D_s and D_p) on welding results. In the graph, the acceptable welds,

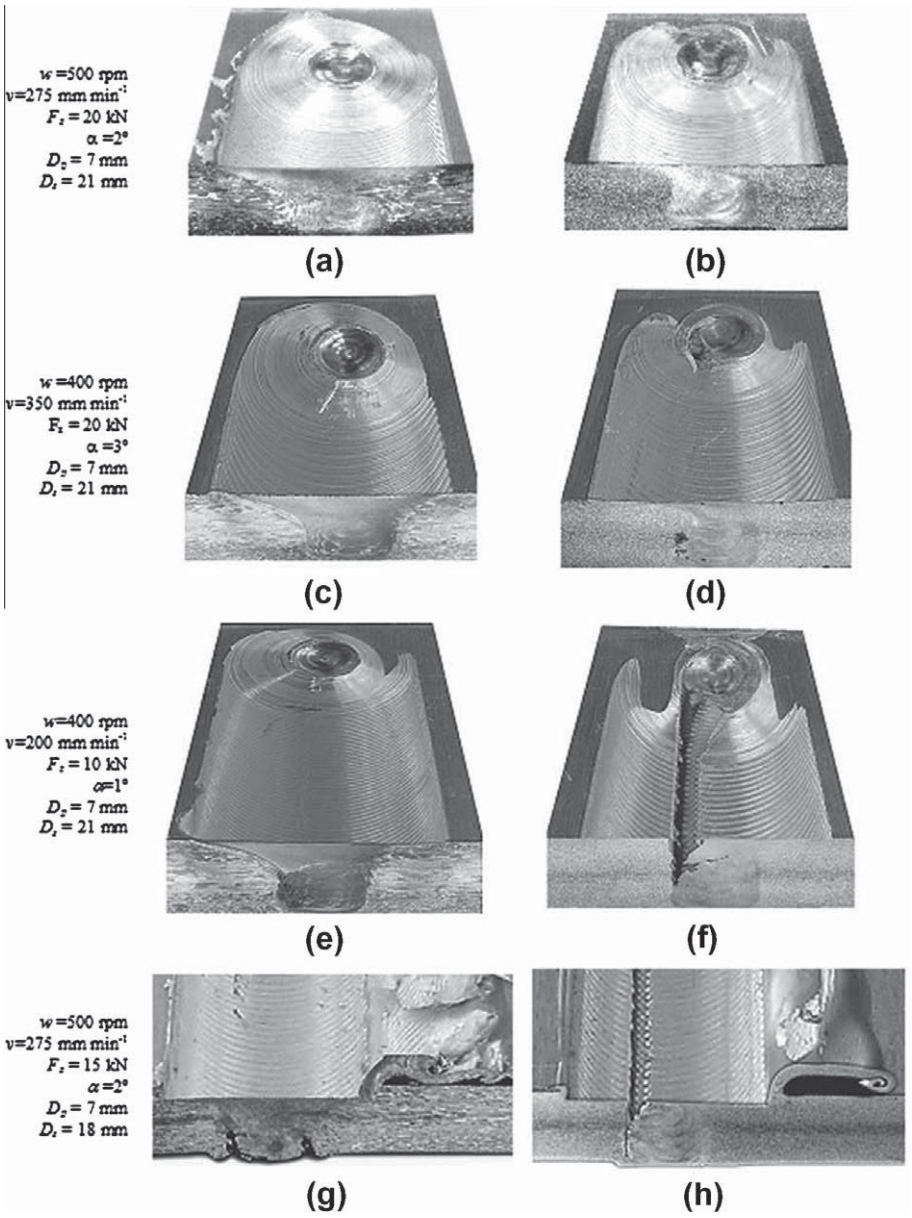

Fig. 1. Top views and cross-sections of AA 6082 (a, c, e and g) and AA 5083 (b, d, f and h) welds.

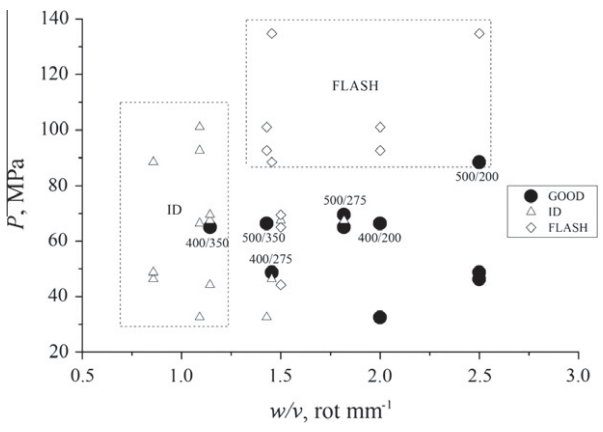

Fig. 2. Welding results for the AA6082 alloy.

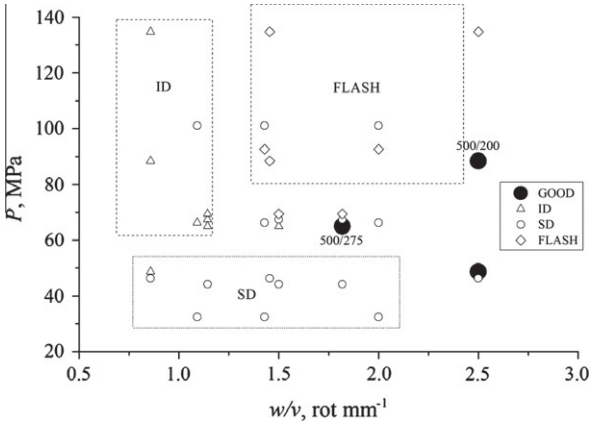

Fig. 3. Welding results for the AA5083 alloy.

named GOOD welds, are identified using large black symbols, and the welds with defects, by using smaller symbols of different types. The results identified as GOOD also comprise welds with very small defects, which were not considered important for the global strength of the welded plates [18]. The tool rotation to traverse speed (w/v) ratio, corresponding to the GOOD welding results, are also explicitly identified in the graph. Comparing Figs. 2 and 3, relative to the AA6082 and AA5083 alloy, respectively, it is possible to conclude that, for the range of welding parameters tested in this work, the AA6082 base material have higher weldability than the AA5083 base material, since a larger number of GOOD welds was obtained for that alloy. Actually, it is possible to observe that meanwhile for the AA5083 alloy, it was impossible to obtain GOOD welds using the tool rotation rates of 300 and 400 rpm and the tool traverse speed of 350 mm/min, for the AA6082 alloy, it was only impossible to obtain GOOD welds using the tool rotation speed of 300 rpm. However, it is important to remark that the number of non-acceptable welds was very high for both alloys, showing that the process is very sensitive to the combination of tool and machine parameters.

In Figs. 2 and 3, process parameter domains, corresponding to a larger incidence of each defect type, were delimited. Comparing the pictures it is possible to conclude that, for both base materials, flash was mainly formed for the higher values of w/v, corresponding to the higher heat input conditions, and for the higher values of pressure, P, corresponding to the use of the smaller shoulder diameter tool (D_s = 15 mm). For the lower w/v values, internal flaws (ID) were the main type of defect detected for both alloys. However, for the AA5083 alloy, for almost the entire range of w/v values, surface flaws (SD) were also detected for the lower pressure conditions, corresponding to the utilisation of very low axial loads (10 and 15 kN). In contrast, for the AA6082 alloy, no strong limitation in axial load was found, being possible to obtain GOOD welds for all the loads tested. Finally, defects of varying types, according to the global combination of process parameters, were detected for the welds performed with tool tilt angle $\alpha = 1°$. These situations, which are not explicitly identified in Figs. 3 and 4, justify some dispersion of the weld inspection results in both graphs.

Another important conclusion, which can be drawn from present work, is the existence of a close relation between weld morphology and base material type. Actually, comparing the pictures in Fig. 1, where AA6082 and AA5083 weld cross sections are displayed, it can be depicted a completely different morphology for welds performed under exactly the same welding conditions. As it is possible to observe in the figure, independently of the welding conditions, the weld cross-sections are wider for the AA6082 plates, being characterised by a well-defined shoulder influence zone, extending to the mid-plates thickness. Instead, for the AA5083 welds, the TMAZ is almost restricted to the pin influence zone with a very small evidence of material being dragged by the shoulder. In previous works [4,5,10,27,28], the evolution of welds morphology and dimensions was related with the variation in welding parameters. However, since each pair of welds shown in Fig. 1 was performed using exactly the same welding conditions, it is from now possible to say that the weld morphology also depends on base material properties.

In Fig. 1 it is also shown, for each weld, the final print left by the tool at the end of the welding operation. As it is possible to conclude from the figure, for the AA6082 weld, the shoulder mark is almost perfectly round, except for the lower axial load weld (Fig. 1.e), showing that the material was dragged easily by the shoulder. For the AA5083 weld, the final print left by the shoulder clearly shows that the shoulder-workpiece contact area was restricted to the trailing side of the tool, especially for the cold welds, performed at 400 rpm (Fig. 1d and f). Again, since the AA6082 and AA5083 welds were performed under the same welding conditions, the differences in contact conditions have to be related with intrinsic base material properties.

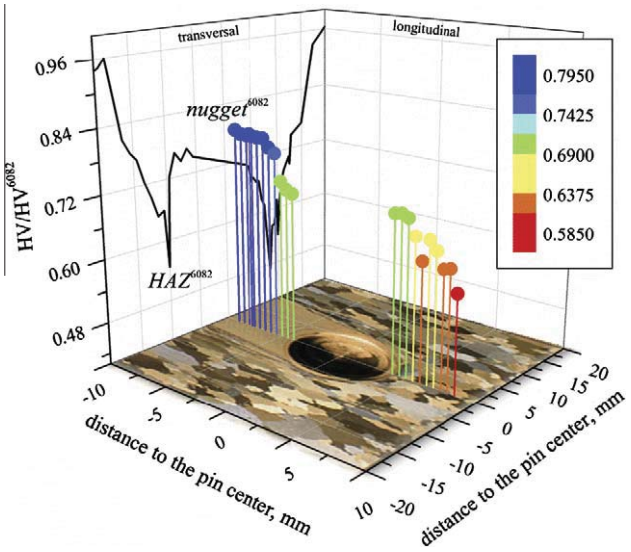

Fig. 4. Transverse and longitudinal hardness for a AA6082 weld. Welding conditions: w = 500 rpm, v = 275 mm min^{-1}, F_z = 20 kN, $\alpha = 2°$, D_p = 7 mm and D_s = 21 mm. HV^{6082} is the initial base material hardness.

In Figs. 4 and 5 are shown transverse and longitudinal hardness profiles, obtained near the end of the weld, where is located the final hole left by the pin, for the welds in Fig. 1a and b. Actually, these welds will be used as reference in the comparative analysis to be developed in the next items, since they were performed using welding parameters which enabled to obtain non-defective welds for both base materials. Fig. 4 shows that the AA6082 weld display the W shape hardness profile characteristic of the heat-treatable alloys friction stir welds, which was already deeply analysed by Sato et al. [29] and Upadhyay and Reynolds [30] in previous publications. From the figure it is possible to confirm that the intense hardness drop in the HAZ, relative to the initial base material hardness (HV^{6082}), extends to the front of the tool where the tool dragging action will be exerted. For the AA5083 welds, no variation

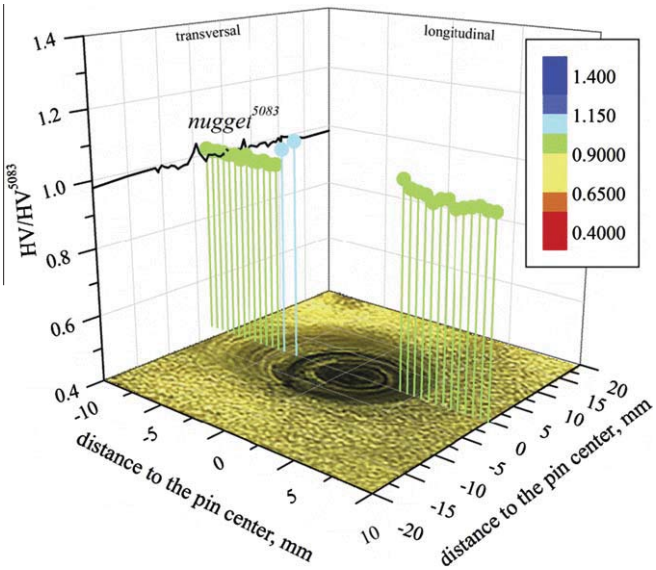

Fig. 5. Transverse and longitudinal hardness for a AA5083 weld. Welding conditions: w = 500 rpm, v = 275 mm min^{-1}, F_z = 20 kN, $\alpha = 2°$, D_p = 7 mm and D_s = 21 mm. HV^{5083} is the initial base material hardness.

relative to the initial base material hardness (HV^{5083}) was registered, nor in the TMAZ, nor in the HAZ surrounding the tool, as can be depicted from Fig. 5. The hardness evolution for AA5xxx friction stir welds was already deeply analysed in literature [23].

3.2. Mechanical characterisation results

In Fig. 6 are shown stress–strain curves for both base materials, obtained in tension and shear, at room temperature in quasi-static conditions (5 mm min^{-1}). Analysing the curves it is possible to conclude that the AA5083 alloy displays much lower yield strength than the AA6082 alloy, in both shear and tension. However, despite displaying much lower tensile yield strength, the AA5083 alloy exhibits strong Portevin-Le Châtelier effect and pronounced hardening with plastic deformation, attaining tensile strength values very close to that of the AA6082 alloy. From the shear test results, which enable to compare the plastic behaviour of both base materials until values of plastic deformation higher than that attained in tension, it can be concluded that, meanwhile for the AA6082 alloy, an almost steady-state flow stress is attained after moderate values of plastic deformation, for the AA5083 alloy, the flow stress keeps increasing with loading, attaining values higher than that registered for the AA6082 alloy. Inside the graph of Fig. 6 is also show a smaller graph where the hardness registered for the tensile and shear samples, of both base materials, before and after plastic deformation, is compared. The hardness values for the deformed samples are that measured near the rupture section, where extreme values of plastic deformation were attained. From the graph it is possible to conclude that despite the hardness values relative to the non-deformed alloys are very different (HV^{5083} = 87 $Hv_{0.2}$ and HV^{6082} = 120 $Hv_{0.2}$), they become similar after plastic deformation. In fact, meanwhile for the AA5083 alloy, the hardness strongly increases with plastic deformation, for the AA6082 alloy, the hardness registered for the deformed and non-deformed samples is very similar. These hardness results enhance again the higher sensitivity of the AA5083 alloy to strain hardening.

Since FSW involves plastic deformation at high temperatures, the plastic behaviour of the base materials was also analysed at temperatures ranging from 240 to 500 °C. In Fig. 7 are shown the engineering stress–strain curves corresponding to the tensile tests performed at temperatures ranging from 240 °C to 500 °C, for the AA5083 alloy, and from 240 °C to 400 °C, for the AA6082 alloy. Inserted in the graph is also shown the evolution of the yield stress (Y_0) with temperature, for both base materials. From both graphs it is possible to conclude that, for the tensile testing conditions used, the yield strength of the base materials become closer at increasing temperatures. It is also possible to observe that the AA6082 alloy displays much smaller strain to failure, than the AA5083 alloy, for the entire range of temperatures. Actually, meanwhile the plastic behaviour of the AA6082 alloy is characterised by strong work softening after peak stress values very close to the yield stress, the plastic behaviour of the AA5082 alloy is characterised by strong work hardening with plastic deformation, at 240 °C, and almost steady flow stress behaviour at the higher temperatures (300–500 °C).

It is well known that, for sufficiently high deformation temperatures, dynamic recovery, and in particular conditions, dynamic recrystallisation, take place during plastic deformation [31], promoting the steady flow stress behaviour registered in Fig. 7, for the AA5083 non-heat treatable alloy. For the heat-treatable alloys, in artificially aged condition, like the AA6082-T6 alloy, concomitantly to dynamic recovery and/or dynamic recrystallisation phenomena, dynamic precipitation also takes place during hot plastic deformation [32]. Dynamic precipitation, which is faster than precipitation in static conditions, due to the increased particle diffusion coefficients in the presence of dense dislocation tangles, easily promotes overageing of the artificially aged microstructure resulting in intense softening with plastic deformation [33], as was registered for the AA6082 alloy, in Fig. 7. According to Wouters et al. [34], the very low ductility experienced by the AA6082 alloy in the high temperature tests should also be related with intense coarsening of precipitates. The mechanisms of failure by coalescence of microvoids, due to localised strain discontinuities, such as that associated with second phase particles, grain boundaries, and dislocation pile-ups, are well documented in literature [35].

4. Analysis of plastic behaviour versus weldability

During friction stir welding, once steady state welding conditions are attained, the dragging action of the tool over the base material will develop under constant load [14]. So, it is reasonable to assume that the AA6082 alloy, which experiences strong softening with plastic deformation at increasing temperatures, will have good weldability in FSW since it will easily undergo intense plastic deformation under constant load, for a large range of temperatures. In opposition, the AA5083 alloy, which displays work-hardening until 240 °C and steady flow stress at higher temperatures, will

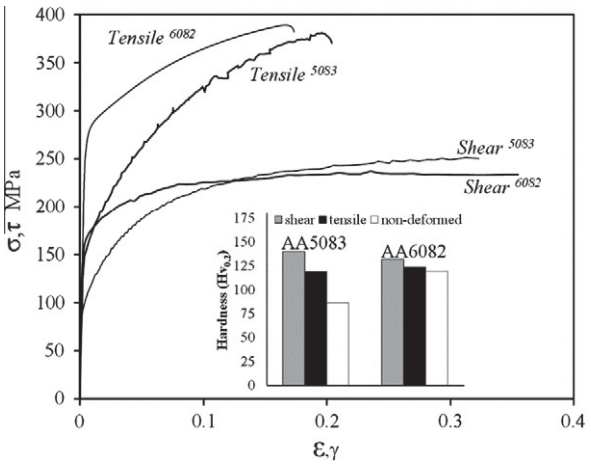

Fig. 6. Base materials tensile and shear stress–strain curves (T = 25 °C, 5 mm min^{-1}).

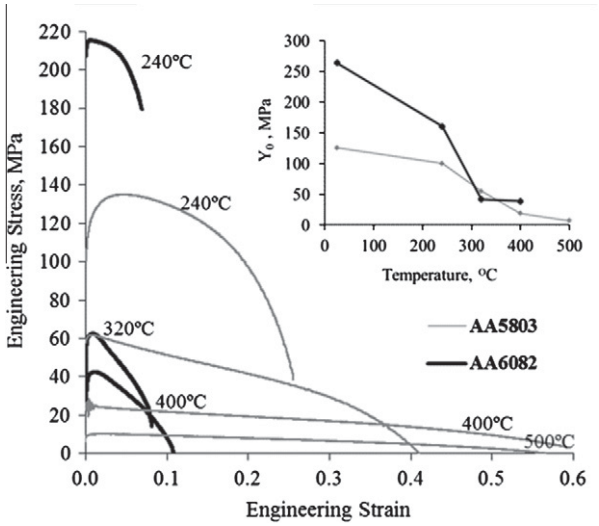

Fig. 7. Engineering tensile stress–strain curves and evolution of base materials yield stress with temperature.

be less efficiently deformed under constant loading conditions. Effectively, comparing the weld shapes displayed in Fig. 1, it is possible to depict that, independently of the welding conditions, the nugget of the welds is much broader for the AA6082 alloy, than for the AA5083 alloy, which corroborates the previous assumptions.

For the AA6082 welds it is even possible to identify in each weld cross-section of Fig. 1 a wide zone of severely deformed but non-recrystallised TMAZ material, which also evidences the intense plastic deformation of this material at temperatures lower than that attained in the nugget. For the AA5083 alloy, nor a deep shoulder influence zone, nor a wide non-recrystallised TMAZ, are visible in any of the welds cross-sections, which also points for the lower efficiency of the tool in dragging the AA5083 base material. Finally, it is also important to consider that the AA6082 alloy displayed very low ductility at high temperatures, which was already related with microvoid coalescence at the grain and large particle boundaries. Assuming that this microvoid coalescence mechanisms are active during FSW, due to intense plastic deformation taking place, the mixing of the materials from the pin and shoulder flow layers should be facilitated by the internal decohesion of the material. Again, material mixing from different flow layers will be much more difficult for the AA5083 alloy, which displays continuous plastic deformation and very high elongation at increasing temperatures.

Despite the important differences in plastic behaviour at high temperatures depicted from the mechanical characterisation work, and the possible relation between it and the material flow behaviour during FSW pointed in previous paragraphs, it is important to observe that the heating and cooling conditions to which the materials were subjected before and after tensile testing are much gentler than that experienced by the materials during FSW. Actually, since the plastic behaviour of the AA6082 alloy is conditioned by solubilisation and precipitation mechanisms, which are strongly time and temperature dependent, an important question is whether at the very fast heating and loading conditions experienced during FSW, the flow softening mechanism discussed during Fig. 7 analysis will be active.

In order to analyse the sensitivity of the AA6082 alloy to overageing at very high heating rates, very small samples of the AA6082 alloy were heated at 30 °Cs^{-1} using a Theta 5528 vertical infra-red furnace. The volume of each sample was approximately 90 mm^3 with a cross-section of 3 × 3 mm and the testing temperatures ranged from 240 °C to 600 °C. The use of very small samples and very fast heating conditions intended to simulate the very small volume of material processed by the FSW tool at each revolution and the fast heating conditions experienced during welding. According to previous studies [2,7,36], the heating rates in the thermal simulation tests were even higher than that experienced during welding. After cooling and some days of natural ageing, the hardness of the thermal simulation samples was evaluated. In Fig. 8 is plotted the evolution of the hardness ratio HV/HV^{6082} with temperature, for all the thermal (*Thermal*^{6082} results) and mechanical (*Tensile*^{6082} and *Shear*^{6082} results) testing samples studied in this work. Analysing the results corresponding to the thermal simulation samples, it is possible to conclude that for temperatures ranging from 240 to 400 °C, which are much lower than the solubilisation temperature of the AA6xxx alloys, which ranges from 510 °C to 595 °C, the hardness registered for the very small thermal simulation samples is already lower than that of the base material (HV/HV^{6082} ≅ 0.90). For the 500 and 600 °C thermal simulation samples, which according to references [2,10,13,36–38] were heated to temperatures in the range of that under the tool during FSW, the hardness is much lower than that of the base material (HV/HV^{6082} ≅ 0.45), which point for the occurrence of overageing at heating rates much higher than that experienced in

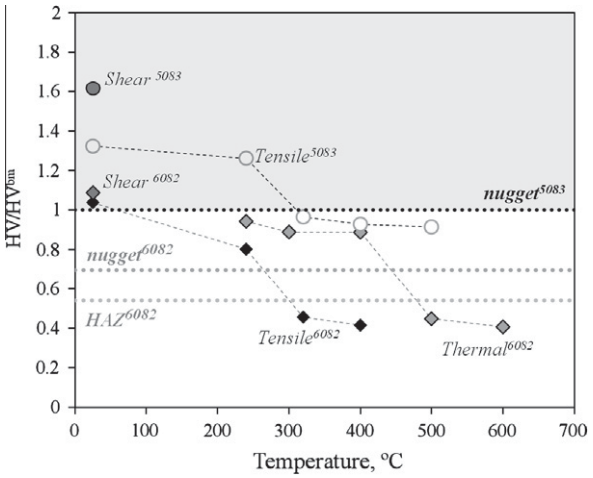

Fig. 8. Hardness ratio (HV/HV^{bm}) versus temperature (HV – average hardness corresponding to the welds and mechanical and thermal simulation samples; HV^{bm} – initial base material hardness).

FSW. In Fig. 8 is also plotted a line (*HAZ*^{6082}) corresponding to the average hardness ratio of the HAZ, in front of the tool, obtained from the hardness profile in Fig. 4. It is possible to see that the average hardness for the 300 and 400 °C tensile samples and for the 500 and 600 °C thermal simulation samples is very close to that of the HAZ. So, it is reasonable to assume that despite being subjected to different thermal cycles, the materials of the different samples are characterised for having the same overaged structure, and in this way, the same plastic properties.

From Fig. 4, where are plotted the transverse and longitudinal hardness profiles for the AA6082 reference weld, it was already concluded that the overaged HAZ domain encompasses the full perimeter in front of the tool. This material, which displays flow softening at increasing plastic deformation and temperatures, will be easily dragged by the toll into the shear layer surrounding the pin, where the weld is formed [19]. In the shear layer, where the overaged HAZ material will be subjected to intense non-uniform deformation, for one or more tool revolutions, precipitate dissolution will be facilitated by the large number of moving dislocations [33] originating new small coherent particles which will be dispersed in the plastically deformed volume. This will contribute for improving the local strength in the nugget, relative to the surrounding HAZ, as is shown in Figs. 4 and 8 (*nugget*^{6082} results).

Contrary to that registered for the AA6082 weld, for the AA5083 weld no hardness decrease relative to the base material was registered, nor in the TMAZ, nor in the HAZ around the tool, as it was already shown in Fig. 5, where are displayed the transverse and longitudinal hardness profiles for the AA5083 reference weld. Comparing now in Fig. 8 the hardness ratios (HV/HV^{5083}) corresponding to the AA5083 tensile samples (*Tensile*^{5083} results) with the hardness ratio corresponding to the weld (*nugget*^{5083}), it is possible to conclude that, contrarily to the weld, the tensile samples display some hardness decrease relative to the base material. Actually, since this alloy displayed steady flow behaviour during the high temperature tensile tests, which is traditionally attributed to the occurrence of intense recovery during plastic deformation, after tensile testing it is expected that the recovered samples microstructure have lower hardness than the moderately strain-hardened base material, in the H111 condition. It is also important to stress that during welding, despite base material is subjected to high temperature plastic deformation, the strain rates are well above the quasi-static limits [3,10,14,39,40]. At very high strain rates, the dislocation generation rate may rise to a level that reduces the effective time for recovery, resulting in a less recovered

structure and increased flow stresses with plastic deformation [31]. This behaviour, which explains the higher hardness values of the weld relative to the tensile samples, also points for increased difficulties in welding the AA5083 alloy. At high strain rates, the increase in flow stress with plastic deformation would prevent intense plastic flow under constant load, which explains the very small amount of material dragged by the toll evidenced by the AA5083 weld cross-sections in Fig. 1. However, it is also important to point that the level of hardening during plastic deformation at high temperatures and strain rates, such as in FSW, is much lower than that experienced during plastic deformation at room temperature or at 240 °C, as it is possible to deduce by comparing in Fig. 8 the hardness ratios for the shear ($Shear^{5083}$) and tensile ($Tensile^{5083}$) samples with that of the weld ($nugget^{5083}$).

Finally, the differences in contact conditions at the tool-workpiece interface, depicted by analysing Fig. 1, can also be explained based in the plastic properties of the base materials. According to Schmidt and Hattel [3], during tool plunge and the first part of the dwell period, a large amount of heat is generated by frictional dissipation, increasing the temperature of the under-shoulder material. Consequently, under similar axial load conditions, the extreme thermal softening experienced by the AA6082 alloy will lead to further submerging of the tool, relatively to the AA5083 alloy, which explains the strong differences in contact area between the AA6082 and AA5083 welds, especially evident for the very low axial load situation illustrated in Fig. 1e and f. Schmidt and Hattel [3] also advocate that sticking conditions at the tool-workpiece interface will be developed when the friction shear stress at the interface exceeds the yield shear stress of the underlying base material. Present results show that sticking conditions will easily develop during FSW of the AA6082 alloy, which presents decreasing flow stress with plastic deformation, and sliding or partial sliding/sticking conditions will prevail for the work-hardenable AA5083 alloy.

5. Conclusions

The influence of the high temperature plastic behaviour of two aluminium alloys, very popular in welding construction, on friction stir weldability, was analysed in this work. It was found that the AA6082 alloy, which according to the base materials mechanical characterisation results, is sensitive to intense flow softening during high temperature plastic deformation, displays good weldability in FSW. For the AA5083 alloy, which according to the base materials mechanical characterisation results, displays steady flow behaviour at increasing temperatures, a very poor weldability was registered under the same welding conditions of the AA6082-T6 alloy. This behaviour results from the strong influence of the plastic properties of the base materials, at high temperatures, on material flow during welding, as well as on contact conditions at the tool workpiece interface. The very important influence of base material plastic properties on friction stir weldability depicted in this work, was never addressed before in FSW literature, which traditionally relates material flow during welding, as well as welds morphology and defects, with tool geometry and/or processing conditions.

Acknowledgements

The authors are indebted to the Portuguese Foundation for the Science and Technology (FCT) and FEDER for the financial support.

References

[1] Nandan R, DebRoy T, Bhadeshia HKDH. Recent advances in friction-stir welding – process, weldment structure and properties. Prog Mater Sci 2008;53:980–1023.
[2] Song M, Kovacevic R. Thermal modeling of friction stir welding in a moving coordinate system and its validation. Int J Mach Tools Manuf 2003;43:605–15.
[3] Schmidt H, Hattel J. A local model for the thermomechanical conditions in friction stir welding. Modell Simul Mater Sci Eng 2005;13:77–93.
[4] Colegrove PA, Shercliff HR, Zettler R. Model for predicting heat generation and temperature in friction stir welding from the material properties. Sci Technol Weld Joining 2007;12:284–97.
[5] Arora A, Nandan R, Reynolds AP, DebRoy T. Torque, power requirement and stir zone geometry in friction stir welding through modeling and experiments. Scripta Mater 2009;60:13–6.
[6] Assidi M, Fourment L, Guerdoux S, Nelson T. Friction model for friction stir welding process simulation: calibrations from welding experiments. Int J Mach Tools Manuf 2010;50:143–55.
[7] Jamshidi Aval H, Serajzadeh S, Kokabi AH. Evolution of microstructures and mechanical properties in similar and dissimilar friction stir welding of AA5086 and AA6061. Mater Sci Eng A 2011;528:8071–83.
[8] Khandkar MZH, Khan JA, Reynolds AP. Prediction of temperature distribution and thermal history during friction stir welding: input torque based model. Sci Technol Weld Joining 2003;8:165–74.
[9] Miles MP, Decker BJ, Nelson TW. Formability and strength of friction-stir-welded aluminum sheets. Metall Mater Trans A 2004;35A:3461–8.
[10] Colegrove PA, Shercliff HR. CFD modelling of friction stir welding of thick plate 7449 aluminium alloy. Sci Technol Weld Joining 2006;11:429–41.
[11] Ren SR, Ma ZY, Chen LQ. Effect of welding parameters on tensile properties and fracture behavior of friction stir welded Al–Mg–Si alloy. Scripta Mater 2007;56:69–72.
[12] Cabibbo M, McQueen HJ, Evangelista E, Spigarelli S, Di Paola M, Falchero A. Microstructure and mechanical property studies of AA6056 friction stir welded plate. Mater Sci Eng A 2007;460–461:86–94.
[13] Hwang Y-M, Kang Z-W, Chiou Y-C, Hsu H-H. Experimental study on temperature distributions within the workpiece during friction stir welding of aluminum alloys. Int J Mach Tools Manuf 2008;48:778–87.
[14] Nandan R, Roy G, Debroy T. Numerical simulation of three-dimensional heat transfer and plastic flow during friction stir welding. Metall Mater Trans A 2006;37:1247–59.
[15] Jacquin D, de Meester B, Simar A, Deloison D, Montheillet F, Desrayaud C. A simple Eulerian thermomechanical modeling of friction stir welding. J Mater Process Technol 2011;211:57–65.
[16] Jayaraman M, Sivasubramanian R, Balasubramanian V. Establishing relationship between the base metal properties and friction stir welding process parameters of cast aluminium alloys. Mater Des 2010;31:4567–76.
[17] Balasubramanian V. Relationship between base metal properties and friction stir welding process parameters. Mater Sci Eng A 2008;480:397–403.
[18] Rodrigues DM, Leitão C, Louro R, Gouveia H, Loureiro A. High speed friction stir welding of aluminium alloys. Sci Technol Weld Joining 2010;14:676–81.
[19] Leal RM, Leitão C, Loureiro A, Rodrigues DM, Vilaça P. Material flow in heterogeneous friction stir welding of thin aluminium sheets: effect of shoulder geometry. Mater Sci Eng A 2008;498:384–91.
[20] Leitão C, Leal RM, Rodrigues DM, Vilaça P, Loureiro A. Material flow in friction stir welding. Microsc Microanal 2008;14:87–90.
[21] Leitão C, Leal RM, Rodrigues DM, Loureiro A, Vilaça P. Mechanical behaviour of similar and dissimilar AA5182-H111 and AA6016-T4 thin friction stir welds. Mater Des 2009;30:101–8.
[22] Rodrigues DM, Loureiro A, Leitão C, Leal RM, Chaparro BM, Vilaça P. Influence of friction stir welding parameters on the microstructural and mechanical properties of AA 6016-T4 thin welds. Mater Des 2009;30:1913–21.
[23] Tronci A, McKenzie R, Leal RM, Rodrigues DM. Microstructural and mechanical characterisation of 5XXX-H111 friction stir welded tailored blanks. Sci Technol Weld Joining 2011;16:433–9.
[24] Leitão C, Galvão I, Leal RM, Rodrigues DM. Determination of local constitutive properties of aluminium friction stir welds using digital image correlation. Mater Des 2012;33:69–74.
[25] ASTM E8M-04. Standard test methods for tension testing of metallic materials (Metric).
[26] ASTM E21-98. Standard test methods for elevated temperature tension tests of metallic materials.
[27] Zhang Z, Chen JT. The simulation of material behaviors in friction stir welding process by using rate-dependent constitutive model. J Mater Sci 2008;43:222–32.
[28] Rosales MJC, Alcantara NG, Santos J, Zettler R. The backing bar role in heat transfer on aluminium alloys friction stir welding. In: Rosa LGMF, editor. Mater Sci Forum; 2010. p. 459–64.
[29] Sato YS, Park SHC, Kokawa H. Microstructural factors governing hardness in friction-stir welds of solid-solution-hardened Al alloys. Metall Mater Trans A 2001;32:3033–42.
[30] Upadhyay P, Reynolds AP. Effects of thermal boundary conditions in friction stir welded AA7050-T7 sheets. Mater Sci Eng A 2010;527:1537–43.
[31] Zhou M, Clode MP. Constitutive equations for modelling flow softening due to dynamic recovery and heat generation during plastic deformation. Mech Mater 1998;27:63–76.
[32] Cerri E, Evangelista E, Ryum N. On the effect of plastic deformation on the coarsening of theta-phase precipitation in an Al–Cu alloy. Metall Mater Trans A 1997;28:257–63.
[33] Verlinden B, Wouters P, McQueen HJ, Aernoudt E, Delaey L, Cauwenberg S. Effect of different homogenization treatments on the hot workability of aluminum alloy – AA2024. Mater Sci Eng A 1990;123:229–37.

[34] Wouters P, Verlinden B, McQueen HJ, Aernoudt E, Delaey L, Cauwenberg S. Effect of homogenization and precipitation treatments on the hot workability of an aluminium alloy AA2024. Mater Sci Eng A 1990;123:239–45.
[35] ASM. ASM Handbook – Fractography; 1987.
[36] Zhang Z, Zhang H. Material behaviors and mechanical features in friction stir welding process. Int J Adv Manuf Technol 2007;35:86–100.
[37] Su JQ, Nelson TW, Mishra R, Mahoney M. Microstructural investigation of friction stir welded 7050-T651 aluminium. Acta Mater 2003;51:713–29.
[38] Amancio-Filho ST, Sheikhi S, dos Santos JF, Bolfarini C. Preliminary study on the microstructure and mechanical properties of dissimilar friction stir welds in aircraft aluminium alloys 2024-T351 and 6056-T4. J Mater Process Technol 2008;206:132–42.
[39] Sato YS, Takauchi H, Park SHC, Kokawa H. Characteristics of the kissing-bond in friction stir welded Al alloy 1050. Mater Sci Eng A 2005;405:333–8.
[40] Nandan R, Roy GG, Lienert TJ, Debroy T. Three-dimensional heat and material flow during friction stir welding of mild steel. Acta Mater 2007;55:883–95.

Annex G

VISCOPLASTIC MATERIALS BEHAVIOUR AND ITS INFLUENCE ON FRICTION STIR WELDABILITY

Dulce Rodrigues, CEMUC – University of Coimbra, Coimbra, Portugal

Carlos Leitão, CEMUC – University of Coimbra, Coimbra, Portugal
Altino Loureiro, CEMUC – University of Coimbra, Coimbra, Portugal
Rui Louro, ISQ, Oeiras, Portugal

SYNOPSIS

With the objective of clarifying the influence of materials plastic behaviour in friction stir weldability, two base materials, a non-heat-treatable (AA 5083-H111) and a heat-treatable aluminium (AA 6082-T6) alloy, characterized by markedly different strengthening mechanisms and microstructural evolution at increasing temperatures, which conduct to markedly different viscoplastic behaviour, were compared. The plastic properties of the base materials, under different testing conditions, which include tensile testing at different temperatures and strain rates, were analysed and compared. The two base materials were also welded under varied welding conditions, using different FSW tools and welding parameters, in order to characterize its weldability in FSW. An important relation between material flow during friction stir welding and the plastic behaviour of the base materials, at different temperatures and strain rates, was found. The obtained results also show that materials plastic properties also influence the contact conditions at the shoulder-base material interface.

INTRODUCTION

The establishment of accurate relationships between Friction Stir Welding (FSW) process parameters, material flow during welding and weld properties, taking into account the viscoplastic behaviour of the base materials, can be an important step towards the universal application of the process. However, despite it is consensual between the welding community that FSW is a solid state process, in which plastic deformation plays a major role in the joining mechanics, studies relating viscoplastic materials behaviour with material flow and/or heat generation during the process are still very scarce. In fact, over the past decade, most of published literature on FSW was focused on the microstructural and mechanical characterization of the welds, the understanding of material flow mechanisms during the process, and finally, the analysis of the heat generation and dissipation under the action of the moving tool. Concerning this last aspect, regardless of being currently accepted that heat generation during the process results simultaneously from friction and plastic deformation, there is still no consensus regarding which will be the dominant heat generation mechanism [1-3]. The assumption of heat generation by plastic deformation also enhances the importance of considering the plastic behaviour of the materials in process parameters analysis and development.

However, exploring the relation between plastic behaviour and material flow during FSW is a very difficult task, either by experimental means or by numerical simulation, due to

the difficulty in characterizing the flow behaviour of the materials at the temperatures and strain rates attained in the FSW process, and so, the difficulty in modelling the process. In addition, the strongly non-linear behaviour of the materials, associated with the extremely high deformations and rotations involved in the process makes its numerical simulation extremely difficult. Due to these huge difficulties, despite significant efforts in understanding the thermal histories and temperature distributions in the welds were already spent, using both experimental work and numerical predictions [3-12], most of the numerical models used were only able to describe the evolution of flow stress with temperature and strain rate, neglecting its evolution with plastic deformation. Colegrove and Shercliff [3,8] modelled the plastic behaviour of the base materials by using a bi-linear relationships to describe the evolution of the flow stress with temperature, at different strain rates, and assuming abrupt softening near the solidus temperature of the materials. Other authors assumed a non-linear evolution of the flow stress with temperature and strain rate [9,10,13,14]. Schmidt and Hattel [7] were the only ones modelling materials behaviour in FSW by using the Johnson-Cook viscoplatic model. However, the objective of its investigation was not the analysis of materials plastic properties in FSW response.

A common feature from the cited numerical works was the overestimation of the maximum temperature attained in the process. This problem was overcome by the different authors by using different solutions, such as manipulating the heat generation and exchange during the process, the contact area between the tool-workpiece interface and/or the contact conditions. Any possible influence of the plastic properties of the materials in heat-generation during the process was never addressed.

In current work, the viscoplastic behaviour of two base materials, a non-heat-treatable (AA5083-H111) and a heat-treatable aluminium (AA6082-T6) alloy, was analysed by performing tensile tests at different temperatures and strain rates. The two base materials were also welded under varied welding conditions, using different FSW tools and welding parameters, in order to characterize its weldability in FSW. Important relations between material flow during friction stir welding and the plastic behaviour of the base materials, at different temperatures and strain rates, were found.

EXPERIMENTAL PROCEDURE

Two base materials, a non-heat-treatable (AA5183-H111) and a heat-treatable aluminium (AA6082-T6) alloy, widely used in welding fabrication, were used in this study. The plastic behaviour of the base materials, supplied in 6 mm thick plates, was analysed by performing tensile tests at different temperatures and strain rates. The tests were performed using Instron 4206 and 8800 FastTrack machines, under the testing conditions resumed in Table 1. As show in Table 1, the tensile tests were performed at temperatures ranging from room temperature to 500 ºC. At room temperature, testing speeds ranging from 5 mm/min (static conditions) to 3000 mm/min (dynamic conditions) were used. Strain data acquisition was performed using ARAMIS Optical 3D Deformation & Strain Measurement system. Temperature data acquisition during the dynamic tests was performed using a FLIR P Series Infrared thermographic camera.

Table 1 – Tensile and shear testing conditions

Tensile Tests	Testing speed [mm/min]	5					500	2000	3000
	Testing temperature [ºC]	25	240	320	400	500	25	25	25

Table 2 – Friction Stir Welding parameters

Tool Parameters	Pin Diameter, d_p [mm]		Shoulder Diameter, d_s [mm]			α [º]		
	6	7	15	18	21	1	2	3
Process parameters	v [mm/min]			w [RPM]			F_z [kN]	
	200	275	350	300	400	500	10	15	20

In order to analyse the weldability in friction stir welding of the base materials, they were welded under varied FSW conditions. The same tool geometry, characterized by a conical shoulder with a cone angle of 5º and a cylindrical threaded pin, was used in all the welding tests. This tool geometry is the most traditional and the one with the highest industrial and research interest due to its simplicity, which reduces the number of design variables in study, and by the fact that its production is relatively simple, compared with more complicated tool designs such as scrolled shoulders, whorl pins, triflutes, etc. It is also important to enhance that the material flow mechanism in FSW with conical tools was already accurately established in literature, which is highly helpful for understanding its relation with the viscoplastic behaviour of the base materials. Despite the geometry was maintained, the tool dimensions, namely, the pin (d_p) and shoulder (d_s) diameters were varied, according to Table 2. The pin length was set so as to guarantee that, during the welding operation, the lowermost surface of the pin does not come in contact with the backing bar and that it remains at 0.1 mm or less from the backing anvil. Bead-on-plate welds were produced for the two different types of plates. This procedure enables to eliminate the influence of sheet positioning and clamping on the resulting weld quality and eases the preparation. For the different types of tools tested in this work, the welding speed (v), rotating speed (w), vertical force (F_z) and pitch angle (α) were also varied. Table 2 sumarizes the different process and tool parameters tested in this work. The testing plan, established by combining the different tool and processing parameters, determined a total of 36 welds to be performed for each base material.

After welding, all sheets were visually inspected for surface defects like excessive flash and surface flaws. Transverse specimens for metallographic analysis were cut from the welds, using water jet cutting, cold mounted, polished, etteched with Poultons modiefied reagent and observed using the Zeiss Stemi 2000-C and Zeiss Axiotech 100HD microscopes, for detecting large and very small internal flaws, respectively. In the next sections, the friction stir welding results for both alloys will be compared and the main differences enhanced. Then, the differences in friction stir weldability of these alloys will be analysed and explained based in the mechanical characterization of the base materials.

FRICTION STIR WELDABILITY

As it was mentioned, qualitative inspection of the welds was performed by visual inspection, for detecting surface defects, followed by metallographic analysis, in order to detect internal flaws. The results of these inpections enabled to detect three basic types of defects: Excessive flash (F), example in Fig. 1.a, surface flaws (SD), example in Fig. 1.b, and internal voids (ID), example in Fig. 1.c. Under some welding conditions, the pin was broken (BP) and it was not possible to performe the weld.

The torque registered by the welding machine, for all the FSW tests, except that which conducted to tool destruction, is plotted in Fig. 2, as a function of the rotation to traverse speed ratio (W/v). In the graph, symbols with different shapes are used for typifying the welding results obtained in each test. For example, the welds with no defects, named GOOD welds, are identified by the larger round symbols, and the welds with surface defects (SD), by small square symbols. The results identified as GOOD comprise the non-defective

welds, but also the welds with very small defects (example in Fig. 1.d), wich were not considered important for the global strength of the welded plates. The tool rotation and traverse speed (W/v), corresponding to the good weld practices, are also explicitly identified in both graphs in order to simplify the analysis of the results.

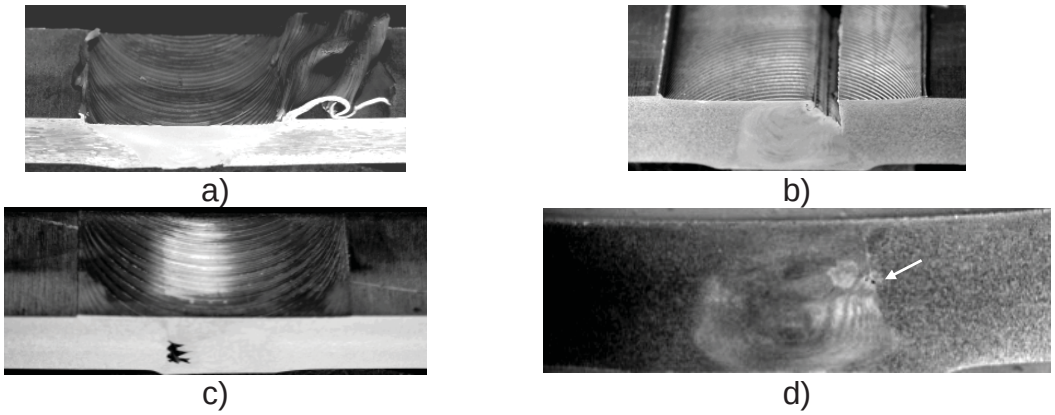

Fig.1 – Tipical welding defects: a) Flash (F), b) Surface defect (SD), c) Internal defect (ID) and d) very small defect.

Comparing the results in the graph of Fig. 2, it is possible to conclude that, for the range of welding parameters tested in this work, the AA 6082 alloy presents higher weldability, than the AA 5083 alloy, since a large number of acceptable welds (good and small defect welds) were obtained. However, it is important to remark that the number of non-acceptable welds (*F*, *SD*, *ID* and *BP*) was very high for both alloys, showing that the process is very sensitive to the choice of tool and machine parameters.

A more detailed analysis of the welding results enabled to establish close relations between the weld defect type and the welding parameters in use. Namely, Flash formation was related to the smaller shoulder diameter tools and the most small tool tilt angle (α= 1º). Another important limiting factor for the successful welding accomplishment was the incorrect choice of the axial load. However, the sensibility of the welds to this parameter is strongly related with the base material nature. In fact, for the AA 5083 alloy, it was found that the utilization of very low axial loads (10 and 15 kN) conducted to important surface and internal welding defects. On the other hand, for the AA 6082 alloy, no strong limitation in axial load was found, being possible to obtain welds absent of internal or surface defects for all the loads tested. Finally, for the AA 5083 alloy, serious limitations in rotation and traverse speeds were detected. In fact, 300 rpm, 400 rpm and 350 mm/min process parameters conducted to defect formation in any combination of process and tool parameters. Low rotation speeds and high traverse speeds conducted to the formation of large internal defects. Large internal defects also occurred for the AA 6082 alloy, for the low rotation speed of 300 rpm.

Another important aspect registered in present work was the markedly different morphology of the welds obtained from the different base materials, under the same welding conditions. In order to better illustrate this aspect, AA 6082 and AA 5083 weld cross sections are shown in Fig. 3.a to f. In the figure, each pair of AA 6082 and AA 5083 welds (a) and b), c) and d), e) and f) were performed using exactly the same welding conditions and the same welding equipment. As it is possible to observe in the figure, independently of the welding conditions, the weld cross-section is wider for the AA 6082 plates, being characterized by a well defined shoulder influence area, extending to the plate mid thickness. On the other hand, for the AA 5083 plates, the TAMZ is clearly restricted to the pin influence area with a very small evidence of material being dragged by the shoulder. For the welds performed with very low axial load (10kN), shown in figures 3.a and 3.b, it is even possible to observe a regular cross-section for the AA 6082 weld, despite with some evidence of incomplete tool

penetration, and a large surface defect for the AA 5083 weld. According to previous authors [3,8,12,15,16], the morphology and dimension of the TMAZ, which is associated with the quantity of material dragged by the tool in each rotation, is strongly influenced by the welding parameters. However, since each pair of welds shown in Fig. 3 was performed using exactly the same welding conditions, it is possible to say that the weld morphology also depends on base material properties.

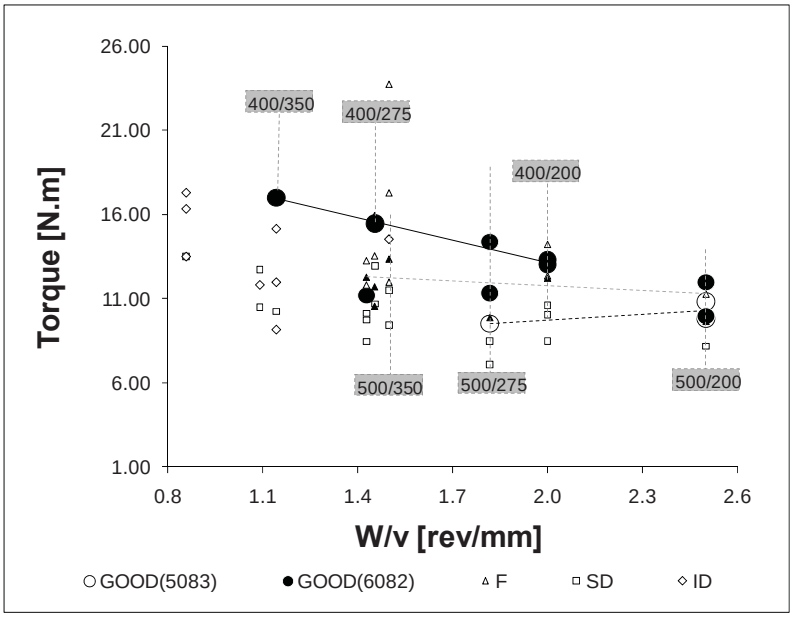

Fig. 2 – Average torque versus tool rotation/traverse speed ratio (W/v).

In Fig. 3 is also shown, for each weld, the final print left by the tool at the end of the welding process. As it is possible to conclude from the figure, for the AA 6082 weld, the shoulder mark is almost perfectly round, except for the low axial load weld (Fig. 3.a), showing that the material was dragged easily by the shoulder. For the AA 5083 weld, the final print left by the shoulder clearly shows that the shoulder-workpiece contact area was restricted to the trailing side of the tool, especially for the cold welds, performed at 400 rpm (Figs. 3.b and f). Again, since the AA 6082 and AA 5083 welds were performed under the same welding conditions, the differences in contact conditions have to be related with intrinsic base

MECHANICAL CHARACTERIZATION OF THE BASE MATERIALS

Figure 4.a shows tensile stress-strain curves, obtained for both base materials in static conditions (5mm/min), at room temperature. Comparing the curves plotted in the graph it is possible to conclude that the AA 5083 alloy, with 148 MPa yield strength, is much softer than the AA 6082 alloy, with 290 MPa yield strength. However, despite being softer, the AA 5083 alloy exhibits strong Portevin-Le Châtelier effect and pronounced hardening with plastic deformation, attaining tensile strength values close to that of the AA 6082 alloy. Deformation until maximum load is also higher for the AA 5083 alloy.

Since FSW involves plastic deformation at high temperatures and strain rates, the plastic behaviour of the base materials was analysed at temperatures ranging from room temperature to 500 ºC, which corresponds to the temperature range registered by several authors during friction stir welding of aluminium alloys under several welding conditions. In Fig 4.b is shown the evolution of the yield stress of both base materials with increasing

temperatures. As it is possible to see in the graph, for temperatures above 300 ºC, the differences in yield stress between the base materials are much less pronounced than for temperatures under 300 ºC, which points the necessity of analysing the evolution of the flow stress with plastic deformation, at high temperatures, for both base materials, in order to understand the corresponding differences in FSW weldability.

In order to illustrate the evolution of the flow stress with plastic deformation and temperature, in Figs. 5.a and b are shown the tensile stress-strain curves, obtained at the different temperatures, for the AA 6082 and AA 5083 alloys, respectively, and in Figs. 5.c and d are plotted the hardening rates ($d\sigma/d\varepsilon$), calculated from the previous curves. In the hardening rate graphs, positive values of $d\sigma/d\varepsilon$ indicate the occurrence of hardening with plastic deformation and negative values indicate softening.

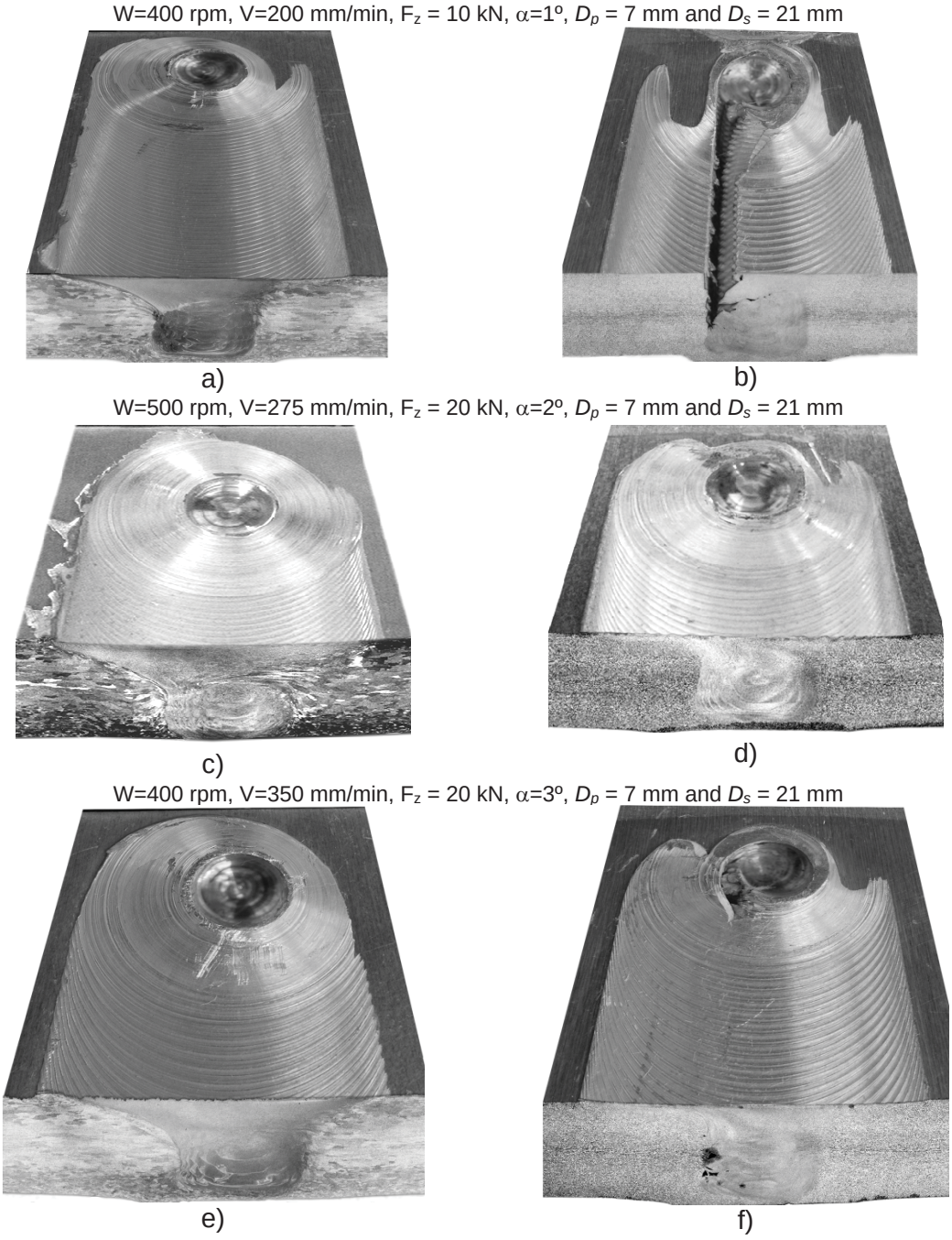

Fig. 3 – Transverse cross-sections of AA 6082 (a, c and e) and AA 5083 (b, d and f) welds.

From Figs. 5.a and c it is possible to conclude that the AA 6082 alloy, at room temperature, experiences moderate hardening with plastic deformation, attaining the maximum load after plastic deformation values ranging 0.13. After maximum load, necking is nucleated, and a sharp drop in strength is registered in the tensile curves, which is traduced by the negative hardening rate values after 0.13 plastic strain. However, for temperatures above 240 ºC, the hardening rate for the AA 6082 alloy sharply decreases after yielding, attaining negative values for very small plastic deformation levels (ε<0.004). These results indicate that the material experiences strong softening with plastic deformation at increasing temperatures, which is traduced by a strong decrease of the flow stress of the material with plastic deformation, as shown in Fig. 5.a. On the other hand, from Figs. 5.b and d, it is possible to conclude that, at room temperature, the AA 5083 alloy experience stronger hardening than the AA 6082 alloy. The hardening behaviour also extends until higher values of plastic deformation (ε=0.21). It is also possible to observe that, contrarily to the AA 6082 alloy, the AA 5083 alloy display hardening until 0.05 plastic deformation, even at 240 ºC, and very small softening with plastic deformation at temperatures higher than 240 ºC. In fact, the almost constant values of the hardening rate indicate an almost perfectly plastic behaviour of this alloy at high temperatures, which means that the flow stress remains nearly constant with plastic deformation (Fig. 5.b). It is also important to enhance that, according to Figures 4.b, 5.a and 5.b, for temperatures above 300 ºC, the decrease in flow strength with increasing temperatures is sharper for the AA 5083 alloy.

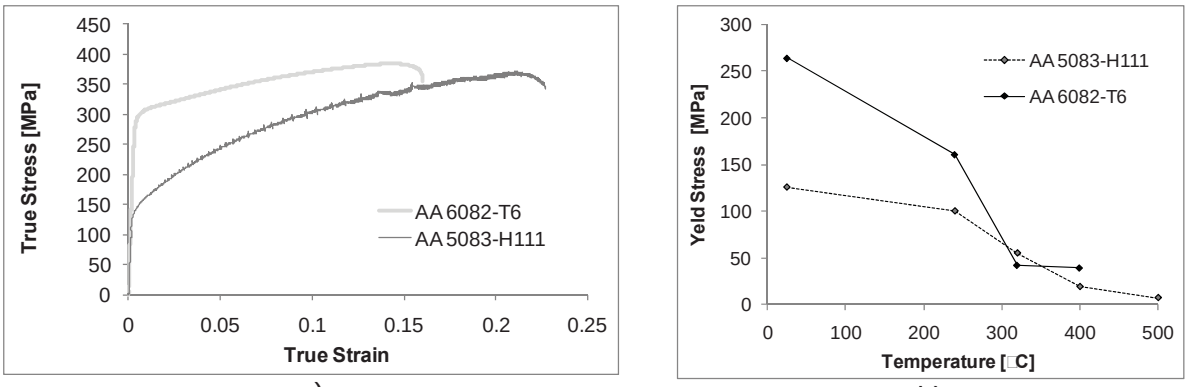

a) b)

Fig. 4 – a) Base materials tensile stress-strain curves (T=25ºC, 5 mm/min). b) Yield stress versus temperature.

Another important subject in FSW analysis is the heat generation during the process, which is usually assumed to result from friction, at the tool-base material interface, and plastic deformation. In fact, despite during quasi-static plastic deformation the heat generated by plastic work is lost by heat conduction and radiation, at very high strain rates, as that experienced by the material during FSW, a portion of this heat remains within the material, causing temperature increase and thermal softening. The temperature rise (ΔT) associated with plastic deformation can be directly obtained from stress-strain curves, by computing

$$\Delta T = \frac{0.9}{\rho C_p}\int_0^{\varepsilon}\sigma(\varepsilon)d\varepsilon \qquad (1)$$

where ρ and C_p are the density and heat capacity of the materials, respectively. In this expression it is assumed the very usual 0.9 conversion factor, which implies that 90% of the work of deformation is changed to heat.

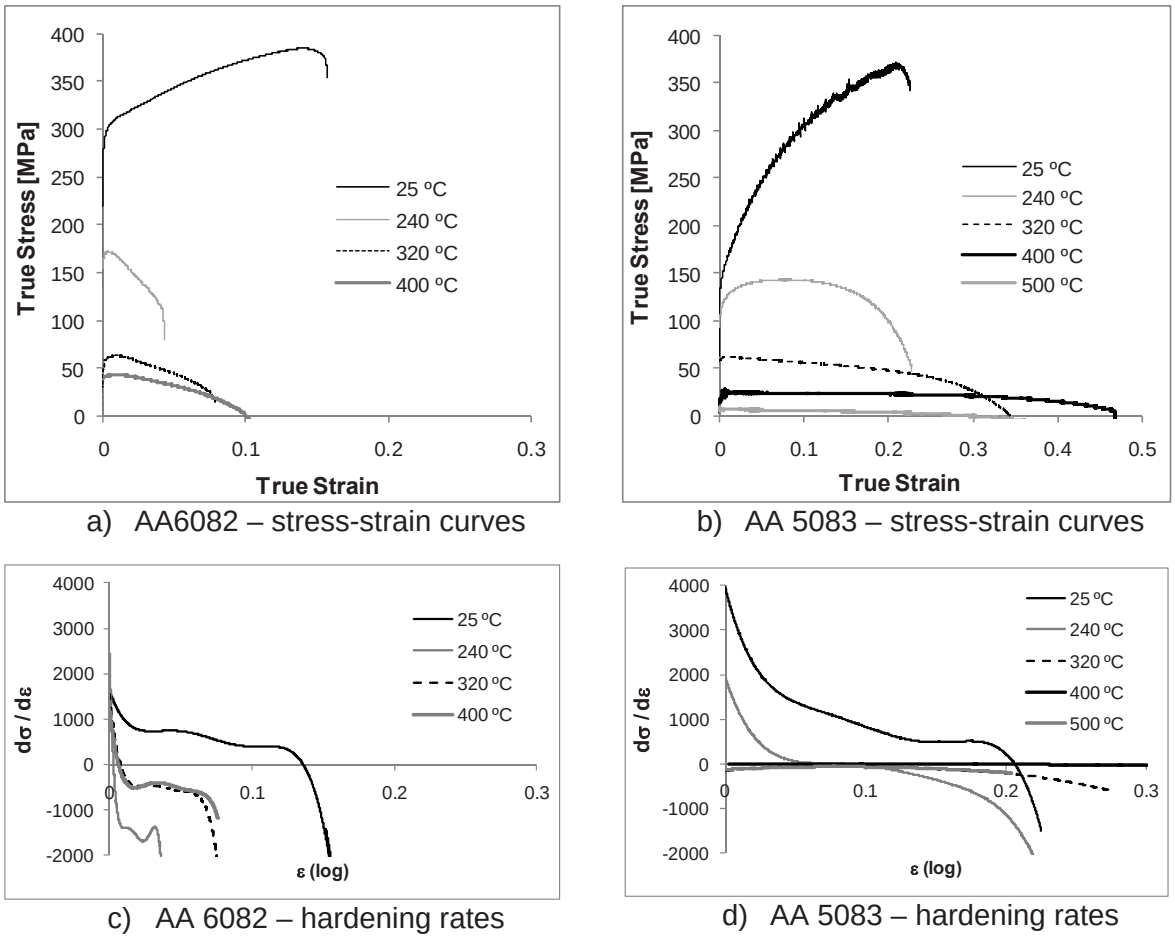

a) AA6082 – stress-strain curves

b) AA 5083 – stress-strain curves

c) AA 6082 – hardening rates

d) AA 5083 – hardening rates

Fig. 5 – Tensile stress-strain curves and hardening rates

In Fig. 6 are shown the tensile stress-strain curves for both alloys, obtained in tensile tests performed with 5 mm/min and 3000 mm/min testing speeds, and the temperature fields registered at maximum load for the samples tested at 3000 mm/min (dynamic conditions), acquired using the thermographic camera. It is important to point that strain data acquisition for the 3000 mm/min curves was performed using the optical system. The 5 mm/min curves were registered using an electrical extensometer. According to the figure, for this range of testing speeds, the materials behaviour is relatively independent of the strain rate. However, for the AA 6082 alloy, some increase in flow stress at the highest strain rate was already registered, which indicates a higher sensitivity of this material to strain rate.

According to the thermographic results, under the same testing conditions (3000 mm/min), the temperature rise was higher for the AA 5083 alloy (ΔT^{exp}= 70 ºC), which experienced higher plastic deformation until rupture, than for the AA 6082 alloy (ΔT^{exp}= 16 ºC). The temperature rise, for both alloys, was also calculated using Eq. (1) by computing the plastic work from the stress-strain curves in Fig. 6. It is important to enhance that these stress-strain curves correspond to points close to the necking region, somewhere inside the area where the maximum temperatures were registered. From Eq. 1 it was obtained ΔT^{Eq}= 40 ºC, for the AA 5083, alloy and ΔT^{Eq}= 22 ºC, for the AA 6082 alloy. These values are different from that registered by the thermographic camera, which can be associated with several factors, namely, the inaccuracy of the material constants in Eq. 1, obtained from bibliography [17], the inaccuracy of the conversion factor used (0.9), and finally, the inability in fully capturing the strain fields in the sample until the exact moment of the records of the

thermographic camera, displayed in Fig. 6. In fact, strain data acquisition rates for the Aramis system were much smaller than that of the thermographic camera.

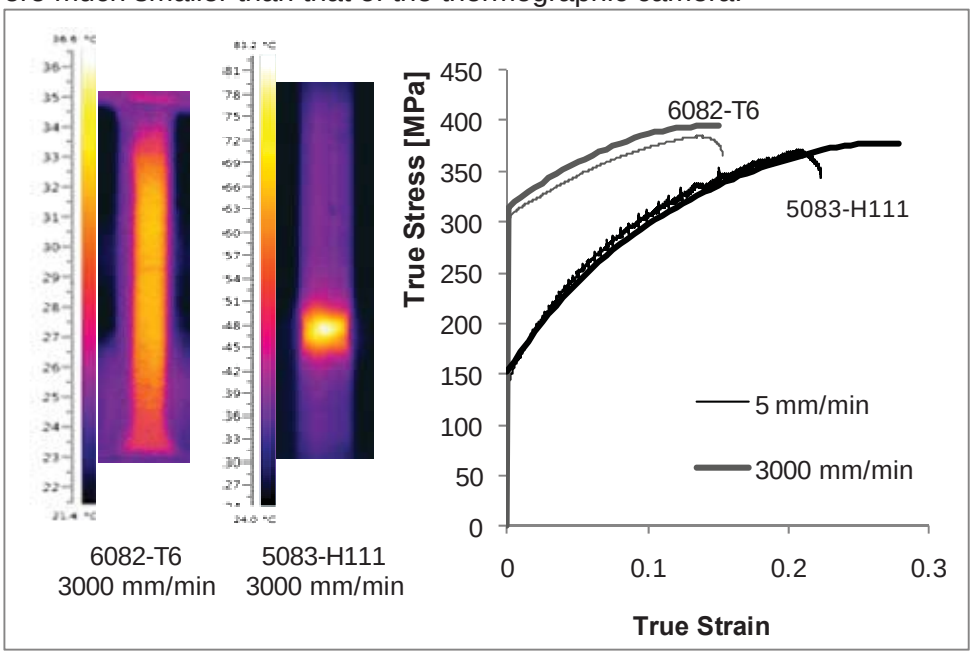

Fig. 6 – Stress-strain curves and temperature fields, close to maximum load, for 5 mm/min and 3000 mm/min tensile tests.

DISCUSSION AND CONCLUSIONS

During friction stir welding, once steady state welding conditions are attained, the dragging action of the tool over the base material will develop under constant load. So, after analysing Fig. 5 results, it is reasonable to expect that the AA 6082 alloy, which experiences strong softening with plastic deformation at increasing temperatures, will have increased weldability in FSW, since it will undergo intense plastic deformation under constant load at high temperature. On the other hand, for work-hardening materials, like the AA 5083 alloy, continued plastic deformation require increasing stress levels. According to Fig. 5, under constant load conditions like that occurring in FSW, plastic deformation of the AA 5083 alloy it will be impossible, for temperatures less than 320 ºC, and less efficient than for the AA 6082 alloy, for temperatures above 320 ºC, which is in accordance with the weld shapes displayed in Fig. 3.

The contact conditions at the tool-workpiece interface will be also determined by the plastic properties of the base materials. According to Schmidt and Hattel [7], during tool plunge and the first part of the dwell period, a large amount of heat is generated by frictional dissipation, increasing the temperature of the under-shoulder material. Consequently, under similar axial load conditions, the extreme thermal softening experienced by the AA 6082 alloy will lead to further submerging of the tool, relatively to the AA 5083 alloy, which explains the strong differences in contact area between the AA 6082 and AA 5083 welds, especially evident for the very low axial load situation illustrated in Figs. 3.a and b. Schmidt and Hattel [7] also advocate that sticking conditions at the tool-workpiece interface will be developed when the friction shear stress at the interface exceeds the yield shear stress of the underlying base material. When the contact shear stress is smaller than the base material yield shear stress, sliding conditions will prevail. Present results also show that sticking conditions will easily develop during FSW of the AA 6082 alloy, which presents decreasing flow stress with plastic deformation, and sliding or partial sliding/sticking conditions will prevail for the work hardenable AA5083 alloy. These assumptions are confirmed by the morphological observations in Fig. 3.

Assuming sticking conditions at the pin-workpiece interface, for both base materials, and that under sticking conditions heat is mainly generated by plastic deformation [7], according to Fig. 6 results, heat generation by plastic dissipation will be more intense in the very narrow layer of material deformed by the pin at high strain rates, than in its surroundings. For the AA 5083 alloy, the sharp temperature increase in this very small volume of plastically deformed material will promote intense localized softening, which in addition to the sliding contact conditions at the shoulder/workpiece interface, leads to localized deformation near the pin surface, as it is evident by the AA 5083 TMAZ shapes in Figs. 5. b, d and f. However, for the AA 6082 alloy, the concurrent effect of sticking conditions at the shoulder/workpiece interface and pronounced softening with plastic deformation, for a large range of temperatures, results in much larger deformation areas as it is visible for these welds in Figs. 5.a, c and d. Schmidt and Hattel [7] also concluded that the development of sticking contact conditions at the tool/matrix interface is important for the success of the deposition process, which is in accordance with present results.

Finally, Arora et al. [12] found decreasing FSW torque values with increasing rotational speeds and attribute this behaviour to the easier material flow at high temperatures and strain rates. In Fig. 2 are shown the torque results obtained in the FSW tests of both alloys. In the graph were also plotted trend lines fitting the torque results corresponding to the GOOD welds. In the case of the AA 6083 alloy, two different trend lines were plotted, one fitting 400 rpm results and another fitting the 500 rpm results. Comparing the results relative to this alloy, it is possible to confirm that the torque decreases when increasing the tool rotation. However, meanwhile for 400 rpm the torque also strongly decreases with increasing advancing speed, for 500 rpm, the torque results are very similar, indicating quasi-steady heat generation and deformation. Another important aspect is that, under the same tool rotation speed (500 rpm), the torque results for the AA 5083 alloy are lower than that registered for the AA 6082 alloy. These will be surely related with the lower amount o material displaced by the tool during AA 5083 welding, which was already related with the plastic behaviour of the material.

ACKNOWLEDGEMENTS

The authors are indebted to the Portuguese Foundation for the Science and Technology (FCT) and FEDER for the financial support.

REFERENCES

[1] C. Genevois*, et al.*, "Comparative study on local and global mechanical properties of 2024 T351, 2024 T6 and 5251 O friction stir welds," *Mater Sci Eng A,* vol. 415, pp. 162–170, 2006.

[2] J.-Q. Su*, et al.*, "Microstructural investigation of friction stir welded 7050-T651 Aluminum," *Acta Mater,* vol. 51, pp. 713-729, 2003.

[3] P. A. Colegrove*, et al.*, "Model for predicting heat generation and temperature in friction stir welding from the material properties " *Sci Technol Weld Joining,* vol. 12, pp. 284-297, 2007.

[4] M. Song and R. Kovacevic, "Thermal modeling of friction stir welding in a moving coordinate system and its validation," *Int J Mach Tool Manu,* vol. 43, pp. 605-615, 2003.

[5] M. Z. H. Khandkar*, et al.*, "Prediction of temperature distribution and thermal history during friction stir welding: input torque based model " *Sci Technol Weld Joining,* vol. 8, pp. 165-174, 2003.

[6] M. P. Miles*, et al.*, "Formability and Strength of Friction-Stir-Welded Aluminum Sheets," *Metal Mater Trans A,* vol. 35A, pp. 3461-3468, 2004.

[7] H. Schmidt and J. Hattel, "A local model for the thermomechanical conditions in friction stir welding," *Model Simul. Mater. Sc. Eng.,* vol. 13, pp. 77-93, 2005.
[8] P. A. Colegrove and H. R. Shercliff, "CFD modelling of friction stir welding of thick plate 7449 aluminium alloy " *Sci Technol Weld Joining,* vol. 11, pp. 429-441, 2006.
[9] S. R. Ren*, et al.*, "Effect of welding parameters on tensile properties and fracture behavior of friction stir welded Al-Mg-Si Alloy," *Scripta Mater,* vol. 56, pp. 69-72, 2007.
[10] M. Cabibbo*, et al.*, "Microstructure and mechanical property studies of AA6056 friction stir welded plate," *Mat Sci Eng A,* vol. 460-461, pp. 86-94, 2007.
[11] Y. M. Hwang*, et al.*, "Experimental study on temperature distributions whitin the workpiece during friction stir welding of aluminum alloys," *Int J Mach Tool Manu,* vol. 48, pp. 778-787, 2008.
[12] A. Arora*, et al.*, "Torque, power requirement and stir zone geometry in friction stir welding through modeling and experiments," *Scripta Mater,* vol. 60, pp. 13-16, 2009.
[13] R. Nandan*, et al.*, "Numerical simulation of three-dimensional heat transfer and plastic flow during friction stir welding " *Metal Mater Trans A,* vol. 37A, pp. 1247-1259, 2006.
[14] A. Arora*, et al.*, "Strains and strain rates during friction stir welding," *Scripta Mater,* vol. 61, pp. 863-866, 2009.
[15] Z. Zhang and J. T. Chen, "The simulation of material behaviors in friction stir welding process by using rate-dependent constitutive model " *J Mater Sci,* vol. 43, pp. 222-232, 2008.
[16] M. Rosales*, et al.*, "The backing bar role in heat transfer on aluminum alloys friction stir welding," *Mater Sci Forum,* vol. 636-637, pp. 459-464, 2010.
[17] ASM Comittee, “ASM Handbook - Properties and Selection - Nonferrous Alloys and Special-Purpose”, *ASM Handbook*, vol. 2, pp. 360-364, 1995.
[18] Automation Creations, “MatWeb – Material properties data - Aluminum 6082-T6”, Avaiable:*http://www.matweb.com/search/DataSheet.aspx?MatGUID=fad29be6e64d4e95a241690f1f6e1eb7*.

Annex H

Journal of Materials Processing Technology 212 (2012) 2051–2057

Contents lists available at SciVerse ScienceDirect

Journal of Materials Processing Technology

journal homepage: www.elsevier.com/locate/jmatprotec

Using torque sensitivity analysis in accessing Friction Stir Welding/Processing conditions

C. Leitão [a], R. Louro [b], D.M. Rodrigues [a,*]

[a] CEMUC, Mechanical Engineering Department, University of Coimbra, Portugal
[b] ISQ, Weld and Quality Institute, Portugal

ARTICLE INFO

Article history:
Received 27 February 2012
Received in revised form 8 May 2012
Accepted 16 May 2012
Available online xxx

Keywords:
FSW
Torque
Welding parameters
Materials properties

ABSTRACT

The use of Friction Stir Processing (FSP) techniques for the joining and/or transforming of metallic materials is being object of intensive research since the earliest development of the Friction Stir Welding (FSW) technology in 1991. Despite of this, an accurate understanding of the main welding/processing mechanisms and its relation with the process parameters is still missing. Current paper intends to provide some further insight on this subject by discussing the relations between processing parameters, classified as independent variables, and the corresponding welding results, classified as dependent variables, using torque sensitivity analysis. The relation between base materials properties, plate thickness, welding conditions and torque evolution were also explored, which constitutes a novelty relative to the previous studies on this subject.

1. Introduction

Since its development in the nineties, the friction stir processing (FSP) techniques, such as Friction Stir Welding (FSW) and Friction Stir Surfacing (FSS), which were developed for joining and/or improving locally material properties by using solid state processing principles, are being developed and applied based on trial and error analysis for optimizing processing conditions. Actually, full understanding of FSW/P mechanisms and/or thermomechanical principles was not achieved yet, still missing important data relating process parameters and material properties with processing conditions and processed components mechanical and metallurgical characteristics. According to Colligan and Mishra (2008), such understanding should be helpful in deciding how to change process conditions to achieve desired effects, such as improving materials strength, eliminating weld/processing defects and transferring welding/processing procedures to new processing conditions and/or materials. Finding a process output parameter, enabling full control of processing conditions and insuring suitable welding/processing results, is also an important step in consolidating the widespread application of FSW/P techniques at the industrial level.

Recently, Longhurst et al. (2010) proposed the use of the spindle torque registered by the welding machines as a process control parameter for FSW, in alternative to the commonly used plunge depth or vertical force controlled setups. According to them, using torque control, it is possible to adapt easily the weld process to changing workpiece characteristics, since it provides a more suitable indicator of the tool depth into the workpiece than axial force. Pew et al. (2007) argue that registering the torque during welding, and using it for evaluating the heat input during the process, not only enables to avoid the difficult and time consuming task of setting thermocouples before welding, but also enables post-weld analysis of the temperature fields. Khandkar et al. (2003), for example, developed an extensive numerical study of temperature distributions and thermal histories during friction stir welding by using an input torque based thermal model.

Some studies on the evolution of the spindle torque, with different processing variables, are also available in the scientific databases. Meanwhile, Cui et al. (2010) observed that torque depends mainly on rotational and welding speeds, Peel et al. (2006) and Arora et al. (2009) reported that the torque is relatively insensitive to the welding speed, since this parameter does not affect the temperature field as much as the rotation rate. Actually, several other works, such as that reported recently by Jacquin et al. (2011), clearly show that the spindle torque continuously decreases with increasing tool rotation speed. In all these works, the decrease in torque with increasing rotational speed was related to the decreasing flow strength of the base materials at increasing temperatures. This conclusion also points for a strong relation between torque and base material characteristics, which still needs to be explored. Colligan and Mishra (2008) showed that the welding torque also

* Corresponding author. Tel.: +351 239 790 700; fax: +351 239 790 701.
E-mail address: dulce.rodrigues@dem.uc.pt (D.M. Rodrigues).

0924-0136/$ – see front matter © 2012 Elsevier B.V. All rights reserved.
http://dx.doi.org/10.1016/j.jmatprotec.2012.05.009

Table 1
Welding parameters.

Alloy	Thickness [mm]		Process parameters		Tool parameters			
			v [mm min^{-1}]	ω [RPM]	D_s [mm]	D_p [mm]	α [°]	F_z [kN]
AA5083-H111	4 mm	Set1	300	400	13	5	1	7
			400	500	15	6	2	11
			500	600	18		3	15
		Set2	300–700	400–1100	15	6	3	15
	6 mm	Set1	200	300	15	6	1	10
			275	400	18	7	2	15
			350	500	21		3	20
		Set2	50–350	300–1000	21	7	3	20
AA6082-T6	3 mm	Set1	800	1000	10	4	1	5
			950	1150	12	5	2	7
			1100	1300	15		3	9
	6 mm	Set1	200	300	15	6	1	10
			275	400	18	7	2	15
			350	500	21		3	20
		Set2	200–1000	500–1000	21	7	3	20

depends on tool parameters, such as shoulder and pin dimensions. However, the range of welding conditions tested was so limited that this aspect still needs further research.

Actually, in spite of being well established the strong relation between torque and welding/processing conditions, all the studies reported to date are focused on a limited range of processing parameters, and most of them analyse results for a very specific material, tool geometry or plate thickness. Current paper intend to provide some further insight on this subject by discussing the relations between a broad range of processing conditions, classified as independent variables, and the corresponding welding results, classified as dependent variables, using torque sensitivity analysis. The welding conditions tested included not only testing varied processing parameters, which enabled to compare present data with previous studies from other authors, but also analysing the relation between base materials properties, plate thickness, welding results and torque evolution, which constitutes a novelty relative to the previous studies on this subject.

2. Experimental procedure

The two base materials used in this study were a non-heat-treatable AA5083-H111 and a heat-treatable AA6082-T6 aluminium alloy, each supplied in two different plate thicknesses: 6 mm and 4 mm, for AA5083-H111 alloy, which will be labelled as 5_6 and 5_4, respectively, and 6 and 3 mm, for the AA6082-T6 alloy, which will be labelled as 6_6 and 6_3, respectively. Bead-on-plate welds were produced in order to avoid any influence of sheet positioning and clamping on torque sensitivity analysis.

Tools with conical shoulders, with a cone angle of 5°, and cylindrical threaded pins, were used in all welding tests. Although the geometry was maintained, the tool dimensions, namely, the pin (D_p) diameter, shoulder (D_s) diameter and pitch angle (α) were varied. For each tool tested, the welding speeds (v), rotating speeds (ω) and vertical forces (F_z) were varied according to the values displayed in Table 1. Using the parameters identified as *Set1*, Taguchi analysis was performed in order to establish a testing plan for each base material and plate thickness, as described in Louro et al. (2010), which determined a total of 114 welding tests to be performed. After analysing *Set1* welding results, some supplementary tests were scheduled for both base materials (identified as *Set2*, in Table 1), in order to accomplish a more comprehensive analysis of their welding behaviour.

After welding, all welds were visually inspected for identifying defects such as flash and surface flaws. Transverse weld specimens were also prepared, cold mounted, polished, etched and observed using the Zeiss Stemi 2000-C and Zeiss Axiotech 100HD microscopes, for detecting large and very small internal flaws, as well as for analysing welds' morphology. Finally, using the FSW machine output data, the average torque values, for each welding test, were listed and analysed in relation to welding results.

3. Torque sensitivity analysis

3.1. Influence of plates thickness and process parameters

In Figs. 1 and 2 are plotted the average torque values versus the rotational to weld speed ratio (ω/v), corresponding to all welding tests performed for the AA5083 and AA6082 alloys, respectively. The results plotted in the figures are categorised according to the classification adopted after weld inspection: the welding conditions conducting to welds with no defects or very small defects, which were labelled as *GOOD*, are represented by large circles, and the welding conditions conducting to welds with defects, such as flash (*F*), surface flaws (*SD*) and internal voids (*ID*) are represented with smaller symbols, of different shapes, according to the defect type. Welding conditions, for which the pin was broken (*BP*), precluding the execution of the weld, are also identified. A detailed

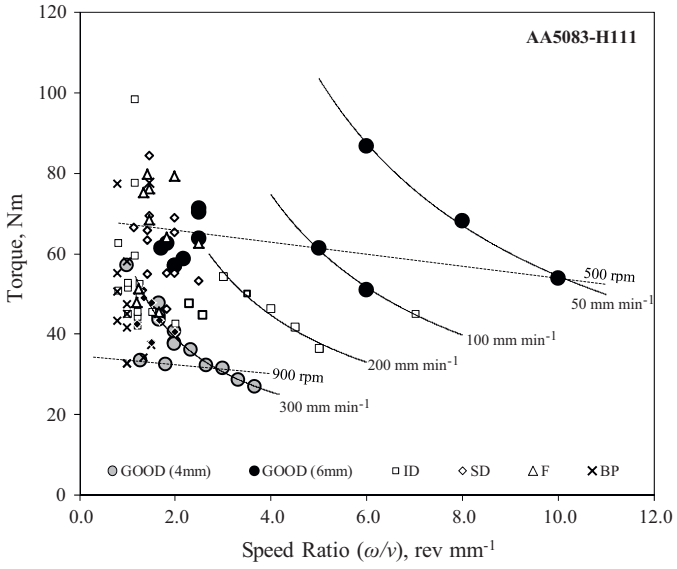

Fig. 1. Torque evolution with (ω/v) and weld inspection results for the AA5083 welds.

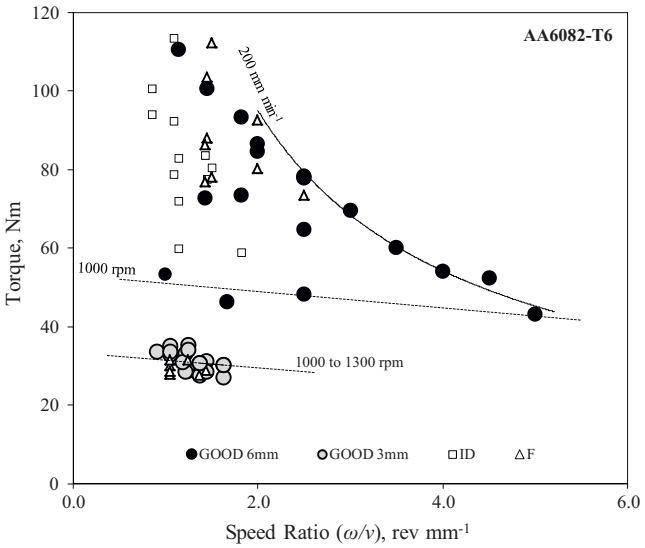

Fig. 2. Torque evolution with (ω/v) and weld inspection results for the AA6082 welds.

analysis of the welding results and its relation with processing parameters and base materials properties can be found in Rodrigues et al. (2010) work.

Analysing the results in Figs. 1 and 2, it is possible to conclude that, for the lower ω/v range, corresponding to *Set1* parameters, for which a large number of defective welds were produced for both alloys, which is evidenced by the large number of very small symbols almost aleatorily distributed, no clear tendency in the evolution of the torque results with process parameters can be found. This shows that the torque registered during welding is very sensitive to non-equilibrium welding conditions conducting to the formation of very large weld defects. It is also possible to conclude that for a same range of ω/v values, independently of the base material, much lower torque values were registered in thinner than in thick plates welding. For the 6_3 plates, contrary to that registered for the 6_6, 5_6 and 5_4 plates, only very small torque variations were registered, even using a broad range of welding conditions (*Set1* parameters) conducting to both *GOOD* and defective welds.

Some trend-lines were schematized in Figs. 1 and 2, fitting the torque evolution with ω/v, for some selected welding and rotational speeds corresponding mostly to *GOOD* welding conditions. More precisely, the torque values fitted by each trend line correspond to welds performed using *Set2* parameters, which correspond to a unique tool and axial load, but varying welding and rotational speeds. Analysing the trend lines plotted for the 5_6, 6_6 and 5_4 welds, it is possible to conclude that, independently of the base material, and plate's thickness, for a constant welding speed, the torque values strongly decrease with increasing rotational speed. For a constant rotational speed, and varying welding speeds, no important changes in torque were registered. These results are in accordance with previous authors findings, already reported in paper introduction. On the other hand, from Figs. 1 and 2 it is also possible to conclude that for the lower range of ω/v values, corresponding to *Set1* of testing conditions, i.e., welding tests performed using different tools and axial loads, the torque values corresponding to the *GOOD* welds also display strong variations, even for welding conditions corresponding to equal rotational and welding speeds (same ω/v).

In order to better illustrate this aspect, in Fig. 3, are plotted some torque results, corresponding to selected *GOOD* welding conditions, together with an explicit identification of the shoulder diameter (D_s) and axial load (F_z) corresponding to each test. Since previous

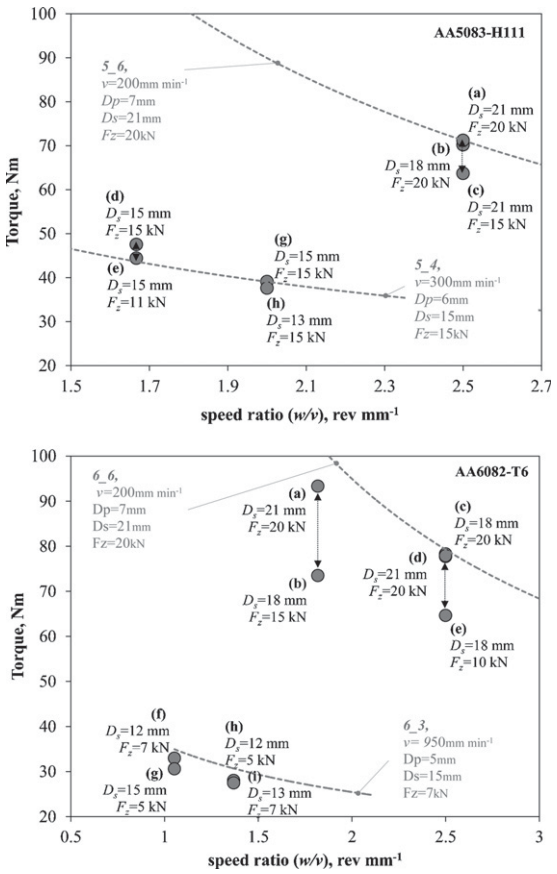

Fig. 3. Influence of vertical force, tilt angle and shoulder diameter on torque.

analyses of welding results from Rodrigues et al. (2010) showed that varying the pin diameter (D_p) had no influence on welding results, and tool tilt angles (α) lower than 3° conducted mostly to defective welding, no influence of these two parameters on *GOOD* welding torque results was reported. Fig. 3a and b shows that, for both base materials, higher torque sensitivity to varying welding conditions was registered in thicker plates welding (5_6 and 6_6) than in thinner plates welding (5_4 and 6_3), since higher variations in torque values were registered for the former tests by varying a single welding parameter. The figure also shows that, despite the strong influence of the shoulder diameter (D_s) on weld quality, depicted in previous analyses of the welding results, performed by Rodrigues et al. (2010), this parameter had a very small influence on registered torque since, independently of the plate thickness and of the base material, very similar torque values were registered when the only parameter varied was the shoulder diameter. Contrary to this, important differences in torque results were reported when varying the axial load. This is in accordance with Longhurst et al. (2010) who proposed the use of the spindle torque registered by the welding machines as a process control parameter for FSW, instead of displacement or force control devices, pointing for the extreme sensitivity of this parameter to varying tool position, and consequently, varying axial load.

3.2. Influence of base materials properties

In order to analyse the influence of base material properties on torque results, in Fig. 4 are plotted the torque values corresponding to a similar range of welding conditions (*Set1* parameters), for both base materials and same plate thickness (5_6 and 6_6 welds), and also torque results corresponding to optimized welding conditions for each alloy (*Set2* parameters). The figure shows very

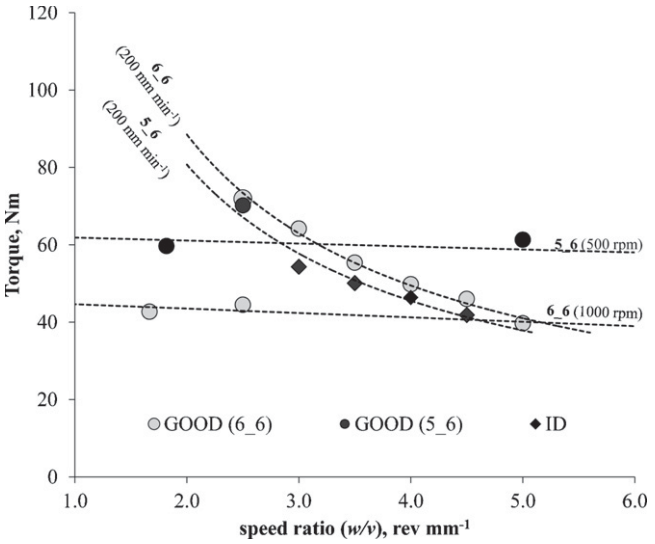

Fig. 4. Torque evolution with speed ratio for constant rotational and weld speeds.

similar torque evolution for both alloys, at constant welding speed (200 mm min^{-1}) and increasing rotation speeds. However, as is also clearly evidenced in the figure, the welding results under these welding conditions were drastically different for both alloys. Meanwhile, for the AA6082 alloy, only *GOOD* welds were obtained for the full set of rotation speeds plotted in the figure, for the AA5083 alloy, several welds with internal defects were produced using exactly the same welding parameters.

The results in Fig. 4 also show that for the AA5083 alloy the torque values corresponding to the optimized welding parameters (*Set2* parameters) are, in a general manner, higher than those corresponding to AA6082 *GOOD* welding conditions. Actually, for the AA5083 alloy, it was already pointed that welding at increasing tool rotation speeds, which is the main factor in reducing the torque values, the welds obtained displayed internal defects. For this alloy, as can be depicted by analysing the 100 and 50 mm min^{-1} curves plotted in Fig. 1, welding results were improved by using rotation speeds equal or lower than 500 rpm and welding speeds lower than 200 mm min^{-1}. On the other hand, for the AA6082 alloy, once optimized the tool geometry and axial load (*Set1* tests), non-defective welds were produced by simultaneously increasing the tool rotation and traverse speeds (*Set2* tests), which according Mononen et al. (2003) is very interesting in terms of industrial productivity. Naturally, increasing the tool rotation speed, decreases the spindle torque, which enabled performing non-defective welding at much lower torque than that required for AA5083 non-defective welding.

Since in Fig. 4, in spite of the very different welding results obtained in 5_6 and 6_6 welding, very similar torque evolution was registered for both base materials, the following equation was used for adjusting the torque results corresponding to both alloys:

$$T = a \times \omega^{-b}. \quad (1)$$

In this equation, a and b are constants, depending on process parameters, plate thickness and base material characteristics, which were found as the main factors in affecting the welding conditions.

From current and previous analyses performed by Rodrigues et al. (2010), it was possible to conclude that both the tool parameters and tool axial load are very restrictive parameters, which should be carefully selected before optimizing tool traverse and rotation speeds, namely, shoulder diameter should not be less than 3.5 times plate thickness, tool tilt angle should not be less than 3° and optimal axial load should also be estimated before welding

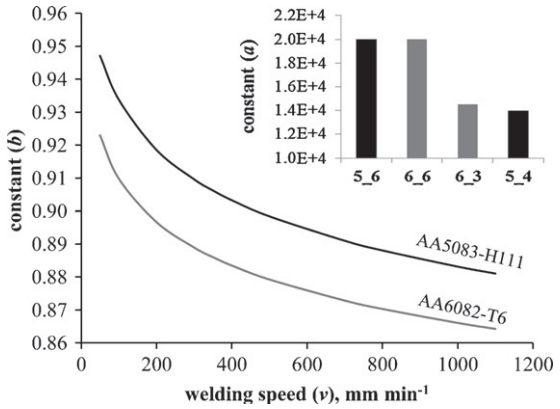

Fig. 5. Influence of the base material and weld speed on constant (b); thickness effect on constant (a).

by, for example, performing welding tests in position control. After that, tool rotation and traverse speeds should be optimized in order to provide the better compromise between weld quality and productivity. Based on this assumptions, constants a and b in Eq. (1) were determined considering the plate thickness and the tool rotation and traverse speeds as the main independent variables in the process. For each alloy, both constants were identified by adjusting the equation, using simple log-linearization, to the torque values corresponding to *Set2* welding conditions, i.e., unique tool parameters and axial load and varying rotation and welding speeds. The results obtained are shown in Fig. 5, where it is possible to see that meanwhile the constant a was found to vary mainly with plate thickness, being almost independent of base material characteristics, the constant b it was found to strongly vary with welding speed, following similar evolution for both alloys, but with consistently higher values for the AA5083 alloy. This indicates that torque sensitivity to welding speed is directly related to the material properties.

In Figs. 6 and 7 are plotted, for the AA5083 and AA6082 alloys, respectively, the torque results corresponding to *GOOD* welding conditions as function of the rotation and traverse speeds. In the same figures are shown the curves corresponding to Eq. (1), plotted using the welding parameters for each set of experimental results plotted in the figure. It is possible to see that the equation satisfactorily fits all the experimental results shown in the graph. From the figure it is also possible to see that the AA5083 alloy displays much higher torque variation with tool welding speed than the AA6082

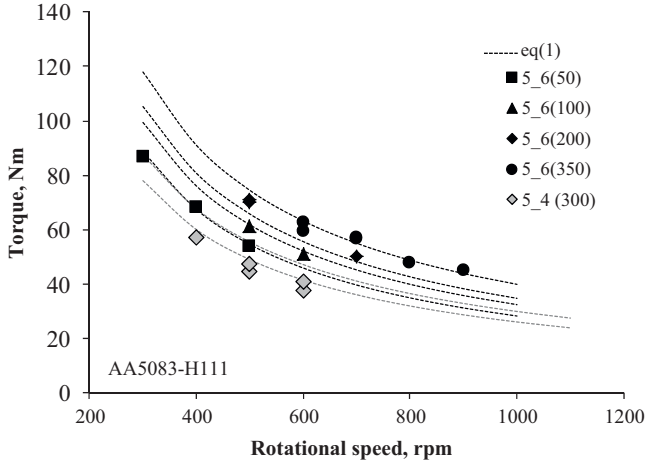

Fig. 6. Theoretical and Experimental torque comparison for the AA5083 welds.

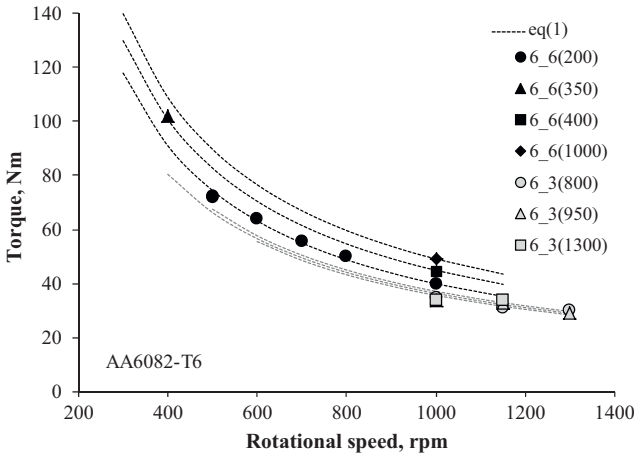

Fig. 7. Theoretical and experimental torque comparison for the AA6082 welds.

alloy. Actually, for the 6_3 welding conditions, almost no evolution of the torque results with varying welding speed was registered.

4. Discussion

From Fig. 4, it was concluded that using optimized tool parameters and axial force, conducting to non-defective welds production, the evolution of the torque with tool rotation and traverse speed is very similar for both base materials, in spite of higher torque values being registered for non-defective welding of the AA5083 alloy, than for the AA6082 alloy.

Arora et al. (2009) stated that increasing the tool rotation speed, increases the temperature, decreasing the flow stresses associated to material stirring during the process, which decreases the spindle torque. So, the differences in torque levels for the AA5083 and AA6082 alloys must be related to the use of lower rotation rates for non-defective FSW of the AA5083 alloy. Actually, as already mentioned, for this alloy it was found that increasing the rotation speed (from 500 rpm to 1000 rpm) at a constant welding speed of 200 mm min^{-1}, promoted the formation of internal defects, with non-conventional morphology, which is illustrated in Fig. 8, where 600 and 1000 rpm welds are compared with non-defective welds produced at lower tool rotation and welding speeds. In this figure, it is possible to see that the internal defects registered for welds produced at higher tool rotation consist of small discontinuities, at the advancing side of the tool, where the pin and shoulder governed material flows merge together. The morphology of the discontinuity suggests that merging/mixing of the materials from the two different flow volumes was unsuccessful, which, according to Iordachescu et al. (2009), this is associated with low heat input during welding and may be suppressed by increasing the tool rotation speed. However, from current study, it is obvious that for the AA5083 alloy, increasing the tool rotation rate did not improved material flowability.

Leitão et al. (2012) analysed the plastic behaviour of both base materials at high temperatures, and its relation with their weldability in FSW, and reported that the AA6082 alloy, which is sensitive to dynamic precipitation and overageing under intense non-uniform deformation, displays good weldability in FSW, since it is easily dragged by the tool during welding. Under similar welding conditions, the AA5083 alloy, which in quasi-static conditions displays steady flow behaviour at increasing temperatures, and may be sensitive to hardening at high strain rates, displayed poor weldability in FSW, due to the increased difficulty in dragging this base material during welding. Differences in plastic behaviour between both base materials should also justify the differences in base materials sensitivity to the tool rotation and traverse speeds, depicted from current welding inspection work and torque sensitivity analyses.

In fact, according to the results shown in current paper, the AA5083 alloy displays increased weldability at decreasing tool

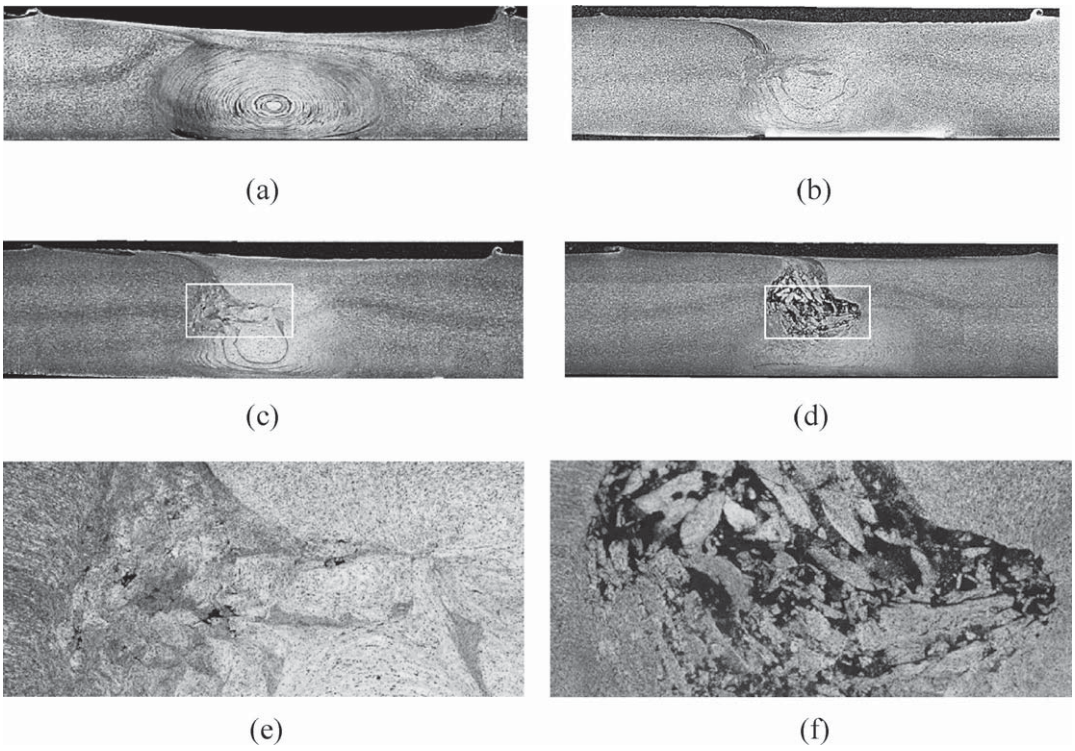

Fig. 8. Cross-sections of the 5_6 welds for rotational/weld speeds of 500/50 (a), 500/200 (b), 600/200 (c) and 1000/200 (d), and detailed view pictures of the signalized areas for the 600/200 weld (e) and 1000/200 weld (f).

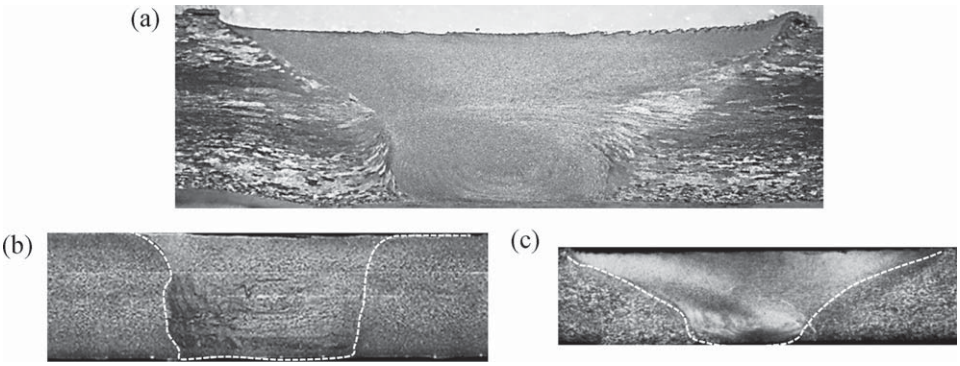

Fig. 9. Cross-sections of 6_6, 5_4 and 6_3 welds corresponding to rotational/weld speeds of 500/200 (a), 900/700 (b) and 1150/800 (c), respectively.

rotation and welding speeds. Assuming that this material is strain rate sensitive, as stated by Kim et al. (2010), at the high strain rates experienced during FSW, the dislocation generation rate in the stir volume may rise to a level that increases the effective time for recovery, resulting in increased flow stresses during welding.

According to Long et al. (2007), which performed studies in FSW, and Dehghani and Chabok (2011), which performed studies in FSP, the strain rate during FSW/P increases with increasing tool rotation speed. Therefore, it is expectable that the AA5083 weldability, which is related with the plastic behaviour of the material at high strain rates, will diminish at increasing tool rotation rates. By diminishing the tool rotation rate, diminishes the strain rate during the process, improving AA5083 flowability. Actually, it was observed that the 5_6 plates weldability was deeply improved by simultaneously diminishing the tool rotation and welding speeds. By diminishing the tool rotation rate, diminishes the strain rate during the process. Diminishing the welding speed insures a more uniform temperature distribution across plate thickness, as stated by Zhang et al. (2011), insuring a more uniform distribution of heat between the shoulder and pin governed flow volumes, which will conduct to more uniform material flow characteristics and improved material merging between the different flow layers. The longitudinal tool displacement per revolution (v/ω [mm rev^{-1}]) also becomes lower at decreasing welding speeds, diminishing the volume of material displaced by the tool at each revolution, which will also contribute for improving merging/mixing between the different material flow layers. Comparing Fig. 8a and b it is possible to confirm that diminishing the welding speed improved material flow, since meanwhile the weld performed at the lower welding speed (Fig. 8a) displays a well-defined onion ring structure, the weld performed at higher welding speed (Fig. 8b) shows much less defined material flow features and "incomplete" onion ring structure, which points for a less efficient material mixing between the shoulder and pin driving flow volumes.

It is also important to enhance that when welding the AA5083 alloy in the lower plate thickness, non-defective welding results were obtained even at high tool rotation rates, which should be a result of a more uniform temperature and material flow across the thickness. Figs. 8 and 9 show, for both base materials, that the interface between the shoulder and pin governed flow volumes become less evident by diminishing the plate thickness, indicating a more efficient through thickness material mixing, which deeply contributed in diminishing the amount of defects for both alloys.

The strong influence of plate thickness on welding conditions was also patent from the torque sensitivity analysis, since much higher differences in torque values were reported in thicker than in thinner plates welding by changing the processing conditions. Actually, for each base material, at similar rotation rates, the torque values registered in thinner plates welding were much lower than those registered in thicker plates welding. This should be related to the lower amount of material being processed at each revolution, as well as to more favourable material flow across the thickness under the more uniform through thickness temperature in thinner plates welding. The strong influence of plate thickness on welding conditions and torque evolution was also patented by adjusting the torque governing equation (Eq. (1)) to the experimental results, when it was found that constant a value is mainly influenced by plate thickness.

Finally, strong variations in torque results were also registered in thick plates welding by varying the axial load, which also has a strong influence on through thickness material flow and heat generation during welding. Very small axial load values conducted to inadequate material flow, with important surface or internal defects being formed, and very high axial load values promoted material expulsion from the stirring volume, conducting to massive flash formation. Torque results and weld inspection revealed that there is a much narrow interval for optimal axial load than for the tool traverse and rotational speeds.

5. Conclusions

From present results it was possible to depict a strong influence of base material plastic behaviour and plate's thickness on welding results and on torque registered during welding. Despite of this, for constant tool parameters and axial load, the evolution of torque with tool traverse and rotation speed was found to be independent from both factors, being described by a unique power law equation. Modelling of torque results enabled to conclude that meanwhile the tool rotation speed and plate's thickness are the main factors in determining torque values, due to its strong influence on heat generation and through thickness heat distribution and material flow, the welding speed had no strong influence on average torque levels. Base material plastic properties also have a strong, but indirect, impact on torque results. Actually, plastic properties determine the sensitivity of the base materials, and consequently welding conditions, to varying tool rotation and traverse speeds, determining by that way torque results. Torque results were also found to be very sensitive to varying axial load, mainly in thicker plates welding, due to the above-mentioned reasons. No influence of varying shoulder diameter on torque results was reported.

Acknowledgements

The authors are indebted to the Portuguese Foundation for the Science and Technology (FCT) through COMPETE program from QREN and to FEDER for the financial support.

References

Arora, A., Nandan, R., Reynolds, A.P., DebRoy, T., 2009. Torque, power requirement and stir zone geometry in friction stir welding through modeling and experiments. Scripta Materialia 60, 13–16.

Colligan, K.J., Mishra, R.S., 2008. A conceptual model for the process variables related to heat generation in friction stir welding of aluminum. Scripta Materialia 58, 327–331.

Cui, S., Chen, Z.W., Robson, J.D., 2010. A model relating tool torque and its associated power and specific energy to rotation and forward speeds during friction stir welding/processing. International Journal of Machine Tools and Manufacture 50, 1023–1030.

Dehghani, K., Chabok, A., 2011. Dependence of Zener parameter on the nanograins formed during friction stir processing of interstitial free steels. Materials Science and Engineering A 528, 4325–4330.

Iordachescu, M., Iordachescu, D., Ocana, J.L., Vilaca, P., Scutelnicu, E., 2009. FSW – characteristic flaws in aluminium alloys joints. Metalurgia International 14, 135–138.

Jacquin, D., de Meester, B., Simar, A., Deloison, D., Montheillet, F., Desrayaud, C., 2011. A simple Eulerian thermomechanical modeling of friction stir welding. Journal of Materials Processing Technology 211, 57–65.

Khandkar, M.Z.H., Khan, J.A., Reynolds, A.P., 2003. Prediction of temperature distribution and thermal history during friction stir welding: input torque based model. Science and Technology of Welding & Joining 8, 165–174.

Kim, D., Badarinarayan, H., Kim, J.H., Kim, C., Okamoto, K., Wagoner, R.H., Chung, K., 2010. Numerical simulation of friction stir butt welding process for AA5083-H18 sheets. European Journal of Mechanics – A/Solids 29, 204–215.

Leitão, C., Louro, R., Rodrigues, D.M., 2012. Analysis of high temperature plastic behaviour and its relation with weldability in friction stir welding for aluminium alloys AA5083-H111 and AA6082-T6. Materials & Design 37, 402–409.

Long, T., Tang, W., Reynolds, A.P., 2007. Process response parameter relationships in aluminium alloy friction stir welds. Science and Technology of Welding & Joining 12, 311–317.

Longhurst, W.R., Strauss, A.M., Cook, G.E., Fleming, P.A., 2010. Torque control of friction stir welding for manufacturing and automation. International Journal of Advanced Manufacturing Technology 51, 905–913.

Louro, R., Leitao, C., Gouveia, H., Loureiro, A., Rodrigues, D., 2010. In: Rosa, L.G.M.F. (Ed.), Taguchi analysis of the effect of process parameters in friction stir welding. Materials Science Forum, 1150–1156.

Mononen, J., Sirén, M., Hänninen, H., 2003. Cost comparison of FSW and MIG welded aluminium panels. Weld World 47, 32–35.

Peel, M.J., Steuwer, A., Withers, P.J., Dickerson, T., Shi, Q., Shercliff, H., 2006. Dissimilar friction stir welds in AA5083-AA6082. Part I: Process parameter effects on thermal history and weld properties. Materials Science and Engineering A 37A, 2183–2193.

Pew, J.W., Nelson, T.W., Sorensen, C.D., 2007. Torque based weld power model for friction stir welding. Science and Technology of Welding & Joining 12, 341–347.

Rodrigues, D.M., Leitao, C., Louro, R., Gouveia, H., Loureiro, A., 2010. High speed friction stir welding of aluminium alloys. Science and Technology of Welding & Joining 15, 676–681.

Zhang, X.X., Xiao, B.L., Ma, Z.Y., 2011. A transient thermal model for friction stir weld. Part II: effects of weld conditions. Materials Science and Engineering A 42A, 3229–3239.